NMR Studies of Selective Population Inversion and Spin Clustering

Jean S. Baum
Ph.D. Thesis

Lawrence Berkeley Laboratory
University of California
Berkeley, California 94720

February 1986

The United States Department of Energy has the right to use this thesis for any purpose whatsoever including the right to reproduce all or any part thereof.

LBL - 21259

NMR Studies of Selective Population Inversion and Spin Clustering

Copyright © 1986

Jean S. Baum

This work was supported by the Director, Office of Basic Energy Sciences, Materials Sciences Divsion of the US Department of Energy under Contract DE-AC03-76SF-000-98.

NMR STUDIES OF SELECTIVE POPULATION INVERSION AND SPIN CLUSTERING

Jean Baum

Abstract

This work describes the development and application of selective excitation techniques in Nuclear Magnetic Resonance. Composite pulses and multiple-quantum methods are used to accomplish various goals, such as broadband and narrowband excitation in liquids, and collective excitation of groups of spins in solids. These methods are applied to a variety of problems, including non-invasive spatial localization, spin cluster size characterization in disordered solids and solid state NMR imaging.

A class of continuously phase modulated radiation pulses that result in coherent population inversion on resonance as well as over a large range of transition frequencies and radiation field strengths are presented. The inversion behavior is explained by treating the pulses as highly efficient adiabatic sweeps. A method is presented for generating a sequence of phase-shifted radiofrequency pulses, generally called composite pulses, from the continuously modulated pulse. Simulations of the inversion performance, and experimental results, are given.

Multiple-quantum NMR is used to understand aspects of nuclear spin dynamics in solids and to develop new techniques for studying spin clustering and materials characterization. The progressive appearance of multiple-quantum transitions with increasing excitation time is shown to depend on the formation of multiple-spin correlations. Therefore, a time-resolved multiple-quantum experiment, whose

statistics are very sensitive to inter-atomic distances, is employed to determine the spatial distribution of atoms in materials lacking long range order. Experiments are performed by studying the time-dependence of the multiple-quantum coherences, and results are presented on the hydrogen distribution in model systems of selectively deuterated organic solids. In addition, the technique is used to study the nature and extent of hydrogen clustering in hydrogenated amorphous silicon.

Both composite pulses and multiple-quantum methods are applied to spatial localization and solid state NMR imaging. A spatially selective composite pulse sequence is designed and used to excite chemically shifted NMR signals from localized regions in space, in a non-invasive manner. Finally, the properties of multiple-quantum coherence are used to improve, by an order of magnitude, the spatial resolution possible in solid state imaging experiments. Both approaches are illustrated experimentally on phantom samples.

TO MY PARENTS AND SISTER

ACKNOWLEDGMENTS

Working in the laboratory of Professor Alexander Pines over the last five years has been a very special experience. I would like to thank Alex for his constant support and encouragement, and for providing me with numerous ideas. His approach to science and high standards have guided my research.

Rob Tycko has greatly influenced my development in NMR. I thank him for inspiring me, and for the many discussions, on composite pulses and other aspects of NMR, during which he shared his insights. Michael Munowitz and Allen Garroway made numerous contributions to the multiple-quantum NMR studies. In addition, Michael's willingness to devote time to conversations about my research, and NMR in general, are much appreciated. I benefitted from interesting discussions with Jeffrey Reimer, who introduced me to hydrogenated amorphous silicon, and Herman Cho.

In addition, I would like to thank Joel Garbow, Jim Murdoch, Dan Weitekamp, Mel Klein, Karen Gleason, Miriam Gochin, David Zax, John Millar, Ann Thayer and David Shykind for enlightening conversations and assistance with different facets of my work. Dione Carmichael has always been very helpful, and Theresa Allyn patiently and expertly typed the manuscript.

To my friends, particularly John, thank you.

TABLE OF CONTENTS

I. BACKGROUND.....1

A. Introduction.....1

B. Nuclear Spin Hamiltonians.....3

1. Zeeman Interaction.....3

2. Radio-Frequency Interaction.....5

3. Rotating Frame Transformation.....5

4. Chemical Shift Hamiltonian.....8

5. Dipolar Hamiltonian.....8

C. Density Operator.....9

1. Equilibrium Density Operator.....10

2. Evolution of the Density Operator.....11

3. Expansion of the Density Operator in Different Basis Sets.....13

a. Pauli-Spin Matrices.....13

b. Outer Product Eigenbasis.....14

c. Single Spin Product Operators.....15

D. Pulse Sequences.....16

E. Average Hamiltonian Theory.....19

F. References.....21

I. BROADBAND AND ADIABATIC INVERSION OF A TWO-LEVEL SYSTEM BY PHASE MODULATED PULSES.....22

A. Introduction.....22

1. Background.....22

2. Organization.....25

B. Derivation of Phase Modulated Pulses for Population Inversion.....26

1. Frames of Reference.....26

2. Derivation of Phase Modulation from Magnetization Trajectories.....28

3. Inversion Performance Off Resonance.....34

4. Transformation to Amplitude-Modulated Pulses.....37

C. Population Inversion by Adiabatic Sweeps.....40

1. Criteria for Adiabatic Inversion.....40

2. Linear Sweep.....43

3. Modulated Inversion Pulse.....45

4. Constant Adiabaticity Pulse.....46

D. Inversion in an Inhomogeneous Radio-Frequency Field.....52

E. Generation of Discrete Composite Pulses from Continuously Phase Modulated Pulses.....55

1. General Method of Approximation Using Magnetization Trajectories.....55

2. Pulse Sequences with Unrestricted Phases.....57

3. Composite Pulses with Constant Phase Increments.....62

F. Experimental Methods.....67

G. Summary.....68

H. Appendix.....70

I. References.....72

III. MULTIPLE-QUANTUM NMR IN SOLIDS: THEORY AND EXPERIMENTAL CONSIDERATIONS.....74

A. Introduction.....74

B. Generalized Multiple-Quantum NMR Experiment.....75

1. Preparation Period.....77

2. Evolution Period.....84

a. $H_{int} = H_{zz}$.....84

b. $H_{int} = \Delta\omega I_z$ 84

c. Time Proportional Phase Incrementation 85

3. Mixing Period 88

4. Detection Period 89

C. Multiple-Quantum Intensities 90

1. Statistical Model for Line Intensities 90

2. Time-Reversed Excitation in Solids 93

D. Pulse Sequence Design 96

E. Experimental Implementation 100

1. Preparation Period 100

2. Evolution Period 100

3. Mixing Period 101

4. Detection Period 102

5. Tune-Up Procedure 105

6. Spectrometer Implementation 106

a. Phase Shifter 106

b. Split Ram 109

F. References 111

IV. MULTIPLE-QUANTUM NMR STUDIES OF CLUSTERING IN SOLIDS 114

A. Introduction 114

B. Multiple-Quantum Dynamics in Solid State NMR 118

1. Multiple Spin Processes and Time Development of the Dipolar Coupling Network 118

2. Time Development of Multiple-Quantum Coherences 123

3. Monitoring of Time Reversal Via the Refocusing of Multiple-Quantum Coherence 127

4. Measurement of an Effective System Size

in Solids.....132

C. Study of Clustering in Solids.....135

1. Uniform Distributions.....135

a. Adamantane.....135

b. Squaric Acid.....137

2. Isolated Clusters: Liquid Crystal.....139

3. Concentration Effects:
1,8-dimethylnaphtalene-d_6.....139

4. Two-Gaussian Model.....148

5. More Dilute Spin Systems and Clusters.....151

a. 1,8 dimethylnaphtalene-d_{10}.....151

b. Hexamethylbenzene.....154

c. 1,2,3,4,-tetrachloronaphtalene-
bis(hexachlorocyclopentadiene)-adduct.....158

D. Application to Hydrogen Clustering in
Hydrogenated Amorphous Silicon.....163

1. Background.....163

2. Experimentals Results and Discussion.....166

3. Conclusion.....173

E. Conclusion.....174

1. Extension of the Multiple-Quantum
Experiment in Solids.....174

a. Maintaining a Fixed t_1 Period.....174

b. Scaled Pulse Sequence.....175

2. Summary.....177

F. Appendix.....180

G. References.....184

V. APPLICATIONS OF COMPOSITE PULSES AND MULTIPLE-QUANTUM METHODS TO IN-VIVO NMR AND IMAGING.....186

A. Spatially Selective NMR with Broadband Radiofrequency Pulses.....186

1. Introduction.....186

2. Development of Pulse Sequences.....187

a. Narrowband Localized Excitation (NOBLE).....187

b. Selective Inversion Sequences.....189

c. Read Sequences.....190

3. Experimental Demonstration of NOBLE.....194

a. Experimental Design.....194

b. Experimental Results.....196

4. Discussion of Spatial Localization Methods.....201

5. Conclusion.....205

a. Composite $\pi/2$ Pulses.....205

b. Summary.....206

B. NMR Imaging of Solids by Multiple-Quantum Resonance.....208

1. Introduction.....208

2. n-Fold Increase in Gradient Strength.....209

3. Experimental Design.....209

4. Experimental Results and Discussion.....213

C. References.....218

VI. APPENDIX: COMPUTER PROGRAMS.....222

I. BACKGROUND

A. Introduction

In NMR, sophisticated radio-frequency pulse sequences are often designed to excite a desired response from the nuclear spin system. In this dissertation, two general categories of excitation are addressed. The first is the tailored excitation of nuclear spins over different radio-frequency field strengths and transition frequencies. The second is the collective excitation of groups of spins, in a solid, via multiple-quantum NMR. Theoretical approaches to these problems, and the development and application of new techniques are the subject of this work. Applications include spin cluster size characterization in materials lacking long-range order, solid state NMR imaging, and the non-invasive excitation of NMR signals from a localized region of a sample.

A general analytical procedure for deriving continuously phase modulated pulses that result in coherent population inversion on resonance as well as over a large range of transition frequencies or radio-frequency field strengths is presented in Chapter II. The inversion behavior is explained by treating the pulse as an efficient adiabatic sweep. A method for generating a sequence of phase-shifted radiofrequency (rf) pulses, generally called a composite pulse, from the continuously modulated pulse is given.

The general principles of multiple-quantum NMR, including the time-reversal excitation needed in solids, are described in Chapter

III. Experimental considerations for the multiple-quantum experiments used in Chapter IV are presented.

A time-resolved multiple-quantum NMR experiment is presented in Chapter IV. It is used to investigate multiple-quantum dynamics in solid-state NMR and to characterize the hydrogen distribution in materials lacking long-range order. By studying the time-development of the multiple-quantum spectral intensities, the nature and extent of clustering can be ascertained in disordered solids. Many model compounds containing a range of hydrogen distributions - isolated clusters, concentrations of clusters, uniform distributions - are investigated experimentally. In addition, the technique is used to study the hydrogen distribution in hydrogenated amorphous silicon.

Spatial localization and solid-state NMR imaging are discussed in Chapter V. Composite pulses, narrowband in space and broadband in frequency are found through a computer search, and used experimentally with a surface coil to selectively excite a localized region of a phantom sample. Multiple-quantum NMR is used to overcome some of the problems associated with solid-state NMR imaging. By relying on the property that an n-quantum coherence feels an effective gradient which is n times its actual strength, imaging in solids is possible with rather small magnetic gradients. The technique is illustrated experimentally on a phantom sample.

In the rest of this chapter the spin Hamiltonian and the description of the spin system in terms of the density operator are introduced. Different basis sets used for the formalism of broadband excitation and multiple-quantum NMR are presented. Average Hamiltonian

theory is very briefly described.

B. Nuclear Spin Hamiltonians

1. Zeeman Interaction

The Zeeman Hamiltonian, which describes the interaction of the nuclear dipole moment with the static external field, is introduced. Generally, the overall spin Hamiltonian

$$H = H_{ext} + H_{int} \tag{1.1}$$

is a sum of internal and external couplings. The external Hamiltonian includes all interactions of the spins with the magnetic field, either static or oscillating. The internal Hamiltonian includes all interactions of spins with their local environment; for example, dipolar, chemical shift and indirect scalar interactions.[1-4]

The energy of interaction of a nuclear magnetic dipole moment $\underset{\sim}{\mu}$ with a magnetic field $\underset{\sim}{B}_o$ is

$$E = -\underset{\sim}{\mu} \cdot \underset{\sim}{B}_o \ . \tag{1.2}$$

The magnetic moment is proportional to the nuclear spin angular momentum vector $\underset{\sim}{I}$. Thus when the field $\underset{\sim}{B}_o$ is along the z direction, the Zeeman Hamiltonian becomes

$$H = -\underset{\sim}{\mu} \cdot \underset{\sim}{B}_o = -\gamma I_z B_o \tag{1.3}$$

$$= -\omega_o I_z \quad ,$$

where γ is the gyromagnetic ratio and ω_o is expressed in angular frequency units of rad/sec. The eigenstates of H are the set $\{|m\rangle\}$ defined as

$$I_z|m\rangle = m|m\rangle \tag{1.4}$$

$$I^2|m\rangle = I(I + 1)|m\rangle \tag{1.5}$$

where $m = -I, -I+1, \ldots, I-1, I$.

A nucleus of spin I has $(2I + 1)$ eigenstates labelled by m, the eigenvalue of I_z. For N interacting nuclei, the number of eigenstates becomes $(2I + 1)^N$ and the eigenoperator I_z,

$$I_z = \sum_{i=1}^{N} I_{zi}, \tag{1.6}$$

now yields the total Zeeman quantum number,

$$M_i = \sum_{i=1}^{N} m_i \quad , \tag{1.7}$$

the sum of the individual spin Zeeman quantum numbers. These eigenstates will be labelled $\{|M_i\rangle, |M_j\rangle \ldots\}$, and can be composed of linear combinations of products of single spin states $|m_i\rangle$, $|m_j\rangle$. The ith state is denoted by $I_z|M_i\rangle = M_i|M_i\rangle$.

2. Radiofrequency Interaction

The radio-frequency field is applied perpendicular to the static field and results in the Hamiltonian

$$H_{rf} = -\omega_1(t)2\cos[\omega t + \phi(t)]\, I_x \tag{1.8}$$

where $\omega_1(t)$ is the amplitude of the field, ω the frequency and $\phi(t)$ the phase.

3. Rotating Frame Transformation

The interaction of the nuclei with the large static field can be removed by a transformation to a new frame of reference rotating at or near the Larmor frequency; this interaction representation is called the rotating frame.[5,6] Under the unitary transformation

$$T = e^{-i\omega I_z t} \tag{1.9}$$

the laboratory frame Hamiltonian H_L becomes

$$H_R = i\,\frac{dT}{dt}\,T^{-1} + TH_LT^{-1} \tag{1.10}$$

in the rotating frame. Hence, when an oscillating rf field is applied to the system to produce a laboratory frame Hamiltonian

$$H_L = -\omega_o I_z + 2\omega_1(t)\ I_x(\cos(\omega t + \phi(t))) + H_{int}\ , \qquad (1.11)$$

the rotating frame Hamiltonian becomes, after the transformation of Equation (1.10)

$$H_R = \Delta\omega I_z + \omega_1(t)\ (I_x\cos\phi(t) + I_y\sin\phi(t)) + H_{int}^{(o)}\ , \qquad (1.12)$$

where $\Delta\omega = \omega - \omega_o$ is the resonance offset and $H_{int}^{(o)}$ is the part of H_{int} that commutes with I_z. A picture of the rotating frame is shown in Figure (1.1). The resonance offset term lies along the z-axis and pulses are applied in the x,y plane with an amplitude ω_1. The phase, $\phi(t)$, of a pulse is defined relative to the x-axis. According to this secular approximation, I_z and H_{int} share a common set of eigenstates[7]

$$I_z\ |M_i\rangle = M_i\ |M_i\rangle \qquad (1.13)$$

$$H_{int}\ |M_i\rangle = \omega_i\ |M_i\rangle \qquad (1.14)$$

From now on the subscripts will be dropped, and all interactions will be assumed in the rotating frame unless otherwise stated.

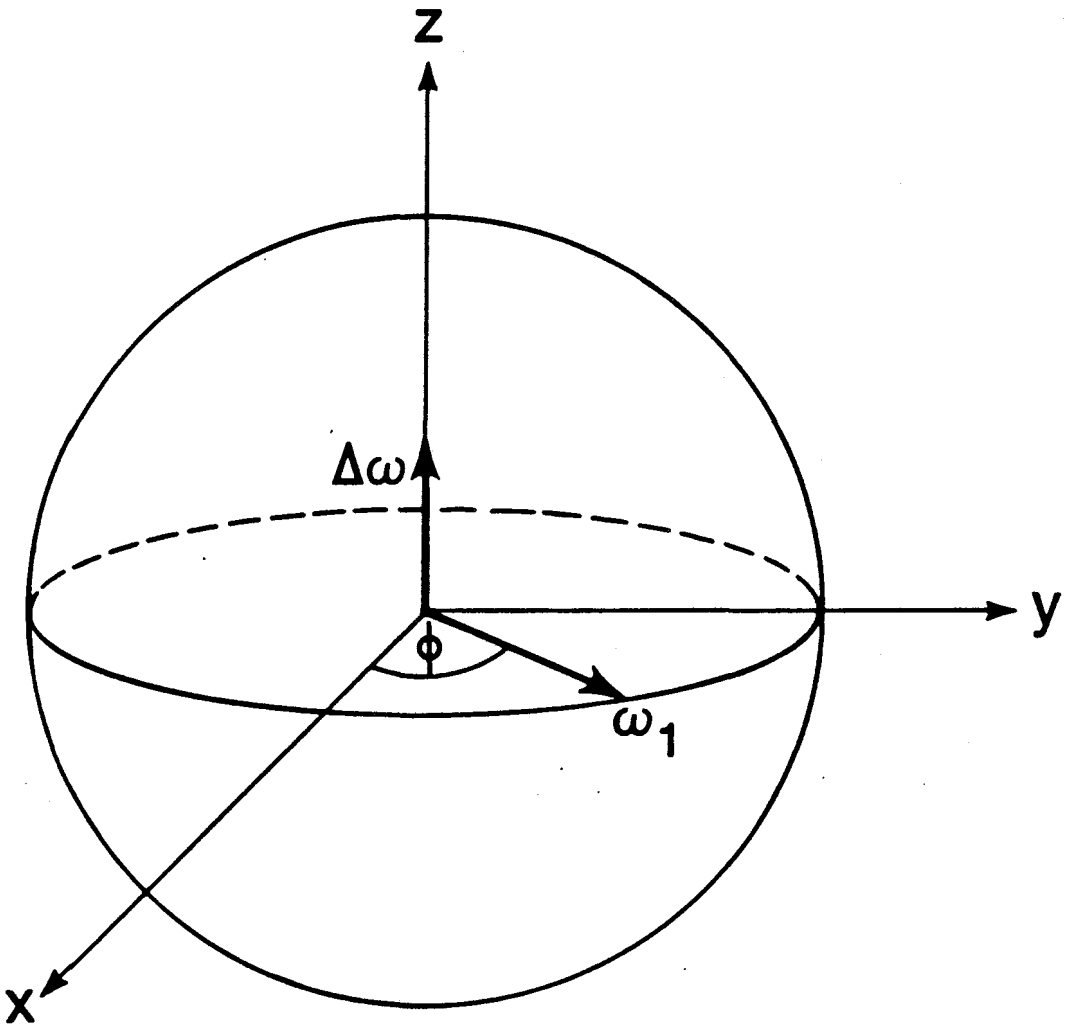

XBL 859-11359

Figure 1.1. The Rotating Frame.

The time dependence of the radio-frequency Hamiltonian is removed in the rotating frame. The resonance offset, $\Delta\omega = \omega_0 - \omega$, is the difference between the Larmor frequency and the rf carrier frequency and appears along the z-direction. The pulse amplitude and phase are denoted by ω_1 and ϕ, respectively. The phase of the pulse gives the direction of the radiation in the x-y plane.

4. Chemical Shift Hamiltonian

Each nucleus feels a magnetic field from the electrons surrounding it. In high field, the secular part of the chemical shift Hamiltonian is

$$H_{cs} = -\sum_i \sigma_i I_{zi} \tag{1.15}$$

where the sum is over individual nuclei. The chemical shift and resonance offset terms are both linearly dependent on the z component of the angular momentum operator and will, for convenience be combined into one term, the resonance offset Hamiltonian,

$$H_z = \Delta\omega I_z. \tag{1.16}$$

5. Dipolar Hamiltonian

The direct interaction between two magnetic dipoles in high field is described by the secular part of the homonuclear dipole-dipole interaction

$$H_{zz} = -\sum_{i<j} D_{ij} \; [\, 3I_{zi}I_{zj} - I_i \cdot I_j] \tag{1.17}$$

where $\vec{r}_{ij}$ is the vector connecting spin i to spin j. The dipolar coupling constant is

$$D_{ij} = \sum_{i<j} \frac{\gamma_i \gamma_j \hbar}{r_{ij}^3} \left(\frac{1}{2}\right) \left(3\cos^2 \theta_{ij} - 1\right) \tag{1.18}$$

where θ is the angle between the internuclear vector $\bar{r}_{ij}$ and the laboratory z - axis. The sum is over all pairwise interactions. The dipolar interaction, which involves products of angular momentum operators, is a bilinear interaction.

C. Density Operator

The spins are described by a wavefunction

$$|\Psi(t)\rangle = \sum_i c_i(t)|M_i\rangle \tag{1.19}$$

which is expanded in a complete orthonormal basis set $\{|M_i\rangle\}$ with complex coefficients

$$c_i(t) = |c_i(t)| \exp(i\alpha_i) \tag{1.20}$$

The phase factor α_i is arbitrary and thus the spin system cannot usually be described directly by a single state.[8,9] The density operator is particularly convenient for systems that are described as mixed states, and is defined as

$$\rho(t) = \sum_k P_k \, |\psi_k(t)\rangle\langle\psi_k(t)| \qquad (1.21)$$

where P_k represents the probability of describing the spin system by $|\psi_k(t)\rangle$. In general, the diagonal elements of the density matrix representation, $|c_i(t)|^2$, are associated with the populations, while the off diagonal elements yield statistical averages of the cross coefficients $C_n(t)C_m^*(t)$ and $C_m(t)C_n^*(t)$.

When off-diagonal elements are nonzero, a coherent superposition of states has been established. For example, for isolated spins -1/2, phase coherence between the $|+1/2\rangle$ and $|-1/2\rangle$ states will have occurred. For N coupled spins it is possible to excite multiple-quantum coherences between $|M_i\rangle$ and $|M_j\rangle$, where ΔM, the difference in Zeeman quantum number, now assumes any integer value up to N; i.e.

$$\Delta M = M_i - M_j = n \qquad \text{where } n = 0, \pm 1, \ldots, \pm N \quad . \qquad (1.22)$$

An important point to note is that only single-quantum coherence, $\Delta M = \pm 1$, can ever be detected directly, as an oscillating time-dependent voltage, by an NMR receiver coil.

1. Equilibrium Density Operator

At equilibrium, the density matrix is diagonal, with the relative populations given by the Boltzmann factors. This arises from

$$\rho_{eq} = \exp(-H_L/k_BT)/\mathrm{Tr}[\exp(-H_L/k_BT)] \qquad (1.23)$$

where H_L is the laboratory frame Hamiltonian. The Zeeman term is the largest term in the Hamiltonian and $k_BT >> \omega_o$ in the high temperature approximation. Therefore ρ_{eq} can be approximated by

$$\rho_{eq} = \frac{1}{Z}(1 + \frac{\omega_0}{k_BT} I_z) \tag{1.24}$$

where Z, the partition function, is a normalization constant. The unit operator commutes with all other operators, therefore Equation (1.24) reduces further to

$$\rho_{eq} = bI_z \quad \text{where } b = (\frac{\omega_0}{k_BT})(\frac{1}{Z}) \tag{1.25}$$

The constant multiplying I_z is usually omitted. At equilibrium, the off diagonal elements,

$$\overline{C_m^*(t)C_n(t)} = |C_m||C_n|e^{i(\alpha_n - \alpha_m)t} \tag{1.26}$$

are zero owing to the random phase approximation; i.e. no phase coherence exists between $|M_i>$ and $|M_j>$.

2. <u>Evolution of the Density Operator</u>

The Liouville-von Neumann Equation

$$\frac{d\rho(t)}{dt} = i\,[\rho(t),\, H(t)], \tag{1.27}$$

determines the time development of the density operator.[9] The formal solution to this differential equation is

$$\rho(t) = U(t)\;\rho(0)\;U(t)^{-1}\;. \tag{1.28}$$

When H(t) is time-dependent, the expression for the propagator is

$$U(t) = T\,\exp(-i\int_0^t H(t')dt') \tag{1.29}$$

where T is the Dyson time ordering operator.[10] If we assume that the time-dependent Hamiltonian is piecewise-constant, i.e. if the Hamiltonian is equal to H_1, H_2, H_3,..., H_n for successive times t_1, t_2, t_3,..., t_n, then the propagator can be written as

$$U(t) = \exp(-iH_n t_n)\;\ldots\;\exp(-iH_2 t_2)\;\exp(-iH_1 t_1). \tag{1.30}$$

When H is time-independent, the propagator reduces to

$$U(t) = e^{-iHt}\;, \tag{1.31}$$

and the density operator becomes

$$\rho(t) = \exp(-iHt)\ \rho(0)\ \exp(iHt) \quad . \tag{1.32}$$

Once the density operator has been calculated, the expectation value of an operator is

$$A(t) = \mathrm{Tr}\ (\rho(t)A) \ . \tag{1.33}$$

3. Expansion of the Density Operator in Different Basis Sets

The most general form of the density operator is given by the expansion

$$\rho(t) = \sum_s b(t)\ B_s \quad , \tag{1.34}$$

where the operators B_s form a complete orthogonal basis set.[11]

a. Pauli Spin Matrices

For N noninteracting spins-1/2, which behave as an isolated spin-1/2 or two-level system, the density operator can always be expressed as a linear combination of $\{1, I_x, I_y, I_z\}$ plus normalization constants:[12,13]

$$\rho(t) = b_z(t)I_z + b_x(t)I_x + b_y(t)I_y + b1 \tag{1.35}$$

The coefficients of $\rho(t)$ form a three dimensional vector equivalent to the magnetization vector

$$\langle M_x \rangle = Tr(I_x \rho(t)) = b_x(t)$$

$$\langle M_y \rangle = Tr(I_y \rho(t)) = b_y(t) \qquad (1.36)$$

$$\langle M_z \rangle = Tr(I_z \rho(t)) = b_z(t)$$

The density operator in this case is

$$\rho(t) = \vec{M}(t) \cdot \vec{I} \qquad (1.37)$$

where $\vec{M}$ is the unit magnetization vector. In Chapter II, the effect of a pulse sequence on an isolated spin is described by the trajectory of the magnetization vector $\vec{M}(t)$ on a unit sphere.

b. Outer Product Eigenbasis

Many basis sets can be used. For the multiple-quantum discussion of Chapters III and IV, two specific choices, the outer product and single-spin product bases are particularly convenient. The first is the orthonormal outer product eigenbasis formed by the components $\{|M_i\rangle\langle M_j|\}$. Most expressions will be of the form

$$\rho(t) = \sum_{M_i, M_j} \langle M_i|\rho(t)|M_j\rangle \; |M_i\rangle\langle M_j| \qquad (1.38)$$

Nonvanishing off-diagonal elements indicate a coherent superposition between states $|M_i\rangle$ and $|M_j\rangle$; the order of the coherence is $n = M_i -$

M_j. When n is greater than one, a multiple quantum coherence has been established. Because the observable operator is proportional to

$$I_+ = \frac{1}{\sqrt{2}}(I_x + I_y)$$

the NMR signal

$$S(t) = Tr[\rho(t)\ I_+] \tag{1.39}$$

can only be obtained from single quantum coherences. Therefore, multiple quantum coherences must be detected indirectly in a two-dimensional experiment.

c. Single Spin Product Operators

The 2^{2N} orthogonal single-spin product operators

$$B_s = 2^{(q-1)} \prod_k^N (I_{k\nu})^{a_{sk}} \tag{1.40}$$

completely describe a system of N coupled spins-1/2.[14] In the above expression k is the index of the nucleus; ν = x, y, or z; q is the total number of single spin operators in the product; and a_{sk} = 1 for q nuclei and a_{sk} = 0 for the N-q remaining nuclei. The multiple quantum order, n, can be read easily by adding the orders of individual raising and lowering operators. For example, there may be single-quantum/single-spin terms such as I_{xi} or I_{yi}; zero quantum/single-spin terms such as I_{zi}; "combination" single-

quantum/three-spin terms may look like $I_{+1}\ I_{+2}\ I_{-3}$; and, finally, the two N-quantum, N-spin terms are $I_{+1}\ I_{+2}\ I_{+3} \cdots I_{+N}$ and $I_{-1}\ I_{-2} \cdots I_{-N}$.

D. Pulse Sequences

If all internal interactions can be neglected for the duration of the pulse, i.e. if $H_{rf} \gg H_{int}$, then the Hamiltonian of the spin system during the pulse is merely $H = \omega_1 I_\phi$, assuming the pulse is applied on resonance, $\Delta\omega = 0$. This situation is referred to as the δ-pulse limit and is usually a good approximation in liquids. If the length of each pulse is τ and the flip angle defined as $\omega_1^0\tau = 0$, then the propagator for a pulse,

$$U(\tau) = e^{-i\theta I_\phi} \tag{1.41}$$

is a rotation operator in the operator space spanned by $\{1, I_x, I_y, I_z\}$. After a pulse applied in the x-direction, the spin system is described by the density operator

$$\begin{aligned} \rho(t) &= e^{-i\theta I_x}\ I_z\ e^{i\theta I_x} \\ &= I_z \cos\theta - I_y \sin\theta \end{aligned} \tag{1.42}$$

This is shown in Figure (1.2). Pulse sequences in NMR can take on

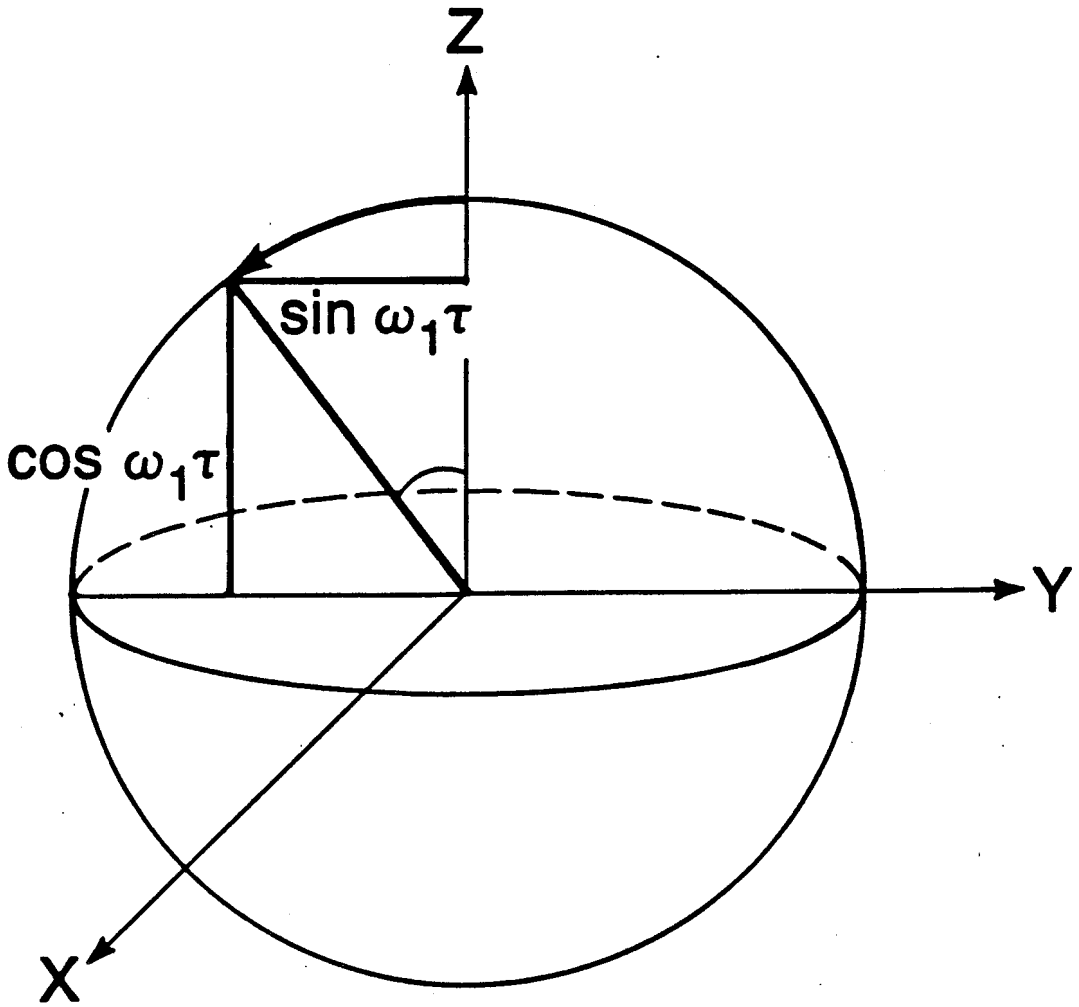

XBL 859-11358

Figure 1.2. The equilibrium density operator, proportional to I_z, is represented by a vector pointing along z. Here a pulse, with amplitude ω_1 is applied along the x-direction of the rotating frame for a time τ, causing the vector to rotate by an angle $\omega_1\tau$ about the x-axis.

many different forms: for instance, pulses can be followed by delays during which internal interactions are allowed to act on the density operator; pulses can be followed directly by other pulses. Many possibilities exist.

In Chapter II, the form of the radiofrequency pulse itself is changed and is continuously phase modulated in time. The continuously modulated radio-frequency (rf) can be divided into numerous piecewise-constant rf pulses, resulting in sequences of contiguous pulses with different phases. These are denoted by $(\theta_i)_{\phi 1}$, $(\theta_2)_{\phi 2}$, ..., $(\theta_n)_{\phi n}$ where θ_i represents the flip angle and ϕ_i the phase of the ith pulse. The propagator for the piecewise-constant rf Hamiltonian follows directly from Equation (1.30). These different pulse sequences are applied to noninteracting spin 1/2 particles and their effects can be visualized by following the trajectory of the magnetization on the unit sphere.

In Chapters III and IV, pulse sequences consisting of pulses followed by delays are applied to solids. Again, the Hamiltonian can be considered piecewise-constant but the calculation of the evolution of the density operator can be enormously complicated for these coupled spin systems. Now, contrary to the case for isolated particles, the evolution does not take place in a space spanned by $\{1, I_x, I_y, I_z\}$, but rather is described in the basis sets of Equations (1.38) and (1.40). Instead, average Hamiltonian theory[4,15] can be used to calculate an effective time-independent Hamiltonian, H_{eff}, which acts for the duration of the pulse sequence and brings about the same change as the piecewise-constant Hamiltonian.

E. Average Hamiltonian Theory

The overall propagator in average Hamiltonian theory can be described by

$$U(t_c) = e^{-iH_{eff}\, t_c} \; . \tag{1.43}$$

provided that the radio-frequency interaction is cyclic over the cycle time t_c. By applying the Magnus Expansion,[16] the propagator takes the form

$$U(t_c) = \exp[-i(\bar{H}^{(0)} + \bar{H}^{(1)} + \ldots \bar{H}^{(n)})t_c] \tag{1.44}$$

where

$$\bar{H}^{(0)} = \frac{1}{t_c} \int_0^{t_c} \tilde{H}_{int}(t)dt \tag{1.45}$$

$$\bar{H}^{(1)} = \frac{-i}{2t_c} \int_0^{t_c} dt_2 \int_0^{t_2} dt_1 [\tilde{H}_{int}(t_2), \tilde{H}_{int}(t_1)] \tag{1.46}$$

and

$$\tilde{H}_{int}(t) = U_{rf}^{-1}(t) \; H_{int}(t) U_{rf}(t) \quad . \tag{1.47}$$

Here a transformation $U_{rf}(t)$ has been defined from the rotating frame to an interaction representation usually called the toggling frame. Provided that $H_{eff}t_c << 1$, then higher order terms become neligible. $\bar{H}^{(o)}$ is called the average Hamiltonian and $\bar{H}^{(i)}$ is the ith order correction term to the average Hamiltonian. All odd orders $\bar{H}^{(1)}$, $\bar{H}^{(3)}$ etc.. can be made to vanish when the sequence is symmetrized, i.e. when

$$\tilde{H}(t) = \tilde{H}(t - \tau) \ . \tag{1.48}$$

In order to design a pulse sequence, it is convenient to consider the succession of orientations of the angular momentum operator I_z in the toggling frame $\tilde{I}_z$,

$$\tilde{I}_z = \exp(iH_{rf}(t)t)I_z\exp(-iH_{rf}(t)t) \ . \tag{1.49}$$

For instance, a 90_y pulse which transforms $\tilde{I}_z(t_1) = I_z$ to $\tilde{I}_z(t_2) = -I_x$ can be denoted by the shorthand notation $(Z\bar{X})$.[17,18] In the δ pulse limit, this transition is instantaneous whereas when finite pulse widths are considered, $\tilde{I}_z$ varies continuously between t_1 and t_2. In solids, where the internal interactions may be comparable to H_{rf}, it is important to consider the effects of the former during the pulse and work with finite pulse widths.

F. References

1. A. Abragam, The Principles of Nuclear Magnetism, Oxford University Press, Oxford and London (1963).

2. C. Slichter, Principles of Magnetic Resonance, Springer-Verlag, Berlin, 2nd ed. (1978).

3. M. Mehring, Principles of High Resolution NMR in Solids, Springer-Verlag, Berlin, 2nd ed. (1983).

4. U. Haeberlen, High Resolution NMR in Solids: Selective Averaging, Adv. Magn. Reson., Supplement 1, Academic Press, New York (1976).

5. I.I. Rabi, N.F. Ramsey and J. Schwinger, Rev. Mod. Phys. **26**, 169 (1954).

6. A. Messiah, Quantum Mechanics, John Wiley and Sons (1976).

7. J.H. van Vleck, Phys. Rev. **74**, 1168 (1948).

8. R.C. Tolman, The Principles of Statistical Mechanics, Oxford University Press, Princeton, N.J. (1955).

9. J. von Neumann, Mathematical Foundations of Quantum Mechanics, Princeton University Press, Princeton, N.J. (1955).

10. F.J. Dyson, Phys. Rev., **75**, 486 (1949).

11. U. Fano, Rev. Mod. Phys., **29**, 74 (1957).

12. R.P. Feynmann, F.L. Vernon, and R.W. Hellwarth, J. Appl. Phys. **28**, 49 (1957).

13. F. Bloch, Phys. Rev. **70**, 460 (1946).

14. O.W. Sorensen, G.W. Eich, M.H. Levitt, G. Bodenhausen, and R.R. Ernst, Prog. NMR Spectrosc. **16**, 163 (1983).

15. U. Haeberlen and J.S. Waugh, Phys. Rev. **175**, 453 (1968).

16. W. Magnus, Commun. Pure Appl. Math. **7**, 649 (1954).

17. D.P. Burum and W.-K. Rhim, J. Chem. Phys. **71**, 944 (1979).

18. D.P. Burum, M. Linder, and R.R. Ernst, J. Magn. Reson. **44**, 173 (1981).

II. BROADBAND AND ADIABATIC INVERSION OF A TWO LEVEL SYSTEM BY PHASE MODULATED PULSES

A. Introduction

1. Background

The implementation of population inversion between energy states is an important requirement of many techniques in nuclear magnetic resonance (NMR) and coherent optical spectroscopy, including relaxation time[1] measurements, spin or photon echoes[2,3] and spin decoupling.[4] The simplest way to coherently invert populations is with a single π pulse, i.e. a pulse of radiation such that the product of amplitude in angular frequency units and the time in seconds equals π. For good population inversion to be achieved, the difference between the radiation frequency and the resonant frequency of the transition for which populations are inverted must be much smaller than the radiation amplitude. In other words, the inversion bandwidth of a single π pulse is quite limited. Often it is the case experimentally that the bandwidth of resonant frequencies is comparable to or greater than the available radiation amplitude. In NMR, the bandwidth may result from static magnetic field gradients, chemical shifts or spin couplings. In coherent optics, this may be due to inhomogeneous broadening from crystal strains or Doppler shifts.

An established technique in NMR for inverting spin populations over a large bandwidth is Adiabatic Rapid Passage[5], in which the frequency of applied radio frequency (rf) radiation is swept through the

resonances at a constant rate that is small compared to the rf amplitude but large compared to the inverse of the relaxation times. Adiabatic sweeps have been employed in coherent optics as well[6-11]. An alternative approach to broadband inversion in NMR was proposed some time ago by Levitt and Freeman[12]. They suggested using a sequence of phase-shifted pulses, collectively called a composite π pulse, to produce inversion over a broad bandwidth. Composite pulses have led to a wide range of applications. Several approaches to their design in NMR[4,12-27] and coherent optics[28-29] have been described. The original work was based on computer simulations of spin trajectories and geometrical intuition[13]. This was followed by a more formal analysis in terms of rotation operators.[14-16] More recent developments include an approach based on coherent averaging theory[17,18] and the introduction of iterative methods for generating composite π pulses.[4,19-22] The coherent averaging theory approach and another based on a fictitious spin-1/2 formalism have led to composite pulses for coupled spin systems.[23-25]

This paper introduces an approach to broadband population inversion that bridges between adiabatic sweeps and composite π pulses.[26] This work -- which was subsequently appreciated by Silver, Joseph, and Hoult[27] -- was orginally motivated by the self-induced transparency effect[30] observed in coherent optical spectroscopy. The phenomenon of self-induced transparency, first discovered and studied by McCall and Hahn, occurs when a radiation pulse with an area of 2π and amplitude modulated according to a hyperbolic secant function brings a two-level absorbing system from its ground state back to its ground state re-

gardless of its resonance frequency. In that sense, a hyperbolic secant pulse is a perfectly broadband 2π pulse. Allen and Eberly have proposed a similar class of pulses for population inversion, but with both phase and amplitude modulation[31]. If $\omega_1(t)$ is the amplitude and $\phi(t)$ is the phase of the radiation, the pulse of Allen and Eberly may be written:

$$\omega_1(t) = (\omega_1^0/\sin\gamma)\operatorname{sech}(\omega_1^0 t) \tag{2.1}$$

$$\dot{\phi}(t) = (\omega_1^0\cot\gamma)\tanh(\omega_1^0 t) \tag{2.2}$$

where t extends from $-\infty$ to $+\infty$. γ is a parameter that determines the depth of the modulation, with no phase modulation when γ equals $\pi/2$ and increasing phase modulation as γ approaches zero. This pulse inverts populations in a two-level system regardless of the values of γ and ω_1^0, provided that the radiation frequency exactly equals the resonance frequency, i.e. "on resonance". Allen and Eberly point out that the pulse resembles an adiabatic sweep for small values of γ, due to the equivalence of phase modulation and frequency modulation. Thus, it may be anticipated that a pulse with phase modulation similar to that of Equation (2.2) will have broadband inversion properties. The performance of a class of phase modulated pulses related to Equations (2.1) and (2.2) is investigated in detail below. Comparisons with adiabatic sweeps are made.

The relation to a composite π pulse arises from considering a com-

posite π pulse as a single phase-modulated pulse, with a piecewise-constant phase function. A composite π pulse may then be regarded as an approximation of a continously phase-modulated pulse. One way to generate composite π pulses would be by approximating the continously varying phase function of a pulse similar to that of Equations (2.1) and (2.2) by a piecewise-constant function. Procedures for generating composite π pulses from continuously phase modulated pulses are developed below.

2. Organization

In Section II, a class of phase-modulated, constant-amplitude pulses are derived from consideration of the magnetization trajectory. Simulations of population inversion performance are given. A general transformation from a pulse with a modulated phase and a constant amplitude to a pulse with both phase and amplitude modulation is introduced, in order to demonstrate the relationship between our pulses and those of Allen and Eberly.

Section III treats phase-modulated pulses as adiabatic frequency sweeps. Criteria for adiabatic inversion are discussed. They lead to the concept of the efficiency of an adiabatic sweep and to the derivation of a new class of phase-modulated pulses based on efficiency considerations. A comparison of the inversion performance of linear sweeps, pulses derived in Section II, and pulses derived from considerations of efficiency is made.

The treatment of adiabaticity in Section III suggests that the phase modulated pulses of Section II may invert spin populations over

large ranges of rf amplitude as well as large ranges of resonant frequencies. The inversion performance as a function of the rf amplitude is treated in Section IV. Section V describes a method for deriving discrete composite pulse sequences from continously phase-modulated pulses. Experimental results are presented.

B. Derivation of Phase Modulated Pulses for Population Inversion

1. Frames of Reference

We begin with a description of two frames of reference, shown in Figure (2.1), that are of importance in the remainder of the paper. The first of these is the usual rotating frame.[32] If an isolated spin or two level system with resonance frequency ω_0 is irradiated with an rf pulse with any general amplitude and phase modulation, its motion in the usual rotating frame is determined by the Hamiltonian H^{PM} (where PM refers to Phase Modulation):

$$H^{PM} = \Delta\omega I_z - \omega_1(t)[I_x\cos\phi(t) - I_y\sin\phi(t)] \tag{2.3}$$

$\omega_1(t)$ and $\phi(t)$ are the pulse amplitude and phase; $\Delta\omega$ is the difference between ω_0 and the rf carrier frequency ω, i.e. the resonance offset. H^{PM} is derived from the laboratory frame Hamiltonian by the transformation T^{PM}:

$$T^{PM} = \exp(-i\omega I_z t) \tag{2.4}$$

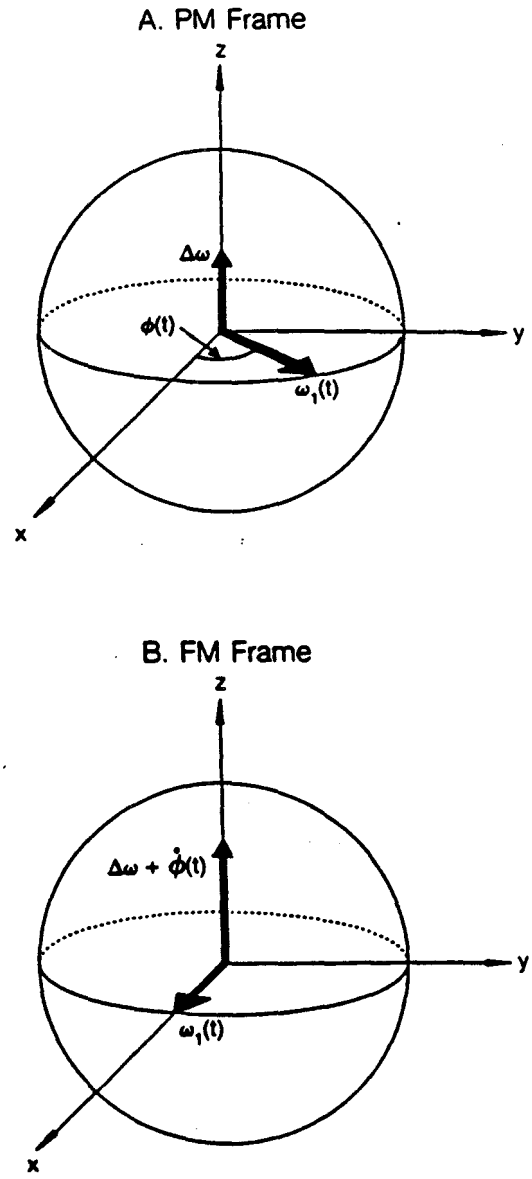

Figure 2.1. a). Phase Modulated (PM) frame. b). Frequency modulated (FM) frame. The resonance offset, $\Delta\omega = \omega_0 - \omega$, is the difference between the Larmor frequency and the rf carrier frequency. The pulse amplitude and phase are denoted by $\omega_1(t)$ and $\phi(t)$, respectively. In the PM frame which is the equivalent of the usual rotating frame used in NMR, the phase of the pulse which varies with time, gives the direction of the radiation in the xy plane. In the FM frame, the direction of the radiation in the xy plane is fixed, and the time derivative of the phase function, $\dot{\phi}(t)$, appears along the z direction as an additional resonance offset. The two frames are related by a rotation about the z axis by $\phi(t)$.

In this reference frame, which we call the PM frame, the rf frequency appears constant and the phase, i.e. the direction in the xy plane, varies. This is seen in Figure (2.1a).

An alternate rotating frame transformation that is useful in dealing with continuously modulated pulses is accomplished by the unitary operator T^{FM} (where FM refers to Frequency Modulation):

$$T^{FM} = \exp[-i(\omega t + \phi(t))I_z] \tag{2.5}$$

In the FM frame, the Hamiltonian is:

$$H^{FM} = (\Delta\omega + \dot{\phi}(t))I_z - \omega_1(t)I_x \tag{2.6}$$

and the time derivative of the phase function appears as an additional resonance offset with the xy plane component constant in direction, as shown in Figure (2.1b). That a phase-modulated pulse can be viewed in either the PM or FM frames is a statement of the equivalence of phase and frequency modulation. Of course, due to the design of a typical pulsed NMR spectrometer with its constant frequency reference, spin evolution is normally observed in the PM frame. For our purposes, the FM frame serves as a useful tool for deriving modulated pulses.

2. Derivation of Phase Modulation from Magnetization Trajectories

An isolated spin can be described in the FM frame by a density operator $\rho(t)$ of the following form:

$$\rho(t) = \underset{\sim}{M}(t)\cdot\underset{\sim}{I} \tag{2.7}$$

where $\underset{\sim}{M}(t)$ is a three-vector proportional to the magnetization and $\underset{\sim}{I}$ is a three-vector whose components are the angular momentum operators[33]. With Equation (2.6), $\underset{\sim}{M}(t)$ satisfies the Bloch equations without relaxation:

$$\frac{d\underset{\sim}{M}}{dt} = (-\omega_1(t),\ 0,\ \dot{\phi}(t) + \Delta\omega) \times \underset{\sim}{M} \tag{2.8}$$

If the initial condition for $\underset{\sim}{M}$ is known and if $\dot{\phi}(t)$ and $\omega_1(t)$ are given, then Equation (2.8) determines the evolution in time of $\underset{\sim}{M}$. For arbitrary $\dot{\phi}(t)$ and $\omega_1(t)$, Equation (2.8) can be solved by numerical methods for ordinary differential equations. Alternatively, $\dot{\phi}(t)$ and $\omega_1(t)$ may be approximated by piecewise-constant functions possibly by dividing time into small intervals over which $\dot{\phi}(t)$ and $\omega_1(t)$ are assigned their respective values at the midpoint of each interval. For each interval with constant $\dot{\phi}(t)$, the evolution of $\underset{\sim}{M}$ is simple. M precesses around the effective field vector with x component $-\omega_1$ and z component $(\dot{\phi} + \Delta\omega)$ at an angular rate equal to $(\omega_1^2 + (\dot{\phi} + \Delta\omega)^2)^{1/2}$. The length of $\underset{\sim}{M}$ is conserved. If $\underset{\sim}{M}$ is assumed to have unit length, $\underset{\sim}{M}$ follows a trajectory on a unit sphere. A trajectory of $\underset{\sim}{M}$ from +z to -z corresponds to the inversion of spin state populations.

An important question which now arises is the following: given a trajectory for M(t), how can we determine the $\dot{\phi}(t)$ and $\omega_1(t)$ which will yield that trajectory? We begin our consideration of this question with a class of trajectories that is of particular importance in the rest of the paper, namely those that follow a great circle from +z to -z in the FM frame, as depicted in Figure (2.2a). The appendix presents a formalism for treating other trajectories. A great circle trajectory is of the form:

$$\underset{\sim}{M}(t) = (\cos\gamma \cos\varepsilon,\ \sin\gamma \cos\varepsilon,\ -\sin\varepsilon) \tag{2.9}$$

where γ is a constant azimuthal angle and ε is a polar angle. ε is a function of t that is to be determined. Since the trajectory depends on the resonance offset, we specify that $\Delta\omega = 0$, i.e. that Equation (2.9) should hold on resonance. In addition, we initially search for a pulse with a constant amplitude equal to ω_1^0. The general case of amplitude modulation is treated later. Equations (2.8) and (2.9) lead to:

$$(\dot{\varepsilon}\cos\gamma\sin\varepsilon,\ -\dot{\varepsilon}\sin\gamma\sin\varepsilon,\ -\dot{\varepsilon}\cos\varepsilon)$$

$$= (-\dot{\phi}\ \sin\gamma\cos\varepsilon,\ -\omega_1^0\sin\varepsilon + \dot{\phi}\ \cos\gamma\cos\varepsilon,\ -\omega_1^0\sin\gamma\cos\varepsilon) \tag{2.10}$$

which implies:

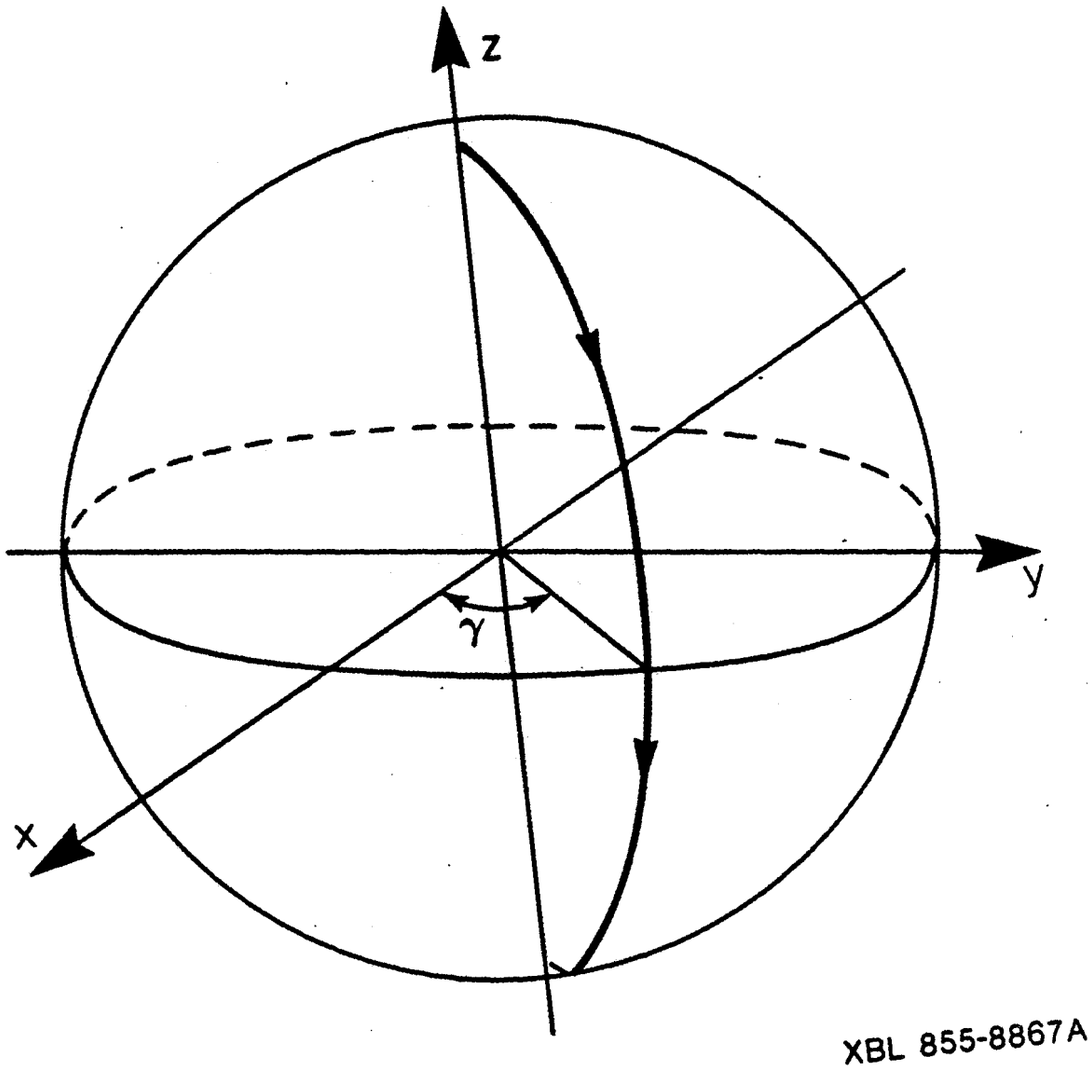

Figure 2.2. Inverting magnetization trajectories for an on-resonance spin the FM (a) and PM (b) frames calculated from Equations (2.9, 2.11) and (2.13, 2.14) respectively, with $\gamma = 0.1$.

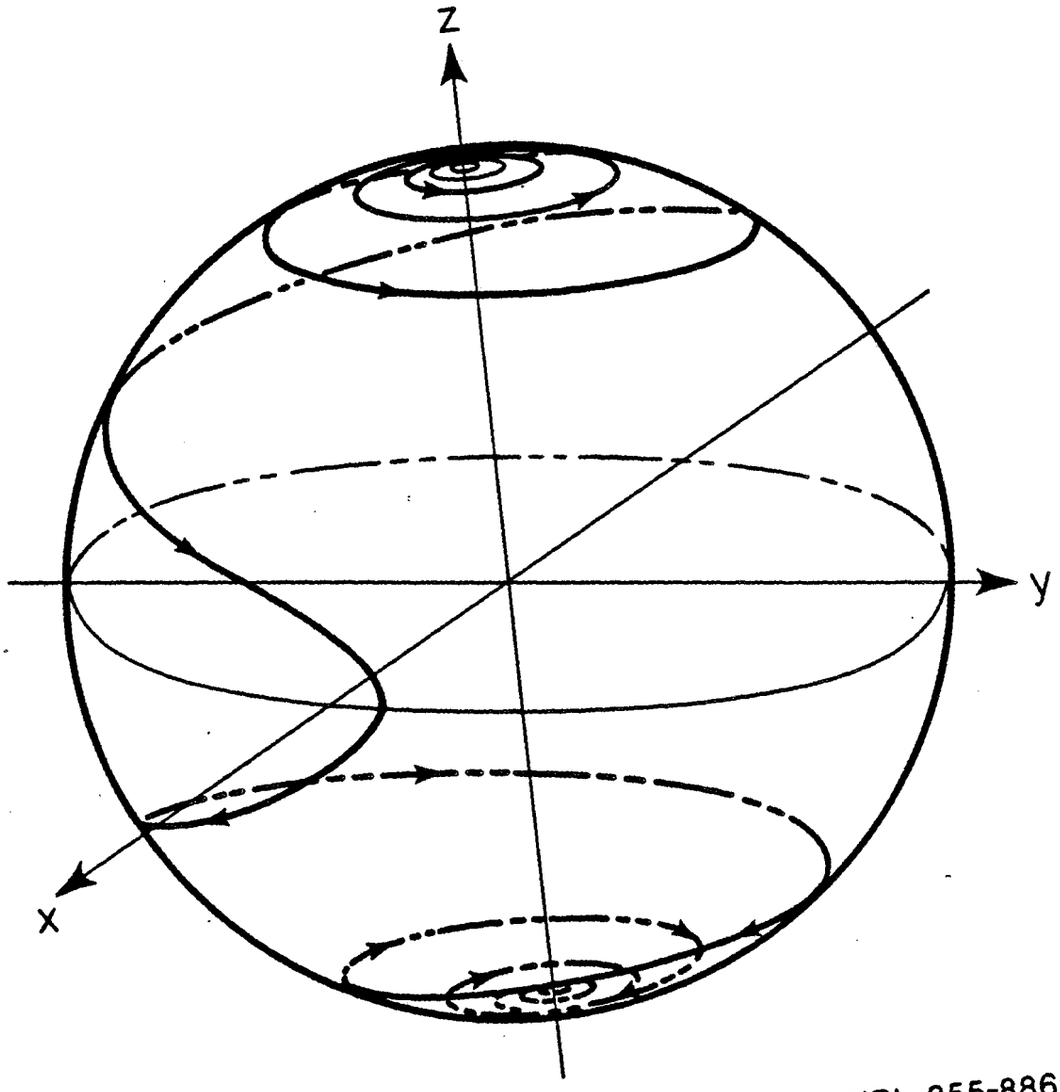

XBL 855-8869A

$$\varepsilon = (\omega_1^0 \sin\gamma)t \tag{2.11}$$

$$\dot{\phi} = \omega_1^0 \cos\gamma \tan(\omega_1^0 \sin\gamma t) \tag{2.12}$$

$$-\frac{\pi}{2\omega_1^0 \sin\gamma} < t < \frac{\pi}{2\omega_1^0 \sin\gamma}$$

Equation (2.12) dictates a class of phase-modulated pulses that invert spin populations exactly on resonance, since it is derived from the inverting trajectory in Equation (2.9). With $\gamma = \pi/2$, the phase is constant, the PM and FM frames coincide, and a standard π pulse is recovered. $\underset{\sim}{M}(t)$ is confined to a plane perpendicular to the plane of the effective field. As γ approaches zero, the phase modulation deepens, the pulse length increases, and the plane of the magnetization trajectory approaches coincidence with the plane of the effective field, suggesting adiabatic behavior. Equation (2.11) indicates that $\underset{\sim}{M}(t)$ moves with a constant angular velocity along the trajectory of Equation (2.9) regardless of the value of γ, provided that ω_1 is constant.

The derivation of the phase modulation has been carried out in the FM frame. Since the PM and FM frames are related by a rotation about z by $\phi(t)$, the trajectory in the PM frame does not follow a great circle but is still an inverting trajectory. This is shown in Figure (2.2b). To obtain $\phi(t)$, we integrate Equation (2.12):

$$\phi(t) = -\cot\gamma \ln[\cos(\omega_1^0 \sin\gamma t)],$$

where:

$$\frac{\pi}{2\omega_1^0 \sin\gamma} < t < \frac{\pi}{2\omega_1^0 \sin\gamma}$$

$\dot{\phi}(t)$ and $\phi(t)$ are plotted in Figure (2.3). A pulse specified by Equations (2.12) and (2.13) will be referred to as a Modulated Inversion Pulse (MIP). The magnetization trajectory in the PM frame (Figure 2.2b) is:

$$M_x^{PM} = \cos[\gamma+\phi(t)]\cos((\omega_1^0 \sin\gamma)t)$$

$$M_y^{PM} = \sin[\gamma+\phi(t)]\cos((\omega_1^0 \sin\gamma)t) \qquad (2.14)$$

$$M_z^{PM} = -\sin((\omega_1^0 \sin\gamma)t)$$

3. <u>Inversion Performance Off Resonance</u>

Although the MIP is derived so as to invert spin populations on resonance, the appearance of adiabatic behavior suggests that spin populations may be inverted over large ranges of resonance offsets as γ approaches zero. Figure (2.4) shows simulations of the inversion performance of the MIP as a function of the resonance offset for

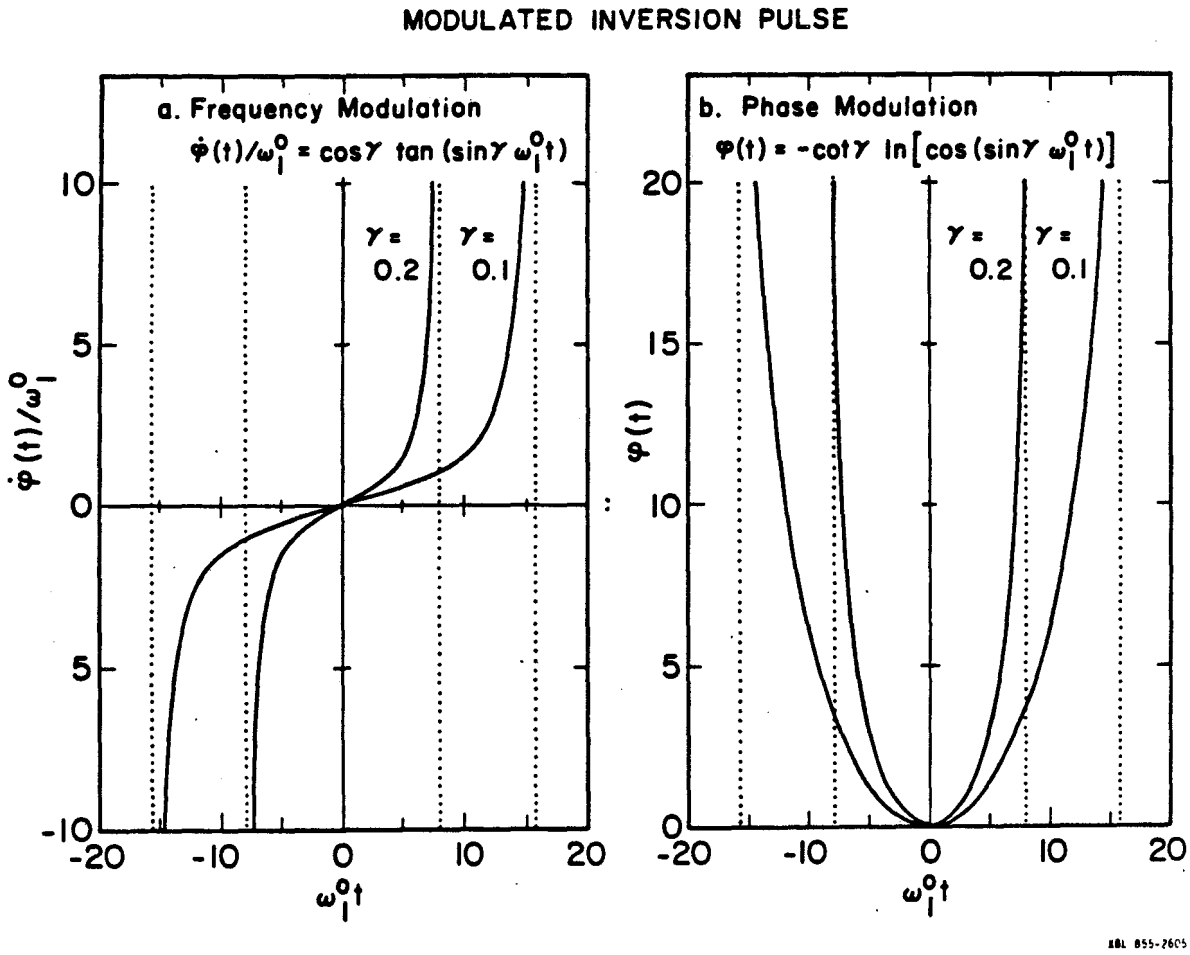

Figure 2.3. Continously frequency (a) and phase (b) modulated inversion pulse (MIP) plotted versus ω_1^0 for values of $\gamma = 0.2$ and $\gamma = 0.1$. The pulse amplitude is constant and the phase modulation increases as γ decreases. Also, as $\gamma \to 0$, the overall pulse length increases ($2\omega_1^0 t = \pi/\sin\gamma$). The MIP is an exact analytical solution to the problem of population inversion on resonance ($\Delta\omega = 0$) for all values of γ.

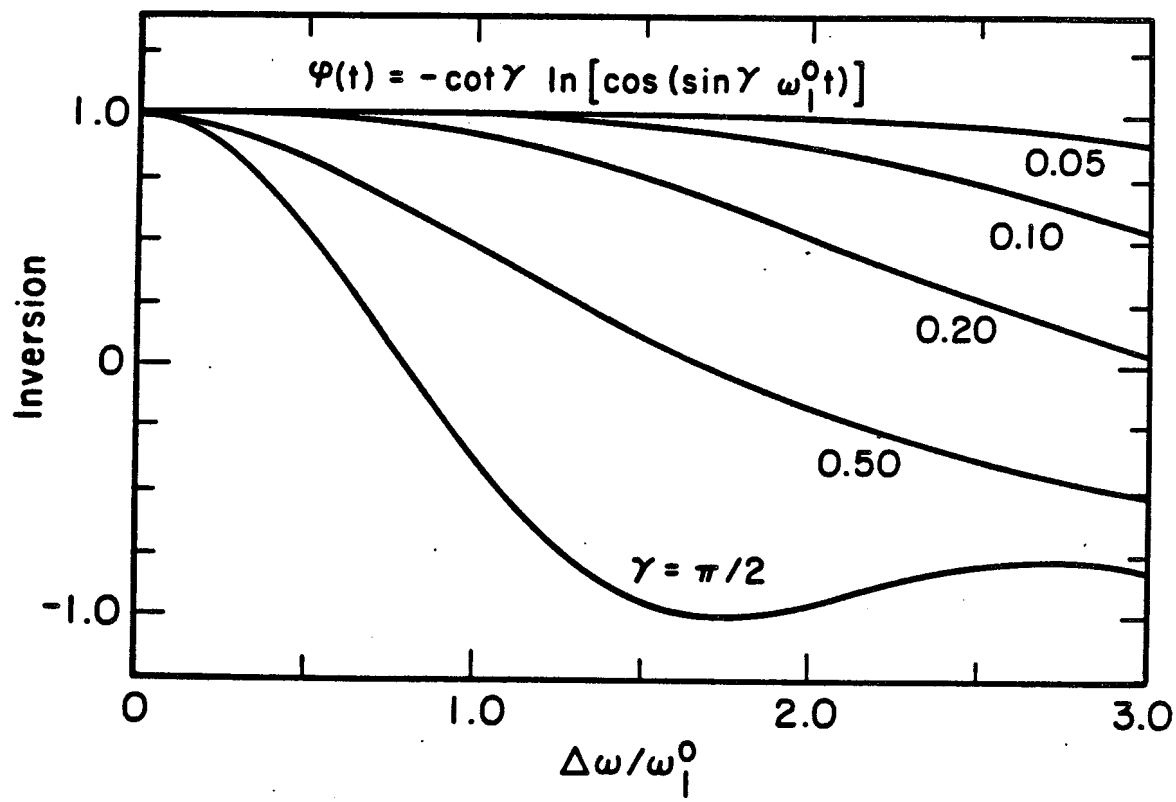

XBL 855-2601

Figure 2.4. Simulations of spin inversion from the MIP as a function of the relative resonance offset for various values of γ. Inversion is defined as the negative of the final z component of the spin angular momentum; initially the spin system has a z component of +1. For all values of γ, the inversion is always perfect on resonance. For $\gamma = \pi/2$, i.e. no phase modulation, the MIP is equivalent to a standard π pulse, which can be used here as a reference. As $\gamma \to 0$, i.e. increasing phase modulation, good inversion is accomplished over an increasingly large range of frequencies.

several values of γ. The extent of inversion is defined to be the negative of the final z component of $\underset{\sim}{M}$. Apparently, the range of offsets for which the inversion is nearly complete can be made as large as desired by taking γ to be sufficiently small.

4. Transformation to Amplitude-Modulated Pulses

Equation (2.13) is derived above with the assumption of a constant pulse amplitude. Although there is at most one rf phase function that yields a given magnetization trajectory on resonance with a given constant rf amplitude, there may be an infinite variety of combinations of phase and amplitude functions, if amplitude modulation is allowed. Here we present a method for converting a phase-modulated, constant-amplitude pulse to a pulse with both phase and amplitude modulation that produces the same trajectory on resonance.

The essential idea becomes apparent from considering a single pulse with a constant phase ϕ_0, a constant amplitude ω_1^0, and a length τ. The effect of such a pulse when $\Delta\omega = 0$ is to produce a rotation of $\underset{\sim}{M}$ by an angle $\omega_1^0\tau$ about an axis in the xy plane at an angle ϕ_0 to the x axis. Since it is only the area of the pulse that matters, however, the net effect is unaltered if the pulse amplitude is changed, provided that the pulse length is also changed so that the pulse area remains equal to $\omega_1^0\tau$. In general, a phase-modulated, constant-amplitude pulse can be approximated to arbitrarily high accuracy by a sequence of many constant-phase, constant-amplitude pulses. In order to transform the overall pulse to some desired amplitude modulation,

it is then only necessary to increase or decrease the amplitudes of the individual pulses and correspondingly decrease or increase their lengths. The total pulse area must remain constant. Figure (2.5) illustrates the procedure.

Mathematically, the amplitude transformation is a distortion of time. In general, suppose a pair of functions $\omega_1(t)$ and $\phi(t)$ produce a certain magnetization trajectory, with:

$$\int_{-\infty}^{\infty} \omega_1(t)dt = A \tag{2.15}$$

If there is another amplitude function $\bar{\omega}_1(t)$, also with area A, then we implicitly define a time transformation $t' = h(t)$ by the relation:

$$\int_0^{t'} \omega_1(u)du = \int_0^{t} -\omega(u)du \tag{2.16}$$

<u>The phase function $\bar{\phi}(t) = \phi(h(t))$, along with the amplitude function $\bar{\omega}_1(t)$, will produce the same magnetization trajectory.</u>

Thus we have arrived at the most general procedure for finding phase and amplitude combinations that produce a desired magnetization trajectory. We first derive a unique constant-amplitude pulse. Then we may transform to any other amplitude function of the same area, with the trajectory uniquely determining the pulse area.

To derive the pulses of Allen and Eberly, we transform the pulses

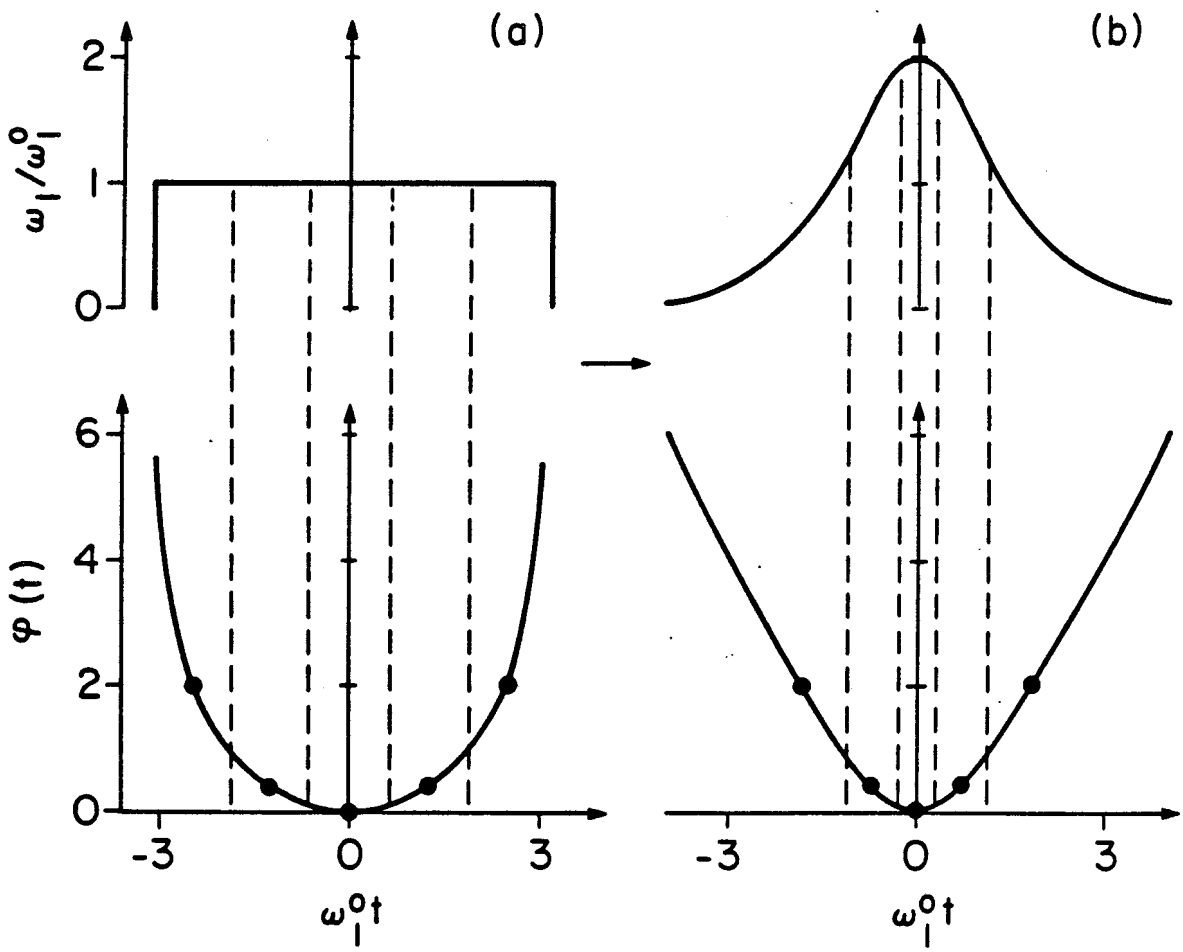

XBL 855-2604

Figure 2.5. Schematic representation of the transformation from a pulse with constant amplitude and phase modulation (a) to a pulse with both amplitude and phase modulation (b). In (a) the total time interval is divided into subintervals of length τ, represented by the dashed lines, which are each assigned a constant phase and a flip angle = $\omega_1\tau$. The transformation from (a) to (b) is effected by choosing the desired overall amplitude modulation, and then changing the lengths of the individual pulses while still maintaining that their flip angle remain equal to $\omega_1\tau$. The new phase modulation emerges from the time transformation.

of Equation (2.13) to the amplitude function of Equation (2.1). The corresponding time transformation is:

$$h(t) = \frac{1}{\omega_1^0 \sin\gamma} \tan^{-1}(\sinh \omega_1^0 t) \tag{2.17}$$

While the pulses of Equations (2.1) and (2.2) and of Equation (2.12) yield the same on-resonance trajectory, the utility of the pulses lies in their ability to invert spins off resonance. The significant, dimensionless quantity that characterizes off-resonance behavior is the ratio $\Delta\omega/\omega_1$. In simulations, we find that the constant amplitude pulses of Equation (2.13) give inversion over a larger range of resonance offsets than the amplitude-modulated pulses of Equations (2.1) and (2.2). An explanation for this is that $\Delta\omega/\omega_1$ is always at its minimum for the constant amplitude pulses.

C. Population Inversion by Adiabatic Sweeps

We saw in Section B that modulated pulses invert spins perfectly on resonance and also over a large range of frequencies as $\gamma \to 0$. Because the on-resonance magnetization trajectories are suggestive of adiabaticity, we now treat the above pulse in the framework of adiabatic sweeps and compare different adiabatic approaches.

1. Criteria for Adiabatic Inversion

The Hamiltonian of Equation (2.6) can be written:

$$H^{FM} = \underset{\sim}{\omega}_{eff}(t)\cdot\underset{\sim}{I} \tag{2.18}$$

$$\omega_{eff}(t) = (-\omega_1(t),\ 0,\ \Delta\omega + \dot{\phi}(t)) \ . \tag{2.19}$$

Spin populations may be inverted adiabatically if $\dot{\phi}(t)$ and $\omega_1(t)$ are such that the direction of $\underset{\sim}{\omega}_{eff}(t)$ moves from -z to +z, or from +z to -z, at a sufficiently slow angular rate. In that case, the magnetization, or spin density operator, is said to follow the effective field $\underset{\sim}{\omega}_{eff}(t)$.

If $\underset{\sim}{\omega}_{eff}(t)$ is written as:

$$\underset{\sim}{\omega}_{eff}(t) = \omega_{eff}(t)(-\cos\theta,\ 0,\ \sin\theta) \ , \tag{2.20}$$

$$\theta = \tan^{-1}[(\Delta\omega + \dot{\phi}(t))/\omega_1(t)] \ , \tag{2.21}$$

the two criteria for adiabatic inversion by a pulse between times $-t_0$ and t_0 can be stated as follows:[6,7,26]

1. $\left| \frac{d}{dt}\ \theta(t) \right| \ll \omega_{eff}$

2. $\theta(\pm t_0) \cong \pm\pi/2$.

Criterion 1 states that the effective field must change direction

slowly compared to the rate at which $\underset{\sim}{M}^{FM}$ precesses. In order to quantify criterion 1, we define the adiabaticity factor Q(t) according to:

$$Q(t) = \omega_{eff}(t)/[\frac{d}{dt}\theta(t)] \tag{2.22}$$

The larger the value of Q(t), the more adiabatic the frequency sweep.

In what follows, we consider only sweeps for which ω_1 is constant and non-zero. Therefore, criterion 2 requires that the sweep begin far below resonance and end far above resonance, such that $|\Delta\omega + \dot{\phi}(\pm t_0)| >> \omega_1$.

There are many possible forms for $\dot{\phi}(t)$ that result in adiabatic inversion. We call a sweep efficient if it accomplishes population inversion in a comparatively short time. Different forms of sweeps may have different efficiencies for the following reason. Consider criterion 1. Taking ω_1 to be constant, ω_{eff} is smallest when $\theta = 0$ and $\dot{\phi}(t) = -\Delta\omega$, i.e. when the sweep passes through resonance. It is at this time that criterion 1 is most restrictive so that $|d\theta(t)/dt|$ must be smallest. When the sweep is far from resonance, $|d\theta(t)/dt|$ may be larger while still satisfying criterion 1 since ω_{eff} is larger. If $|d\theta(t)/dt|$ indeed becomes larger far from resonance, criterion 2 may be satisfied for comparatively small values of t_0.

In the remainder of this Section, three forms of sweeps are examined in light of the above criteria for adiabaticity. The factors that limit their inversion bandwidths are discussed, and their efficiencies are contrasted.

2. Linear Sweep

The simplest and most commonly used frequency sweep is a linear sweep defined by:

$$\dot{\phi}(t) = -kt, \; -t_0 < t < t_0 \tag{2.23}$$

where k is the constant sweep rate. Since k is constant, criterion 1 is satisfied for all values of $\Delta\omega$ once k is small enough so that criterion 1 is satisfied at any particular value of $\Delta\omega$. For $\Delta\omega = 0$, a linear sweep has:

$$Q(t) = [(\omega_1^0)^2 + \dot{\phi}(t)^2]^{3/2} / k\omega_1^0 \tag{2.24}$$

Q(t) has its minimum at t = 0, where $Q(0) = (\omega_1^0)^2/k$. Simulations show that the maximum value of k for which populations are inverted adiabatically with $\Delta\omega = 0$ is given approximately by $k_{max} = 0.2(\omega_1^0)^2$. This limit is determined by simulating the effects of linear sweeps with t_0 taken to be very large.

For values of k less than or equal to k_{max}, criterion 1 is satisfied throughout the sweep. With k fixed, the choice of t_0 determines whether criterion 2 is satisfied.

Simulations of inversion as a function of $\Delta\omega/\omega_1^0$ for linear sweeps with $k = 0.2(\omega_1^0)^2$ and various values of t_0 are shown in Figure (2.6). For the inversion to be essentially complete for $\Delta\omega = 0$, the minimum

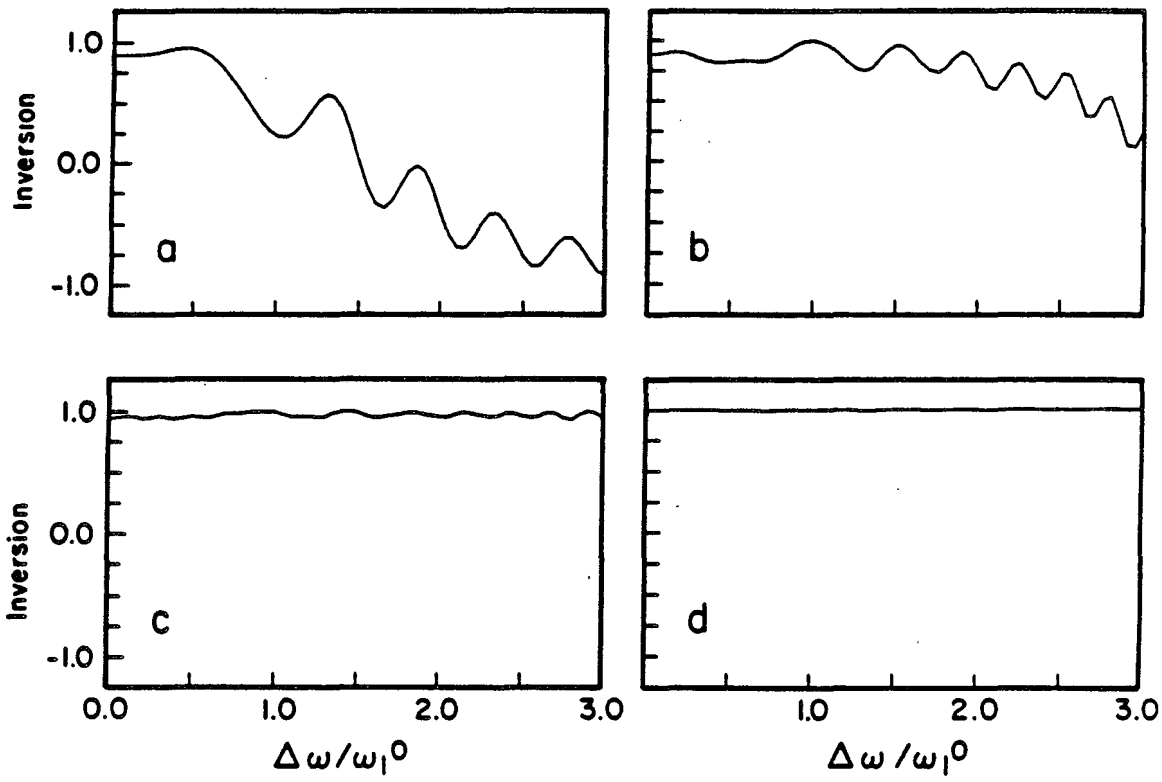

Figure 2.6. Simulations of inversion as a function of resonance offset, resulting from the linear frequency sweep of Equation (2.23) of the text with $k/(\omega_1^0)^2 = 0.2$. The linear sweep consists of a constant amplitude rf field whose frequency is changing at a constant rate of $k/(\omega_1^0)^2$. The overall lengths of the sweeps are $2\omega_1^0 t_0 = 15.82$ (a) 31.46 (b) 62.86 (c) 200.0 (d). The minimum overall length required to achieve adiabatic inversion on resonance is approximately $2\omega_1^0 t_0 = 100$. Once inversion is achieved on resonance, it is also accomplished over a large range of resonant frequencies. The overall lengths of 6 (a), (b) and (c) are equal to the overall lengths of the sweeps used to simulate inversion performance from the MIP in Figure (2.4) when $\gamma = 0.20$, 0.10, and 0.05 respectively.

length of the sweep must be given approximately by $2t_0 = 100\omega_1^0$. Inversion is achieved over a large range of resonant frequencies because criterion 2 is satisfied for a large range of resonant frequencies once it is satisfied for $\Delta\omega = 0$. In other words, $\phi(\pm t_0)$ is only a weak function of $\Delta\omega$ when $|\phi(\pm t_0)| \cong \pi/2$. However it is still criterion 2 that ultimately limits the inversion bandwidth for any given value of t_0.

3. Modulated Inversion Pulse

When treated as a frequency sweep, the MIP of Equation (2.12) and Figure (2.3a) satisfies criterion 2 for all values of γ and $\Delta\omega$. This is because $\dot{\phi}(t)$ becomes infinite at the beginning and end of the pulse. Thus, it is criterion 1 that determines whether the MIP functions as an adiabatically inverting frequency sweep. Recall that the MIP was derived in Section B in such a way that the inversion at $\Delta\omega = 0$ is complete regardless of γ. The adiabatic nature of the inversion is therefore expressed not by the inversion at $\Delta\omega = 0$, but rather by the appearance of a large inversion bandwidth as γ decreases.

The adiabaticity factor for the MIP with $\Delta\omega = 0$ is given by:

$$Q(t) = [1 + (\cos\gamma t \tan\omega_1^0 \sin\gamma t)]^{3/2}/[\cos\gamma \sin\gamma(1 + \tan^2\omega_1^0 \sin\gamma t)] \tag{2.25}$$

$Q(t)$ has its minimum at $t=0$, where $Q(0) = (\cos\gamma\sin\gamma)^{-1}$. Broadband inversion occurs when γ is less than or about equal to 0.20, as was

seen in Figure (2.4). When $\gamma = 0.20$, $Q(0) = 5.1$. This result is consistent with the finding that a linear sweep effectively inverts populations only when the sweep rate k is less than or about equal to $0.2(\omega_1^o)^2$, making the adiabaticity factor for a linear sweep greater than or equal to 5. Thus, the adiabaticity factor appears to be a meaningful quantity for predicting the performance of a frequency sweep. In addition, the agreement of the adiabaticity factors for the MIP and the linear sweep supports the contention that the broadband properties of the MIP are due to the adiabatic nature of the inversion.

A comparison of Figures (2.4) and (2.6) reveals that nearly complete inversion is achieved by the MIP in less time than by a linear sweep. The sweeps in Figures (2.6a), (2.6b), and (2.6c) require the same total time as the MIP in Figure (2.4) with $\gamma = 0.20$, $\gamma = 0.10$, and $\gamma = 0.05$, respectively. The inversion results in Figure (2.4) are generally superior, however. Thus, the MIP is a more efficient frequency sweep. This is because the instantaneous sweep rate, i.e. $\dot{\phi}$ is greater at the beginning and end of the sweep than at $t = 0$.

The fact that the sweep rate is not constant makes criterion 1 the limiting factor on the inversion bandwidth for the MIP. At resonant frequencies for which the sweep rate is rapid as the sweep passes through resonance, defined by the condition $\dot{\phi}(t) = -\Delta\omega$, criterion 1 is not satisfied and populations are not inverted.

4. <u>Constant Adiabacity Pulse</u>

A third class of frequnecy sweeps may be derived by making the

restriction that Q(t) be constant when $\Delta\omega = 0$.

$$Q(t) = q \tag{2.26}$$

Based on the above discussion, such a sweep with $q \cong 5$ is expected to be particularly efficient for adiabatic inversion.

Equation (2.26) implies:

$$q \frac{d\theta}{dt} = \omega_{eff} \tag{2.27}$$

In addition, we have:

$$\omega_{eff} \cos\theta = \omega_1^0 \tag{2.28}$$

$$\omega_{eff} \sin\theta = \dot{\phi} \tag{2.29}$$

Equations (2.27) and (2.28) imply:

$$\sin\theta = \omega_1^0 t/q \tag{2.30}$$

Equations (2.29) and (2.30) lead to:

$$\dot{\phi}(t) = (\omega_1^0)^2 t/[q^2-(\omega_1^0)^2 t^2]^{1/2} \quad , -q/\omega_1^0 < t < q/\omega_1^0 \tag{2.31}$$

Equation (2.31) defines the desired frequency sweep, which we refer to as the constant adiabaticity pulse (CAP). Integration of Equation (2.31) gives the equivalent phase modulation:

$$\phi(t) = -[q^2 - (\omega_1^0)^2 t^2]^{1/2} + q \tag{2.32}$$

Note that $\phi(t)$ remains finite, although $\dot{\phi}(t)$ becomes infinite at $t = \pm q/\omega_1^0$.

Figure (2.7) is a comparison of the frequency and phase modulations of the CAP, the MIP, and the linear sweep. The specific parameters in Figure (2.7) are chosen so that the adiabaticity factor at $t = 0$ is the same for the three sweeps. For a given minimum adiabaticity factor the CAP requires the least total time of the three sweeps.

The adiabaticity factors as functions of time for the CAP, the MIP, and the linear sweep with $\Delta\omega = 0$ are shown in Figure (2.8). The adiabaticity factor has its minimum value throughout the sweep for the CAP. The adiabaticity factor for the MIP remains close to its minimum value for a greater portion of the sweep than for a linear sweep.

The inversion performance as a function of $\Delta\omega$ for the CAP with various values of q is shown in Figure (2.9). The values of q are chosen so that the overall lengths of the sweeps in Figure (2.9) are the same as those in Figure (2.4). The bandwidth of the CAP is limited by criterion 1. A comparison of Figures (2.4), (2.6), and (2.9) reveals that the MIP exhibits the best inversion performance for equal sweep lengths.

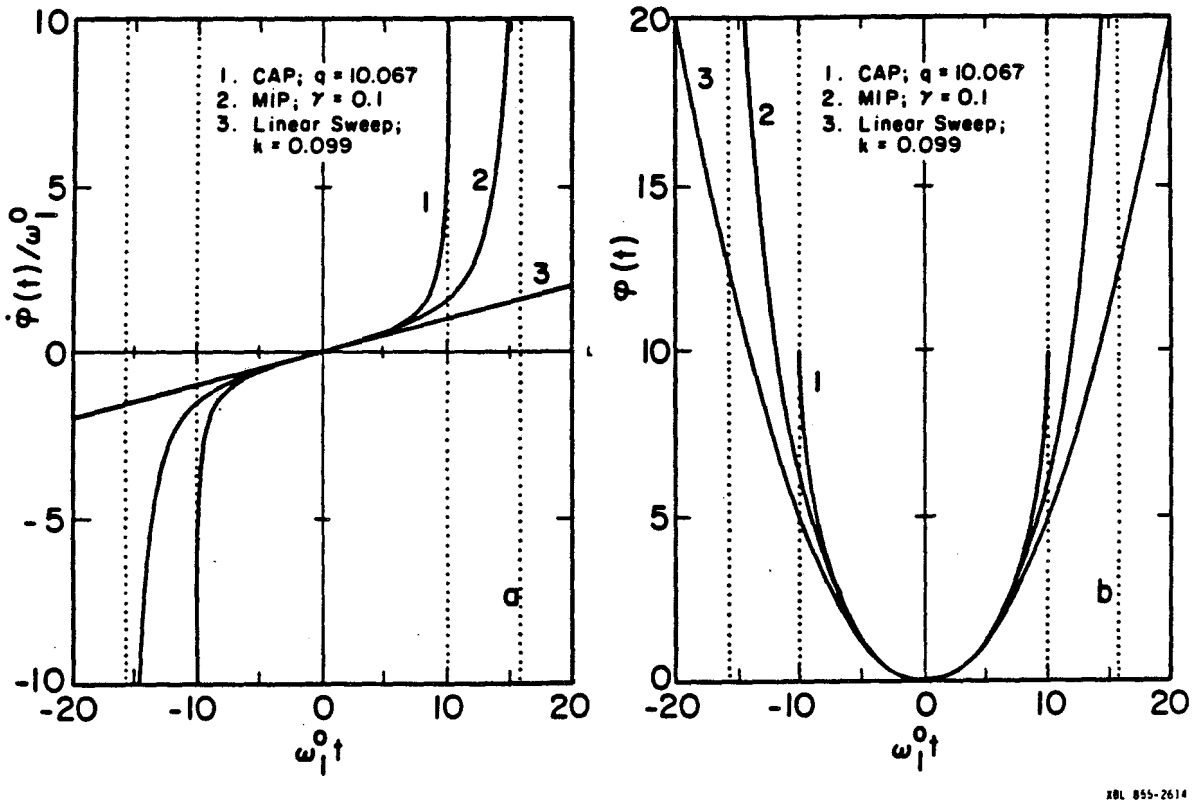

Figure 2.7. Comparison of 3 adiabatic frequency (a) and phase (b) modulated pulses: the constant adiabatic pulse (CAP), the MIP and the linear sweep. The CAP, a constant amplitude pulse, was derived from considerations of efficiency for adiabatic sweeps. In this figure, the parameters were chosen such that the adiabaticity factor Q(t) defined by Equation (2.22), be equal to 10.067 for all three pulses at t = 0. The larger the value of Q(t), the more adiabatic the sweep.

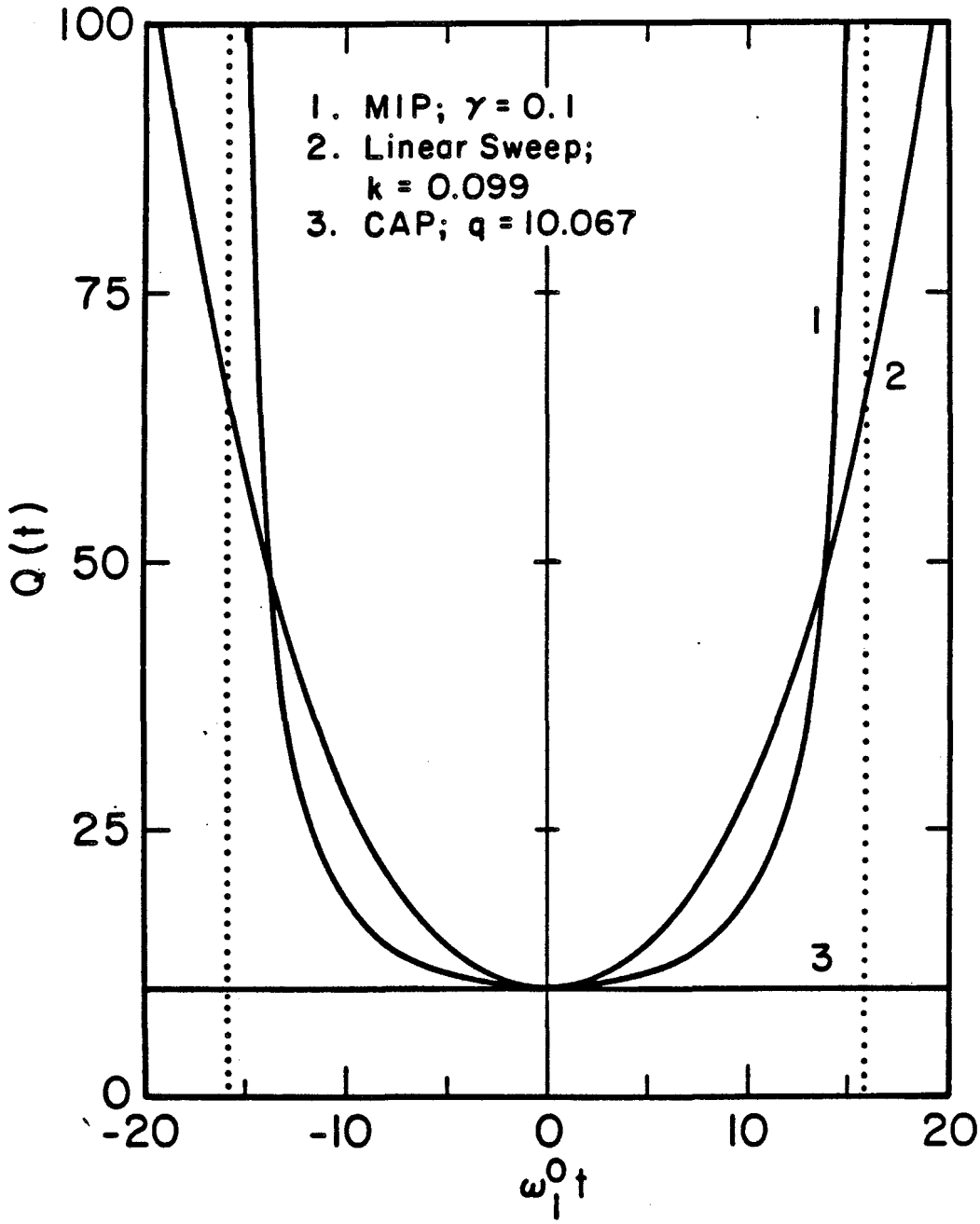

XBL 855-2610

Figure 2.8. Comparison of the adiabaticity factors Q(t) with $\Delta\omega = 0$ for the MIP, the linear sweep and the CAP. Q(t) is defined in the text by Equations (2.25), (2.24), and (2.26) respectively. The efficiency of the sweep is determined by the length of time Q(t) remains close to its minimum; the linear sweep is the least efficient sweep.

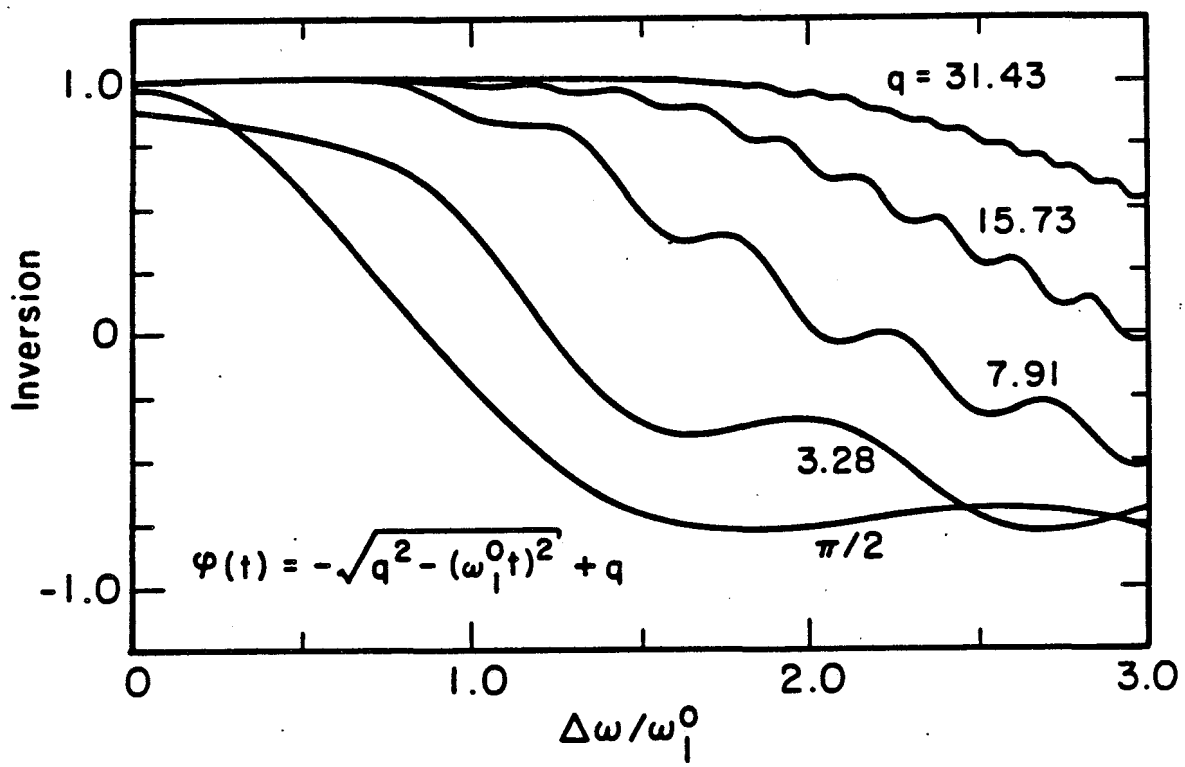

XBL 855-2609

Figure 2.9. Simulations of inversion as a function of $\Delta\omega/\omega_1^0$ for the CAP. The overall lengths of the sweeps were chosen such that they correspond to the overall lengths of the sweeps of Figure (2.4) ($q = \pi/2\sin\Upsilon$, the overall length is 2q). Simulations indicate that when $Q(0) > 5$, the CAP, the MIP and the linear sweep exhibit adiabatic inversion over a large range of frequencies. A comparison of Figures (2.4), (2.5(a)(b)(c)) and (2.8) indicate that the MIP produces the best adiabatic broadband inversion for equal sweep lengths and always inverts on resonance spins.

D. Inversion in an Inhomogeneous RF Field

Although the MIP was derived by considering a particular class of inverting trajectories for a spin on resonance, Sections B and C show that the MIP may invert spin populations over large ranges of resonance frequencies due to its adiabatic characteristics. Adiabatic sweeps may invert populations over large ranges of rf amplitudes as well as resonance frequencies. Therefore, in this section we investigate the inversion performance of the MIP as a function of ω_1. Deviations of ω_1 from its nominal value of ω_1^0 arise experimentally from rf inhomogeneity and from miscalibration of the rf field. In coherent optics, it is the laser beam profile that is the analogous source of amplitude inhomogeneity.

The inversion performance as a function of ω_1 may be anticipated by referring to the criteria for adiabatic inversion discussed in Section C. For the MIP, criterion 2 is automatically satisfied, since $\dot{\phi}(t)$ becomes infinite at $\pm t_0$. Once criterion 1 is satisfied for $\omega_1 = \omega_1^0$, it is satisfied even more strongly for $\omega_1 > \omega_1^0$. Therefore, it is expected that essentially complete inversion may be achieved over a large range of ω_1 when the MIP becomes adiabatic, i.e. for $\gamma < 0.20$.

Figure 2.10 shows simulations of inversion as a function of ω_1 for the MIP with various values of γ. The above predictions are verified. Figure (2.11) shows a simulated contour plot of inversion as a function of ω_1 and $\Delta\omega$ simultaneously for the MIP with $\gamma = 0.10$. A large region of essentially complete inversion is apparent.

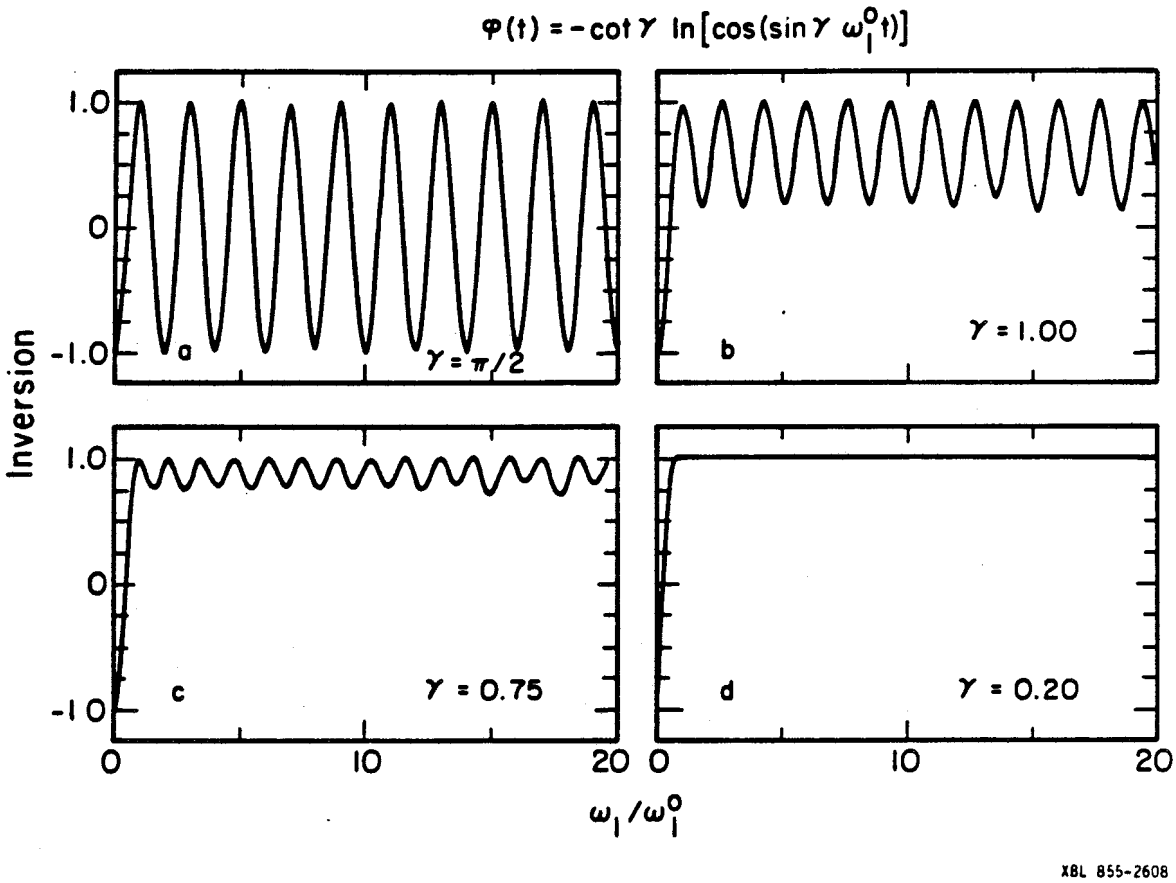

Figure 2.10. Simulations of inversion as a function of ω_1/ω_1^0 for the MIP with values of γ as shown. When $\gamma < 0.2$ ($Q(0) > 5$), the inversion becomes perfect over a very large range of ω_1.

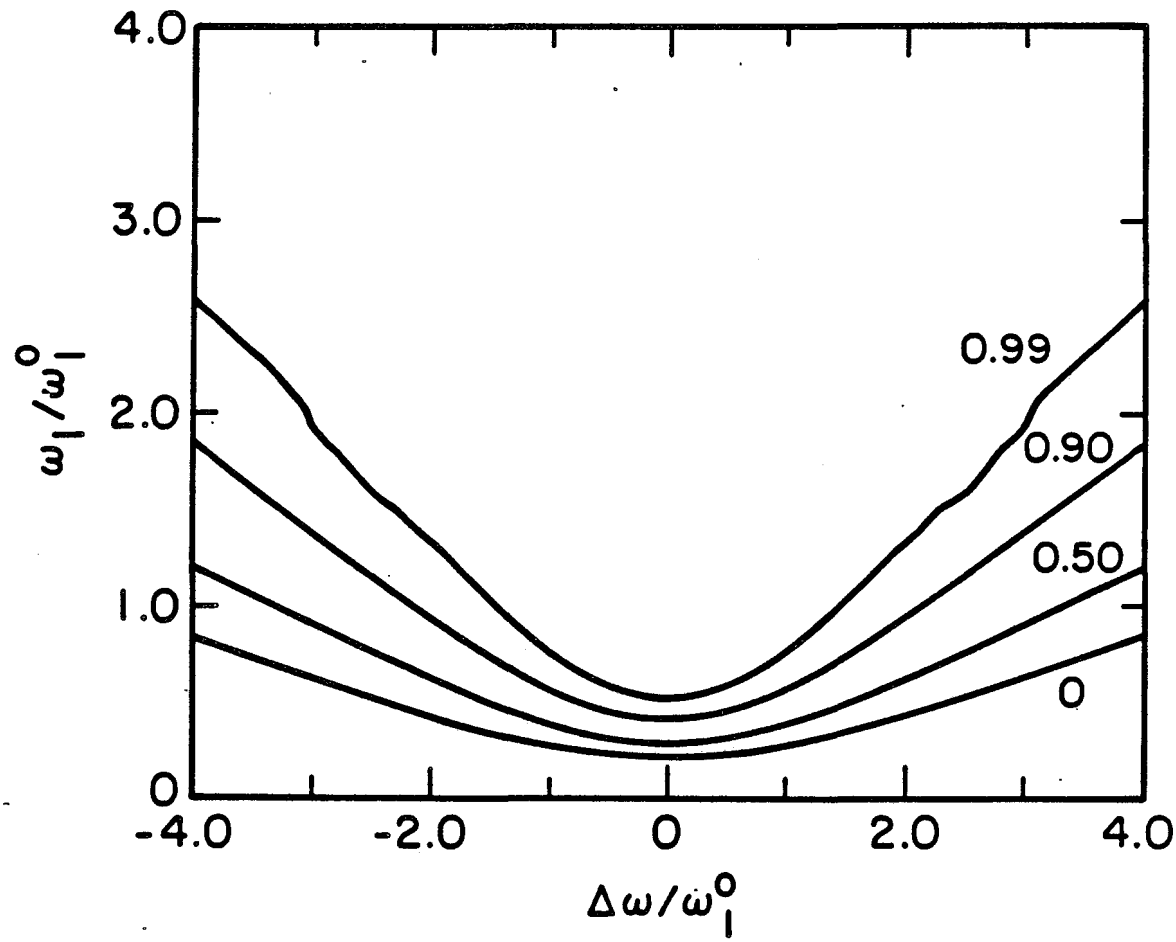

XBL 8412-5493

Figure 2.11. Simulated contour plot of population inversion as a function of $\Delta\omega$ and ω_1 for the MIP with $\Upsilon = 0.10$. The MIP compensates simultaneously for resonance offset and rf inhomogeneity effects.

For comparison, Figure (2.12) shows the inversion performance of a linear sweep as a function of ω_1. Much smaller bandwidths are achieved with much longer sweeps. For a linear sweep, criterion 1 of Section D is again satisfied for $\omega_1 > \omega_1^0$ once it is satisfied for $\omega_1 = \omega_1^0$. However, criterion 2 is not automatically satisfied. Rather, $\theta(t_0)$ is a strong function of ω_1 when $|\theta(t_0)| \cong \pi/2$, so that criterion 2 is not met at large ω_1.

E. Generation of Discrete Composite Pulses from Continuously Phase Modulated Pulses

It is often difficult to implement the single continuously phase modulated pulse experimentally. Frequently it is more convenient to use a sequence of phase shifted rf pulses forming a composite π pulse. This section describes the method by which we approximate the continous pulse by discrete pulse sequences that have both unrestricted phases as well as rf phases which occur only as multiples of a specified value.

1. General Method of Approximation Using Magnetization Trajectories

The goal is to arrive at a discrete pulse sequence with inversion properties that are very similar to those of the continuously phase modulated pulse. In the computer simulations described above, the MIP is approximated with a large number of pulses, each with a small flip angle, by extracting the individual pulse phases and flip angles from

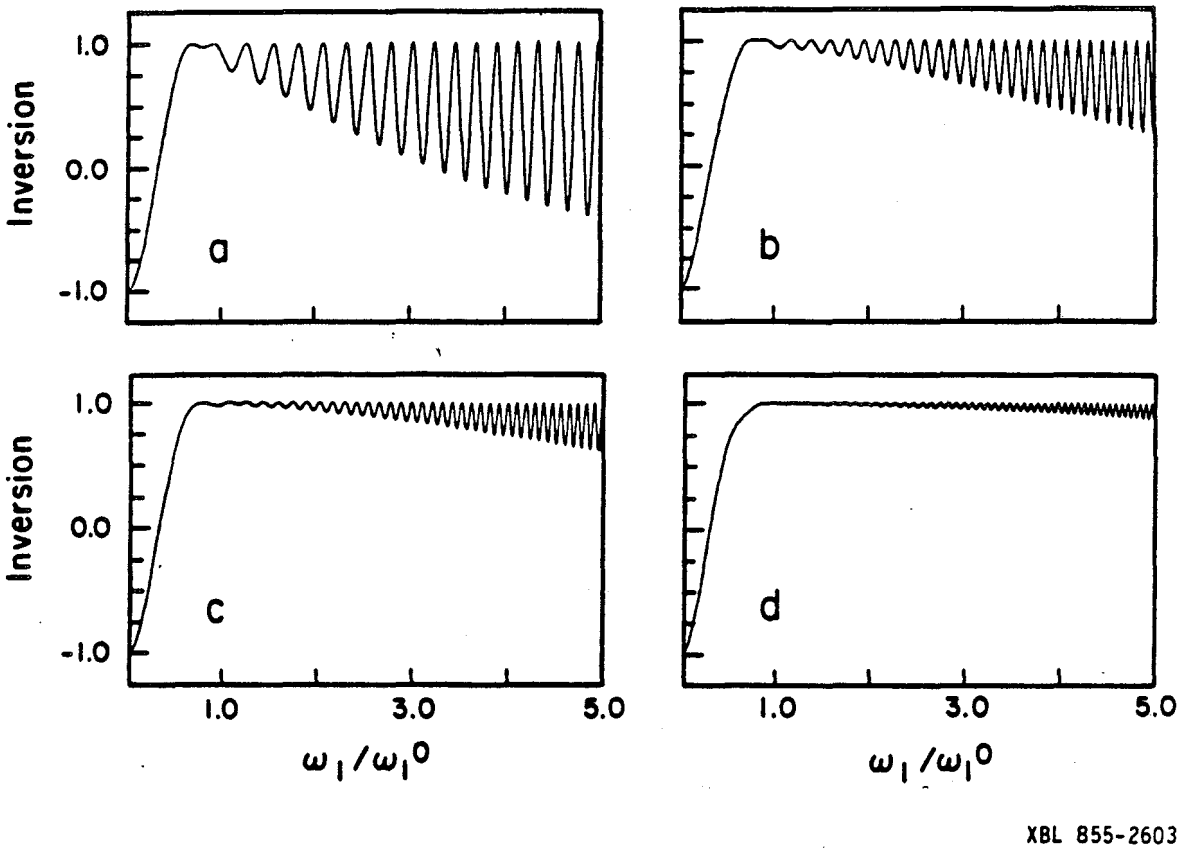

Figure 2.12. Simulated inversion performance as a function of ω_1/ω_1^0 for the linear sweep with $k/(\omega_1^0)^2 = 0.2$. The overall pulse lengths are $2\omega_1^0 t_0 = 31.46$ (a), 62.86 (b), 100.0 (c), 200.0 (d). For longer sweeps that shown in Figure (2.10), the inversion is worse.

$\phi(t)$ in Equation (2.13). This was done by dividing the total time interval into subintervals and assigning a constant phase to each subinterval as shown in Figure (2.13a). As the number of pulses, or subintervals, increases and the flip angles become smaller, this is an increasingly accurate approximation. However, if the number of pulses is small, i.e. less than 100, this is a poor approximation, particularly for small γ. The spin evolution brought about by the MIP over a subinterval is not the same as that brought about by a constant-phase pulse with a phase equal to $\phi(t)$ at the midpoint of that subinterval. Errors in the magnetization trajectory accumulate from one subinterval to the next, so that even on-resonance spins are no longer inverted. Clearly, a new approximation method is needed. Our method is based on following the on-resonance magnetization trajectory $\underset{\sim}{M}^{PM}(t)$.

Figure (2.13b) is a schematic representation of the method used. The first step is to approximate the trajectory of the magnetization by choosing points in time along it. We then calculate the constant phase pulses that give the evolution of the magnetization from one point to the next. The result is a sequence of radiofrequency pulses or a composite pulse whose magnetization trajectory and inverting properties are very similar to those generated from the continuous pulse.

2. <u>Pulse Sequences with Unrestricted Phases</u>

For a 2n-1 pulse sequence, we need to choose 2n + 1 points on the trajectory $\underset{\sim}{M}(t)$. These points are denoted by $\underset{\sim}{M}_0, \underset{\sim}{M}_1, \ldots, \underset{\sim}{M}_n, \ldots \underset{\sim}{M}_{2n}$.

Figure 2.13. a) Schematic diagram of a method for approximating the MIP by a large number of constant phase pulses. The total length of the pulse is divided into a large number of subintervals with lengths inversely proportional to $\dot{\phi}(t)$; this is indicated by the dotted lines. The pulse flip angles are calculated from the subinterval lengths and the constant amplitude. Based on $\phi(t)$, a constant phase is assigned to each subinterval. If the number of pulses is small, this is a poor approximation. b) Schematic representation of the method used to approximate the continously modulated pulse (MIP) by a discrete pulse sequence. The magnetization trajectory $\underset{\sim}{M}^{PM}(t)$ of an on-resonance spin subjected to the MIP is approximated by a discrete number of points. The flip angle and constant phase that give the evolution of the magnetization from one point to the next are calculated. The result of this "connect the dots" technique is a composite pulse whose inversion properties are similar to those of the continuous pulse.

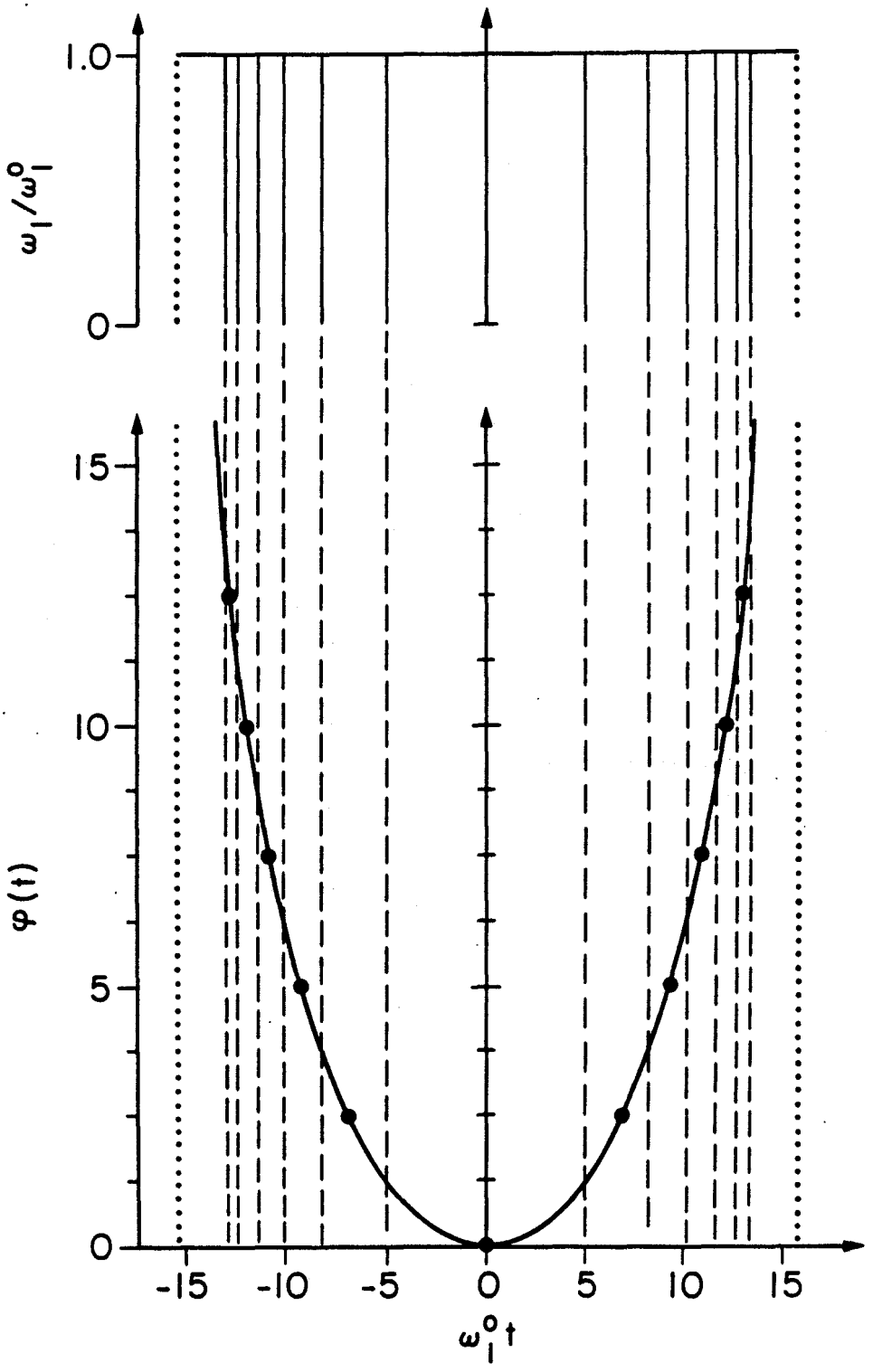

XBL 855-2616

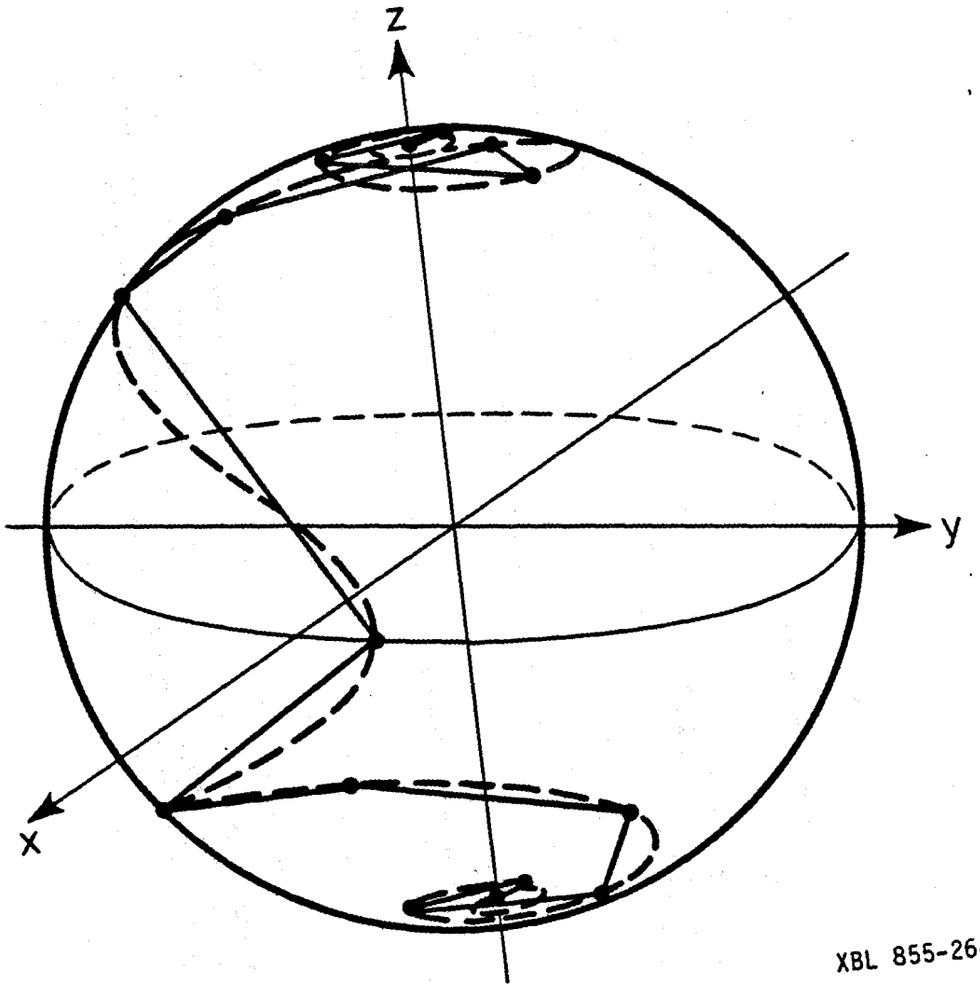

XBL 855-2642

The individual flip angles and phases of the derived pulse sequences are denoted respectively by $\theta_1,\ldots,\theta_{2n-1}$ and $\phi_1,\ldots,\phi_{2n-1}$ where $\theta = \omega_1^0\tau_i$ and τ_i is the length of the ith rf pulse. We set the first point $\underset{\sim}{M}_0 = +z$ and the last point $\underset{\sim}{M}_{2n} = -z$ to ensure that on resonance spins are always perfectly inverted by the discrete pulse sequence. Then in order to follow the trajectory as closely as possible, as indicated in Figure (2.13b), more points are selected in the regions where $\underset{\sim}{M}^{PM}(t)$ spirals more. A weighting function, $\phi(t)$, which is itself a function of γ is used to generate a set of times $(t_1,\ldots,t_{2n-1})$ from which the intermediate points $\underset{\sim}{M}_i = \underset{\sim}{M}^{PM}(t_i)$ can be calculated.

More specifically, the intermediate points are calculated as follows. First, we choose a value $t_c < 0$ which represents a cut-off time for $\phi(t)$. The means by which t_c is chosen is discussed below. We evaluate $\phi(t_c)$ and calculate a set of phases $(\phi(t_1),\ldots,\phi(t_n))$ satisfying

$$\phi(t_i) = \phi(t_c)(n-i)/n. \tag{2.33}$$

Using the set of times $(t_1,\ldots,t_n)$ calculated from the set of phases above, we find $\underset{\sim}{M}_1$ through $\underset{\sim}{M}_n$ by evaluating $\underset{\sim}{M}_i = \underset{\sim}{M}^{PM}(t_i)$. The remaining points are determined by the symmetry of $\underset{\sim}{M}^{PM}(t_i)$; $\underset{\sim}{M}_{2n-i}$ is related to M_i by reflection in the xy plane. Next, we calculate the phases and flip angles of the 2n pulses that move on resonance spins between successive points, i.e. that connect $\underset{\sim}{M}_i$ with $\underset{\sim}{M}_{i+1}$. A sequence of pulses with symmetric phases and flip angles emerges. The central two pulses can be fused into one, since they have the same phase, so

that an odd number of pulses results.

The "connect-the-dot" method described above ensures that on-resonance spins are inverted. Moreover, the fact that the intermediate $\underset{\sim}{M}_i$ are chosen according to constant increments in $\phi(t)$ ensures that more points occur where $\phi(t)$ is larger, in other words where $\underset{\sim}{M}^{PM}(t)$ spirals most rapidly. Thus, we achieve a good approximation to the trajectory generated from the MIP and it may be expected that the broadband inversion properties of the MIP will be preserved.

In this method, there are only two parameters which must be computer optimized in order to get the best inversion performance over resonance offset or rf inhomogeneity effects, for a specified number of pulses. These are γ and t_c, the cut-off time on $\phi(t)$. They are optimized according to a best-average criterion. This means that we cycle through different values of γ and t_c within certain restrictions, and find the values for which the average inversion, over a specified bandwidth of offsets or rf values, is a maximum.

Figure (2.14) illustrates three composite pulse sequences that are optimized for broadband inversion with respect to ω_1. Both simulations and experiments are shown. Inversion results for a single π pulse are plotted as a reference. The inversion performance improves for a larger number of pulses.

3. Composite Pulses with Constant Phase Increments

For reasons of experimental convenience, it would be desirable to derive sequences in which rf phases occur as multiples of a constant phase. In looking at the form of the pulse sequences derived earlier,

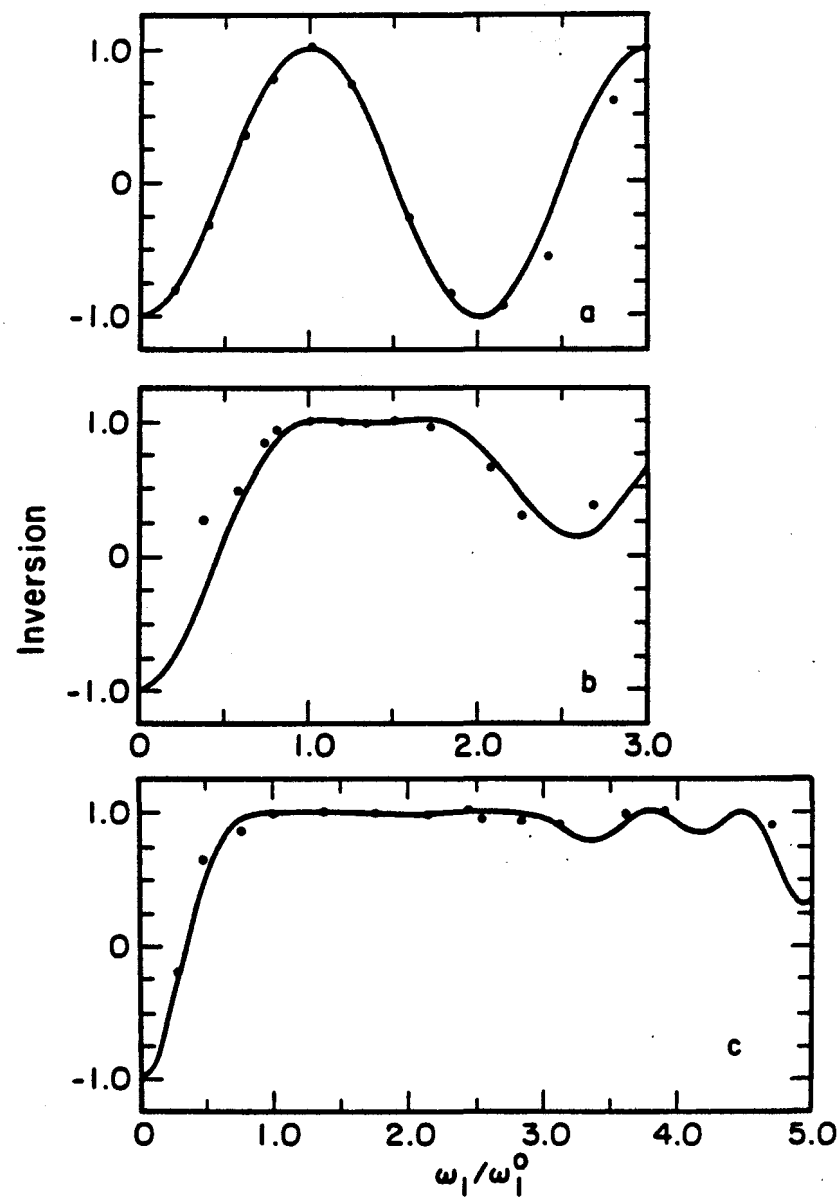

Figure 2.14. Simulations (solid lines) and ^{1}H experimental measurements (dots) of population inversion as a function of ω_1/ω_1^0 for discrete pulse sequences derived from the MIP using the technique described in Figure (2.13b). Results are shown for (a) single π pulse presented as a reference; (b) 3 pulse sequence $(54)_{90}(162.8)_0(54)_{90}$; (c) 31 pulse sequence $(18.3)_{264}(4.8)_{185}(5.3)_{172}(5.7)_{159}(6.3)_{146}$ $(6.9)_{132}(7.6)_{119}$ $(8.5)_{106}(9.4)_{93}(10.6)_{79}(12.0)_{66}(13.9)_{53}$ $(16.4)_{40}(20.2)_{26}(27.3)_{13}(127.0)_0(27.3)_{13}(20.2)_{26}(16.4)_{40}(13.9)_{53}$ $(12.0)_{66}(10.6)_{79}(9.4)_{93}(8.5)_{106}(7.6)_{119}(6.9)_{132}(6.3)_{146}(5.7)_{159}(5.3)_{172}$ $(4.8)_{185}(18.3)_{264}$. The notation is $(\theta)_\phi$ where θ and ϕ are the flip angles and phases of individual pulses in degrees.

we see that the phases ϕ_2 to ϕ_{2n-1} of the 2n-1 pulse sequence occur in constant increments but that ϕ_1 and ϕ_{2n-1} are arbitrary and hold no relationship to the other phases. Our goal in this section is to devise a method whereby we are able to specify the value of the constant phase increment, as well as make the first and last pulse have a phase that is some multiple of that increment.

In our method, the values of the phases, ϕ_2 to ϕ_{2n-2}, of the derived pulse sequence are determined solely from the constant phase increment used on the weighting function $\phi(t)$. The phase of the ith pulse is calculated from the $(i-1)^{st}$ and i^{th} point on the trajectory by

$$\phi_i = \tan^{-1} \frac{M_x(t_i) - M_x(t_{i-1})}{M_y(t_{i-1}) - M_y(t_i)} \quad 2 < i < 2n-1 \tag{2.34}$$

By substituting the values for M_x and M_y of Equation (2.14) into the above equation and using the fact $\phi(t_i) = (n-i)\phi_0$ (Equation 2.33), we find that

$$\phi_i = i\phi_0 + C \tag{2.35}$$

where C is constant. This indicates that the times corresponding to constant phase increments in $\phi(t)$ also correspond to points on $\underset{\sim}{M}(t)$ that may be connected by pulses with constant phase increments. Therefore we can specify ϕ_0 to be any constant phase we desire, and for a 2n-1 pulse sequence all the calculated pulses from the trajec-

tory between 2 and 2n-2 will have phases that differ by a multiple of ϕ_0.

To ensure that the first and last pulse also have a phase that is a multiple of ϕ_0 the following procedure is used. Rather that setting $\underset{\sim}{M}_0$ and M_{2n} at $\pm z$ as before, we now choose $\underset{\sim}{M}_{2n}$ such that the pulse connecting $\underset{\sim}{M}_{2n-1}$ to $\underset{\sim}{M}_{2n}$ have a phase $\phi_{2n-1} = m\phi_0$ where m is an integer. In order to still invert on-resonance spins, we also stipulate that $\underset{\sim}{M}_{2n}$ should remain as close to -z as possible. Therefore, to find the best position for $\underset{\sim}{M}_{2n}$ the flip angle of the last pulse is optimized by setting

$$\theta_{2n-1} = \tan^{-1} \frac{M_x(t_{2n-1})\sin(m\phi_0) - M_y(t_{2n-1})\cos(m\phi_0)}{M_z(t_{2n-1})} \quad . \qquad (2.36)$$

$\underset{\sim}{M}_0$ is found from $\underset{\sim}{M}_{2n}$ by symmetry. As before, the composite pulse is found by calculating the phases and flip angles which connect all the points $\underset{\sim}{M}_i$.

Note that contrary to before, we no longer optimize t_c and thereby ϕ_0, but rather ϕ_0 is chosen and t_c is found from $\phi(t_c) = n\phi_0$. The only parameter to be varied is γ and once again the best average criterion is used to select the pulse sequence that inverts best over the specified range of frequencies and rf amplitudes.

In Figure (2.15), we show computer simulations and experimental data of inversion versus resonance offset for pulse sequences generated by the above method. As expected, when the pulse sequence becomes longer, inversion is achieved over a large range of offsets.

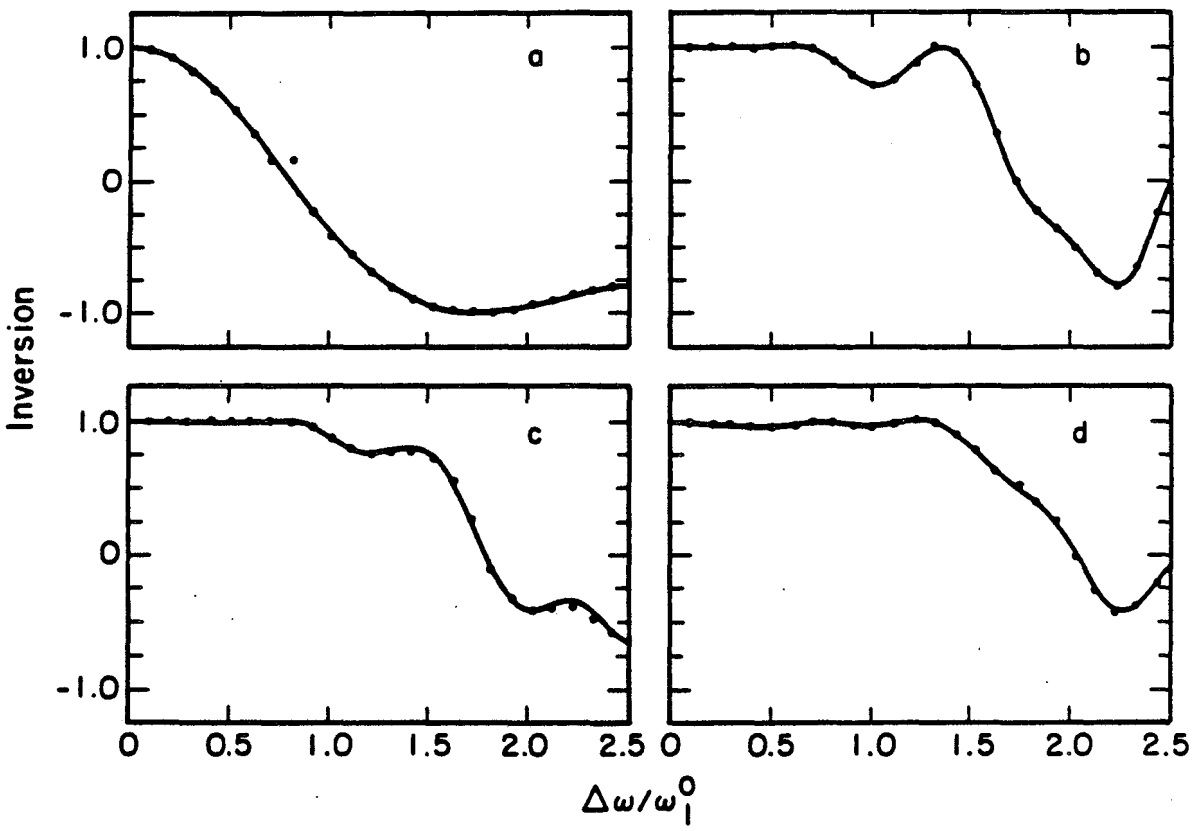

XBL 855-2606

Figure 2.15. Simulations (solid lines) and ^{1}H experimental measurements (dots) of population inversion as a function of $\Delta\omega/\omega_1$ for discrete pulse sequences derived from the MIP. Results are shown for (a) single π pulse presented as a reference; (b) 7 pulse sequence $(39.6)_{315}(68.4)_{180}(87.9)_{90}(275.7)_0(87.9)_{90}(68.4)_{180}(39.6)_{315}$; (c) 11 pulse sequence $(30.2)_{270}(28.7)_{180}(34.9)_{135}(43.8)_{90}(58.9)_{45}(225.4)_0(58.9)_{45}(43.8)_{90}(34.9)_{135}(28.7)_{180}(30.2)_{270}$; (d) 15 pulse sequence $(21.5)_0(19.4)_{270}(23.0)_{225}(27.5)_{180}(33.6)_{135}(42.5)_{90}(57.5)_{45}(222.8)_0(57.5)_{45}(42.5)_{90}(57.5)_{45}(222.8)_0(57.5)_{45}(42.5)_{90}(33.6)_{135}(27.5)_{180}(23.0)_{225}(19.4)_{270}(21.5)_0$.

The inversion bandwidths are comparable to those achieved by recently developed iterative techniques[21-22].

F. Experimental Methods

All of our experiments were performed on a small $H_2O(\ell)$ sample using a homebuilt spectrometer operating at a proton resonance frequency of 360 MHz described in reference 34. The pulse sequence used in the experiments consists of a composite pulse followed by a delay τ = 100ms, followed by a $\pi/2$ detection pulse. Large static field inhomogeneity causes transverse magnetiztion to dephase during τ. The ensuing FID is collected and Fourier transformed to give the final spectra. The resulting peak height is used as a measure of inversion. The peak height resulting from a single $\pi/2$ pulse alone is used as a calibration. A correction is made for spin-lattice relaxation during τ.

Experimental tests of composite pulses designed for broadband inversion with respect to ω_1 were performed on resonance. The rf amplitude was varied with an attenuator following the transmitter. The length of the detection pulse was adjusted to maintain a constant flip angle. Rf amplitudes were calibrated as in reference 23. Phase shifts were generated by a digitally controlled phase shifter capable of $360^{\circ}/256$ phase increments, with a 3μs switching time. The switching time required that delays be inserted between individual pulses. These delays do not affect inversion performance on resonance, although off resonance performance may degrade appreciably.

Experimental tests of broadband inversion with respect to the resonance offset required rf phases in 45° increments. This was accomplished by mixing the outputs of the two quadrature generation circuits in the spectrometer. Each quadrature circuit produces phases in 90° increments. A delay line was inserted between the two circuits, producing a phase difference of 45° between them. A vector voltmeter was used to determine the length of cable needed. The quadrature circuits were driven by a variable IF, allowing the resonance offset to be adjusted. The detection pulse was generated independently with a 30 MHz fixed IF source and maintained on resonance. All experiments were performed with $\omega_1^0/2\pi = 10$kHz. A schematic drawing of this setup can be found in reference 35.

G. Summary

We have described a general analytical procedure for deriving continuously phase modulated pulses that result in coherent population inversion on resonance. In the general case, both the phase and amplitude of the inverting pulse can be modulated continuously. Here, however, we have focussed on a class of constant amplitude, phase modulated pulses characterized by a single parameter γ, the depth of modulation. For small values of γ, when the phase modulation is deepened, the modulated inversion pulse (MIP) inverts spin populations simultaneously over large ranges of resonance frequencies and rf amplitudes.

We have proposed that the inversion behavior can be explained by

treating the MIP as an efficient adiabatic sweep. To support this, the simulated inversion performance of the MIP is compared to two other adiabatic sweeps in light of two criteria for adiabatic inversion. One sweep is the commonly cited linear frequency sweep and the other is a constant adiabaticity pulse derived directly from considerations of efficiency for adiabatic inversion. Comparisons indicate that the broadband properties of the MIP are in fact due to the adiabatic nature of the pulse and that for equal sweep lengths the MIP has superior inversion properties.

Having established the adiabatic properties of the MIP, we then present a method for generating a sequence of phase shifted rf pulses from the continuously phase modulated pulse. The composite pulses are calculated directly from the magnetization trajectory followed by on resonance spins subjected to the MIP. Selected points are chosen along the inverting trajectory and the corresponding constant phase pulses needed to connect these points are found. The broadband properties of the MIP are retained by the discrete pulse sequences, which can then be implemented on most modern NMR spectrometers. This approach connects modulated transparency and inversion pulses used in optics with composite pulses of NMR.

H. Appendix

In this appendix we treat the problem of finding rf pulses that cause on-resonance magnetization to follow a given trajectory. The trajectory in the FM frame is defined by a function $\underset{\sim}{M}(\varepsilon)$, where $\underset{\sim}{M}$ is the unit magnetization vector in Equation (2.7). In the special case of Equation (2.9), ε was a polar angle. In general, ε is simply a variable that parametrizes the trajectory. Here we require that ε lie in a unit interval. We make the restrictions that $\underset{\sim}{M}(\varepsilon)$ be continuous and differentiable. These restrictions are consistent with the physical requirements that the trajectory be smooth and unbroken. A piecewise-differentiable trajectory may be treated by considering each piece separately.

With the rf amplitude constant and equal to ω_1^0, the task is now to determine $\varepsilon(t)$ and $\dot{\phi}(t)$. With the definition:

$$\underset{\sim}{\mu} = \frac{d\underset{\sim}{M}}{d\varepsilon} \tag{2.37}$$

Equation (2.8) becomes:

$$\dot{\varepsilon}\underset{\sim}{\mu} = (-\omega_1^0, 0, \dot{\phi}) \times \underset{\sim}{M} \tag{2.38}$$

leading to:

$$\dot{\phi} = \omega_1^0 \frac{\mu_x}{\mu_z} \tag{2.39}$$

$$\dot{\varepsilon} = - \frac{\omega_1^0 M_y}{\mu_z} \tag{2.40}$$

Equation (2.39) gives the phase modulation as a function of ε. Equation (2.40) gives t as a function of ε:

$$t = -\int_0^{\varepsilon} d\varepsilon' \frac{\mu_z}{\omega_1^0 M_y} \tag{2.41}$$

Inverting Equation (2.41) gives ε as a function of t, which completes the derivation of the phase modulation.

The phase function obtained in this way produces the desired trajectory for $\Delta\omega = 0$ and $\omega_1(t) = \omega_1^0$. For non-zero values of $\Delta\omega$, the same trajectory may be produced by subtracting the constant $\Delta\omega$ from $\dot{\phi}$ in Equation (2.39). Of course, this is equivalent to shifting the rf carrier frequency. The phase function that corresponds to an amplitude modulated pulse can be derived according to the discussion in Section II.D.

Finally, it should be realized that not all trajectories are obtainable. In particular, there is no pulse that produces the desired trajectory if t is not a monotonic function of ε in Equation (2.41).

I. References

1. R.L. Vold, J.S. Waugh, M.P. Klein, and D.E. Phelps , J. Chem. Phys. **48**, 3831 (1968).

2. a) H.Y. Carr and E.M. Purcell, Phys. Rev. **94**, 630 (1954).
   b) S. Meiboom and D. Gill, Sci. Inst. **29**, 688 (1958)
   c) E.L. Hahn, Phys. Rev. **80**, 580 (1950).

3. D. Abella, N.A. Kurnit, and S.R. Hartmann, Phys. Rev. **141**, 391 (1966).

4. M.H. Levitt, R.Freeman, and T. Frenkiel, Adv. Magn. Reson. **11**, 48 (1983).

5. A. Abragam, "The Principles of Nuclear Magnetism" (Oxford University Press, London, 1961), p.44.

6. D. Grischkowsky, "Laser Applications to Optics and Spectroscopy", Vol. II of Physics of Quantum Electronics Series edited by S.F. Jacobs, M. Sargent III, J.F. Scott, and M.O. Scully (Addison-Wesley, Reading, Mass. 1975). p. 437.

7. M.D. Crisp, Phys. Rev. A **8**, 2128 (1973).

8. M.M.T. Loy, Phys. Rev. Lett. **32**, 814 (1974).

9. M.M.T. Loy, Phys. Rev. Lett. **41**, 473 (1978).

10. E.B. Treacy, Physics Letter **27A**, 421 (1968).

11. E.B. Treacy and J. Demaria, Physics Letters **29A**, 369 (1969).

12. M.H. Levitt and R. Freeman, J. Magn. Reson. **33**, 473 (1979).

13. R. Freeman, S.P. Kempsell and M.H. Levitt, J. Magn. Reson. **38**, 453 (1980).

14. M.H. Levitt and R. Freeman, J. Magn. Reson. **43**, 65 (1981).

15. M.H. Levitt, J. Magn. Reson. **48**, 234 (1982).

16. M.H. Levitt, J. Magn. Reson. **50**, 95 (1982).

17. R. Tycko, Phys. Rev. Lett. **51**, 775 (1983).

18. R. Tycko, H.M. Cho, E. Schneider, and A. Pines, J. Magn. Reson. **61**, 90 (1985).

19. M.H. Levitt and R.R. Ernst, J. Magn. Reson. **55**, 247 (1983).

20. A.J. Shaka and R. Freeman, J. Magn. Reson. **59**, 169 (1984).

21. R. Tycko and A. Pines, Chem. Phys. Lett. **111**, 462 (1984).

22. R. Tycko, J. Guckenheimer, and A. Pines, J. Chem. Phys. **83**, 2775 (1985).

23. R. Tycko, E. Schneider, and A. Pines, J. Chem. Phys. **81**, 680 (1984).

24. T.M. Barbara, R. Tycko, and D.P. Weitekamp, J. Magn. Reson. **62**, 54 (1984).

25. M. Levitt, D. Suter, and R. Ernst, J. Chem. Phys. **80**, 3064 (1984).

26. a) J. Baum, R. Tycko, and A. Pines, J. Chem. Phys. **79**, 4643 (1983).
b) J. Baum, R. Tycko, and A. Pines, Phys. Rev. A. **32**, 3435 (1985).

27. M.S. Silver, R.I. Joseph, and D.I. Hoult, Phys. Rev. A. **31**, 2753 (1985).

28. W.S. Warren and A.H. Zewail, J. Chem. Phys. **78**, 2279 (1983).

29. W.S. Warren, J. Chem. Phys. **81**, 5437 (1984).

30. S.L. McCall and E.L. Hahn, Phys. Rev. **183**, 457 (1969).

31. L. Allen and J.H. Eberly, "Optical Resonance and Two-Level Atoms" (John Wiley and Sons, New York, 1975).

32. I.I. Rabi, N.F. Ramsey, and J. Schwinger, Rev. Mod. Phys. **26**, 167 (1954).

33. R.P. Feynman, F.L. Vernon, and R.W. Hellwarth, J. Appl. Phys. **28**, 49 (1957).

34. G. Drobny, Ph.D. thesis, University of California, Berkeley, 1983 (published as Lawrence Berkeley Laboratory Report # LBL-15254).

35. R. Tycko, Ph.D. thesis, University of California, Berkeley, 1984 (published as LBL Report # LBL-18475).

III. MULTIPLE-QUANTUM NMR IN SOLIDS: THEORY AND EXPERIMENTAL CONSIDERATIONS

A. Introduction

Most applications of ^{1}H multiple-quantum NMR spectroscopy have necessarily been limited to small spin systems in isotropic or partially oriented phases, where the size of the system is clearly defined by the nature and extent of the spin-spin coupling.[1,2,3] In liquids, for example, only indirect scalar coupling remains after anisotropic interactions have been averaged to zero by rapid isotropic molecular motion. If instead, the molecules are dissolved in a nematic liquid crystal, translational freedom is retained but reorientation via tumbling is restricted so that intramolecular dipolar coupling becomes the principal interaction among the spins. In either case the spin-spin interactions are short range, and the system usually remains small enough to be characterized by a density operator that can be constructed from a finite, manageable number of basis operators.[4] In this regard, expansions based on fictitious spin-1/2,[5] spherical tensor,[6] and product[7] operators have proved quite useful for describing many experiments involving multiple-quantum effects. Among the numerous applications reported to date have been methods to simplify complicated single-quantum spectra,[8] determine spin connectivity and topology,[9] obtain high-resolution spectra in inhomogeneous magnetic fields,[10] and facilitate coherence transfer and indirect detection in systems containing magnetically rare nuclei.[11] On the other hand,

the extension of ^1H multiple-quantum spectroscopy to strongly coupled solids, where the coupling network includes all the spins in the sample, has also been illustrated recently.[12] This work has demonstrated that high order multiple-quantum coherences can be prepared and detected in solids, provided that time reversal excitation is used to counter the effects of dipolar dephasing.[13]

In this chapter, the basic principles of multiple-quantum NMR are described in Section B, and the need for time-reversal excitation in solids is motivated and explained in Section C. Time reversal excitation requires specialized pulse sequences: their design, using average Hamiltonian theory, is presented in Section D. Experimental considerations for the implementation of multiple-quantum NMR in solids are given in Section E. These include the actual experimental pulse sequence used in Chapter IV, the tune-up procedure, and the spectrometer implementation.

B. Generalized Multiple Quantum NMR Experiment

The general form of a two-dimensional multiple quantum NMR experiment is shown in Figure (3.1).[14,15] The pulse sequence is partitioned into four distinct periods each characterized by a time variable: preparation (τ), evolution (t_1), mixing (τ) and detection (t_2). The multiple-quantum coherences are prepared during the preparation period τ, after which they evolve freely in the presence of local dipolar fields for a time t_1. These unobservable multiple-quantum coherences are converted to observable single quantum coherences dur-

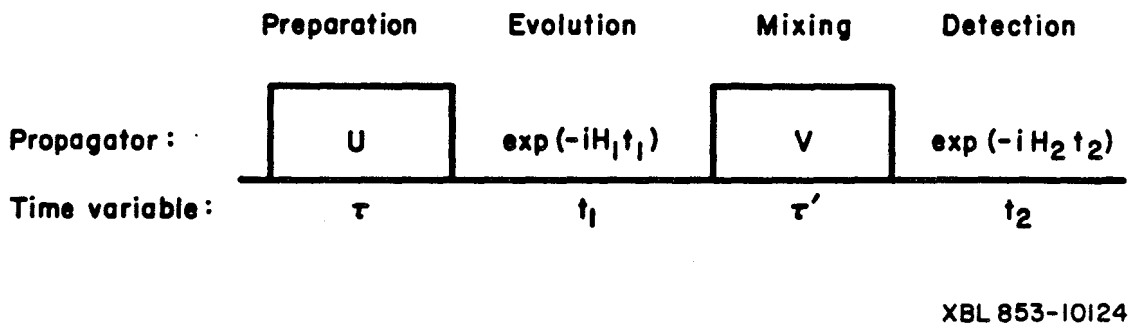

Figure 3.1. General form of the two-dimensional multiple-quantum pulse sequence. Multiple-quantum coherences are created by the preparation period propagator, $U(\tau)$, and respond to local fields during the evolution period t_1. The mixing period propagator, $V(\tau)$, transfers multiple-quantum coherence to single-quantum coherence for detection during t_2.

ing the mixing period τ', after which either a single point or a full free induction decay (FID) is sampled during t_2. The entire experiment is repeated for different values of t_1 to map out the multiple quantum interferogram. Complex Fourier transformation with respect to t_1 results in a multiple quantum spectrum, an example of which is shown in Figure (3.2). In the following sections, all four periods will be examined in detail to clarify their functions.

For simplicity, a form of the multiple quantum experiment consisting of only three pulses (Figure 3.3a) is considered first. The internal Hamiltonian considered here is

$$H_{int} = H_{zz} + H_z \tag{3.1}$$

$$= -\sum_{i<j} D_{ij} \left(3I_{zi} I_{zj} - I_i \cdot I_j\right) - \sum_{i=1}^{N} \Delta\omega_i I_{zi} \quad ,$$

where H_{zz} is the dipolar coupling term and H_z the chemical shift or resonance offset term. The dipolar coupling is

$$D_{ij} = \frac{\gamma_I^2 \hbar}{r_{ij}^3} \quad \frac{3\cos^2\theta_{ij} - 1}{2} \tag{3.2}$$

for a homonuclear interaction.

1. <u>Preparation Period</u>

The pulse sequence during this period determines the form of the

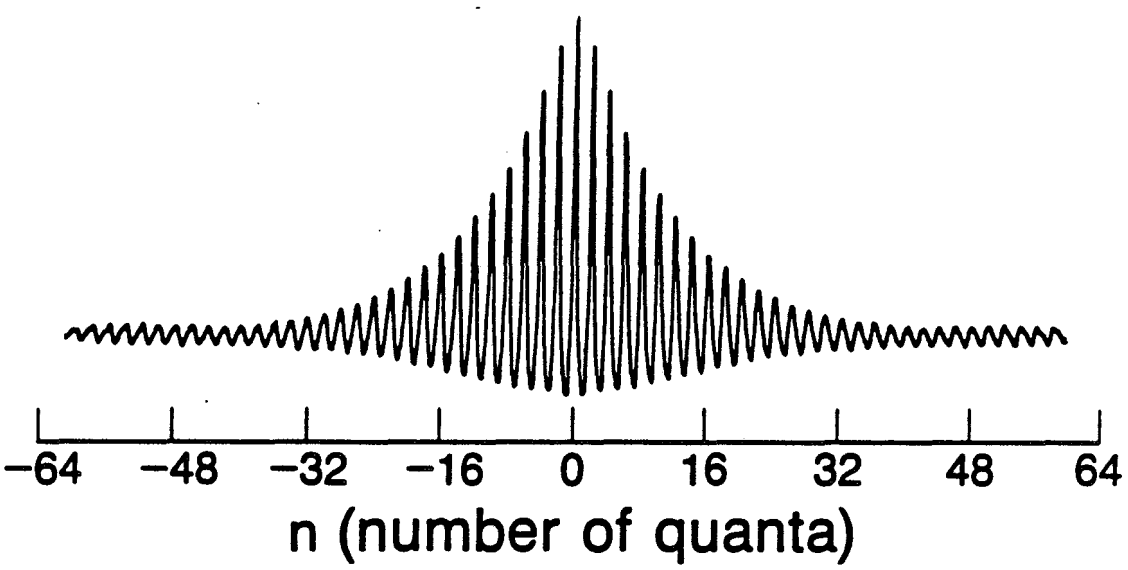

XBL 8512-12835

Figure 3.2. ^{1}H multiple-quantum spectrum of adamantane. In multiple-quantum NMR, coherences between states $|M_i\rangle$ and $|M_j\rangle$ are established where the total Zeeman quantum number, $\Delta M = M_i - M_j = n$, is equal to any integer value up to N, the number of spins in the system. In a solid, individual transitions within each order can not be resolved, resulting in broad lines. Very high multiple-quantum orders, n, can be created by using time-reversal excitation.

Figure 3.3. Pulse sequences for multiple-quantum NMR: a) Basic three pulse experiment suitable for systems where individual transitions can be resolved; b), c) and d) Time-reversal sequences used for solids. The preparation and mixing periods are composed of 8 $\pi/2$ pulses of length t_p with delays as indicated. This combination of pulses and delays creates a two-quantum average Hamiltonian, $\bar{H}_D^{(0)} = 1/3(H_{yy} - H_{xx})$ under which coherences of even order can develop. Time-reversal excitation is accomplished by phase-shifting all of the preparation period pulses by $\pi/2$. Therefore, when the phases of the pulses are x and $\bar{x}$, the sequence produces $\bar{H}_D^{(0)} = 1/3(H_{yy} - H_{xx})$; during the mixing period, when the phases of the pulses are y and $\bar{y}$, the Hamiltonian becomes $-1/3(H_{yy} - H_{xx})$, i.e. the negative of the preparation period Hamiltonian. The differences between the sequences are discussed in detail in Section D of the text. The total preparation/mixing time τ is achieved by repeating the basic pulse cycle m times. To separate the mutliple-quantum orders, the preparation period pulses are incremented by a phase ϕ for each value of t_1. About 2 ms after mixing, the z-component of the magnetization is monitored with standard detection schemes shown in Figure (3.7). The entire sequence is repeated for different values of t_1 to obtain the multiple quantum free induction decay. Fourier transformation with respect to t_1 then yields the multiple-quantum spectrum.

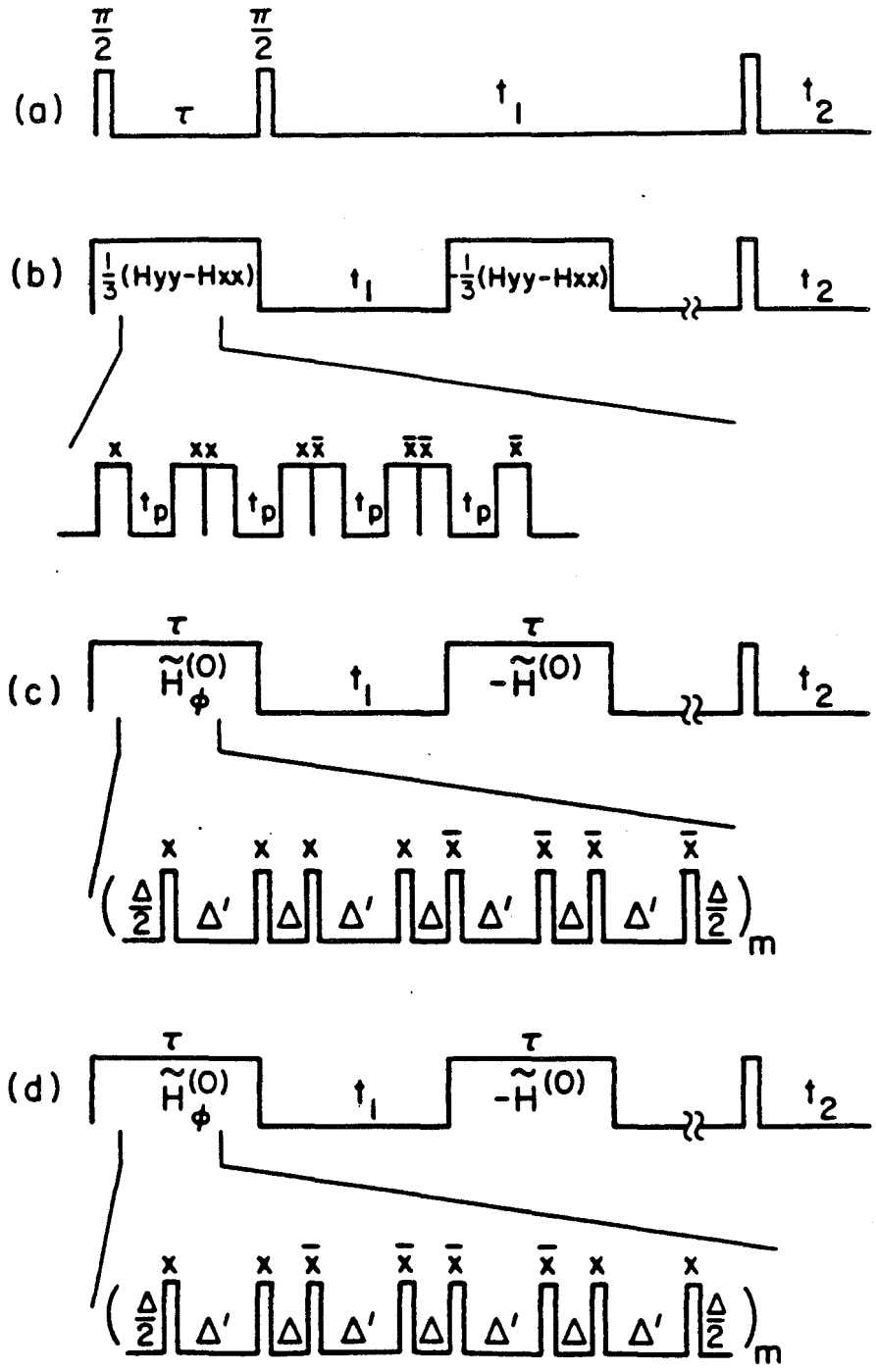
(a)
π/2
π/2
τ
t1
t2
(b)
1/3(Hyy-Hxx)
t1
-1/3(Hyy-Hxx)
t2
x
xx
xx̄
x̄x̄
x̄
tp
(c)
τ
H̃(0)φ
t1
τ
-H̃(0)
t2
x x x x x̄ x̄ x̄ x̄
Δ/2 Δ' Δ Δ' Δ Δ' Δ Δ' Δ/2
m
(d)
τ
H̃(0)φ
t1
τ
-H̃(0)
t2
x x x̄ x̄ x̄ x̄ x x
Δ/2 Δ' Δ Δ' Δ Δ' Δ Δ' Δ/2
m

XBL 861-176

multiple quantum excitation. Even selective ($n=0,\pm2,..,\pm N$), odd selective or both; selective excitation of only one multiple quantum order, etc... are just a few examples of the possible or desired schemes.[1-3] The preparation period addressed here is an even selective sequence of the form $(\pi/2)_x - \tau - (\pi/2)_{\bar{x}}$. The propagator, $U(\tau)$, for this sequence is:

$$U(\tau) = \exp\left(i\frac{\pi}{2}I_x\right) \exp(-iH_{int}\tau) \exp\left(-i\frac{\pi}{2}I_x\right) \tag{3.3}$$

and assuming no resonance offset, $\Delta\omega=0$, $U(\tau)$ becomes

$$U(\tau) = \exp\left(i\frac{\pi}{2}I_x\right) \exp(-iH_{zz}\tau) \exp\left(-i\frac{\pi}{2}I_x\right) \tag{3.4}$$

Two ways can be invoked to understand what happens to the equilibrium density matrix under this pulse sequence: either a step-by-step approach or an effective Hamiltonian approach both leading to the same result can be employed. The latter is the more convenient, although the former will be examined in order to gain insight into single quantum NMR. The equilibrium density operator, proportional to I_z, is acted on by a $(\pi/2)_x$ pulse to give $I_{\bar{y}}$ which then evolves freely under the internal Hamiltonian H_{zz} for a time τ, resulting in

$$\rho(\tau) = \exp(-iH_{zz}\tau)I_{\bar{y}} \exp(iH_{zz}\tau) \tag{3.5}$$

If $\rho(\tau)$ is expanded in the outer product eigenbasis $\{|M_i\rangle\langle M_j|\}$, described in Chapter I, Section C.3.b. then

$$\rho(\tau) = \sum_{i,j} \exp(-i\omega_{ij}\tau) \langle M_i | I_{\bar{y}} | M_j \rangle \; |M_i\rangle\langle M_j| \tag{3.6}$$

where $\omega_{ij} = (\omega_i - \omega_j)$, is the difference in energy between $|M_i\rangle$ and $|M_j\rangle$. The most important point to note is that since $I_{\bar{y}} = -1/2\,[I_+ - I_-]$ only states differing by $\Delta M = \pm 1$ can be connected. Only single-quantum transitions are induced by a single $\pi/2$ pulse.

A second way of viewing the same event is to expand $\rho(\tau)$ into products of single-spin operators which were described in Chapter I, Section C.3.c.[7] Equation (3.5) can be rewritten as

$$\rho(\tau) = I_{\bar{y}} + i\tau\,[I_{\bar{y}}, H_{zz}] - \frac{1}{2}\tau^2\,[\,[\,I_{\bar{y}}, H_{zz}], H_{zz}] + \ldots \tag{3.7}$$

Evaluation of the nested commutators results in products of operators such as $I_{\bar{y}1}$, $I_{z2} \ldots I_{zq}$ where q, the number of interacting spins, ranges from 1 to N. Only single-quantum/multiple-spin terms can arise from this density operator. Conversion of the single-quantum coherences to multiple-quantum coherences is accomplished by the second $(\pi/2)_x$ pulse.

Rather than having the pulses act on the density operator step by step, it is mathematically more convenient to let the pulses act on H_{int} to create an effective Hamiltonian H'_{int},

$$H'_{int} = \exp(-i\tfrac{\pi}{2}I_x)\, H_{int}\, \exp(i\tfrac{\pi}{2}I_x) \tag{3.8}$$

In this case, rotating H_{zz} by $\pi/2$ about the x axis results in

$$H_{yy} = \exp(i\tfrac{\pi}{2}I_x)\ H_{zz}\ \exp(-i\tfrac{\pi}{2}I_x)$$

$$= -\sum_{i<j} D_{ij}(3I_{yi}I_{yj} - I_i \cdot I_j) \qquad (3.9)$$

$$= -\frac{1}{2} H_{zz} + \frac{3}{4} \sum_{i<j} D_{ij}(I_{+i}I_{+j} + I_{-i}I_{-j})$$

The rotated dipolar Hamiltonian, H_{yy}, contains both zero quantum operators from H_{zz} and double quantum operators of the form $I_{+i}I_{+j} + I_{-i}I_{-j}$ from the second term of Equation (3.9). The preparation period density operator becomes

$$\rho(\tau) = \exp\ (-iH_{yy}\tau)\ I_z\ \exp(iH_{yy}\tau) \qquad (3.10)$$

$$= I_z + i\tau\ [I_z, H_{yy}] - \frac{1}{2}\tau^2[[I_z, H_{yy}], H_{yy}] + \ldots \qquad (3.11)$$

The density operator now contains multiple-quantum/multiple-spin terms. Because H_{yy} is a pure zero/double quantum operator, the density operator of Equation (3.11) will excite only zero or even-quantum coherences. Most importantly the Hamiltonian under which $\rho(0)$ evolves must contain bilinear operators to excite multiple quantum coherences.

2. Evolution Period

Multiple-quantum coherences cannot be detected directly. Since the detection coil is only sensitive to single spin operators I_+ or I_-, multiple quantum coherences, for example operators of the form $I_{+1}I_{+2}I_{-3}\ldots I_{+q}$, are not observable. A method of indirect detection is used: the multiple quantum coherences evolve under an internal Hamiltonian for a time t_1, the frequency information is then stored and later retrieved during the detection period in t_2. The evolution of the coherences depends entirely on H_{int}.

a) $H_{int} = H_{zz}$

The density operator after a time t_1 is

$$\rho(\tau, t_1) = \exp(-iH_{zz}t_1)\ \rho(\tau)\ \exp(iH_{zz}t_1) \tag{3.12}$$

$$= \sum_{i,j} e^{-i\omega_{ij}t_1}\ \rho_{ij}(\tau)|M_i\rangle\langle M_j|$$

where $\rho_{ij}(\tau) = \langle M_i|\rho(\tau)|M_j\rangle$. Each multiple-quantum coherence between $|M_i\rangle$ and $|M_j\rangle$ is frequency labelled by ω_{ij}, the energy difference between the two states.

b) $H_{int} = \Delta\omega I_z$

Now the density operator after a time t_1 is:

$$\rho(\tau, t_1) = \exp(-i\Delta\omega I_z t_1)\ \rho(\tau)\ \exp(i\Delta\omega I_z t_1)$$

$$= \sum_{i,j} e^{-n\Delta\omega t_1} \rho_{ij}(\tau) \; |M_i\rangle\langle M_j| \qquad (3.13)$$

This equation indicates that a multiple quantum coherence between $|M_i\rangle$ and $|M_j\rangle$ oscillates at n times the frequency offset rather than the actual frequency offset, $\Delta\omega$. A schematic drawing is presented in Figure (3.4). The n-fold increase in oscillation frequency is used in a number of experiments: in particular, it forms the basis of the NMR imaging experiments in solids[16] described in Chapter 5, and also forms the basis of the method of time proportional phase incrementation, which is used to separate multiple quantum orders in a spectrum.

c) Time Proportional Phase Incrementation[17]

Effectively, the internal Hamiltonian becomes $H_{int} = H_{zz} + H_z$ and the density operator evolves as

$$\rho(\tau, t_1) = \sum_{i,j} e^{-i\omega_{ij}t_1} \; e^{-in\Delta\omega t_1} \; \rho_{ij}(\tau)|M_i\rangle\langle M_j| \qquad (3.14)$$

Clearly without the second oscillating exponential in the equation the different n-quantum coherences would not be readily distinguishable. Performing the experiment with a large enough resonance offset is inconvenient; instead a trick is used. The overall phase of the preparation period is incremented proportionally to t_1, i.e. $\Delta\phi = \Delta\omega' t_1$. This artificially introduces a resonance offset term, $\Delta\omega'$, into the evolution period. Formally, incrementing the phase of each

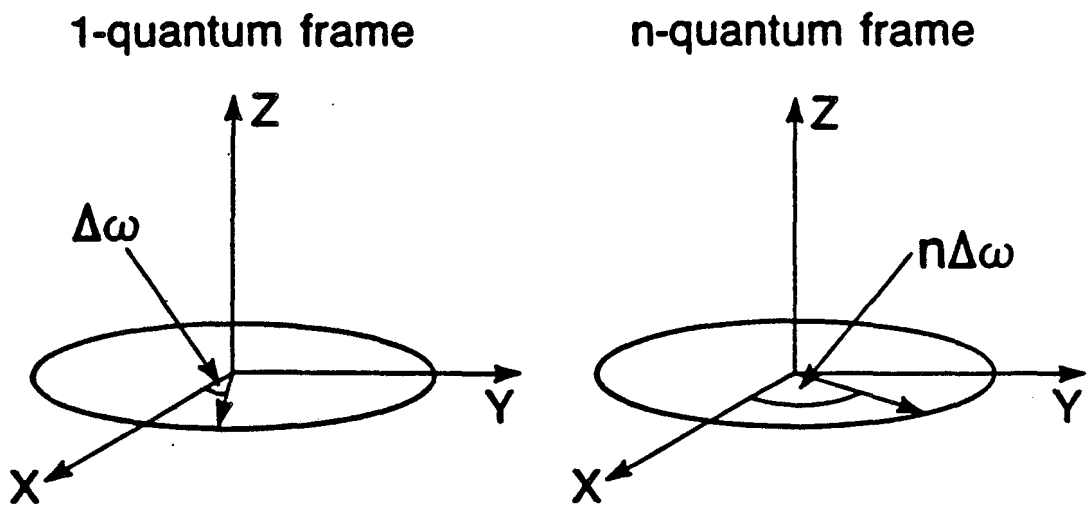

Figure 3.4. An n-quantum coherence between $|M_i\rangle$ and $|M_j\rangle$ oscillates at n times the frequency offset, $\Delta\omega$, rather than the actual offset $\Delta\omega$.

pulse by $\Delta\phi$ corresponds to an overall phase shift of the propagator $U(\tau)$. If the phase of the pulse was I_ϕ, now it is $I_{\phi+\Delta\phi}$, where

$$I_{\phi+\Delta\phi} = \exp(-i\Delta\phi I_z)\ I_\phi\ \exp(i\Delta\phi I_z) \quad . \tag{3.15}$$

The propagator for the pulse is

$$\begin{aligned} \exp(-i\tfrac{\pi}{2}\ I_{\phi+\Delta\phi}) &= e^{-i\frac{\pi}{2}(\exp(-i\Delta\phi I_z)I_\phi\exp(i\Delta\phi I_z))} \\ &= \exp(-i\Delta\phi I_z)\ e^{-i\frac{\pi}{2}I_\phi}\ \exp(i\Delta\phi I_z) \end{aligned} \tag{3.16}$$

as a result of the relationship

$$Ue^{A}U^{-1} = e^{UAU^{-1}} \quad . \tag{3.17}$$

The preparation period propagator becomes

$$\begin{aligned} U_{\Delta\phi}(\tau) &= \exp(-i\tfrac{\pi}{2}I_{\phi+\Delta\phi})\ \exp(-iH_{zz}\tau)\ \exp(i\tfrac{\pi}{2}I_{\phi+\Delta\phi}) \\ &= \exp(-i\Delta\phi I_z)\ U(\tau)\ \exp(i\Delta\phi I_z) \end{aligned} \tag{3.18}$$

since $[I_z, H_{zz}] = 0$. Therefore, the initial propagator is phase shifted by $\Delta\phi$ around I_z; because it is phase shifted proportionally to t_1, so that

$$\Delta\phi = \Delta\omega' t_1 \quad , \tag{3.19}$$

the density operator after t_1 is

$$\rho(\tau, t_1) = \exp(-iH_{zz}t_1)\, U_{\Delta\phi}(\tau)\, \rho(0)\, U^{-1}_{\Delta\phi}(\tau)\, \exp(iH_{zz}t_1) \tag{3.20}$$

Substituting Equations (3.18) and (3.19) into the above, the density operator becomes

$$\rho(\tau,t_1) = \exp(-iH_{zz}t_1)\exp(-i\Delta\omega' I_z t_1)\, \rho(\tau)\, \exp(i\Delta\omega' I_z t_1)\, \exp(iH_{zz}t_1) \tag{3.21}$$

which is equivalent to Equation (3.14). Now the different multiple-quantum coherences oscillate at $n\Delta\omega'$ and are readily separated by Fourier transformation.

3. Mixing Period

Multiple quantum coherences are converted to detectable single quantum coherences during the mixing period. There exists a basic symmetry between the preparation and mixing periods, collectively called excitation periods. Similarly to the preparation period, two approaches can be used to examine the effects of the mixing period. Either one pulse is applied to the system and then single quantum coherences evolve under the dipolar Hamiltonian, for a time τ', into

observable signal proportional to I_+; this approach is similar to the step-by-step analysis of the preparation period. Or else the multiple quantum experiment is considered to be a four pulse experiment with the detected operator now proportional to I_z. The latter is more convenient formally, since the mixing period propagator $V(\tau')$ can now be written as

$$V(\tau') = \exp(i\tfrac{\pi}{2}I_x)\ \exp(-iH_{zz}\tau')\ \exp(-i\tfrac{\pi}{2}I_x). \tag{3.22}$$

$V(\tau')$ is very similar in form to $U(\tau)$, the preparation period propagator.

4. Detection Period

The multiple quantum signal for a preparation time τ and a fixed evolution time t_1 can be detected at this point. The signal is

$$\begin{aligned} S(t) &= \mathrm{Tr}\ \{I_z\rho(t)\} \\ &= \mathrm{Tr}\left[I_z V(\tau')\ \exp(-iH_{zz}t_1)\ U_{\Delta\phi}(\tau)\rho(0)U^{-1}_{\Delta\phi}(\tau)\exp(iH_{zz}t_1)V^{-1}(\tau')\right] \end{aligned} \tag{3.23}$$

The trace is invariant to cyclic permutation, and when $\rho(0) = I_z$,

$$S(t) = \mathrm{Tr}\left[V^{-1}(\tau')I_z V(\tau')\exp(-iH_{zz}t_1)\ U_{\Delta\phi}(\tau)I_z U^{-1}_{\Delta\phi}(\tau)\exp(iH_{zz}t_1\right] \tag{3.24}$$

Expanding the trace in the eigenbasis of H_{zz} results in the expression

$$S(t) = \sum_{i,j} \alpha_{ji}(-\tau)\ \rho_{ij}(\tau)\ e^{-i\omega_{ij}t_1}\ \ e^{in\Delta\omega' t_1} \tag{3.25}$$

where $\alpha_{ji}(-\tau) \quad = \langle M_j |\ V^{-1}(\tau')I_z V(\tau')\ |M_i\rangle$

and $\quad \rho_{ij}(\tau) \quad = \langle M_i |\ U(\tau)\ I_z U^{-1}(\tau)\ |M_j\rangle \quad .$

By repetition of the experiment for different values of t_1, a multiple-quantum free induction decay is mapped out. The signal of a multiple quantum coherence between $|M_i\rangle$ and $|M_j\rangle$ is characterized by:

1) a complex amplitude, $\alpha_{ji}(-\tau)\rho_{ij}(\tau)$, with magnitude and phase.
2) a transition frequency: ω_{ij}
3) an order dependent offset term: $n\Delta\omega$.

The final step is to Fourier transform the signal with respect to t_1.

C. Multiple-Quantum Intensities

1. Statistical Model for Line Intensities

A simple estimate for line intensities assumes that each symmetry allowed coherence will have the same magnitude but random phase.[18] Therefore, in this statistical limit, all symmetry-allowed transitions are excited equally.[19] The integrated spectral intensity per order is the intensity per transition times the number of allowed transitions. The number of allowed transitions are calculated from the energy levels as follows. N coupled spins-1/2 produce 2^N energy levels characterized by their total Zeeman quantum number M as shown in Figure (3.5). The energy levels are divided into N+1 Zeeman manifolds with

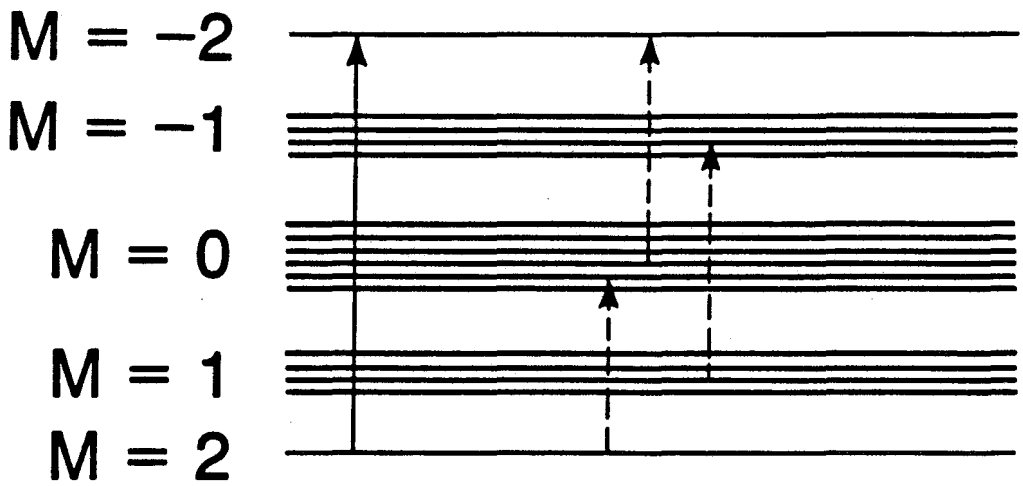

Figure 3.5. Energy level diagram resulting from 4 coupled spins-1/2. The Zeeman manifolds are characterized by their total Zeeman quantum number M. The number of states within each manifold is given by Equation (3.26) which describes the number of ways of choosing p out of N spins to be "up" instead of "down", where $p = N/2 + M_i$. The number of multiple quantum transitions of order $\Delta M = n$ is given by the sum over the products in Equation (3.27). As an example, for 4 coupled spins, there is one 4-quantum transition and 28 two-quantum transitions. Clearly the number of n-quantum transitions decreases with increasing order.

splittings due to dipolar couplings or chemical shifts occurring within each manifold. The number of states is given by

$$\binom{N}{p} = \frac{N!}{(N/2 + M_i)!(N/2-M_i)!} \tag{3.26}$$

within each manifold. In this equation p is defined as the number of spins pointing "up", consistent with the value of M_i. Ignoring symmetry, the number of multiple quantum transitions of order n is given by a sum over the products,[20]

$$\sum_{p=0}^{N-n} \binom{N}{p}\binom{N}{n+p} \qquad n\neq 0, \tag{3.27}$$

which is equivalent to

$$\binom{2N}{N-n} \qquad n\neq 0 \tag{3.28}$$

The number of zero-quantum transitions is equal to

$$\frac{1}{2}\left[\binom{2N}{N} - 2^N\right] . \tag{3.29}$$

Using Stirling's approximation, the number of n-quantum transitions is

$$\frac{4^N}{(N\pi)}1/2 \quad \exp(-n^2/N) \qquad \text{when } n\neq 0 \tag{3.30}$$

for large N and n<<N. The number of transitions drops off in a Gaussian manner and the statistical model predicts that the integrated intensities will therefore decrease rapidly with increasing order. In Chapter IV, this model is used to account for the multiple-

quantum intensities.

2. Time-Reversed Excitation in Solids

The intensity of a multiple quantum coherence between $|M_i\rangle$ and $|M_j\rangle$ is characterized by the product of the two complex numbers, $\alpha_{ji}(-\tau)\rho_{ij}(\tau)$, of Equation (3.25). Figure (3.6) shows the multiple-quantum spectrum of benzene oriented in a liquid crystal. Within each order n, the phases of the individual transitions differ relative to one another. But, as long as the individual transitions do not overlap, a magnitude spectrum can be used to calculate the integrated intensities.

However, in a solid, essentially an infinite spin system, the number of multiple quantum transitions within a particular order is very high. This is readily calculated from Equation (3.28) - for example, already for the six spin system of Figure (3.6), the number of single-quantum transitions is 972. Therefore, in a solid, where the size of the system is essentially unlimited, the numerous multiple-quantum transitions will overlap and destructive interference will drastically reduce the integrated multiple-quantum intensities within an order n. As a result, high multiple-quantum orders, although present, will not be visible. To overcome this problem, all lines within an order should be generated in phase.[2,12] This condition is attained by using a time-reversed mixing period, which imposes the condition $U = V^+$; i.e. the preparation period propagator must be equal to the hermitian conjugate of the mixing period propagator. When $U = V^+$, the intensity of an individual transition becomes:

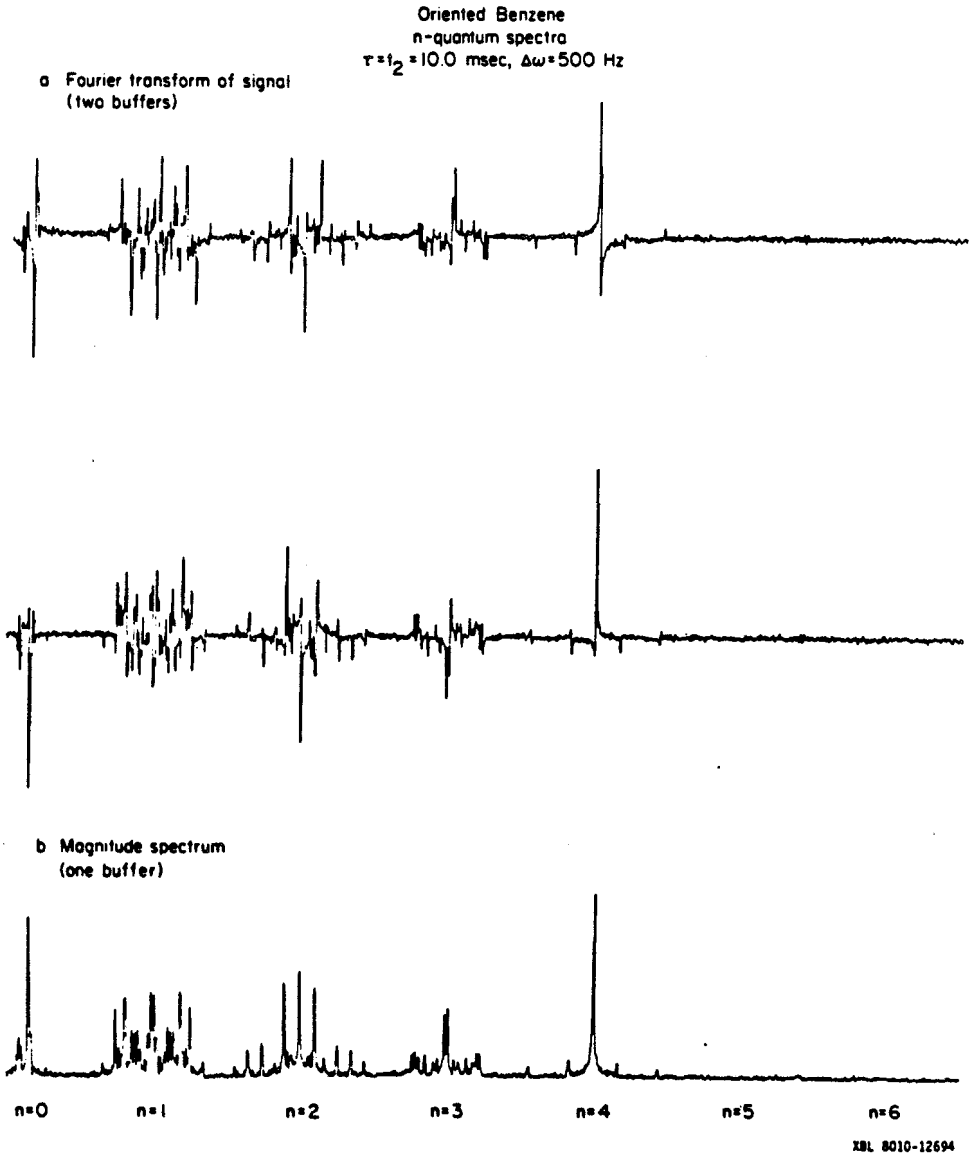

Figure 3.6. Multiple-quantum spectrum of oriented benzene (14 wt % in Eastman nematic liquid crystal # 15320 at 24.0°) obtained by Warren Warren.[18] When individual transitions within each order can be resolved, as here, the wide range of phases apparent in part (a) does not affect the integrated intensity of each order. A magnitude spectrum (b) can be obtained and shows only slight broadening. However, in a solid, where the number of transitions is essentially continuous, overlapping lines with different phases will drastically reduce the integrated n-quantum intensities. To overcome this problem, all lines within an order are generated in phase by using time reversal excitation.

$$\rho_{ij}(\tau)\ \alpha_{ji}(-\tau) = \langle i|U(\tau)I_zU^+(\tau)|j\rangle\langle j|V^+(\tau)I_zV(\tau)|i\rangle$$

$$= \langle i|U(\tau)I_zU^+(\tau)|j\rangle\langle i|(U(\tau)I_zU^+(\tau))^+|j\rangle^* \qquad (3.31)$$

$$= |\langle i|U(\tau)I_zU^+(\tau)|j\rangle|^2$$

$$= |\rho_{ij}(\tau)|^2$$

The Hamiltonians acting during the preparation and mixing periods will be denoted H_P and H_M, respectively. The propagators are

1) $U(\tau) = e^{-iH_P\tau}$

2) $V(\tau) = e^{-iH_M\tau}$

When $U(\tau) = V^+(\tau) = V^{-1}(\tau)$, then $H_P = -H_M$. Time reversal, in this context, means reversing the sign of the preparation period Hamiltonian to create the mixing period Hamiltonian. Now the intensity of a multiple quantum transition will be characterized by $|\rho_{ij}(\tau)|^2$, a real number, rather than $\rho_{ij}(\tau)\alpha_{ji}(-\tau)$, a complex number. Therefore, within an order, different multiple quantum transitions will have different magnitudes but the same phase. We have obtained very high multiple quantum coherences in a solid by using a time reversed mixing period. The multiple quantum spectrum of adamantane in Figure (3.2) is an example of a system in which 64 orders and beyond have been excited.[21]

D. Pulse Sequence Design

Experimentally, a very convenient Hamiltonian that can be used to create multiple-quantum coherence in solids is[22]

$$\bar{H}_D^{(0)} = \frac{1}{3}(H_{yy} - H_{xx}) \tag{3.32}$$

$$= -\frac{1}{\sqrt{2}} \sum_{i<j} D_{ij}(I_{i+}I_{j+} - I_{i-}I_{j-})$$

where

$$I_{j\pm} = \mp \frac{1}{2}(I_{jx} \pm iI_{jy})$$

This Hamiltonian contains only double-quantum operators, as opposed to H_{yy}, which contains both zero and double quantum operators. To create the time-reversed mixing period, i.e. change the sign of the Hamiltonian, a simple phase shift of $\pi/2$ about the z-axis is needed:

$$\exp(-i\frac{\pi}{2} I_z)(H_{yy}-H_{xx})\exp(i\frac{\pi}{2} I_z) = H_{xx}-H_{yy} \tag{3.33}$$

Note that a $\pi/2$ phase shift appied to H_{yy} does not create $(-H_{yy})$ because the zero-quantum operators existing in this Hamiltonian (Equation 3.9) are invariant to z rotations. A variety of pulse sequences can be used in order to create the average Hamiltonian of Equation (3.32) under which coherences of even order can develop. In solids, the δ-pulse limit, where H_{int} is assumed to be much less than H_{rf}, is not a good approximation. Therefore, evolution during the

pulse and finite pulse widths will be assumed for the design of these pulse sequences.

A simple semi-windowless sequence which can be constructed is shown in Figure (3.3b). Here eight pulses of length t_p separated by delays t_p, as shown, result in the average dipolar Hamiltonian of Equation (3.32). In fact, only four pulses are really needed to create the desired average Hamiltonian but eight are used for purposes of symmetrization. In the toggling frame, I_z moves through the sequence

$$(ZY)\ (Y\bar{Z})\ (\bar{Z}\bar{Y})\ (\bar{Y}Z)\ (Z\bar{Y})\ (\bar{Y}\bar{Z})\ (\bar{Z}Y)\ (YZ) \tag{3.34}$$

with delays t_p as indicated. A very brief description of average Hamiltonian theory and the notation used here is given in Chapter I, Section E. The sequence is symmetrized about the midpoint of the cycle with respect to both the resonance offset and dipolar Hamiltonians. The resulting average Hamiltonians and higher order correction terms are

$$\bar{H}_D^{(0)} = \frac{1}{3}(H_{yy} - H_{xx})$$

$$\bar{H}_D^{(1)} = \bar{H}_D^{(3)} = \ldots = \bar{H}_D^{(2n-1)} = 0$$

$$\bar{H}_{OFF}^{(0)} = 0 \tag{3.35}$$

$$\bar{H}_{OFF}^{(1)} = \bar{H}_{OFF}^{(3)} = \ldots = \bar{H}_{OFF}^{(2n-1)} = 0$$

$$\bar{H}_{rf}^{(0)} = 0 \quad .$$

The third pulse sequence shown in Figure (3.3) is very similar to the first but now delays, denoted by Δ and Δ', have been included in order to provide more control to the experimentalist. The delay Δ' still includes the delay t_p from Figure (3.3b). Therefore, when $\Delta' = 2\Delta + t_p$, the average dipolar Hamiltonian is once again $1/3(H_{yy} - H_{xx})$. The odd order correction terms, average resonance offset and rf inhomogeneity Hamiltonians are still identical to those of Equation (3.35).

A third variation of the pulse sequence is shown in Figure (3.3d).[22] Now, in the toggling frame, I_z moves through the sequence

$$(ZY)\ (Y\bar{Z})\ (\bar{Z}Y)\ (YZ)\ (Z\bar{Y})\ (\bar{Y}\bar{Z})\ (\bar{Z}\bar{Y})\ (\bar{Y}Z) \tag{3.36}$$

with delays Δ and Δ' as indicated. Although

$$\bar{H}_D^{(0)} = \frac{1}{3}\,(H_{yy} - H_{xx}) \quad ,$$

$$\bar{H}_D^{(1)} = \bar{H}_D^{(3)} = \ldots = \bar{H}_D^{(2n-1)} = 0 \tag{3.37}$$

$$\bar{H}_{OFF}^{(0)} = 0 \quad \text{and}$$

$$\bar{H}_{rf}^{(0)} = 0$$

now the sequence is no longer symmetrized for resonance offset and the odd order correction terms to the average resonance offset Hamiltonian are no longer zero. But the sequence is symmetrized for rf inhomogeneity resulting in

$$\bar{H}_{rf}^{(1)} = \bar{H}_{rf}^{(3)} = \bar{H}_{rf}^{(2n-1)} = 0. \tag{3.38}$$

In summary, for all three sequences (b,d)$\bar{H}_D^{(0)} = 1/3(H_{yy} - H_{xx})$ and the odd order correction terms to H_D vanish; the resonance offset and rf inhomogeneity average Hamiltonians are both zero. The differences between the sequences arise from the correction terms to these average Hamiltonians: in sequences (b) and (c) all odd order correction terms to the offset Hamiltonian are zero whereas in sequence (d), the odd order correction terms to the rf inhomogeneity Hamiltonian are zero. We designed sequences (b) and (c) to overcome resonance offset effects which are particularly important in multiple-quantum imaging experiments in solids described in Chapter V. Here, coherences must be prepared in the presence of large offsets created by the imposition of an external field gradient. In the experiments described in the next chapter, sequence (c), rather than sequence (b), was used as it was found to be more convenient experimentally. Sequence (d) was also

employed in a few instances and is more appropriate when rf inhomogeneity is a serious problem.

E. Experimental Implementation

1. Preparation Period

Although the density operator prepared at time τ contains predominantly even-order coherences, pulse imperfections can lead to the creation of unwanted odd-order coherences. These can be reduced by cycling the phases of all pulses in the preparation period between 0° and 180° in alternate experiments, and co-adding the resulting signals appropriately.[23] In addition, it is necessary to label the orders of coherence by using the method of TPPI discussed in Section B.1.c.

2. Evolution period

During the evolution period, the system responds to the internal Hamiltonian,

$$H_{int} = H_z + H_{zz} \quad ,$$

where H_z formally contains an order-dependent offset term resulting from TPPI. The interferogram is mapped out point-by-point for successive values of t_1. The spectral width of the multiple-quantum spectrum is given by $1/\Delta t_1$, and the number of orders detected, $(\pm n_{max} + 1)$, is determined by the phase increment, $\Delta\phi = 2\pi/(2n_{max} + 1)$. Both

Δt_1 and $\Delta\phi$ must be chosen so that all signals from different coherence orders fit into the available bandwidth without aliasing and without overlapping. The actual values of Δt_1 and $\Delta\phi$ will be given along with the multiple-quantum spectra shown in the next chapter.

3. Mixing Period

The time-reversed mixing period is implemented by phase shifting all of the preparation period pulses by 90°. The mixing period then contains pulses with phases y and $\bar{y}$. As a result, the average mixing period Hamiltonian is the negative of the average preparation period Hamiltonian of Equation (3.32). The 90° phase shift in the mixing period is chosen relative to the phase of the preparation period at $t_1 = 0$. In other words, it is independent of the incremented phases in the preparation period due to TPPI. As seen in Equation (3.21), the effect of the phase increment can be formally removed from the preparation period and placed in the evolution period. As a result, these phase increments do not affect the phase shift needed for the mixing period.

If, at $t_1 = 0$, the mixing period is not 90° phase shifted from the preparation period, then $U \neq V^{+}$, but V^{+} is still related to U by a rotation around z:

$$V^{+} = e^{-i\beta I_z} \; U \; e^{i\beta I_z} \quad . \tag{3.39}$$

By substituting Equation (3.39) into Equation (3.24), the multiple-quantum signal takes the form

$$S(t) = \mathrm{Tr}\left[e^{-i\beta I_z}\, UI_zU^{+}\, e^{i\beta I_z}\, e^{-iH_{zz}t_1}\; UI_zU^{+}\, e^{iH_{zz}t_1}\right] \quad . \qquad (3.40)$$

Expanding the trace in the eigenbasis of H_{zz} results in

$$S(t) = \sum_{i,j} |\rho_{ij}(\tau)|^2\, e^{-in\beta} e^{-i\omega_{ij}t_1} \quad . \qquad (3.41)$$

Now there exists a phase term, $n\beta$, which determines the overall phase of each order. For instance, when $\beta = 90^{\circ}$, in other words when the preparation and mixing periods appear to have the same phase, then all even orders will be 180° out of phase. It is important to note that within each order, the phases of the individual transitions are all the same due to $|\rho_{ij}(\tau)|^2$, a real number. When TPPI is included, the signal becomes

$$S(t) = \sum_{i,j} |\rho_{ij}(\tau)|^2 e^{-in\beta}\, e^{-i\omega_{ij}t_1}\; e^{-in\Delta\omega' t_1} \qquad (3.42)$$

The multiple-quantum orders, n, are separated by $\Delta\omega'$ and their phases relative to one another are determined by β.

4. Detection Period

After mixing, a 2 ms delay is inserted, during which spurious transverse magnetization is allowed to decay. The desired signal is stored as population information along the z-axis. At this point, the

signal can be detected in many ways. Three schemes are presented in Figure (3.7). The first is just a simple $\pi/2$ pulse. In solids, where the FID decays very rapidly, receiver ringing and pulse breakthrough may distort the signal. A better detection scheme is shown in Figure (3.7b) where a $(\pi/2)_x$ detection pulse is followed by a 100μs spin-locking pulse along y. Now spin temperature inversion, achieved by a 180° phase alternation of the detection pulse, can be used to reduce artifacts arising from receiver ringing. A single point in t_2 in then sampled for each value of t_1, with the width of the single-quantum spectrum determining the optimum receiver bandwidth.

The third detection scheme shown in Figure (3.7c), a pulsed spin locking sequence[24] of the form

$$\frac{\pi}{2}_x - (\theta_y)_n ,$$

results in a large increase in signal to noise over the earlier methods. The pulsed spin-locking is useful for signal enhancement in samples containing low ^1H concentrations. To obtain the maximum signal, the optimal value of θ is roughly 45° and the delay between pulses 40 μsec. One point is sampled after the first pulse and after each θ_y pulse: usually 512 or 768 spin locked points were acquired, subject to the constraints of the $T_{1\rho}$ of the material.[25] All these points are then averaged together to give a final amplitude for a particular value of t_1. Again, 180° phase alternation of the detection pulse is used to reduce reviever ringing artifacts. The entire sequence is repeated for different values of t_1 to obtain the multiple

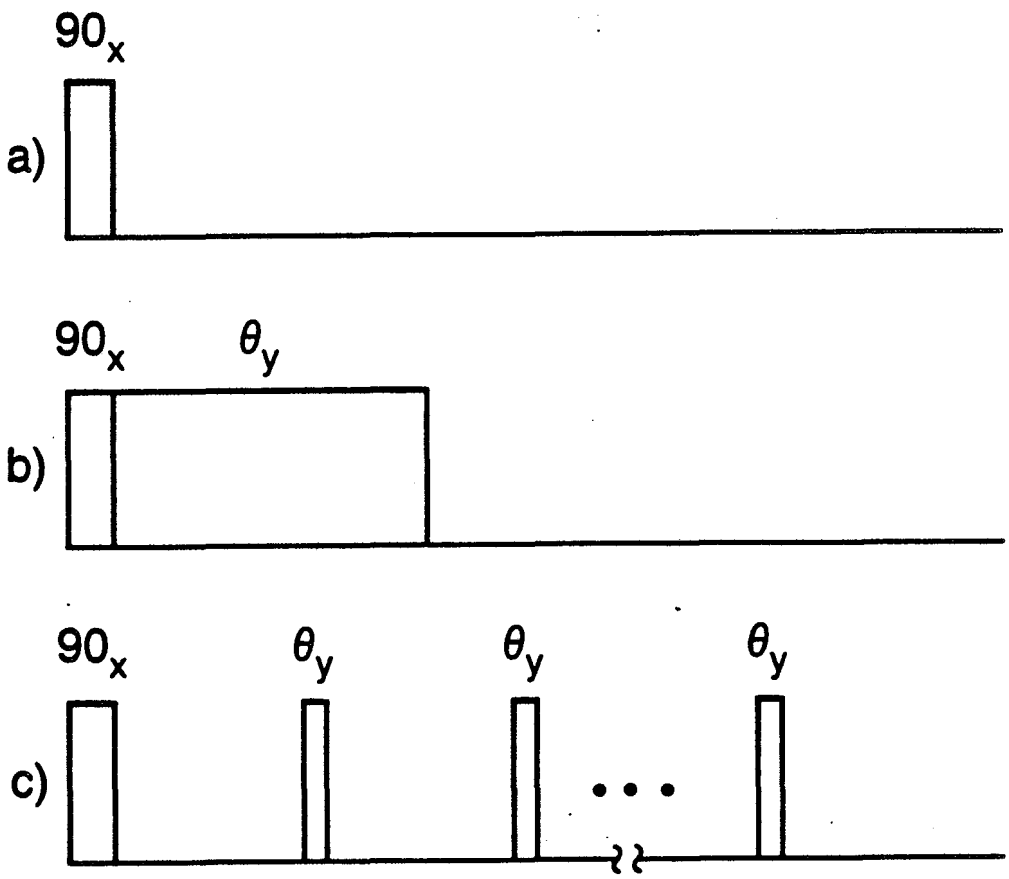

Figure 3.7. Detection schemes used to monitor the final z magnetization in the multiple-quantum experiment in solids. Figure 3.4. describes the pulse sequences up to this point. a) single 90_x pulse used in experiments of Chapter IV, Section B.3. b) a 90_x detection pulse followed by a 100 μsec spin locking pulse along y. This sequence is preferable to (a) as now 180° phase alternation of the detection pulse can be used to reduce artifacts from receiver ringing. For each value of t_1, the magnetization is sampled twice: once with a 90_x detection pulse and once with a $90_{\bar{x}}$ detection pulse, both followed by the spin locking pulse along y. These two points are then subtracted from one another to produce a final point for the t_1 value. c) pulsed spin locking sequence useful for signal enhancement in samples containing low ^1H concentrations. Again, as for (b), 180° phase alternation of the detection pulse is used to reduce artifacts from receiver ringing.

quantum free induction decay.

5. Tune-up Procedure

Usually the sequence of events which leads to the multiple-quantum experiment are the following.

a) Pulse amplitudes and phase are set carefully on a small water sample (either a capillary tube or a spherical bulb) with standard tune-up sequences.[26,27]

b) The preparation and mixing periods of the multiple quantum pulse sequence are placed "back-to-back" by setting $t_1 = 0$ and $\Delta t_1 = 0$ for a fixed preparation time τ. The experiment is then reduced to a simple time reversal procedure. Clearly, if the sequence was working perfectly, then the signal obtained by applying a $\pi/2$ pulse after the "back to back" sequence would be the same as the signal obtained from only a single $\pi/2$ pulse. In order to improve the overall performance of the time-reversal sequence on a solid sample, the amplitude of the rf pulses are adjusted, either on the amplifier itself or with a variable attenuator placed in the rack, to obtain maximum signal.

c) In addition, an optimum cycle time t_c must be found for the sample being studied. The best t_c is selected by varying the delays Δ and Δ' between pulses to optimize the signal for a fixed value of τ. In other words, if τ is chosen arbitrarily at 600 μsec for instance, then two cycles times that may be compared are a 60 μsec cycle applied 10 times or a 40 μsec cycle time applied 15 times. The one resulting in the largest signal at 600 μsec is considered to be the better cycle time. Generally, the longer cycle time applied fewer times appears to

work better. At long τ, signal losses occur because the time reversal sequence begins to fail: pulse imperfections and effects due to higher-order correction terms accumulate over many cycles, and the subsequent degradation in performance ultimately reduces the S/N in the multiple quantum spectra.

6. Spectrometer Implementation

Experiments were performed on two home-built spectrometers operating at ^{1}H Larmor frequencies of 360 MHz and 180 MHz.[28,29] Both spectrometers are equipped with quadrature phase generation circuits that produce rf pulses with relative phases of 0°, 90°, 180°, and 270° at 30 MHz intermediate frequency. Additional phase shifts needed for TPPI are generated by a 30 MHz 8-bit digital phase shifter in series with the quadrature generation network.

The pulse programmer for each spectrometer is governed by a 10 MHz clock, which limits the minimum increment in t_1 to 100 nsec. When additional bandwidth is needed to accommodate the multiple-quantum sepctrum, we use a home-built delayed clock generator to shift the phase of the clock pulses by one, two, or three quarter-cycles. Increments of 25, 50, 75 nsec thus become available, increasing the bandwidth to 40 MHz. Ultimately, the performance of the experiment is limited by the accuracy of the phase shifter.[30]

a. Phase Shifter

The key element in the multiple-quantum experiments is the digitally controlled phase shifter. It is described in detail in

references 28 and 29. Here, the actual steps occurring in the experiment are described, with aid of the schematic diagram of Figure (3.8). At the top of the figure, the phases of the pulses as they must ultimately appear in the pulse sequence are shown. For each value of t_1, the experiment is repeated twice: once the version of part (a) is used and then, for purposes of eliminating the odd multiple quantum orders and artifacts due to receiver ringing, sequence (b) is used. (b) is subtracted from (a) to obtain the final signal amplitude for the value of t_1. The differences between (a) and (b) are that the phase of the preparation period pulses have been shifted by 180° as well as the phase of the detection pulse.

To implement pulse sequences (a) and (b), the quadrature gates and phase shifter are set up as shown at the bottom of Figure (3.8). The quadrature phases for sequences (a) and (b) always remain the same and the phase shifter is used to make the appropriate changes. When the phase shifter is set in increment mode, then the output phase is the sum of the value on the increment counter plus the value loaded in the RAM. Initially the RAM phase is set to 0°. The increment counter can be increased by the amount shown on the thumbwheel switches each time the backpanel INC is strobed. This feature is used to regularly increment the phases of the preparation period pulses for TPPI. To switch between the phase shifted preparation period and the fixed phase mixing period the control word can be toggled, by strobing the TOGGLE gate during the evolution period, between the sum mentioned above and the value indicated on the manual thumbwheel switches. In these experiments, the value on the manual side is set to 100 (= 90°)

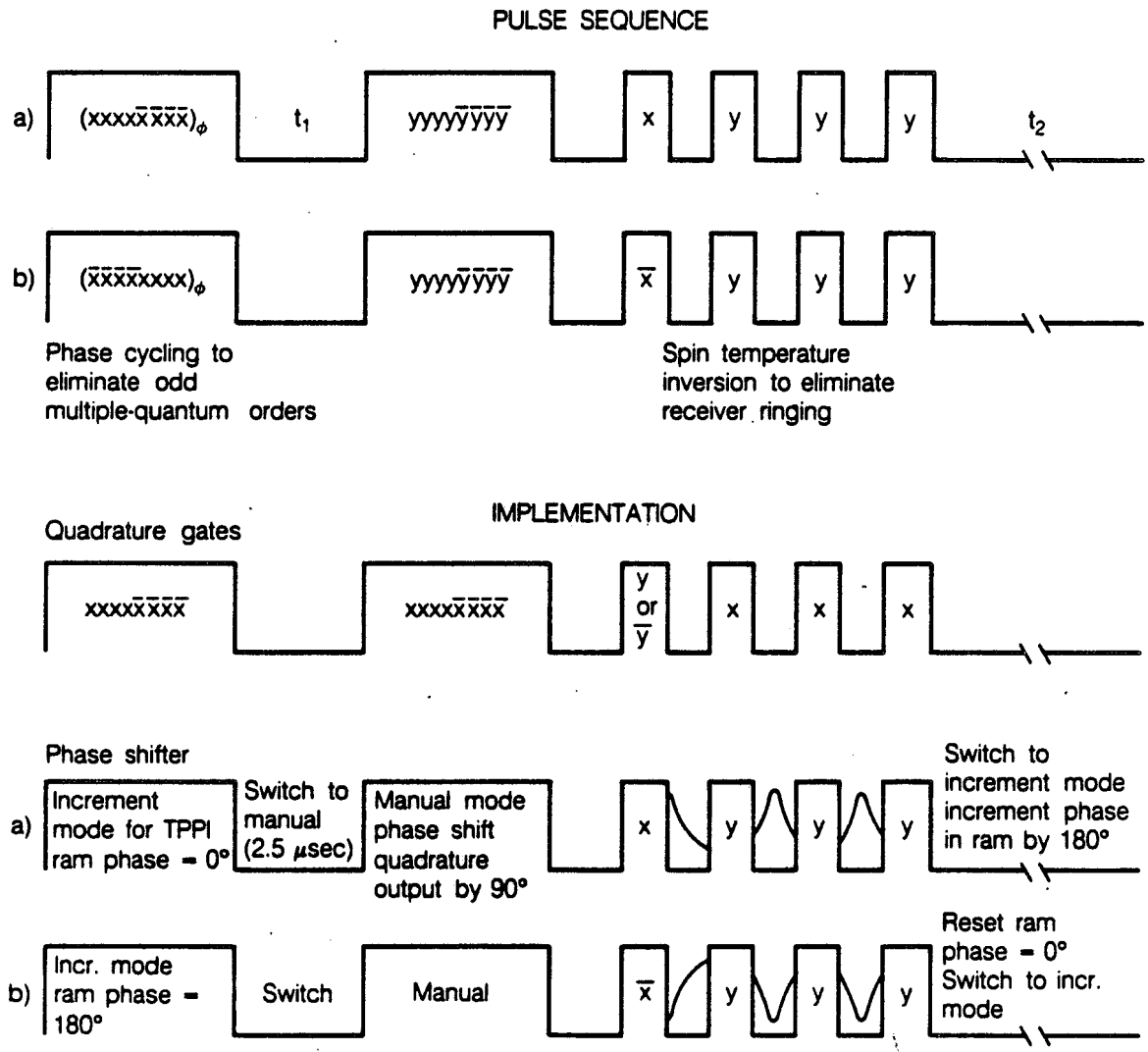

Figure 3.8. Schematic diagram of the time-reversal multiple-quantum pulse sequences. For each value of t_1, the experiment is repeated twice, and sequence (b) subtracted from (a) to obtain the final signal amplitude. To implement the experiment, the phases of the pulses at the output of the quadrature gates and the digitally controlled phase shifter are set up as shown. For parts (a) and (b) of the experiment, the quadrature phases remain the same and the phase shifter is used to make appropriate phase shifts. The details are described in Section E.6.

in order to implement the time-reversed mixing period. The phases of the pulses, which were x and $\bar{x}$ at the output of the quadrature box, are now y and $\bar{y}$ at the output of the phase box. A settling time of roughly 2.5 μsec is needed after toggling between increment and manual. For detection, a fixed phase is still needed, therefore the phase shifter remains on manual. The detection pulse appears as x followed by spin-locking pulses along y. Now part (a) of the experiment has been performed. To execute part (b), the control word is toggled back to increment and the phase in the RAM is incremented by 180° by applying a logic pulse to the backpanel RAM BNC. This occurs during the recycle delay period of part (a). Now the phase of the preparation period is again the sum of the increment counter plus the value loaded in the RAM, which is 180°: the phases which were ($xxxx\bar{x}\bar{x}\bar{x}\bar{x}$) are now ($\bar{x}\bar{x}\bar{x}\bar{x}xxx$). Again the control word is switched, during the evolution period, to the Manual side. The detection pulse which is $\bar{y}$ ($\bar{x}$ after the manual phase shift) is changed by a loop counter in the pulse program. The same sequence of events is then repeated for different values of t_1. During the recycle delay of part (b) the RAM phase is reset to 0° by applying a pulse to the RAC INIT and the control word is toggled to the increment mode.

b. Split Ram

When the spin locked detection sequence was used, then both the repetition of the basic pulse cycle and the acquisition of the data points had to take place in the RAM of the pulse programmer. Therefore, in order to be able to address the RAM contents at two dif-

ferent locations, a "split" RAM was used. Both spectrometers have a 128-128 split in the RAM; this can be changed fairly easily if desired. The most important points to recall in using the split RAM are that it is merely a means of addressing the RAM counter in two different places, and that the contents of the RAM are loaded sequentially. Therefore, to access that RAM at line 0, a "PA 0^1 00" statement should be used in the "FIFO" part of the pulse program; a "PA 03 00" statement should be used to address line 128. Even though different places in the RAM are being accessed, physically there is still only one RAM, labelled as 01 to the microprocessor. Therefore, the output statements in the RAM should all be labelled as 01. The last point in using the split RAM is the following: the RAM is loaded sequentially; therefore, if the first part of the RAM loader contains k output statements, then the second part will begin at line k + 1. If (k + 1) is less than 128, then the address line (which is 128) and the beginning of the second part of the program will not coincide.

F. References

1. G. Bodenhausen, Prog. NMR Spectrosc. **14**, 137 (1981).

2. D.P. Weitekamp, Adv. Magn. Reson. **11**, 111 (1983).

3. M. Munowitz and A. Pines, Adv. Chem. Phys. in press.

4. U. Fano, Rev. Mod. Phys. **29**, 74 (1957).

5. a) S. Vega and A. Pines, J. Chem. Phys. **66**, 5624 (1977).
   b) S. Vega and A. Pines, J. Chem. Phys. **68**, 5518 (1978).
   c) A. Wokaun and R.R. Ernst, J. Chem. Phys. **67**, 1752 (1977).

6. G. Drobny, A. Pines, S. Sinton, D.P. Weitekamp, and D. Wemmer, Faraday Symp. Chem. Soc. **13**, 49 (1979).

7. a) O.W. Sorensen, G.W. Eich, M.H. Levitt, G. Bodenhausen, and R.R. Ernst, Prog. NMR Spectrosc. **16**, 163 (1983).
   b) K.J. Packer and K.M. Wright, Mol. Phys. **50**, 797 (1983).

8. a) W.S. Warren, D.P. Weitekamp, and A. Pines, J. Chem. Phys. **73**, 2084 (1980).
   b) G. Drobny, A. Pines, S. Sinton, W.S. Warren, and D.P. Weitekamp, Philos. Trans. R. Soc. London Ser.A **299**, 585 (1981).
   c) W.S. Warren and A. Pines, J. Chem. Phys. **78**, 2808 (1981).
   d) S. Sinton, D.B. Zax, J.B. Murdoch, and A. Pines, Mol. Phys. **53**, 333 (1984).

9. a) A. Bax, R. Freeman, and S.P. Kempsell, J. Magn. Reson. **41**, 349 (1980).
   b) A. Bax, R. Freeman, and S.P. Kempsell, J. Am. Chem. Soc. **102**, 4851 (1980).
   c) A. Bax, R. Freeman, and T.A. Frenkiel, J. Am. Chem. Soc. **103**, 2102 (1981).
   d) U. Piantini, O.W. Sorensen, and R.R. Ernst, J. Am. Chem. Soc. **104**, 6800 (1982).
   e) M.H. Levitt and R.R. Ernst, Chem. Phys. Lett. **100**, 119 (1983).
   f) L. Braunschweiler, G. Bodenhausen, and R.R. Ernst, Mol. Phys. **48**, 535 (1983).

10. a) D.P. Weitekamp, J.R. Garbow, J.B. Murdoch, and A. Pines, J. Am. Chem. Soc. **103**, 3578 (1981).
    b) J.R. Garbow, D.P. Weitekamp, and A. Pines, J. Chem. Phys. **79**, 5301 (1983).

11. a) L. Mueller, J. Am. Chem. Soc. **101**, 4481 (1979).
    b) Y.S. Yen and D.P. Weitekamp, J. Magn. Reson. **47**, 476 (1982).
    c) A. Bax, R.H. Griffey, and B.L. Hawkins, J. Magn. Reson. **55**, 301 (1983).

12. Y.S. Yen and A. Pines, J. Chem. Phys. **78**, 3579 (1983).

13. a) R.H. Schneider and H. Schmiedel, Phys. Lett. **A 30**, 298 (1969).
b) W.K. Rhim, A. Pines, and J.S. Waugh, Phys. Rev. Lett. **25**, 218 (1970).
c) W.K. Rhim, A. Pines, and J.S. Waugh, Phys. Rev. B. **3**, 684 (1971).
d) A. Pines, W.K. Rhim, and J.S. Waugh, J. Magn. Reson. **6**, 457 (1972).

14. W.P. Aue, E. Bartholdi, and R.R. Ernst, J. Chem. Phys. **64**, 2229 (1976).

15. A. Pines, D. Wemmer, J. Tang and S. Sinton, Bull. Am. Phys. Soc. **23**, 21 (1978).

16. A.N. Garroway, J. Baum, M.G. Munowitz, and A. Pines, J. Magn. Reson. **60**, 337 (1984).

17. a) G. Drobny, A. Pines, S. Sinton, D.P. Weitekamp, and D. Wemmer, Faraday Symp. Chem. Soc. **13**, 49 (1979).
b) G. Bodenhausen, R.L. Vold, and R.R. Vold, J. Magn. Reson. **37**, 93 (1980).

18. J.B. Murdoch, W.S. Warren, D.P. Weitekamp, and A. Pines, J. Magn. Reson. **60**, 205 (1984).

19. D. Wemmer, Ph.D. Thesis, University of California, Berkeley, 1979 (published as Lawrence Berkeley Laboratory Report LBL-8042).

20. a) R.A. Hoffman, Adv. Magn. Reson. **4**, 87 (1970).
b) A. Wokaun and R.R. Ernst, Mol. Phys. **36**, 317 (1978).

21. J. Baum, M. Munowitz, A.N. Garroway, and A. Pines, J. Chem. Phys. **83**, 2015 (1985).

22. W.S. Warren, D.P. Weitekamp, and A. Pines, J. Chem. Phys. **73**, 2084 (1980).

23. E.O. Stejskal and J. Schaefer, J. Magn. Reson. **18**, 560 (1975).

24. a) E.D. Ostroff and J.S. Waugh, Phys. Rev. Lett. **16**, 1097 (1966).
b) W.-K. Rhim, D.P. Burum, and D.D. Elleman, Phys. Rev. Lett. **37**, 1764 (1976).
c) D. Suwelack and J.S. Waugh, Phys. Rev. **B22**, 5110 (1980).
d) M.M. Maricq, Phys. Rev. **B25**, 6622 (1982).

25. A.G. Redfield, Phys. Rev. **98**, 1787 (1955).

26. a) R.W. Vaughan, D.D. Elleman, L.M. Stacey, W.-K Rhim and J.W. Lee, Rev. Sci. Instr. **43**, 1356 (1972).
b) W.-K. Rhim, D.D. Elleman, L.B. Schreiber, and R.W. Vaughan, J.

Chem. Phys. **60**, 4595 (1974).

27. U. Haubenreisser and B. Schnabel, J. Magn. Reson. **35**, 175 (1979).

28. G. Drobny, Ph.D. thesis, University of California, Berkeley, 1983 (published as Lawrence Berkeley Laboratory Report LBL-15254).

29. J.R. Garbow, Ph.D. thesis, University of California, Berkeley, 1983 (published as Lawrence Berkeley Laboratory Report LBL-16119).

30. A. Garroway, J. Magn. Reson. **63**, 504 (1985).

IV. MULTIPLE-QUANTUM NMR STUDIES OF CLUSTERING IN SOLIDS

A. Introduction

In this chapter, we describe the application of nuclear magnetic resonance to the question of clustering in materials lacking long-range order. In such materials, standard methods of structural characterization, such as x-ray crystallography, are not useful. Examples of such disordered materials range from minerals, semiconductors, polymers and liquid crystals, to species adsorbed on surfaces and in zeolites. These materials often display important physical or electrical properties; for example, a critical level of hydrogen incorporation into amorphous silicon renders it a semiconductor used in many industrial applications.[1]

As an example of the type of problem we face in these disordered solids, Figure (4.1) illustrates two extreme, possible, atomic configurations: in the first, the atoms are distributed randomly but uniformly within the sample, and in the second they are grouped together, forming clusters. Usually, an NMR spectrum of a solid will not reveal the basic difference between these two situations. In both cases, the spectrum will normally be broad and featureless; the linewidth, due primarily to the dipolar couplings between spins, does not contain sufficient information to establish any statistical information on the atomic distribution as seen in Figure (4.2).

In contrast, by capitalizing on the dipolar couplings in a different manner, a time-resolved multiple-quantum NMR experiment can be

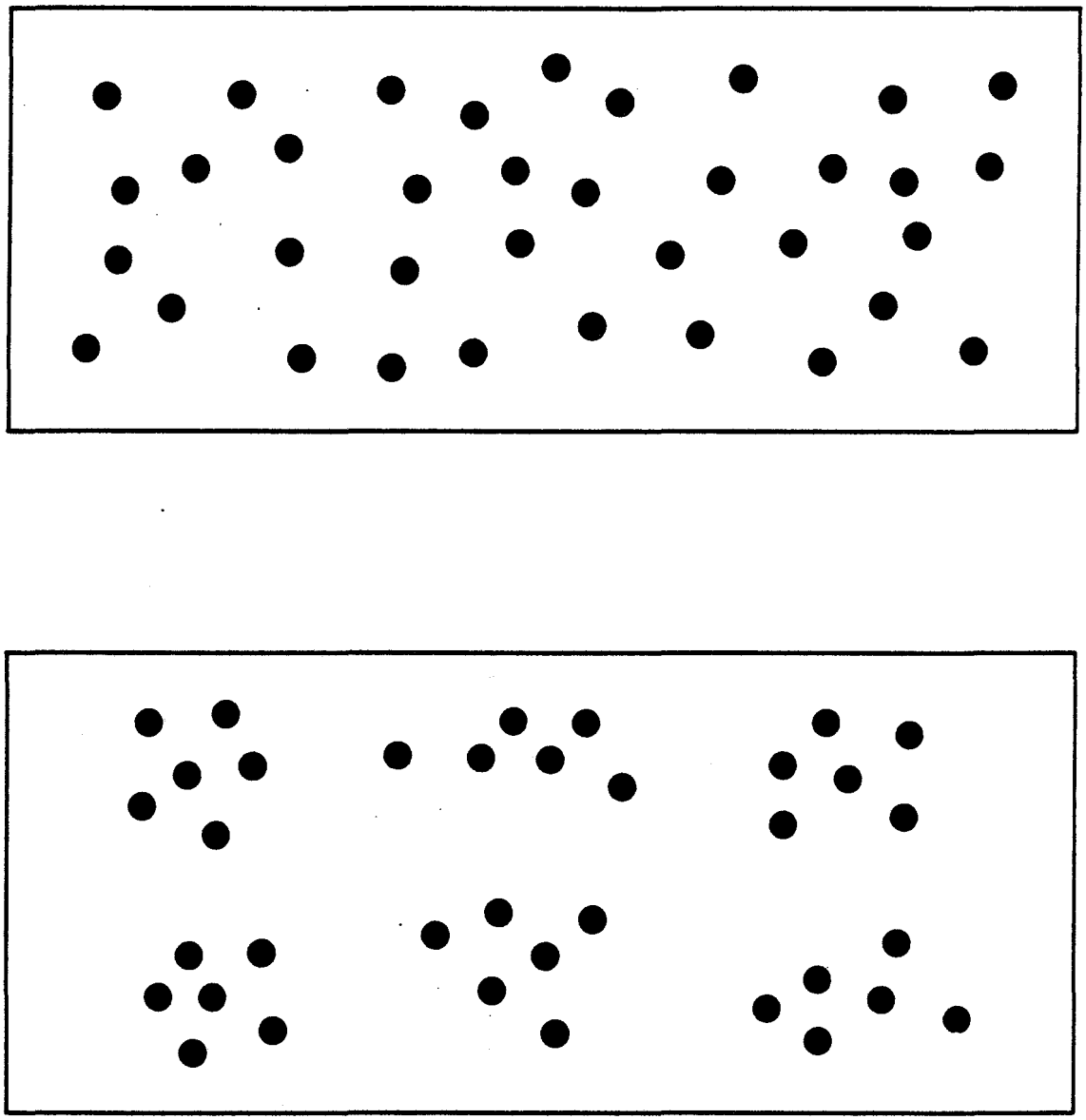

XBL 8511-12717

Figure 4.1. Possible atomic distributions in solids. Uniform and clustered distributions can be distinguished by time-resolved solid-state multiple-quantum NMR.

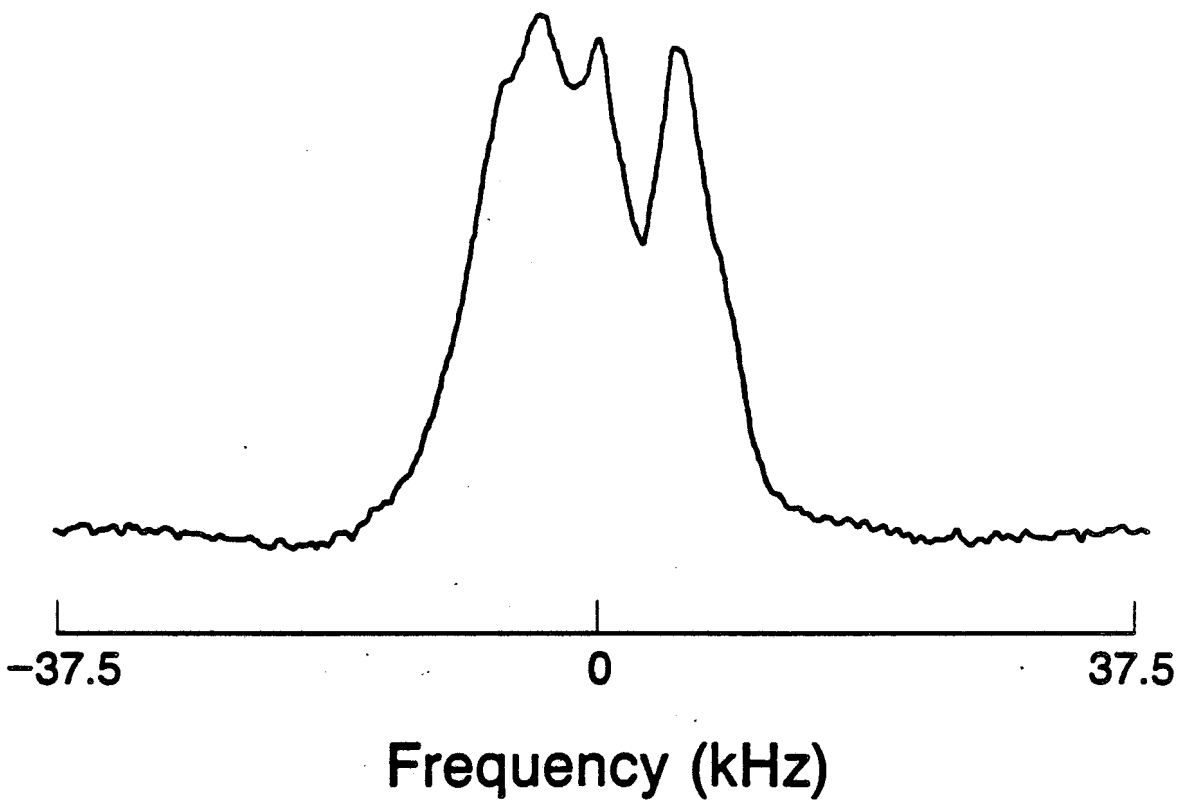

XBL 8512-12775

Figure 4.2. 180 MHz ^1H NMR spectrum of the liquid crystal with chemical formula ($C_{19}H_{21}N$) in the nematic phase. The distribution of ^1H in the sample can not be determined from this broad and essentially featureless spectrum.

used to address the question of atomic distribution in such materials.[2,3,4] For example, if the uniformly distributed material is irradiated with rf quanta in an NMR experiment, it might be expected to absorb them continuously; whereas isolated clusters will absorb only a finite number.[5] We show that indeed a time resolved multiple-quantum experiment, whose statistics are very sensitive to atomic distributions, can be used to probe the nature and extent of clustering in solids.

We begin in Section IV.B, by examining multiple-quantum dynamics in solid-state NMR. The development of multiple-quantum coherence in a solid is followed experimentally and explained by the emergence with time of a widening network of multiple-spin correlations throughout the system. This phenomenon leads to the notion of an instantaneous effective size for the system, which can be calculated directly from the multiple-quantum spectral intensities. The rate of growth of this time-dependent parameter is determined entirely by the distribution of atoms in the sample.

In Section IV.C, the size and extent of ^{1}H clustering is determined in a variety of systems from this point of view. More particularly, model experiments are demonstrated on uniform distributions, totally isolated clusters, and various concentrations of clusters ranging from dilute to fairly dense. For concentrations of clusters, a second time-dependent parameter is introduced in Section IV.C.4 to ascertain the size of the clusters independently of the size of the system, which may include inter-cluster correlations. Emphasis is placed on illustrating how the different distributions affect the multiple-quantum dynamics

and how the tendency to clustering and information on cluster sizes can be determined from the time-dependence of the multiple-quantum intensities. In Section IV.D, we use this technique to study hydrogen clustering in hydrogenated amorphous silicon. Extensions of the experiment and a summary are presented in Section IV.E.

B. Multiple-Quantum Dynamics in Solid State NMR

1. Multiple-Spin Processes and Time Development of the Dipolar Coupling Network.

In multiple quantum NMR individual spins become correlated with one another over time, through their dipolar couplings.[6] In this way, the usual Zeeman selection rule can be overcome and "forbidden transitions", where the difference in magnetic quantum number ΔM is equal to $0, \pm 1, \pm 2, .., \pm N$, can be excited. When $\Delta M = N$, N spins "flip" collectively from the ground state to the highest excited state. Experimentally, such multiple quantum coherences are formed in solids by applying a radio-frequency pulse sequence to the system for a time τ, thereby creating the non-secular Hamiltonian,

$$H = \frac{1}{2} \sum_{i<j} D_{ij} \left(I_{+i} I_{+j} - I_{i-} I_{j-} \right)$$

of Equation (3.32), which induces the spins to act collectively or in a group.[7] The density operator at the end of the preparation period takes the form

$$\rho(\tau) = I_z + i\tau[I_z,H] - \frac{\tau^2}{2}[[I_z,H],H] + \ldots \qquad (4.1)$$

Evaluation of the nested commutators results in products of single-spin operators such as $I_{+1}\ I_{+2}\ I_{+3}\ I_{+4}$; each product of operators is associated with powers of $D_{ij}\tau$. As a result, when $D_{ij}\tau \ll 1$, the associated operator term will not be significant. Symbolically, these products of operators can be visualized as the development of many-body correlations through the pairwise dipolar couplings. A schematic drawing of the time development of spin correlations is shown in Figure (4.3). For short times Equation (4.1) reduces to the first few terms:

$$\rho(\tau) = I_z + i\tau\,[I_z,H] - \frac{\tau}{2}\,[[I_z,H],H] \quad . \qquad (4.2)$$

Now, only low multiple quantum orders will develop and only spins with large dipolar couplings D_{ij} will effectively interact. As the preparation period τ becomes longer, $\rho(\tau)$ will contain longer products of spin operators, indicating that more spins are becoming correlated with one another. In addition, spins with smaller dipole couplings will now be able to interact as well. In order for spins to become correlated, the Hamiltonian must act for a time τ roughly proportional to the inverse of the pairwise dipolar interactions. As a result, the preparation time τ can be short if spins are near one another, and must be longer if spins further apart are to communicate with one another. Therefore the rate at which multiple quantum coherences develop is determined by the dipolar coupling distributions present in the system.

Figure 4.3. In multiple quantum NMR, spins, symbolically represented here by hatched circles, become correlated with one another over time, through pairwise dipolar interactions: the closer the spins, the shorter the time needed for interactions to develop. For uniformly distributed spins (a), correlations will be expected to develop monotonically with time. In a clustered material (b), however, the magnitudes of the inter versus intra-cluster dipolar couplings are quite different. At short times, the number of correlated spins will be limited to the number of atoms in the cluster whereas at long times intercluster interactions will develop and all the spins will become correlated with one another. The difference between clustered and uniform distributions should be observable in the time-dependence of the n-quantum absorption.

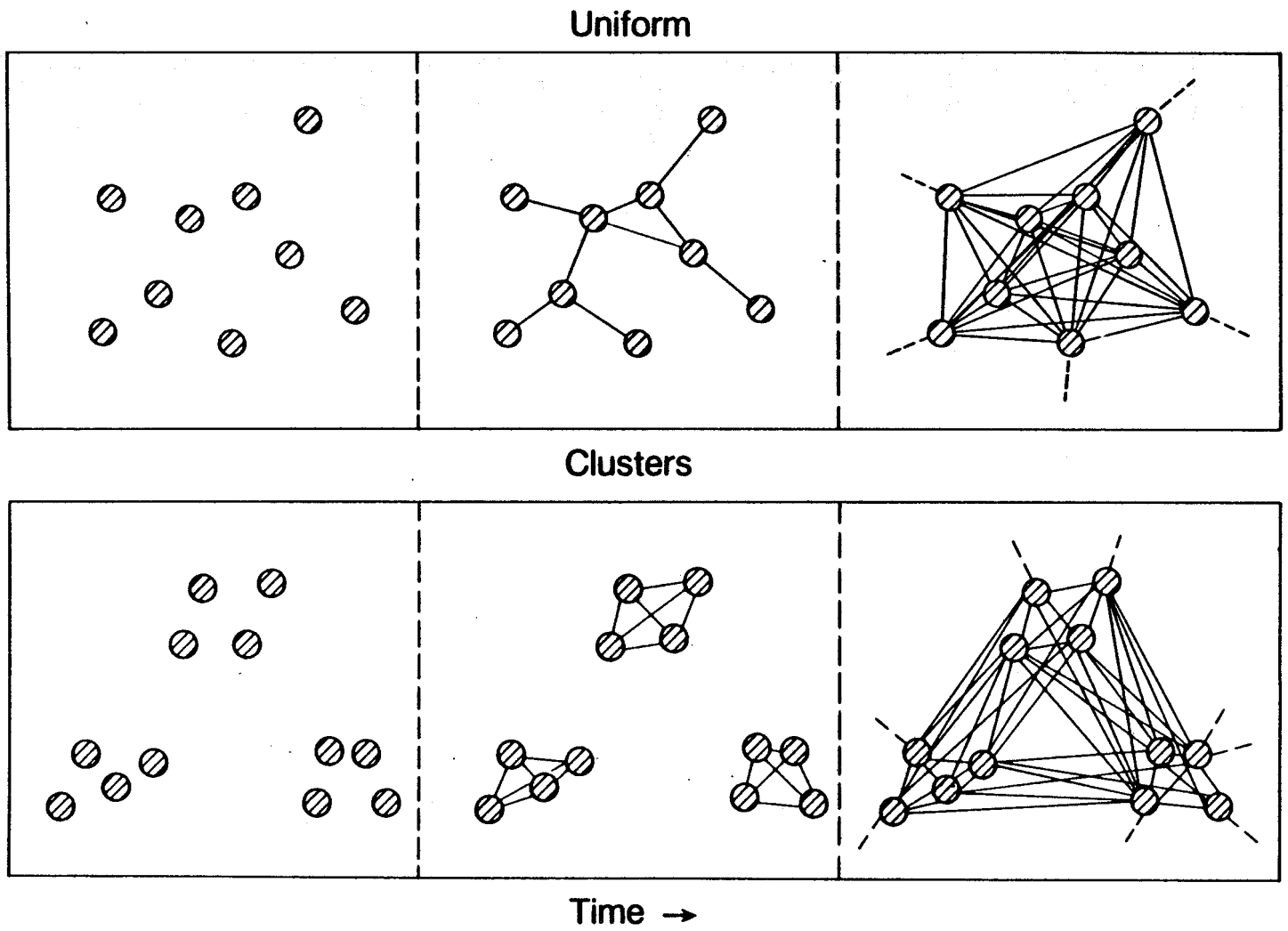

XBL 8511-12718 A

Because the spatial arrangements of atoms are reflected by the magnitude of the dipolar couplings, a time dependent multiple quantum experiment can yield information concerning the distribution of spins in a material. If a solid is composed of a uniform distribution of atoms, where the dipolar couplings between spins may be roughly comparable, then the time development will be expected to look like the one depicted in Figure (4.3a). As the uniformly distributed spins absorb more and more quanta of radiation, the spins become correlated with one another in a continuous manner. Over time, the number of communicating spins is essentially unbounded. And, the effective "size" of the system grows monotonically. However, if a solid contains isolated clusters, then the variation between inter and intra cluster dipolar couplings is large enough to preclude inter-cluster correlations on the experimental time scale. One can imagine clusters as independent groups of size N able to absorb only up to N quanta of radiation. Consequently, as shown in Figure (4.3b) after an initial induction period, during which multiple quantum coherences develop between spins with large dipolar couplings, the number of correlated spins will be expected to remain roughly constant over time and will reflect the size of the isolated cluster. If this group is truly independent of any other groups, then no additional interactions can build up on the experimental time scale. On the other hand, if small but non-negligible dipolar couplings do exist between spins of different groups, then with time, the groups will communicate with one another. If the concentration of clusters is high, less time will be needed for intergroup communication to occur. Ultimately, for very long times, a large network

of correlated spins will develop. Clearly, the difference between a uniform and clustered environment will be reflected directly in both the rate of development, and distribution, of mutliple quantum coherence.

2. Time Development of Multiple-Quantum Coherences

Figure (4.5) contains a set of ^{1}H multiple-quantum spectra obtained from hexamethylbenzene (using sequence (4.4)) with preparation times ranging from 66 μsec to 792 μsec. The most frequently used pulse sequence is adapted from Figures (3.3) and (3.7) and reproduced here for convenience in Figure (4.4). All experimental details are presented in Chapter 3, Section E. The plots of Figure (4.5) illustrate the distribution of spectral intensity over the coherence orders at the specified preparation times. Separation of the different orders has been accomplished by TPPI so that the subspectrum of each order n occupies 156.25 kHz. As coherences of +n and -n are equally probable, the full spectra are naturally symmetric about n = 0. Consequently, only one half of each spectrum is needed to obtain all the information available.

A general tendency for coherence of higher order to develop with time is clearly evident in the spectra shown in Figure (4.5); the results are particularly striking for τ = 792 μsec, where there are strong signals extending out to, and apparently beyond, n = 64. Subspectral structure and linewidths are determined by the response of the prepared system to the local field of all the other spins during the subsequent evolution period. Here, a spectrum of broad featureless

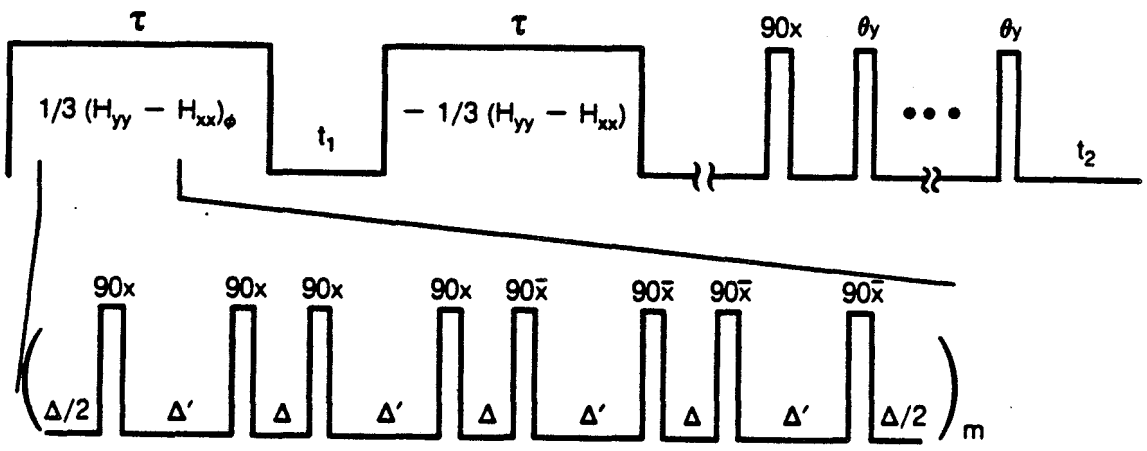

XBL 8512-5061

Figure 4.4. Two-dimensional multiple-quantum pulse sequence for solids. The preparation and mixing periods are composed of 8 $\pi/2$ pulses of length t_p separated by delays Δ and Δ'. The total preparation/mixing time τ is achieved by repeating the basic cycle m times. When the phases of the pulses are x and $\bar{x}$, the Hamiltonian is equal to 1/3 $(H_{yy} - H_{xx})$; during the mixing period, when the phases of the pulses are y and $\bar{y}$, the Hamiltonian becomes - 1/3 $(H_{yy} - H_{xx})$, i.e. the negative of the preparation period Hamiltonian. To separate the mutliple-quantum orders, the preparation period pulses are incremented by a phase ϕ for each value of t_1. During the detection period, a pulsed spin locking sequence is used for signal enhancement in samples containing low ^1H concentrations.

Figure 4.5. 360 MHz ^1H multiple-quantum spectra of hexamethylbenzene for τ = 66 to τ = 792 μsec recorded with the sequence of Figure (4.4). The basic cycle time used for this spectrum is 66 μsec (t_p = 3 μsec, Δ = 2.5 μsec, and Δ' = 8μsec). For τ = 66 to 462 μsec, the t_1 increment is 100 ns and the phase increment is $2\pi/64$; this separates each order by 156.25 kHz. For $\tau \geq 528$ μsec, the t_1 and phase increments are 50 ns and $2\pi/128$, respectively. The distribution of spectral intensity over the coherence orders broadens continously as the preparation time increases. The lowermost trace, an expanded view of the spectrum obtained for τ = 792 μsec, emphasizes the highest orders of coherence observed.

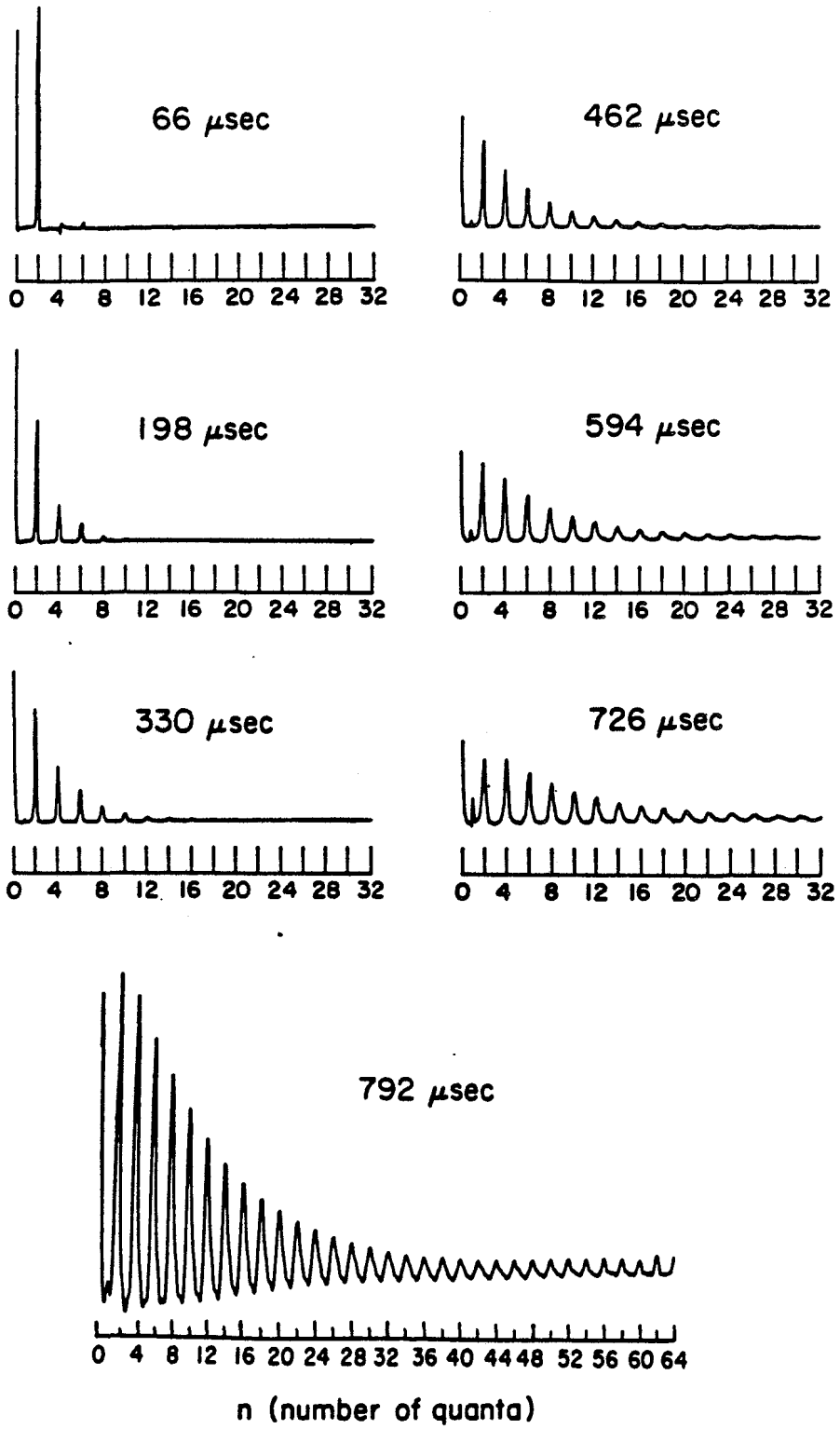
66 μsec
462 μsec
198 μsec
594 μsec
330 μsec
726 μsec
792 μsec
0 4 8 12 16 20 24 28 32
0 4 8 12 16 20 24 28 32 36 40 44 48 52 56 60 64
n (number of quanta)

XBL 854-2054

lines arises from the almost continuous distribution of eigenfrequencies in a sample containing virtually an infinite number of spins.

Monitoring the time development of the multiple quantum coherences in this infinite spin system therefore reveals that correlations do indeed develop between spins in a monotonic fashion. As time progresses, more spins can absorb more quanta of radiation and very high multiple quantum orders can be detected. However, if clusters of spins exist, then the time development of the multiple quantum coherences is expected to be interrupted; the number of interacting spins will be limited, to a large extent, by the size of the cluster. Shown in Figure (4.6) are ^1H multiple-quantum spectra for a polycrystalline sample (shown in the inset) in which hydrogen atom clusters of different molecules are effectively isolated from one another owing to the large perchlorinated cyclopentadiene rings. For this model clustered material, the appearance of the multiple-quantum spectra remain very similar up to 300 μsec, after which many high multiple-quantum orders begin to develop. Now there is a discontinuity in the development of multiple-quantum coherence. The higher orders are attributed to intermolecular interactions. Both materials will be addressed in more detail in a later section.

3. Monitoring of Time Reversal Via The Refocusing of Multiple Quantum Coherence

Although it may appear to be stochastic, the time development of a spin system according to Equation (1.28) is actually well determined,

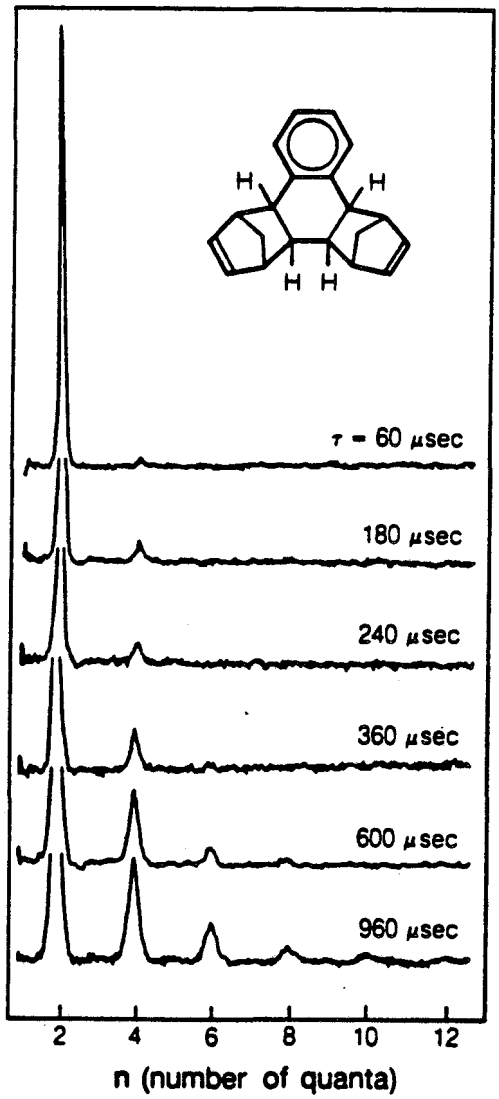

Figure 4.6. 180 MHz ^{1}H multiple-quantum NMR spectra of the polycrystalline sample 1,2,3,4-tetrachloronaphtalene-bis(hexachlorocyclopentadiene)-adduct for τ = 60 to 960 μsec. The basic cycle time is 60 μsec (tp = 2.5 μsec, Δ = 2.5 μsec, Δ' = 7.5 μsec) The t_1 increment is 400ns and the phase increment $2\pi/16$; each order is therefore separated by 78.125 kHz. The time development of the multiple-quantum coherences over time is discontinuous in this clustered material. The spectra change very little over the first 300 μsec, indicating a limited spin system on this time scale. At longer times, when intermolecular interactions develop, the system is no longer bounded and higher multiple-quantum orders arise in the spectrum.

and can be reversed if the sign of the effective internal Hamiltonian is changed. That coherent averaging methods can reverse supposedly irreversible dipolar dephasing has already been amply demonstrated by "magic echo" experiments.[9] However, we can gain added insight into such dephasing and rephasing by visualizing the time reversal process explicitly through multiple-quantum spectroscopy. The novelty here is that we can show how time reversal is effective even for very high-order, multiple-spin processes.

Part (a) of Figure (4.7), shows a pulse sequence designed to reverse the formation of the network of spin correlations occurring in multiple-quantum excitation. The plan is to allow coupling to develop normally for a rather long, fixed time τ_0, and then to refocus the multiple-quantum coherences over the interval τ'. The refocusing during τ' is accomplished by phase shifting the excitation pulses by 90° to change the sign of the average Hamiltonian. The mixing period is altered symmetrically to fulfill the requirement for overall time reversal relative to the preparation period.

The reversibility of multiple-quantum excitation is illustrated experimentally in Figure (4.7b). Shown at the left are three 180 MHz ^1H spectra of adamantane obtained in the usual fashion with sequence (3.3d) and τ = 462, 330 and 66 μsec. Directly opposite are the equivalent refocused spectra, recorded with τ_0 = 528 μsec and τ' = 66, 198 and 462 μsec. In each case, the net forward preparation times are identical, since $\tau = \tau_0 - \tau'$. To the extent that the time reversal works perfectly, the development of all the multiple-quantum coherences during τ_0 will be retraced during the τ' interval, during which the

Figure 4.7. a) Experiment designed to refocus multiple-quantum coherence in solids. High-order coherences created during τ_0 evolve backwards in time during τ' to return to low-order coherences. Phase cycling and spin temperature inversion have not been implemented in this experiment.

b) 180 MHz ^1H spectra of adamantane illustrating the feasibility of refocusing multiple-quantum coherence via time reversal.

Left: Spectra obtained with sequence d of Figure (3.4) for τ = 66, 330, and 462 μsec. High-order coherences develop normally with $\tilde{H}^{(0)} = 1/3(H_{yy} - H_{xx})$ during the preparation period.

Right: Spectra obtained with the sequence in part (a) of this figure for τ_0 = 528 μsec and τ' = 462, 198, and 66 μsec. In each case, the reversal of the time development during τ' leaves the net forward preparation time equivalent to that used for the corresponding spectrum at the left. The observed spectral distribution arises as the system evolves backwards in time from high-order to low-order coherences.

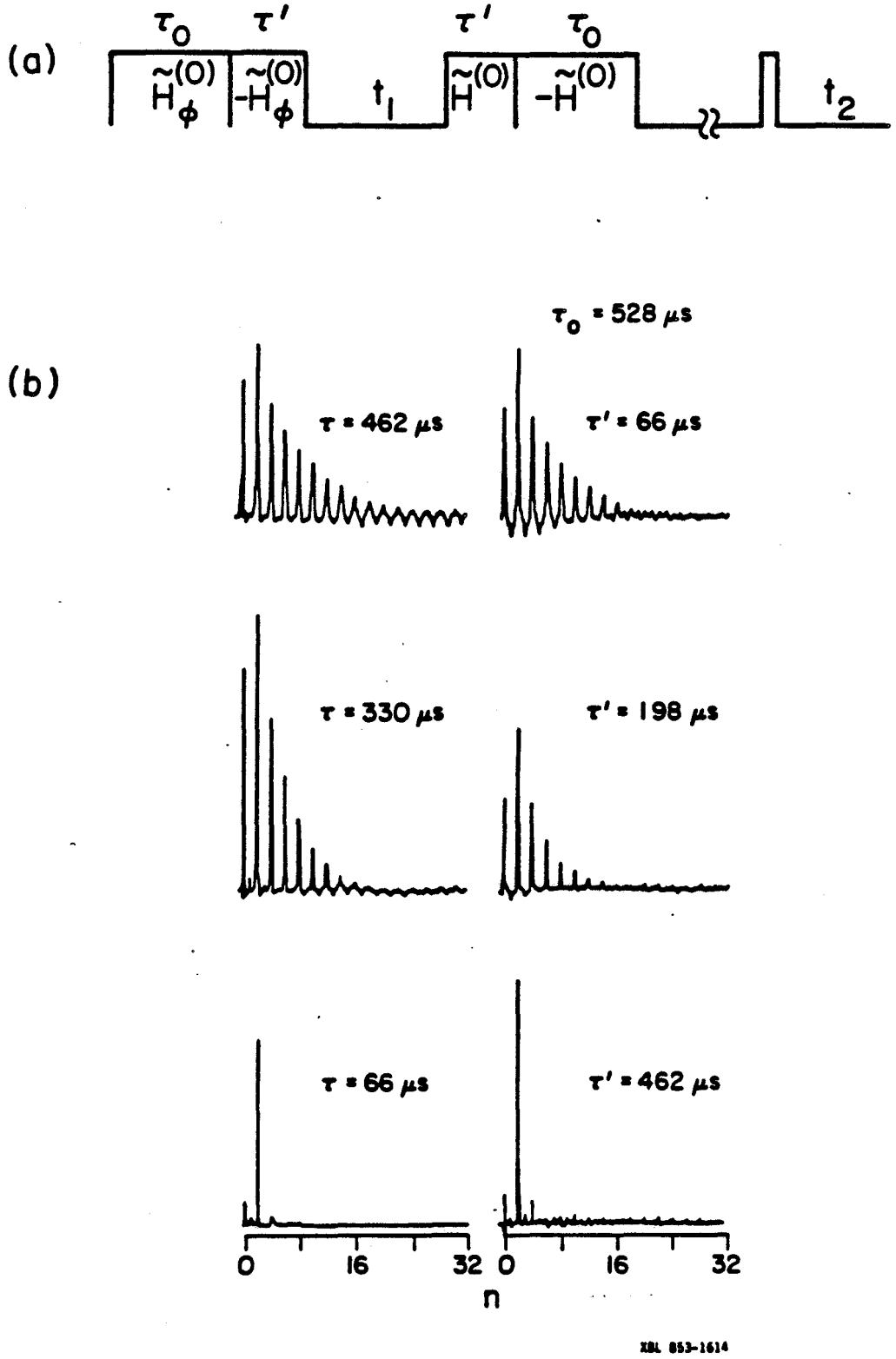
(a)
τ_0
τ'
$\tilde{H}_\phi^{(0)}$
$-\tilde{H}_\phi^{(0)}$
t_1
τ'
τ_0
$\tilde{H}^{(0)}$
$-\tilde{H}^{(0)}$
t_2
(b)
τ_0 = 528 μs
τ = 462 μs
τ' = 66 μs
τ = 330 μs
τ' = 198 μs
τ = 66 μs
τ' = 462 μs
0
16
32
0
16
32
n
XBL 853-1614

clock governing the dipolar Hamiltonian appears to run backwards. Indeed, the spectra to be compared in Figure (4.7) are reasonably similar. In particular, note that for τ = 66 μsec, only two-quantum coherence is observed after normal excitation by the sequence of Figure (3.3 d). For the comparable spectrum produced by the sequence in Figure (4.7a) the system generates coherences up to n = 32 during the initial development period of 528 μsec, and then reverses the process for τ' = 462 μsec to leave primarily two-quantum coherence.

This demonstration of time reversal complements similar single-quantum approaches. For example, in the magic echo experiment, a pulse sequence applied to the system after the free induction signal has decayed can restore the signal to its initial intensity under ideal conditions. However, in the magic echo experiment there is no direct evidence that the time reversal is proceeding through mutliple-spin events. By following the development of multiple-quantum coherence, we have shown here that time reversal can turn back the clock for coherent evolution involving large numbers of nuclear spins.

4. Measurement of an Effective System Size in Solids

The number of correlated spins at a particular preparation time dictates the intensity distribution of the signal over the multiple quantum orders. For a finite N spin system, ignoring symmetry, we showed, in Chapter III, Section C.1 that the integrated spectral intensity per order can be approximated by the intensity per transition times the number of allowed transitions. If all possible coherences have been excited with equal probability, then the integrated intensity

per order can be related to the number of allowed n-quantum transitions[10]; in an N spin system, the number of n-quantum transitions is[11]

$$\binom{2N}{N-n} = \frac{2N!}{(N-n)!(N+n)!} \quad . \tag{4.3}$$

This expression can be approximated by a Gaussian distribution, for large N and n<<N. As a result, the integrated multiple-quantum intensities fall off in a Gaussian manner,

$$I(n) = \exp \frac{-n^2}{N} \quad , \tag{4.4}$$

and are indeed dictated by the size of the system.

In a solid, the exact calculation of the time development of the multiple quantum coherences is impossible owing to the need for prior knowledge of an enormous number of spin-spin couplings. Therefore, for simplicity, we assume that the infinite spin system can be subdivided into finite spin systems which grow in the time-dependent fashion portrayed in Figure (4.3). <u>Then for each preparation time, we can represent the number of spins that have become correlated up to that time by an effective system size $N(\tau)$.</u> This time-dependent parameter is calculated in the manner of Figure (4.8) by fitting the integrated intensities to a Gaussian distribution and associating the standard deviation, σ, of the Gaussian with $(N(\tau)/2)^{1/2}$. The pattern and rate of growth of $N(\tau)$ over time will reflect the distribution of atoms in the sample. Its change with time is determined by the structure of the

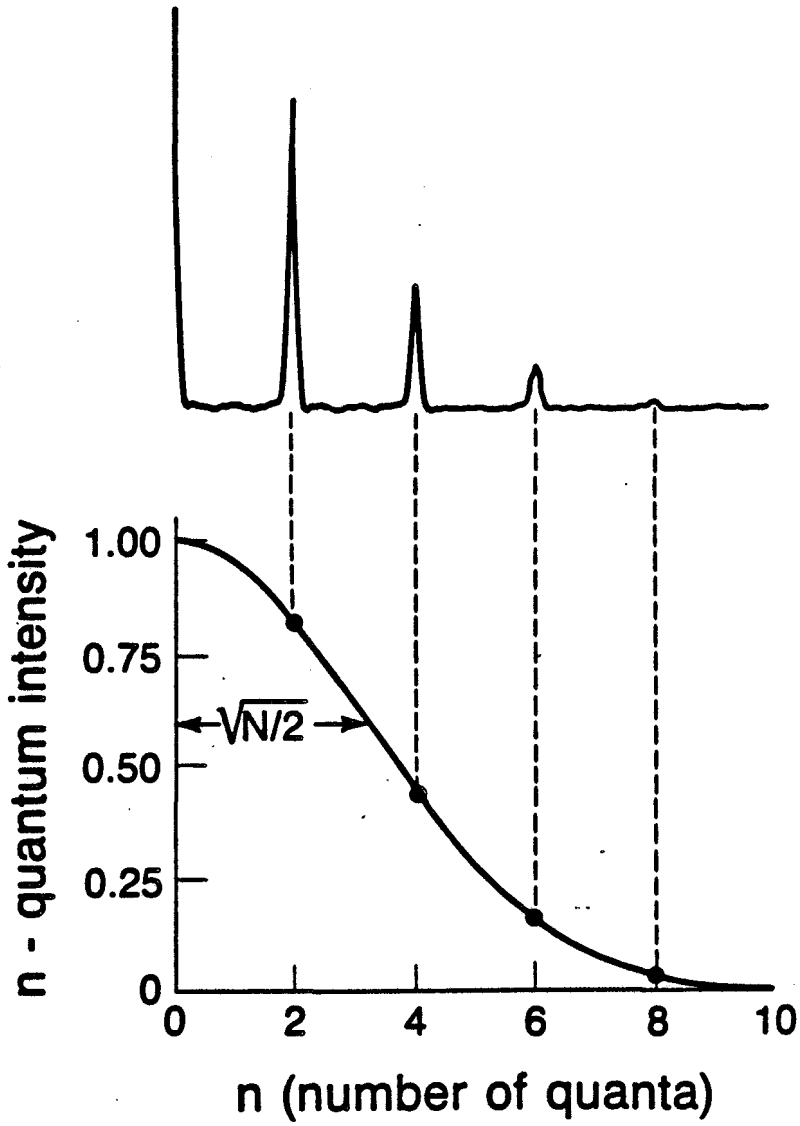

Figure 4.8. Top: 180 MHz ^{1}H multiple quantum spectrum of the liquid crystal p-hexyl-p'-cyanobiphenyl in the nematic phase for a preparation time τ = 660 μsec. In this spectrum, the basic cycle time is 60 μsec, the bandwith 2.5 MHz and the separation between orders 78.125 kHz.

Bottom: The data points are measured from the spectrum above by integrating each peak corresponding to each multiple quantum order. The resulting intensities are then fit to a gaussian distribution whose standard deviation, σ, is associated with $(N/2)^{1/2}$. The solid curve is the plot of the best fit value for N. N, the effective system size characterizes the number of correlated spins, in this case 20, at each preparation time.

solid, and is influenced by factors such as spin topology and the relative magnitudes of intramolecular and intermolecular dipolar interactions. In the following sections, the time-dependent multiple-quantum behavior of uniform distributions, concentrations of clusters and isolated clusters is studied from this point of view. In addition, the degree of clustering in hydrogenated amorphous silicon is determined.

C. Studies of Clustering in Solids

1. Uniform Distributions

a. Adamantane ($C_{10}H_{16}$; polycrystalline)

Adamantane forms a plastic crystal in which the nearly spherical molecules tumble rapidly and isotropically in the solid phase. The motion averages all intramolecular dipolar couplings to zero, but does not eliminate intermolecular couplings. However, the motion leaves only one distinct coupling between every pair of molecules, thereby reducing the adamantane molecule to a point dipole source containing 16 spins. The molecules pack into a face-centered-cubic lattice, with each adamantane molecule surrounded by 12 neighbors at a distance of 6.60 Å, 6 more at 9.34 Å and an additional 16 at 11.4Å.[12]

In Figure (4.9a), we examine the time development of the n-quantum transitions by plotting the integrated intensity of each order, normalized to the total spectral intensity, versus preparation time. The different orders appear to grow in monotonically with time and very high multiple-quantum orders are attained. Values of $N(\tau)$ versus τ are plotted in Figure (4.9b). The intensity of each order was normalized

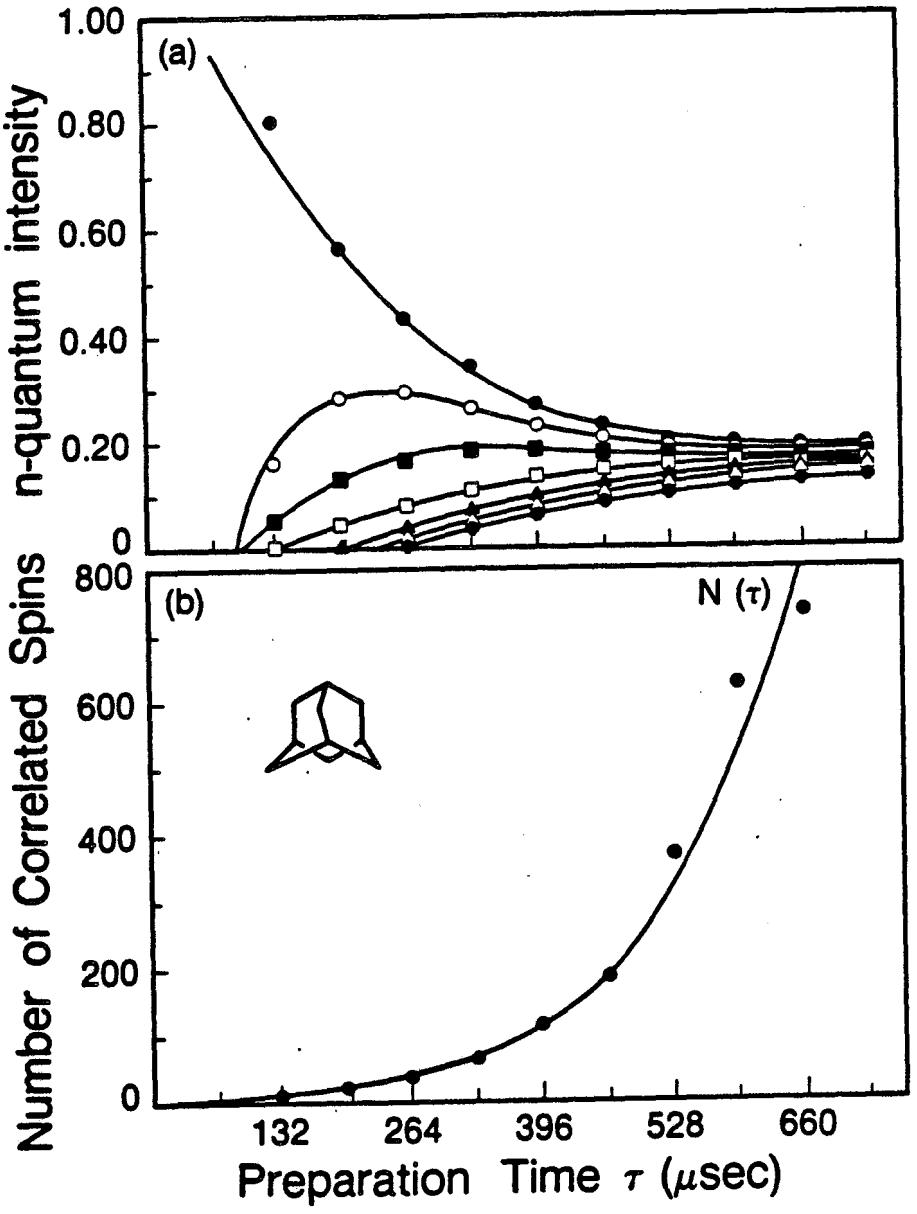

XBL 861-178

Figure 4.9. a) Intensity versus preparation time for n = 2,4,6,8,10,12,14,16 in adamantane. In future plots, the same symbols will be used for the same multiple-quantum orders. The intensity for each order has been normalized relative to the total spectral intensity, and smooth curves have been drawn through the data points to aid the eye. Very high multiple-quantum coherences develop over time in a monotonic fashion.

b) Number of correlated spins versus preparation time for adamantane. The smooth curve through the points emphasizes the continuous expansion of the effective size of the unbounded spin systems.

relative to n = 2 for each preparation time. In this manner reasonable estimates for $N(\tau)$ can be obtained even when the very highest orders possible cannot be observed experimentally. Deviations from strictly statistical behavior are most pronounced in the tail of the distribution, where the combinatorial method consistently underestimates the intensities of the highest orders.[10] The effective size of the system, $N(\tau)$, increases monotonically with time, indicating that the number of correlated spins is steadily growing larger. Based on the discussion in Section B.1, this type of multiple-quantum behavior is expected for a uniform distribution of atoms.

b. Squaric Acid ($C_4O_4H_2$; single crystal)

Squaric acid is monoclinic but pseudo-body-centered-tetragonal at room temperature. It is a layered two-dimensional structure consisting of hydrogen-bonded "squaric" subunits of C_4O_4. The hydrogens form chains perpendicular to the a-c plane, with the hydrogens in different sheets separated by b/2 = 2.6 Å.[13] During the experiment the crystal was oriented with the b axis perpendicular to the static magnetic field. The crystal was doped with chromium ions to reduce the ^1H spin-lattice relaxation time. The time development of the n-quantum intensities for squaric acid, shown in Figure (4.10a), appear very similar to those of adamantane. The chains of hydrogen atoms form an infinite spin system where the number of correlated spins, shown in Figure (4.10b), also increase continually with time.

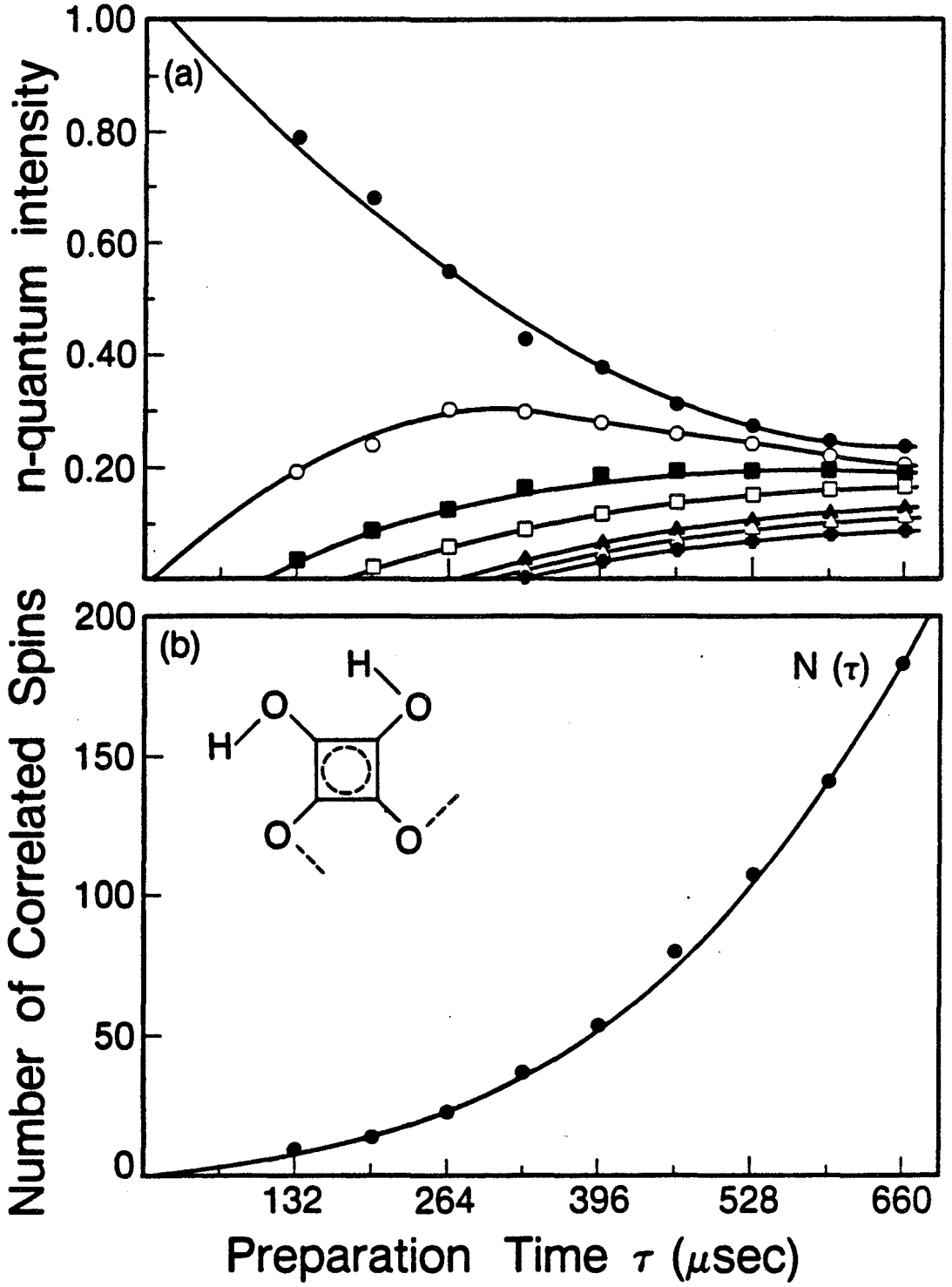

Figure 4.10. a) n-quantum intensity versus preparation time for squaric acid. The numbers of orders increase continuously over time. b) Number of correlated spins versus preparation time. As is characteristic of an infinite spin system, the effective size of the system grows rapidly and uninterruptedly with time.

2. Isolated Clusters: Liquid crystal

In a nematic liquid crystal sample, owing to restricted motion of individual molecules about their long axes, intermolecular dipolar couplings are averaged to zero while intramolecular couplings remain but are scaled down.[14] The nematic phase of the 21 spin p-heptyl-p'-cynabiphenyl ($C_{19}H_{21}N$) liquid crystal sample was thus selected to demonstrate an "ideal" case of truly isolated clusters on the NMR timescale, in the sense that individual molecules maintain solid-like characteristics while still being completely independent of one another. Thus, this liquid crystal which contains 21 protons should be a good model for a 21 spin cluster. Figure (4.11a) shows a plot of the n-quantum intensity normalized to the total intensity, versus preparation time; at short times, the number of multiple quantum orders increases, whereas for times greater than 1000 μsec the number of orders and their relative intensities remain unchanged. Reflecting the trends of the multiple quantum intensity plot, the effective system size $N(\tau)$, plotted in Figure (4.11b), grows for times up to 1000 μsec, after which it remains completely constant with a value of 21. The effective system size does not grow beyond the actual size of the molecule confirming that intermolecular couplings are zero and that only spins within the molecule can become correlated with one another. This type of behavior, the levelling of $N(\tau)$, is characteristic of isolated clusters.

3. Concentration Effects: 1,8-Dimethylnaphtalene-d_6

Solid solutions of six spin clusters were prepared to examine the effects of different degrees of cluster concentrations on the multiple

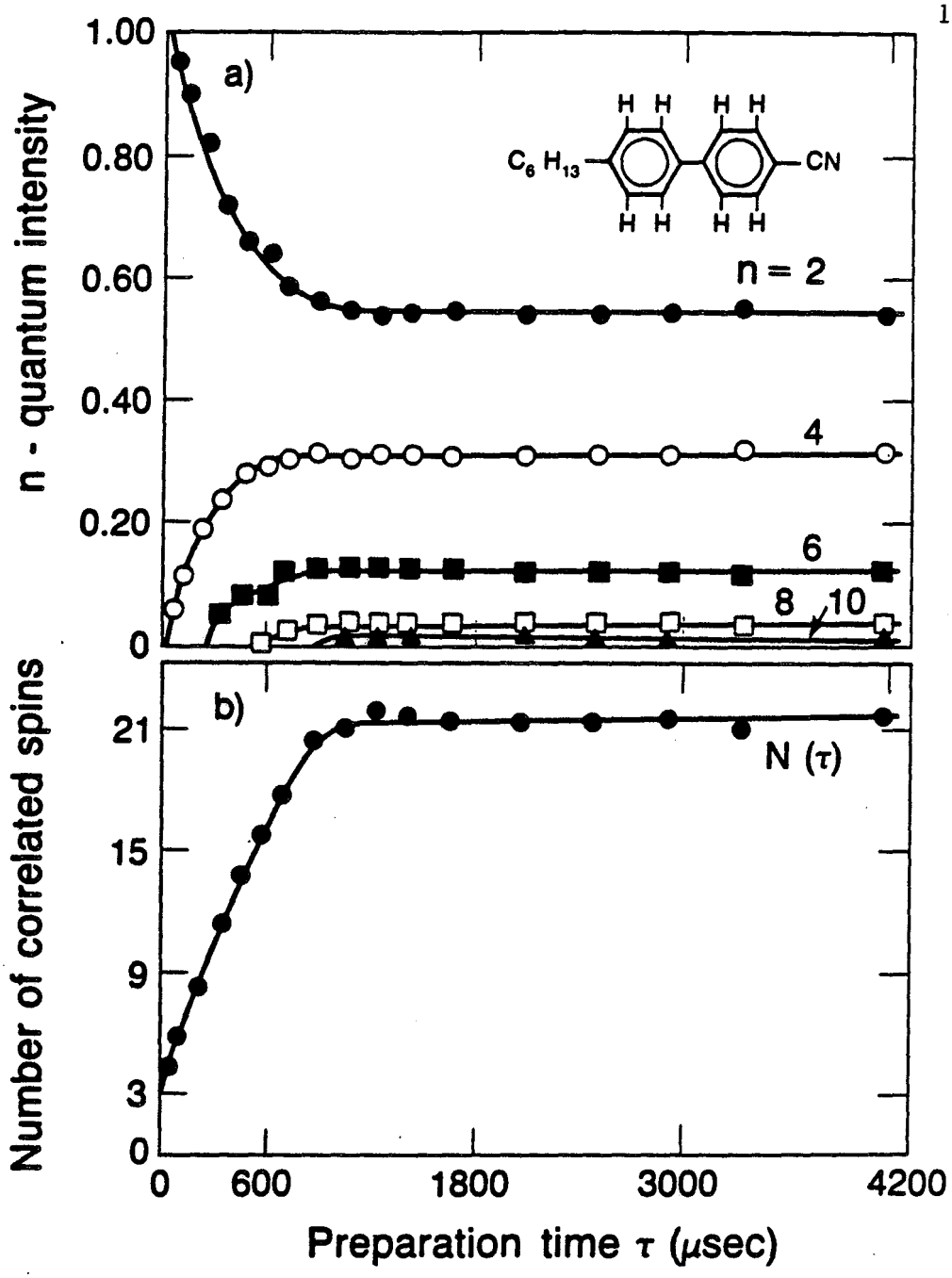

Figure 4.11. a) n-quantum intensity versus preparation time for the liquid crystal p-hexyl-p' cyanobiphenyl in the nematic phase. After roughly 1000 μsec, no new multiple-quantum orders develop and their relative intensities remain unchanged. b) N(τ) versus τ for the liquid crystal sample. After an induction period, the effective system size N(τ) levels off at 21, indicating that the number of interacting spins is limited to the size of the individual liquid crystal molecules which contain 21 protons.

quantum dynamics. The six spin clusters are formed by intimately mixing 1,8-dimethylnaphtalene-d_6 (DMN-d_6) with perdeuterated DMN-d_{12}; three concentration levels, 5, 10 and 20 mole %, are considered in addition to the neat material. For the latter, the shortest intermolecular ^1H-^1H distance is 2.0 Å along the b axis and the intramolecular methyl groups are separated by 2.93 Å.[15] The unit cell is arranged such that the methyl groups of a pair of molecules are pointing toward one another. Dilution of the protonated DMN-d_6 in a perdeuterated lattice forces the inter-cluster distances to increase without affecting the intra-cluster distances. Therefore, relative differences in the development of multiple quantum intensities can be attributed to inter-cluster correlations.

The existence of local spin clusters can already be discerned in the multiple-quantum spectra of the dilute 5 mole % DMN, shown in Figure (4.12) together with comparable spectra from neat DMN. The neat spin system is essentially unbounded, a state which is reflected in the spectra by a steady growth of the number of orders observed. In marked contrast, the spectra obtained from the 1:20 solid solution never extend beyond n = 6.

Figure (4.13) shows plots of the integrated n-quantum intensity to the total intensity for the four samples of DMN described, versus preparation time. Clearly, the trend indicates a more rapid development of multiple-quantum orders as the concentration of the clusters is raised. In the 5 mole % solution, after an initial induction period, the number of orders remains fixed up to roughly 500 μsec, after which the intensities begin to grow slowly. By contrast, the 10 and 20 mole

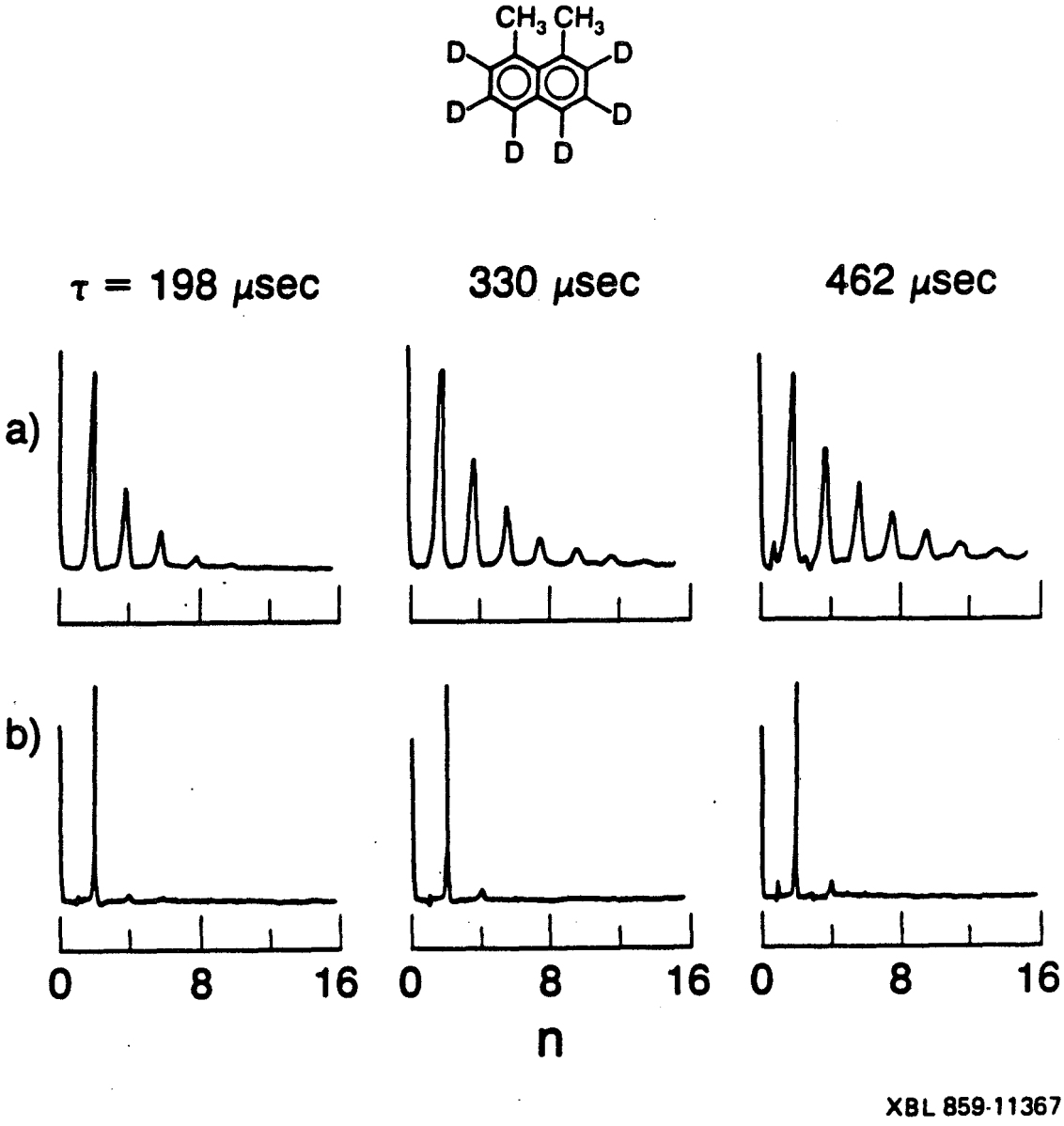

Figure 4.12. 360 MHz ^{1}H multiple-quantum spectra of dimethylnaphthalene recorded with the sequence of Figure (4.4).
Top: Neat DMN, ring positions deuterated.
Bottom: 1:20 solid solution in a perdeuterated host.
The two sets of spectra clearly demonstrate the different multiple-quantum excitation pathways possible in bounded and unbounded spin distributions. Only low order coherence can develop among the six isolated spins in the dilute system; consequently the distribution of multiple-quantum intensity changes very little over the range of preparation times shown. By contrast, the effective size of the neat material increases continuously over the same range of times.

Figure 4.13. n-quantum intensity versus preparation time for solid solutions containing

a) neat 1,8-dimethylnaphtalene-d_6 (DMN-d_6).

b) 20 mole % solution of DMN-d_6 in 1,8-dimethylnaphtalene-d_{12} (DMN-d_{12}).

c) 10 mole % solution of DMN-d_6 in DMN-d_{12}.

d) 5 mole % solution of DMN-d_6 in DMN-d_{12}.

The neat compound and the 5 mole % solution are examples of unlimited and clustered spin systems respectively. The 10 and 20 mole % samples are examples of more concentrated clustered environments. The general trend indicates that as the cluster concentration is lowered, the multiple-quantum intensity distribution changes less with time.

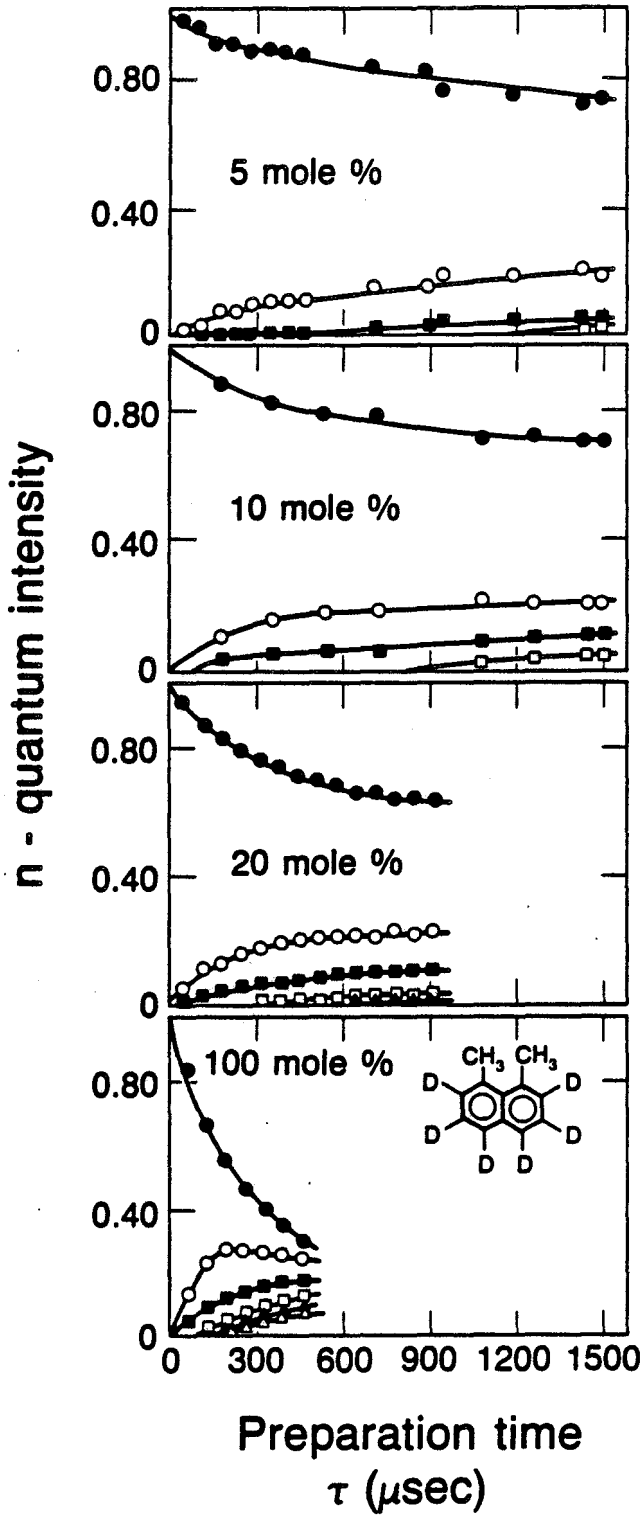

XBL 8512-12778

% solutions show orders growing in slowly all the time. Qualitatively, the features and ultimate intensities of the 10 and 20 mole % samples appear very similar, differing predominantly in the time scale of development. The multiple quantum intensities in the neat material increase very rapidly.

Plots of $N(\tau)$ versus τ are drawn for the 100, 20, 10 and 5 mole % solutions of DMN-d_6, in Figure (4.14). The values of $N(\tau)$ are represented by the smooth solid line. Two extreme behaviors are illustrated in this figure: in the 5 mole % solution, $N(\tau)$ grows very little up to 500 μsec and then begins to increase slowly at longer times, whereas in neat DMN-d_6, $N(\tau)$ increases very rapidly. In the first case, the concentration of clusters is dilute enough to localize the interacting spins to the clusters only, for the duration of 500 μsec; in the second case, the unbounded spin system allows an increasing number of atoms to interact with one another, over time, in a monotonic fashion. In neat DMN-d_6, even though the ring positions are deuterated, the density of spins is high enough and the inter and intra-molecular couplings comparable enough to blur the distinction between a clustered distribution and a uniform environment of hydrogen atoms. In the intermediate cases of 10 and 20 mole % solutions, where the concentration of clusters is raised, but where well-defined groups still exist, $N(\tau)$ grows continuously although more slowly than for neat DMN. On the time scale of the experiment, spins from different groups are close enough together to influence the multiple quantum dynamics to the point where inter-cluster separations are too small to produce a discernible plateau in $N(\tau)$ versus τ. Higher cluster concentration levels result

Figure 4.14. Number of correlated spins versus preparation time for the four solutions of DMN-d_6 described in Figure (4.13). The filled circles represent values for the effective system size $N(\tau)$, and the open ones values for the effective cluster size $N(_c(\tau)$. The size and extent of clustering can be determined from the pattern and rate of growth of $N(\tau)$ and $N_c(\tau)$.

a) both parameters grow uninterruptedly, indicating an unbounded spin system.

b) and c) In both samples, $N_c(\tau)$ remains constant over time, indicating clusters of six atoms; the more rapid growth of $N(\tau)$ in the 20 versus 10 mole % solution reflects the fact that the six spin clusters of DMN-d_6 become closer to one another as the ^1H concentration is raised.

d) After an initial induction period, $N(\tau)$ remains essentially constant up to approximately 500 μsec, indicating a bounded system of six atoms. At longer times when clusters interact, $N_c(\tau)$ remains level at six.

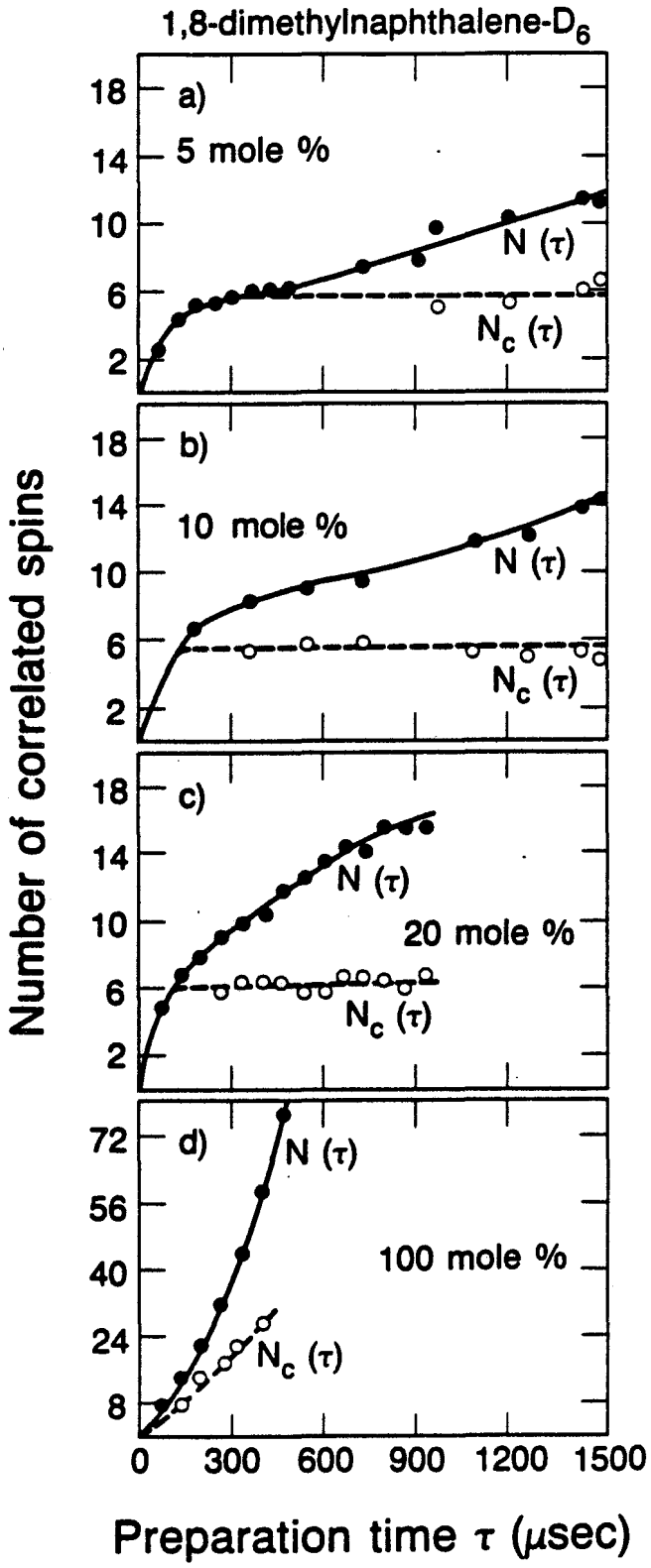

XBL 8512-12782

in more rapid inter-cluster communication, as demonstrated by the steeper growth of $N(\tau)$ for the 20 versus the 10 mole % solution.

4. Two-Gaussian model

In the intermediate cases, where clusters exist but are not sufficiently isolated to preclude small interactions between them, a second time dependent parameter is introduced to ascribe a size to the clusters independently of inter-cluster events. A schematic drawing of a two Gaussian model is presented in Figure (4.15). The simplest approximation is to attribute the multiple quantum intensities to two independent events: the intra-cluster correlations which have already matured, and the inter-cluster correlations that continue to develop between spins of different groups. The multiple quantum intensities due to the subgroup of clustered spins are approximated by a Gaussian whose variance is associated with $N_c/2$, while the remaining intensity is approximated by a second Gaussian of variance $N_2/2$. The total intensity is the sum of both contributions and is written as:

$$I(\Delta M) = m_c e^{-n^2/N_c} + m_2 e^{-n^2/N_2} \quad . \tag{4.5}$$

A least squares iterative program using the Newton-Raphson method is employed to fit the multiple-quantum intensities to the above equation. Now two time-dependent effective sizes can be extracted from the multiple quantum spectral intensities: a cluster size $N_c(\tau)$ arising from the two-Gaussian model, and a system size $N(\tau)$ whose value may incorporate spins from numerous groups. Recall that $N(\tau)$ is calculated

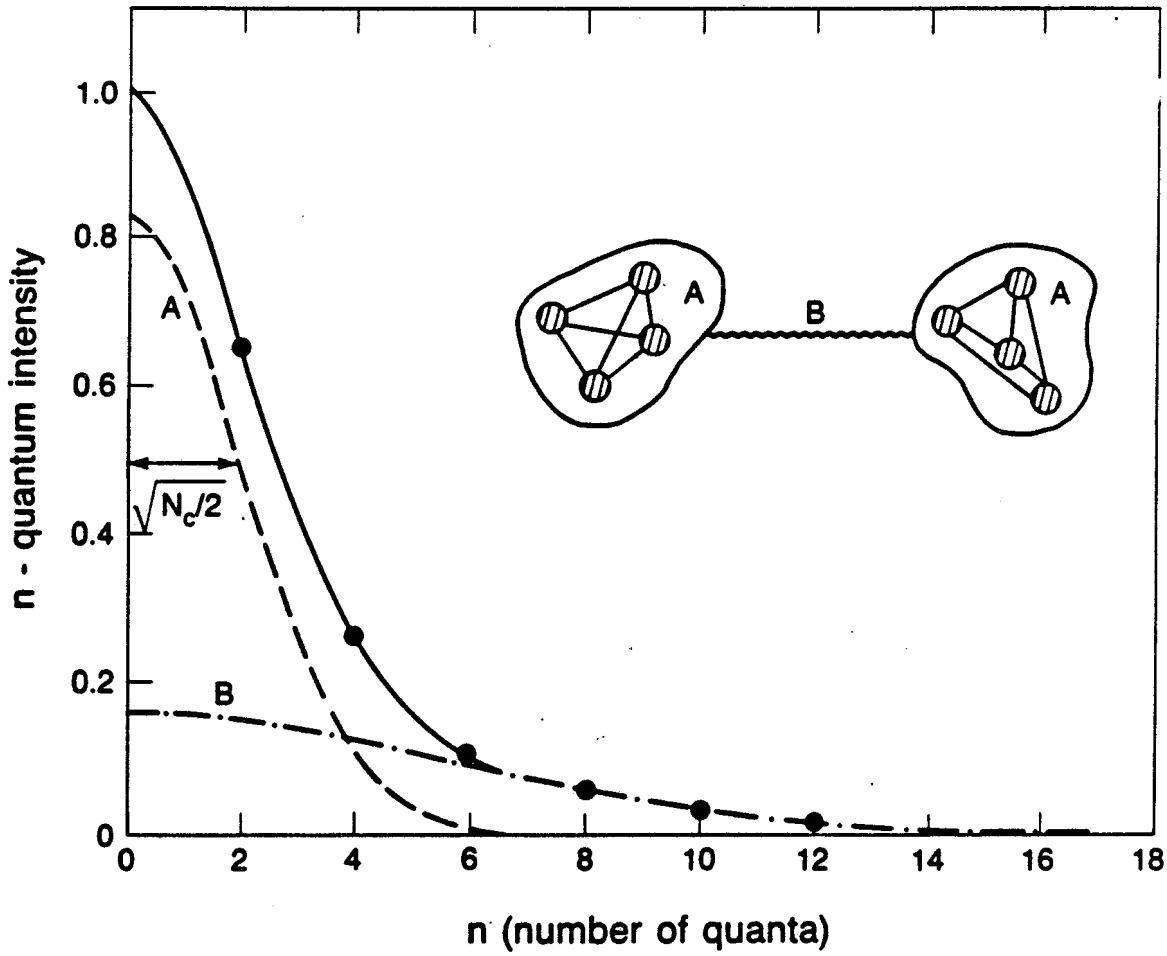

Figure 4.15. Schematic drawing of the two-Gaussian model. The inset represents clusters interacting with one another on the experimental time scale. In order to determine the cluster size, a parameter N_c is introduced to describe events occurring within a cluster, independently of those occuring between clusters. The multiple quantum intensities (filled circles) are the sum of intra and inter-cluster correlations both of which are associated, independently, with a Gaussian of standard deviation $(N_c/2)^{1/2}$ and $(N_2/2)^{1/2}$, respectively. Only when most of the multiple quantum intensity is due to intra-cluster correlations is this approximation valid.

by fitting the integrated intensities to a single Gaussian. The pattern of growth of both parameters will be used to establish the size and extent of clustering in solid samples. In the same spirit as for $N(\tau)$, absence of chance in $N_c(\tau)$ over time is evidence that clusters exist, although they may be near one another. The magnitudes of m_c, m_2 and N_2 will change to account for the increasing number of communicating clusters over time until finally m_2 will become larger than m_c and the approximation will no longer be valid. Only when the correlations due to clusters dominate the multiple quantum intensities, or when $m_c > m_2$, can the inter versus intra-cluster interactions be addressed separately.

Returning to Figure (4.14), the values of $N_c(\tau)$ for the 4 concentrations of DMN are now plotted along with the values of $N(\tau)$ discussed earlier. Considering the two extremes once again, we note that $N_c(\tau)$ is not necessary to determine the cluster size in the 5 mole % solution, as here $N(\tau)$ remains fixed for a sizeable duration of time. $N_c(\tau)$ can be calculated at longer times and results in values close to six. By contrast, $N_c(\tau)$ and $N(\tau)$ both increase in the 100 % DMN sample, confirming that the density of spins is too high to assign a cluster size to this material. For the intermediate concentrations of 10 and 20 mole % where $N(\tau)$ grew uninterruptedly, $N_c(\tau)$ now remains constant over time with values hovering about six. These data confirm that DMN contains predominantly clusters of six atoms which become increasingly close to one another as the ^1H concentration is raised.

5. More Dilute Spin Systems and Clusters

a. 1,8-Dimethylnaphtalene-d_{10}

1,8-dimethylnaphtalene-d_{10} (DMN-d_{10}) is very similar to 1,8-DMN-d_6, but here, in addition to ring deuteration, the methyl groups are partially deuterated as well, leaving only two hydrogen atoms on the entire molecule. The inter and intra-molecular ^1H- ^1H distances are not affected by the additional methyl deuteration. Two solid solutions of DMN-d_{10}, 5 and 10 mole %, were prepared in the same manner as those of DMN-d_6. Plots of the integrated n-quantum intensities appear in the upper portions of Figures (4.16a) and (4.16b). In the 5 mole % solution, where the 2-quantum intensity is essentially dominant at all times, the effective system size $N(\tau)$ is calculated directly from the binomial formula of Equation (4.3). For the 10 mole % solution, the combinatorial formula is used up to 600 μsec, after which the intensities can be approximated by a Gaussian as usual.

A comparison of the six spin and two spin model clusters at comparable ^1H concentrations reveal similar trends for $N(\tau)$ and $N_c(\tau)$; in both 5 % cases, $N(\tau)$ remains level up to approximately 500 μsec after which it increases slowly, whereas in the 10 % cases $N(\tau)$ rises more steeply. What distinguishes the two materials from one another are the actual values of the effective system and cluster sizes. In DMN-d_{10}, contrary to DMN-d_6, $N(\tau)$ remains close to two; in the 10 % solution, $N_c(t)$ can be calculated at long times and lies between three and four. These results demonstrate that the multiple quantum dynamics are sensitive enough to distinguish clearly between two spin and six spin clusters of very similar compounds.

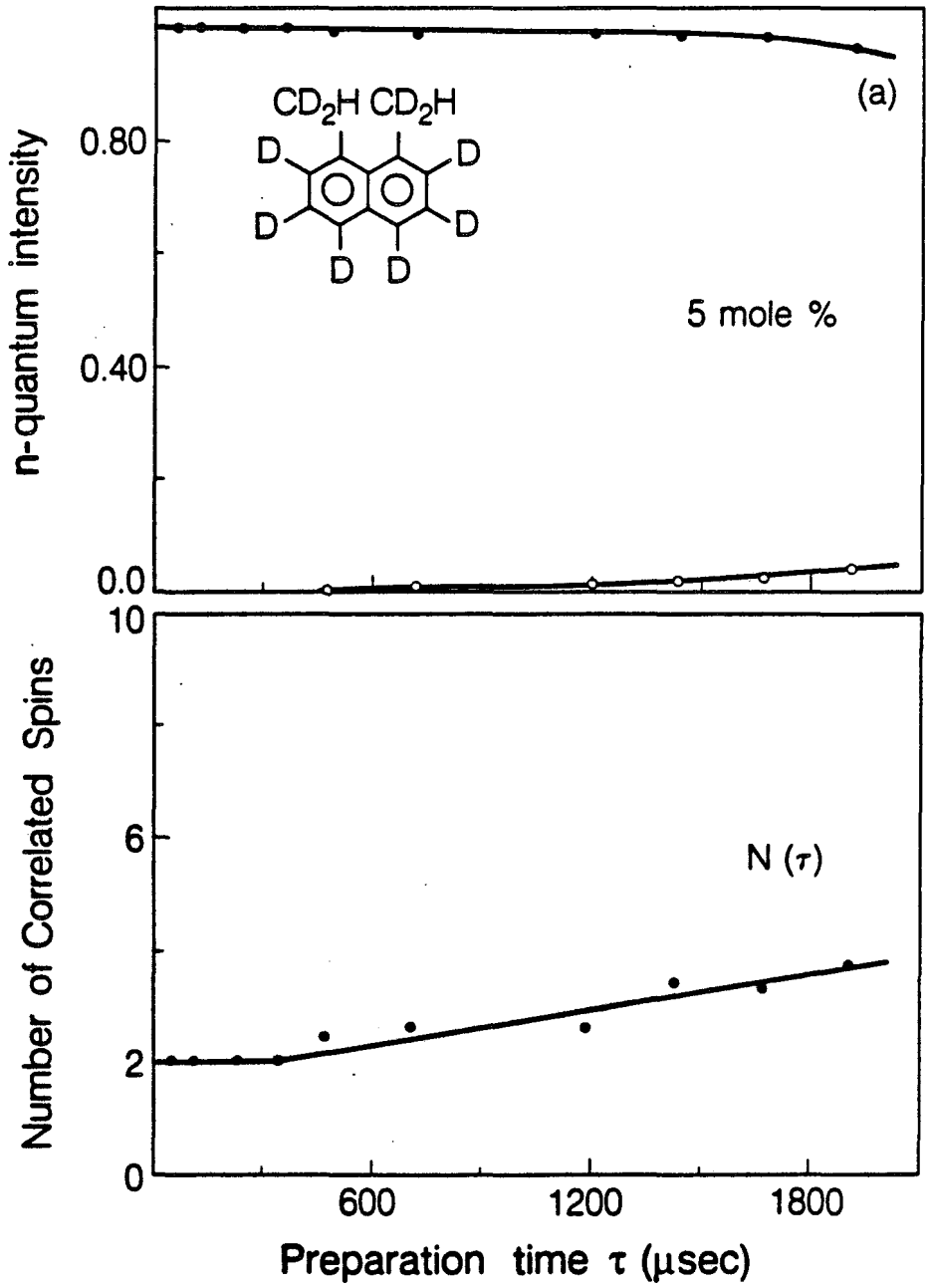

Figure 4.16. n-quantum intensity (top) and number of correlated spins (bottom) versus preparation time for two solid solutions:

a) 5 mole % 1,8-dimethylnaphtalene-d_{10} (diagrammed in the inset) in DMN-d_{12}.

b) 10 mole % DMN-d_{10} in DMN-d_{12}.

For the 5 mole % solution $N(\tau)$ remains close to 2. In the 10 mole % solution, $N(\tau)$ grows with time but $N_c(\tau)$ remains essentially constant hovering between 3 and 4. The cluster size in these samples is very small.

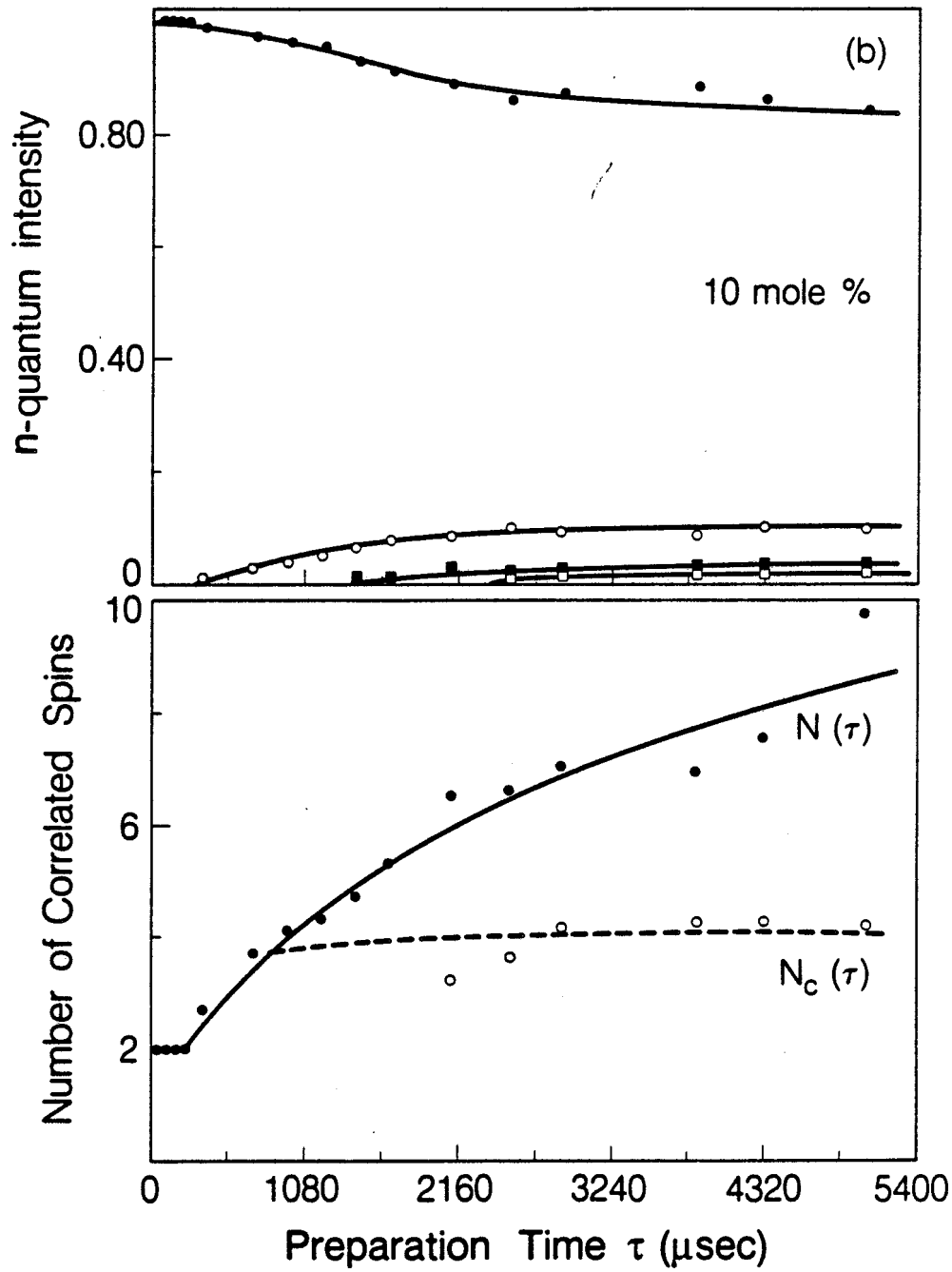

XBL 8512-5060

b. Hexamethylbenzene ($C_6(CH_3)_6$; polycrystalline)

Hexamethylbenzene (HMB) exists in a triclinic unit cell with the planar benzene rings forming a nearly hexagonal net.[16] Two varieties of anisotropic molecular motion determine the dipolar properties of this system. First, each methyl group rapidly reorients about its C_3 axis, rendering the three ^1H nuclei equivalent. Second, the entire molecule undergoes fast-limit six-fold hopping about the C_6 axis of the benzene ring,[17] which reduces the intramolecular dipolar couplings between ortho, meta, and para methyls. Intermolecular couplings remain but, as in adamantane, interacting molecules behave as point sources. Within a molecule, average distances between protons on different methyl groups range from 3.3 A (ortho) to 6.6 A (para), and between molecules, C-C distances range upwards from 3.7A. Sheets of molecules in the a-b plane are separated by 5.3A. The specific systems to be considered here are (1) a solid solution of HMB in perdeuterated HMB with a molar ratio of 1:10, (2) a sample of HMB randomly deuterated to a level of 80-90%, (3) neat sample of HMB, and (4) a 1:20 solid solution as well. All the samples are polycrystalline, the mixtures having been obtained by evaporation of solvent.

Plots of the integrated n-quantum intensity, for neat, randomly deuterated, and the 9 mole % HMB, sample versus preparation time, are presented in Figure (4.17). Measured values of $N(\tau)$ for the two deuterated hexamethylbenzenes and for neat HMB are plotted in Figure (4.18). It is evident that the same series of spectra is eventually obtained in each case, but that the preparation time required to

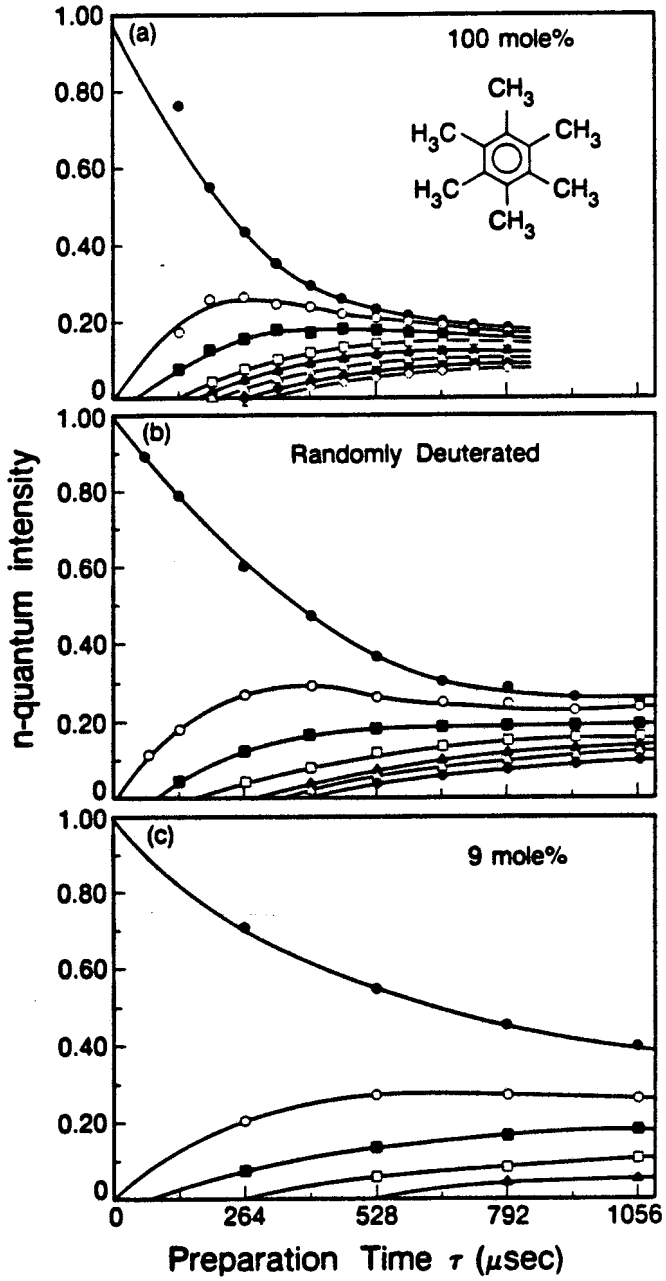

Figure 4.17. n-quantum intensity versus preparation time for solid solutions of hexamethylbenzene (HMB)

a) neat bexamethylbenzene.

b) 80-90% randomly deuterated hexamethylbenzene.

c) 9 mole % HMB-h_{18} in HMB-d_{18}.

The growth of the multiple-quantum orders in the neat material is very similar to that of adamantane (Figure 4.9) and squaric acid (Figure 4.10) as expected. The randomly deuterated material is intermediate between the neat and dilute sample, where few orders grow in slowly over time.

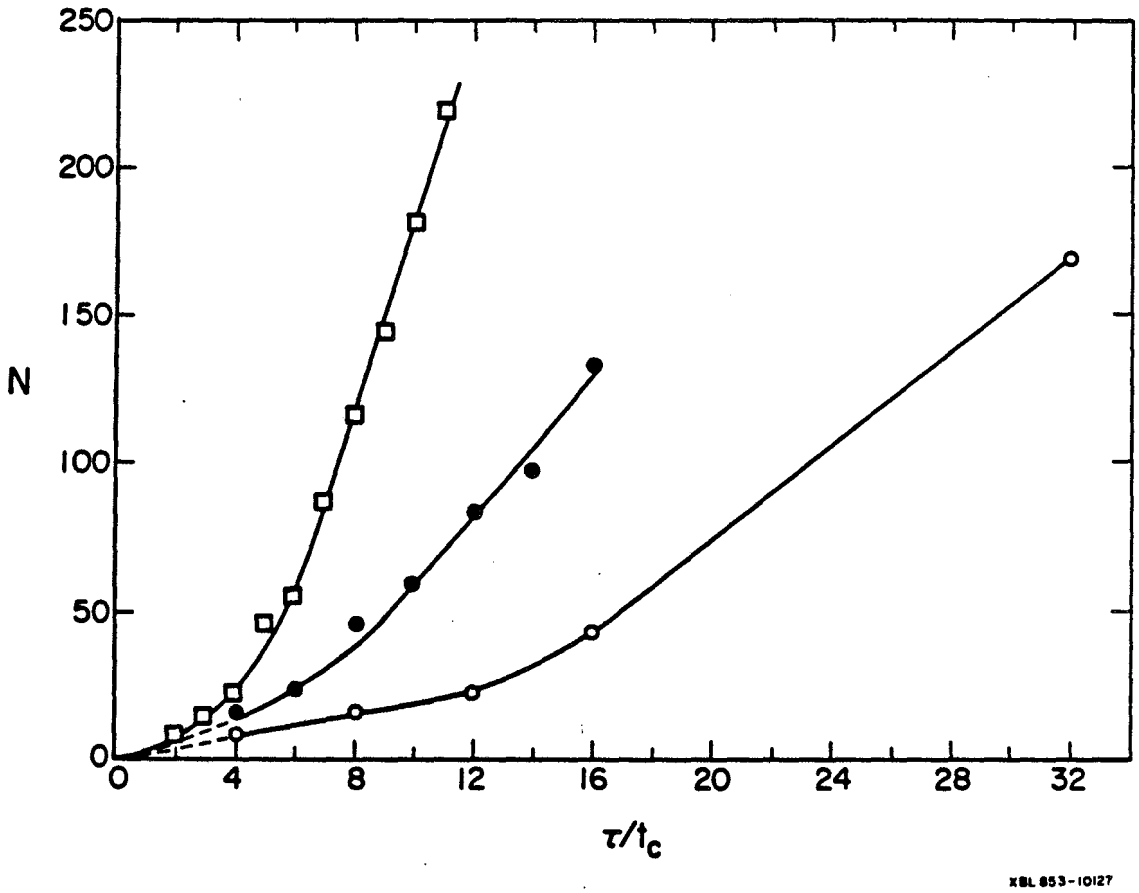

Figure 4.18. N versus τ/t_c for neat hexamethylbenzene (squares), a 1:10 solid solution of HMB-h_{18} in HMB-d_{18} (open circles), and randomly deuterated HMB (shaded circles). The basic cycle time was 66 μsec in these experiments. The rates of increase of the effective size are slower in the two dilute systems.

realize a particular distribution depends strongly on the individualdipolar characteristics. Consequently, we can replace the independent variable, τ, by a scaled variable, $\alpha\tau$, to define a common time dependence for N. It is apparent from the data that $\alpha = 1$ for neat HMB, $\alpha = 1.65 \pm 0.10$ for the randomly deuterated material, and $\alpha = 3.1 \pm 0.3$ for the 1:10 mixture.

Intramolecular dipolar couplings, presumably large, strongly influence multiple quantum spectra at short preparation times. Since the dilution of HMB in a deuterated lattice does not affect these couplings, we might expect to see no changes in the initial development of coherence in the mixture. However, the straightforward scaling of the time dependence for $\tau \gtrsim 250$ μsec clearly indicates that the strongest intramolecular couplings have matured much earlier, apparently before 50 - 100 μsec have elapsed. This is consistent with the crystal and molecular structure of HMB, which forces the longest intramolecular $^1H - {}^1H$ distances to be comparable to, and sometimes greater than the shortest intermolecular distances. It is interesting to note here that the observed scaling factor of ~3 for $N(\tau)$ is close to the predicted scaling of the intermolecular second moment by the square root of the concentration of protonated molecules in the dilute mixture. This prediction follows from treating all distant molecules as point dipole sources, with each reproducing a local field averaged to one distinct value by the rapid six-fold molecular reorientation.

Random deuteration of HMB affects both intramolecular and intermolecular dipolar couplings to some extent. Analysis of this material by multiple-quantum spectroscopy enables us to distinguish it both from

neat HMB and from the other dilute system with approximately the same total number of ^1H nuclei. The growth of $N(\tau)$ with τ for the randomly deuterated molecules is intermediate between the two extremes, a difference more striking than the subtler changes observable in the single-quantum ^1H spectra. We can account for the more rapid formation of spin correlations in the randomly deuterated sample, as compared to the 1:10 mixture, by noting that the distribution of ^1H nuclei is both higher and more uniform throughout the randomly deuterated material. More spins are in a position to communicate with each other at any given time.

For neat and randomly deuterated HMB, the two-Gaussian model is not a good approximation as the values of m_c are usually much larger than the values of m_2. For $\tau \doteq 132$ μsec however, m_c is still less than m_2, and here N_c is equal to 18. For both the 9 and 5 mole % solutions however, the two Gaussian model can be used over longer preparation times; results for the 5 mole % solution are plotted in Figure (4.19b) along with the values of $N(\tau)$. As expected, $N(\tau)$ increases too rapidly to resolve the individual cluster size. On the other hand, the values of $N_c(\tau)$ remain constant, over time, at roughly 15, indicating that fairly large clusters do exist in the dilute sample. The values of $N_c(\tau)$ for the 9 mole % sample are very similar to those of the 5 % sample as can be ascertained from the similar intensity plots of Figure (4.19a) and (4.17c).

C. <u>1,2,3,4-tetrachloronaphtalene-bis(hexachlorocyclopentadiene)-adduct</u> (polycrystalline)

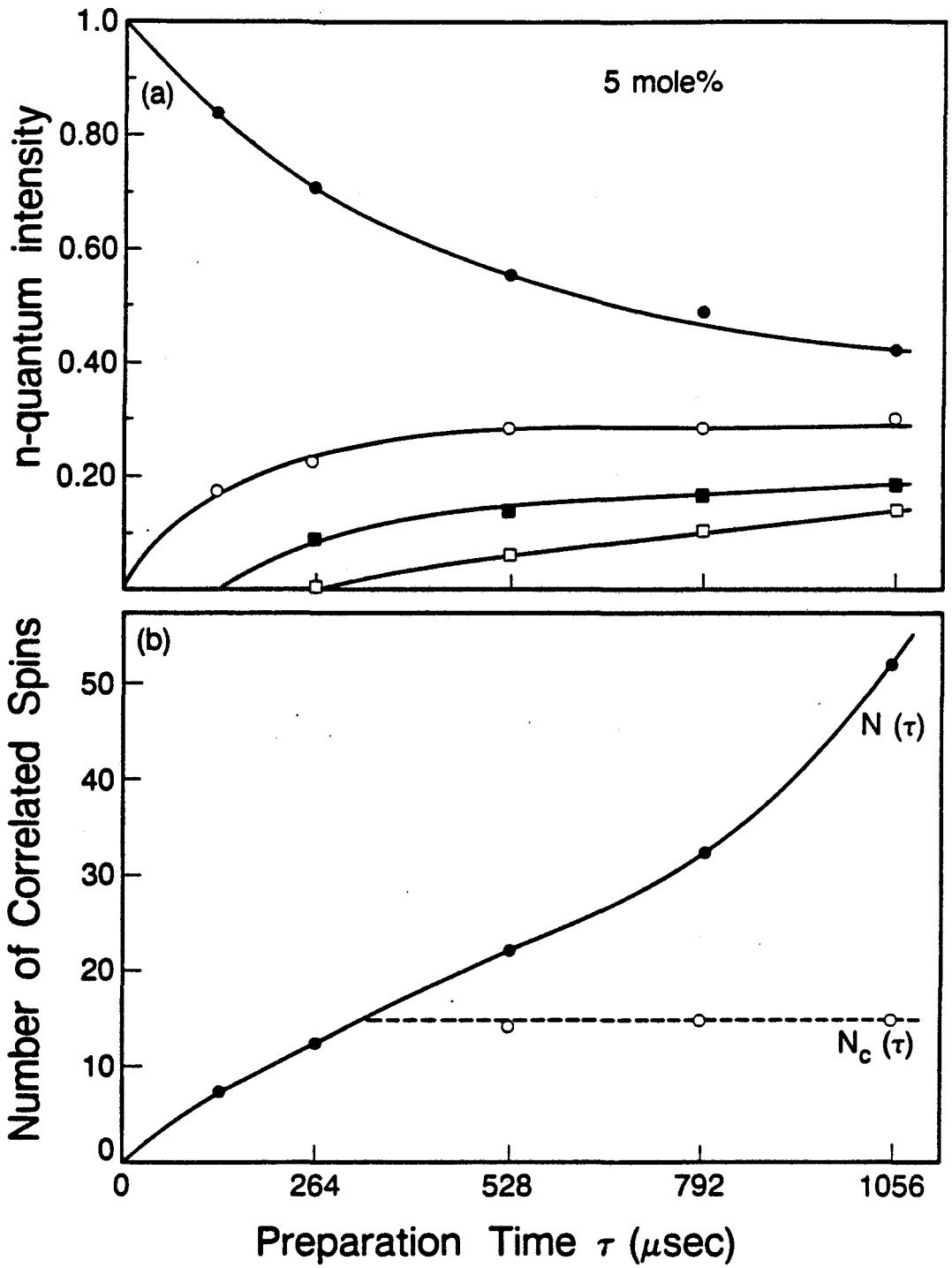

Figure 4.19. a) n-quantum intensity versus preparation time for a 5 mole % solution of HMB-h_{18} in HMB-d_{18}. b) Number of correlated spins versus preparation time for this sample. In the 5 mole % solution, $N(\tau)$ grows steadily whereas $N_c(\tau)$ remains level at roughly 15 indicating fairly large clusters.

This polycrystalline sample encompasses the characteristics of a clustered material as well as a neat sample. On the one hand, the bulky hexachlorocyclopentadiene groups isolate hydrogen atoms of different molecules from one another, creating a sharp variation of inter versus intra-molecular dipolar coupling strengths: on the other hand, the "cluster concentration", or cluster to solvent-atom ratio, is high. No crystal structure is available for this material. The ^1H NMR spectrum is very broad, on the order 50 kHz, and structureless. A zero field NMR spectrum was obtained and computer simulations were performed to determine the positions of the 4 hydrogen atoms. With an assumed C_2 axis of symmetry, only four distances are needed to characterize the hydrogen spectrum: r_{11}=2.83 Å, r_{12}=2.22 Å, $r_{12'}$= 4.34 Å, and r_{22}= 5.01 Å[18].

The integrated multiple quantum intensities in Figure (4.20a) show a discontinuity in the development of the multiple quantum coherence. Up to 300 μsec, only two and a small amount of four quantum coherence have grown; thereafter, many high orders appear rapidly. It is interesting to note the difference between the time development of these intensities relative to those of the liquid crystal sample shown in Figure (4.11a). The plot of $N(\tau)$ versus τ in Figure (4.20b) reflects the trends of the multiple quantum intensities; the effective size of the system remains at four for times ranging up to 300 μsec and then shoots up rather rapidly. From these trends it is clear that correlations develop very quickly for hydrogen atoms within the molecule; at longer times, the smaller dipole couplings become more important and communication occurs between spins on different molecules

Figure 4.20. a) n-quantum intensity versus preparation time for the polycrystalline sample 1,2,3,4-tetrachloronaphtalene-bis(hexachlorocyclopentadiene)-adduct. The 2-quantum intensity is not plotted so that higher multiple-quantum orders can be seen more clearly. The time development of the multiple-quantum intensities is discontinuous.

b) Number of correlated spins versus preparation time for this sample. The effective system size $N(\tau)$ remains at 4 for times up to 300 μsec, indicating that only the 4 hydrogen atoms within the molecule have become correlated thus far. At long times, because of the high density of clusters, a large number of intercluster interactions can develop. As a result, $N(\tau)$ grows rapidly with time, and $N_c(\tau)$ increases as well.

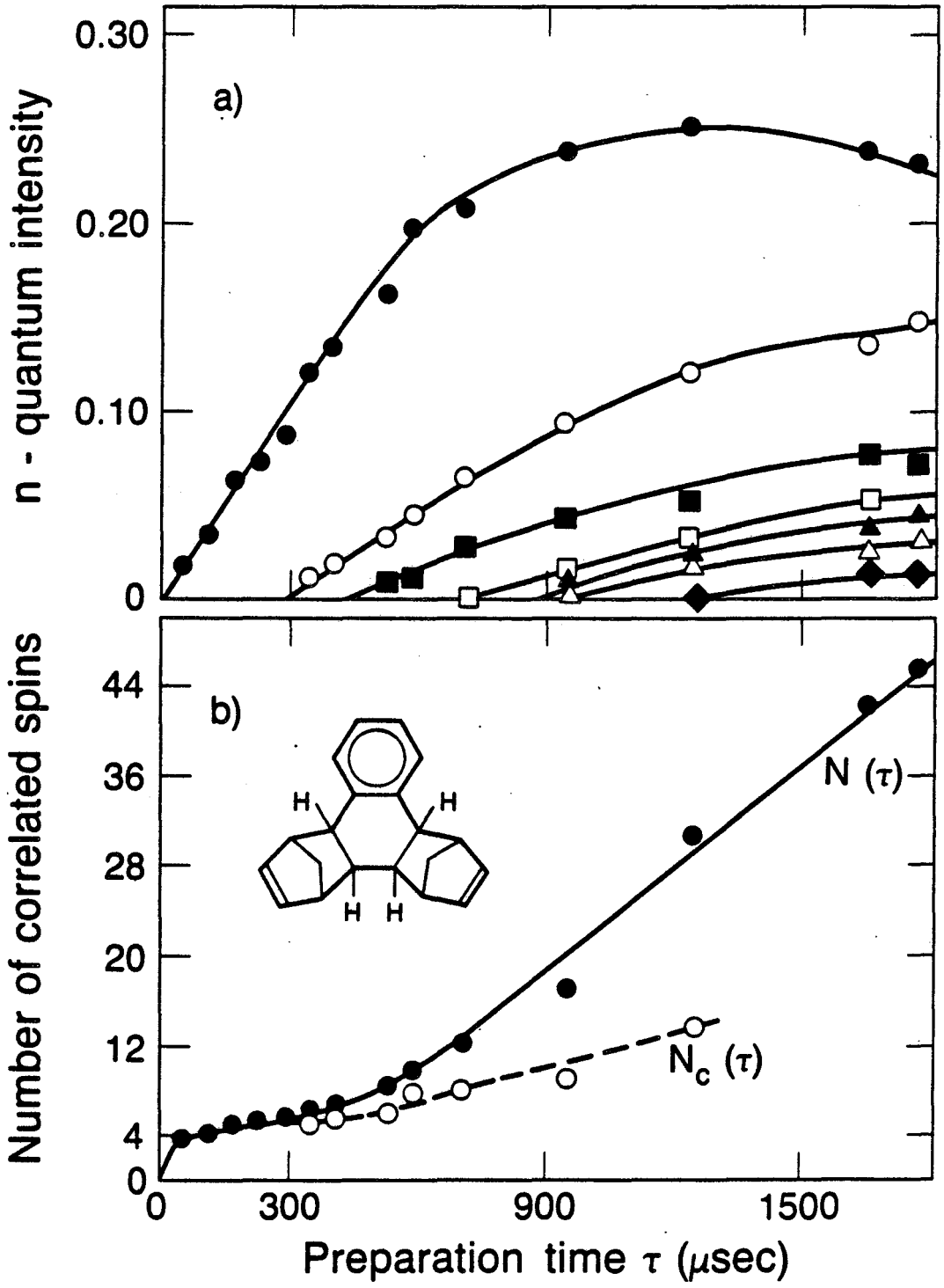

XBL 8512-12783

as well. Due to the high density of spins once intermolecular interactions are allowed, $N_c(\tau)$ grows slowly rather than levelling off at four, thus confirming the two-fold character of this material. The plateau in $N(\tau)$ at short times is evidence of a clustered material of four atoms and the increase in $N_c(\tau)$ and $N(\tau)$ at long times is indicative of a large network of hydrogen atoms.

D. Application to Hydrogen Clustering in Hydrogenated Amorphous Silicon

1. Background

Hydrogen incorporation into amorphous silicon thin films has improved their electrical and optical properties to a point where they now play a significant role in the electronics industry. In addition to passivating "dangling bond" defects, the hydrogen modifies the electronic structure of these materials. Films containing between 8 and 20 atom % hydrogen are "device quality" and have roughly 10^{15} defects/cm^3; films with higher hydrogen content can also be prepared but usually have higher defect densities than device films. In recent years, a number of researchers have characterized amorphous hydrogenated silicon (a-Si:H) by numerous techniques and have furnished information on the relationship between the structure of a-Si:H and its properties.[1]

Structural information gained from electron microscopy indicates that device films can differ from one another to the extent that some show no features down to 10 Å while others show structures on the order

of 100 Å. In contrast, nondevice and polymeric films (>50 atom % ^1H) show columinar growth islands and other structural features. Information on the different types of silicon-hydrogen bonds have been obtained by infrared spectroscopy; predominantly monohydride (Si-H) silicon-hydrogen bonds are observed in device films whereas dihydride ($Si-H_2$), trihydride ($Si-H_3$) and polymeric ($(Si-H_2)_n$) species are observed in the higher hydrogen containing films. From proton nuclear magnetic resonance it has been ascertained that the hydrogen is inhomogeneously distributed in device materials.[19,20] Approximately 4 atom % hydrogen is present as spatially isolated monohydrides and molecular H_2, and gives rise to a narrow (3-4 kHz) resonance line. The remaining hydrogen results in a broad (25 kHz) resonance line indicating clusters of monohydrides. While the magnetic resonance linewidths and magnitude of the narrow component remain constant, the magnitude of the broad component grows with increasing hydrogen content. Heating the material to 600 K causes the hydrogen associated with the broad component to evolve, leaving only a narrow resonance line in the NMR spectrum.

Many questions concerning the distribution of hydrogen in a-Si:H films still remain unanswered. A drawing of local hydrogen structure shown in Figure (4.21) serves to illustrate the issues raised in this Section: What is the nature of the hydrogen distribution responsible for the broad resonance line? How does the dense hydrogen coexist with the dilute hydrogen? On the atomic level, what are the differences between device and nondevice quality films? By using multiple quantum NMR, a technique inherently sensitive to spatial arrangements of atoms,

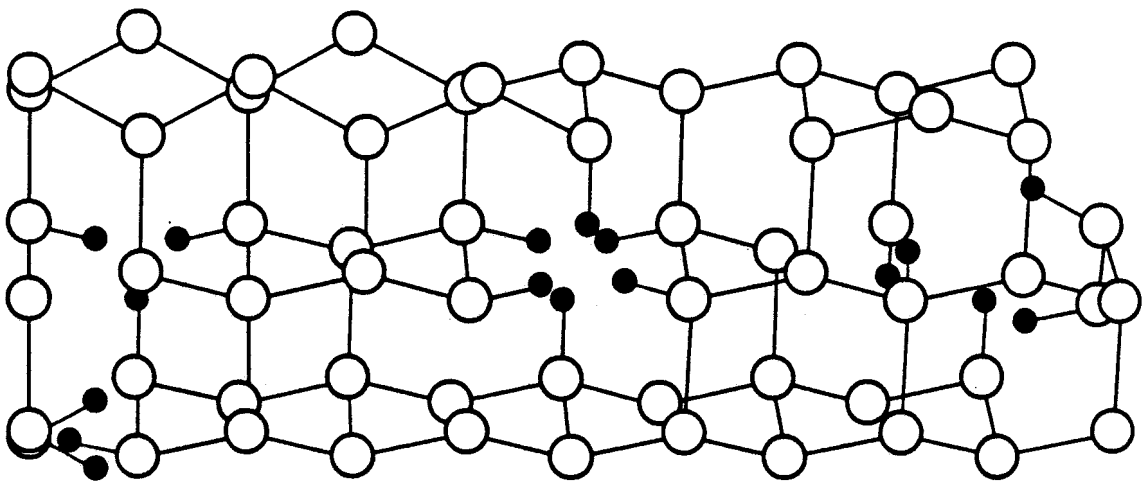

XBL 8510-4450

Figure 4.21. Schematic 3-dimensional drawing of clustered monohydrides in hydrogenated amorphous silicon (a-Si:H). The silicon atoms are in a tetrahedral bonding configuration. Silicon atoms, hydrogen atoms and covalent bonds are represented by open circles, filled circles and solid lines, respectively. The drawing is intended to motivate questions concerning the distribution of hydrogen in a-Si:H thin films.

we present the first study in which the size and extent of hydrogen clustering, in selected a-Si:H thin films, has been determined.

Five different a-Si:H samples, prepared by plasma deposition, are considered: two device quality films with different hydrogen concentrations, one nondevice quality film, one polymeric and one annealed sample. Sample preparation procedures, i.e. the reactant gas composition, the substrate temperature, the power of the rf electrode and the final atom % ^1H, are listed in Table 1.

2. Experimental Results and Discussion

Multiple quantum spectra of the a-Si:H samples for two different preparation times are shown in Figure (4.22). A comparison of the spectra at τ=180 and 360 μsec was made to see whether the intensity distribution of the multiple quantum orders changes with time or remains constant. Two extremes can be observed; the 50 atom% spectra clearly show higher orders at longer times whereas the 8 atom% spectra remain very similar, suggesting a bounded spin system. Although not shown in Figure (4.22), spectra were also obtained to assess the contribution of the isolated monohydrides and molecular H_2 to the multiple quantum experiment. After annealing the 8 atom % ^1H device sample, the remaining hydrogen (< 4 atom %) yields a spectrum with a narrow ^1H resonance line (4 kHz). No multiple quantum coherences are created for short preparation times and only at times greater than 360 μs can small amounts of two quantum coherence be observed. Therefore, on the experimental time scale, the dominant contributions to the multiple quantum spectra result from spins responsible for the broad

Table 1: A-Si:H Sample Preparation Conditions

Sample	Gas Composition	Temperature (oC)	Power (W)	Atom $\%^1H$
Annealed*	100% SiH_4	275	1	4
Device A	100% SiH_4	275	1	8
Device B	5% SiH_4/He	230	18	16
Nondevice	100% SiH_4	75	1	25
Polymeric	100% Si_2H_6	25	1	50

*annealed 600°C, 90 minutes

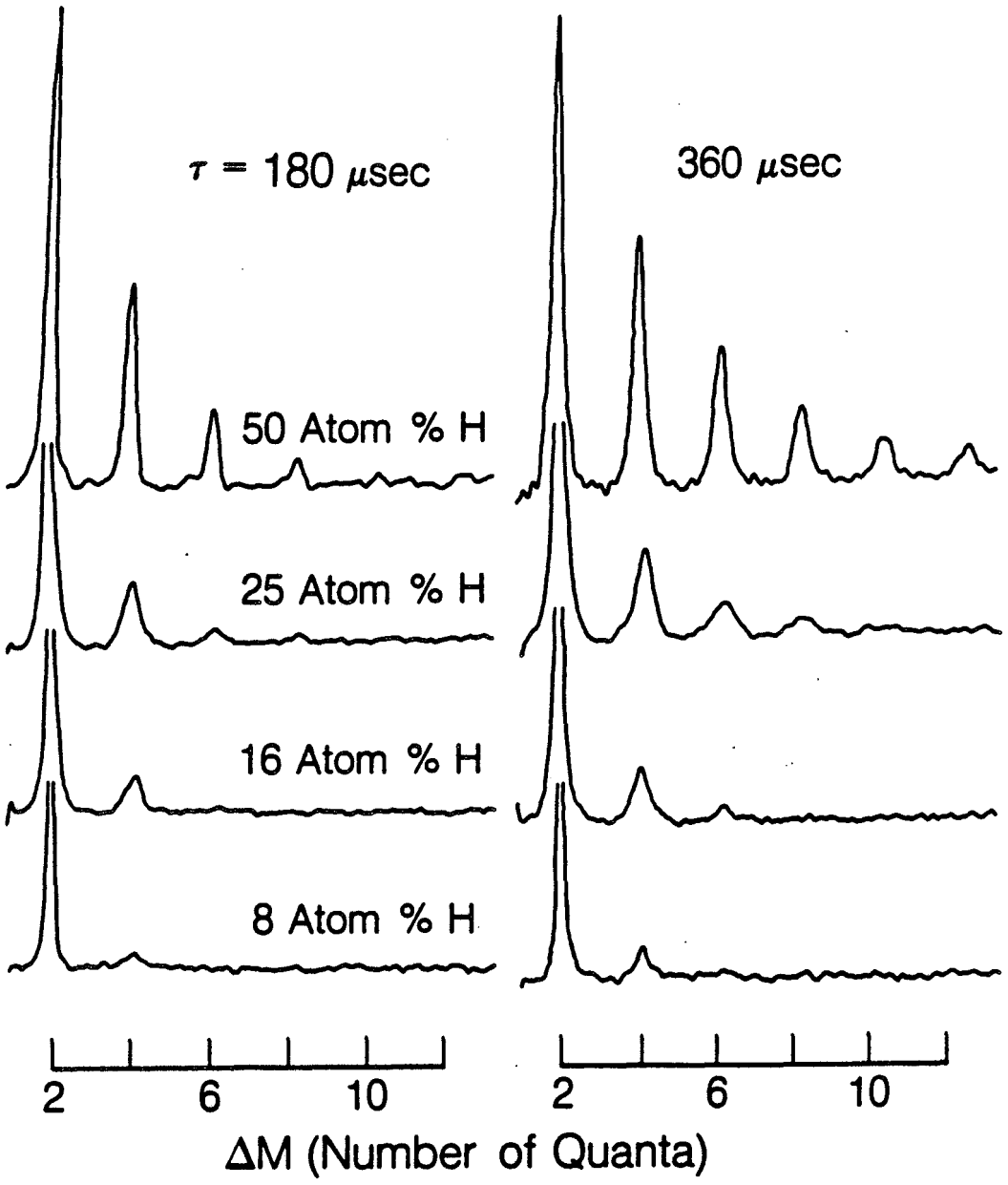

Figure 4.22. 180 MHz ^{1}H multiple quantum spectra of a polymeric, non-device, and two device quality a-Si:H samples are plotted for two different preparation times, τ = 180 and 360 μsec. From top to bottom, these samples contain 50, 25, 16 and 8 atomic % ^{1}H, respectively. Over time, the distribution of intensity across the multiple quantum orders does not change in the 8 atom % sample, suggesting a bounded spin system. As the hydrogen concentration increases, the spectra begin to change more from one preparation time to another.

resonance line.

In order to quantify the number of correlated spins at different preparation times, the intensity distributions of the multiple quantum spectra, plotted in Figure (4.23), have been characterized by the two time-dependent parameters, $N(\tau)$ and $N_c(\tau)$. The number of correlated spins is plotted versus preparation time for the a-Si:H samples in Figure (4.24). Reflecting the trends seen in both the multiple quantum spectra and the intensity plots, $N(\tau)$ remains roughly constant over time for the 8 atom % device quality sample, confirming the hypothesis that the spin system is limited to isolated clusters of atoms. By contrast, $N(\tau)$ grows with time for the 16 atom %, the nondevice 25 atom % and the polymeric 50 atom % ^1H samples. The behavior of $N_c(\tau)$ is indicated by the dashed lines in Figure (4.24). The increase in both $N(\tau)$ and $N_c(\tau)$ for the polymeric sample indicates a uniform distribution of spins. The effective cluster size values of the 16 and 25 atom % samples are now very similar to the values of $N(\tau)$ obtained for the 8 atom % sample, indicating that the 25 %, 16 %, and 8 atom % samples all contain small clusters of four to seven atoms. The uniform distribution of atoms in the polymeric sample is consistent with the fact that it was prepared differently from the others and contains $((Si\text{-}H_2)_n)$ species.

Having established that the two device samples and the nondevice sample all contain clusters of roughly six atoms, we can now distinguish features between them from the pattern of growth of the effective system size, $N(\tau)$, versus time. Depending on how close the clusters are to one another, the increase in $N(\tau)$ will be more or less

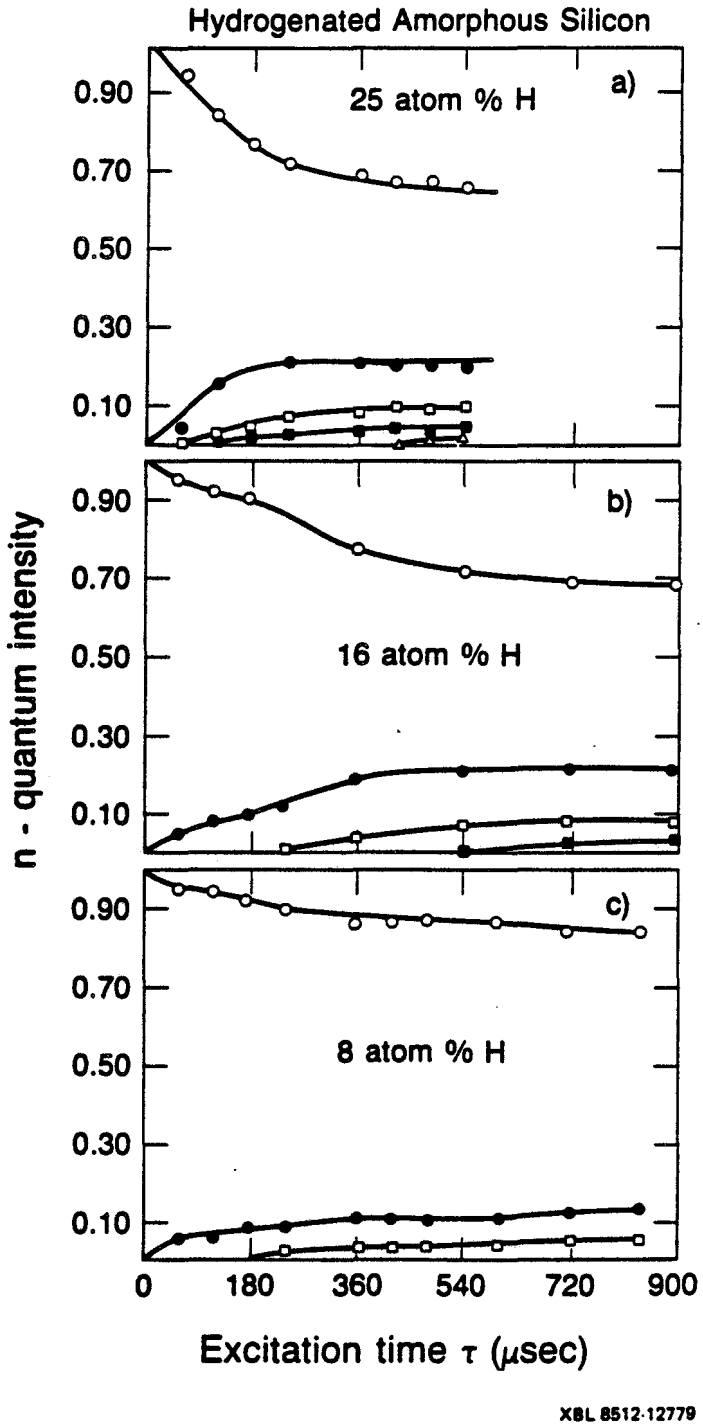

Figure 4.23. n-quantum intensity versus preparation time for hydrogenated amorphous silicon thin films containing a) 25 atom % ^1H; b) 16 atom % ^1H; c) 8 atom % ^1H. As the concentration of hydrogen increases, higher multiple orders develop over a shorter period of time.

Figure 4.24. Number of correlated spins versus preparation time for 50(a), 25(b), 16(c), and 8(d) atom % a-Si:H samples. After an initial induction period, $N(\tau)$ is essentially constant for the 8 atom % sample, remains nearly level up to 250 μs for 16 atom % sample, grows continuously for the 25 atom % sample, and increases very rapidly for the 50 atom % sample. The dashed lines which represent values of $N_c(\tau)$ level off at approximately six for both the 16 and 25 atom % samples. The values of $N(\tau)$ for the 8 atom % sample are very similar to the values of $N_c(\tau)$ for the other two samples. These data indicate that the two device samples (8 and 16 atom %), and the nondevice sample (25 atom %) all contain clusters of approximately six atoms; as the hydrogen concentration is increased, the clusters become closer to one another. In contrast, the polymeric 50 atom % sample is composed of a uniform distribution of spins as evidenced by the growth of both $N(\tau)$ and $N_c(\tau)$.

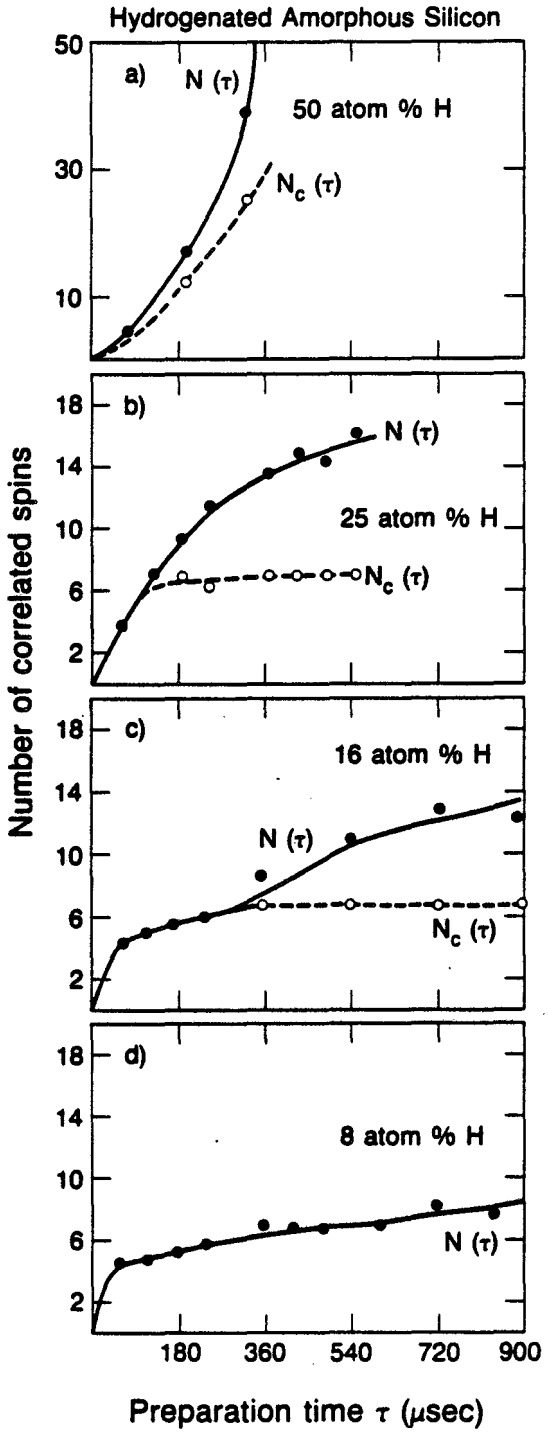

XBL 8511-12715

dramatic. For the 8 at. % device sample, $N(\tau)$ is essentially constant for all times; for the 16 at. % device sample, $N(\tau)$ is nearly level for times up to about 250 μsec, after which it begins to increase and, for the nondevice sample the growth in $N(\tau)$ is continuous. Therefore, what distinguishes one sample from another is that the concentration of clusters increases as the hydrogen concentration is raised. The above results are corroborated by the experiments performed on model compounds with known concentrations of 6 spin clusters. Solid solutions of 1,8 dimethylnaphthalene d_6(ring positions deuterated) in perdeuterated dimethylnaphthalene were prepared and the multiple quantum experiments, done for comparable ^1H concentrations, result in plots of $N(\tau)$ and $N_c(\tau)$ shown in Figure (4.14), that are very similar to those obtained for the a-Si:H samples.

c. Conclusion

In conclusion, by using a time resolved solid state multiple quantum experiment, the extent of ^1H clustering in selected a-Si:H films has been determined. It is found that two device quality films with 8 and 16 atom % ^1H and one nondevice quality film of 25 atom % ^1H all contain clusters of approximately 6 atoms. As the ^1H concentration is increased from 8 to 25 atom %, the multiple quantum experiments indicate that these clusters become physically closer to one another. In contrast, a polymeric sample with 50 atom % ^1H was also investigated and found to consist of a uniform distribution of spins. The geometrical implications of modeling the hydrogen microstructure of a-Si:H with six spin clusters are worth considering. For samples

containing 8, 16, and 25 atom % ^1H, the concentration of cluster defects would be approximately 0.7, 2, and 3.3 "atomic" percent, respectively. If clusters were distributed randomly over a silicon lattice, their average distance from one another would be 14, 10, and 8 Å respectively. This is superimposed on a "random" lattice of isolated monohydride groups with an average spacing of approximately 8 Å. Thus the transition from device quality a-Si:H to nondevice quality (which occurs at roughly 20 atom % ^1H) is seen as increasing the concentration of clusters until their separation roughly equals the separation of dilute monohydride groups. This "lattice saturation" phenomenon may be relevant to electronic structure models based on disorder[21] and quantum well localization.[22]

E. Conclusion

1. Extension of the Multiple-Quantum Experiment in Solids

a. Maintaining a Fixed t_1 Period

In the multiple-quantum experiments described here, the important information is contained in the integrated intensities of the orders rather than in the different spectral frequencies occurring within each order. Therefore, the linewidth is not a necessary component of these experiments. During the t_1 interval of the multiple-quantum experiment, the collectively excited groups of spins evolve in the local dipolar fields of all the other spins. The linewidth or subspectral structure is thus determined during this period. If the t_1 period is kept constant, then each order would appear as an infinitely

sharp line containing the magnitude of the n-quantum coherence.[23] This version of the experiment gives better signal to noise, as the lines are infinitely narrow and is also much shorter, as the number of sampled points is now only (2π/# of detected orders) for a particular preparation time.

A second version of the experiment, which would not only result in the features described above, but would also reveal the integrated intensities versus preparation time all at once, employs the method of parameter proportional phase incrementation.[24] This method was used earlier as a search procedure to select a preparation time which optimizes the intensity of a particular n-quantum order. While the evolution time t_1 is kept fixed, the parameter τ is simultaneously incremented with the phase of the preparation period. The result is an excitation function describing the magnitude of the n-quantum coherence versus preparation time. Therefore, only one experiment would now be needed to obtain the desired intensity information, rather than a set of experiments for different preparation times.

Eliminating the linewidths in the multiple-quantum experiments is reasonable in most cases, although certain materials may require special care. For instance, in hydrogenated amorphous silicon, where the single-quantum linewidth can be decomposed into two resonance lines, it may be important to investigate the multiple-quantum lineshape as well.

b. Scaled Pulse Sequence

One of the problems noted in this chapter concerns the rapid time-

development of the number of correlated spins under the Hamiltonian $1/3(H_{yy}-H_{xx})$. For instance, when the distribution of atoms in the sample is composed of a high concentration of clusters, then inter-cluster correlations may develop too rapidly to resolve the desired intra-cluster interactions. One means by which the size of the cluster can still be ascertained is to approximate the multiple-quantum intensities with the two-Gaussian model.

A second solution is to enhance the time resolution of the experiment by scaling the non-secular Hamiltonian under which the multiple-quantum coherences evolve. Then, the number of correlated spins will develop more slowly and intra-cluster interactions will be more readily distinguished from inter-cluster correlations. The idea behind scaling $(H_{yy}-H_{xx})$ is to "add" a component of $(H_{xx} + H_{yy} + H_{zz})$ to the average dipolar Hamiltonian:

$$\bar{H}_D^{(0)} = a(H_{yy}-H_{xx}) + b(H_{xx} + H_{yy}\ H_{zz}) \quad . \tag{4.6}$$

$H_{yy} - H_{xx}$ is now scaled by $(a/a + b)$ and clearly nothing evolves under $(H_{xx} + H_{yy} + H_{zz})$. A pulse sequence can be constructed by noting first that

$$\bar{H}_D^{(0)} = (b + 2a)\ H_{xx} + bH_{yy} + (b+a)\ H_{zz} \tag{4.7}$$

using $(H_{yy} - H_{xx}) = (H_{zz} + 2H_{xx})$. In addition, we try to obtain $\bar{H}_{\emptyset FF}^{0)} = 0$ and try to symmetrize the sequence with respect to the average

dipolar Hamiltonian. The sequence is designed assuming finite pulse widths.

At this point many pulse sequences can be designed and one in particular is proposed in Figure (4.25). I_z, in the toggling frame, moves between

$$(Z\bar{Y})\ (\bar{Y}X)\ (XY)\ (Y\bar{Z})\ (\bar{Z}\bar{Y})\ (\bar{Y}\bar{X})\ (\bar{X}Y)\ (YZ) \tag{4.8}$$

with delays as indicated. When b = 2a, the calculated average dipolar Hamiltonian is equal to $1/3(H_{yy} - H_{xx})$ as usual; $\bar{H}^{0)}_{QFF} = 0$ and the odd order correction terms to H_D are zero. When b > 2a, $(H_{yy} - H_{xx})$ will be scaled down.

2. Summary

Multiple quantum NMR, a technique which induces spins to act collectively through their dipolar couplings, is used to determine the spatial distribution of atoms in materials lacking long-range order; in particular, the size and extent of clustering is probed. Based on the proximity of spins to one another, correlations between them will develop more or less rapidly. A time-resolved multiple quantum experiment measures both the number of correlated spins and the rate at which these develop. The key feature in the time-dependent experiments is that in clustered materials, where groups are physically isolated from one another, the number of absorbed quanta and correlated spins is essentially bounded, on the experimental time scale, by the size of the cluster. In a uniform distribution, however, the interacting network

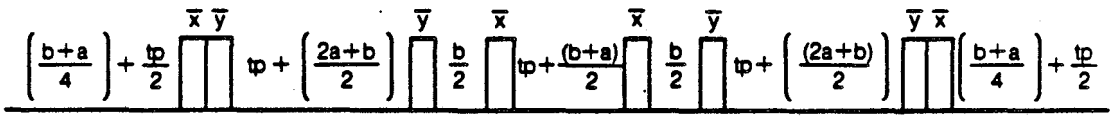

Figure 4.25. Pulse sequence designed to scale (H_{xx} - H_{yy}) by (a/(a + b)). When the multiple-quantum coherences are created under this new Hamiltonian, the number of correlated spins will develop more slowly.

of spins increases monotonically with time. These events are displayed in the multiple quantum spectra by changes in the overall intensity distribution across the mutliple quantum orders. The intensity envelope is quantified by two time-dependent parameters, the effective system size $N(\tau)$ and the effective cluster size $N_c(\tau)$. Thus by studying the trends in $N(\tau)$ and $N_c(\tau)$, i.e. whether they level off or grow with time, we can ascertain the size and extent of clustering in solids.

Model systems containing different hydrogen environments were investigated by this technique: a liquid crystal in which inter-cluster couplings were zero; solid solutions consisting of protonated samples mixed with perdeuterated counterparts in which inter-cluster distances were varied by manipulating the level of dilution; neat protonated polycrystalline solids where inter and intra-cluster dipolar couplings were roughly comparable and hydrogenated amorphous silicon thin films containing different concentrations of hydrogen atoms. The atomic distributions in these materials ranged from truly isolated clusters to uniformly distributed arrangements, with emphasis on the intermediate cases where concentrations of clusters were addressed. These techniques are presently being used to study clustering of molecules adsorbed on zeolites and trapped in silicate glasses.

F. Appendix

To calculate the effective cluster size N_c in Chapter IV, we fit the experimental data to the sum of two gaussians (Equation 4.5)

$$I_n = m_c e^{-n^2/N_c} + m_2 e^{-n^2/N_2} .$$

First, we let I_n = experimentally measured value of the integrated intensity of the nth quantum coherence and I_n^* = predicted value of I_n,

$$I_n^* = \frac{a_1}{\sqrt{b_1}} e^{-n^2/b_1} + \frac{a_2}{\sqrt{b_1}} e^{-n^2/b_2} \qquad (4.9)$$

We want the square error,

$$SE = \sum_n (I_n^* - I_n)^2 , \qquad (4.10)$$

to be a minimum. Therefore, the derivative of the SE with respect to all its predictors should be zero and we try to solve the following four equations simultaneously:

$$\frac{\partial SE}{\partial a_1} = 0 ; \quad \frac{\partial SE}{\partial a_2} = 0 ; \quad \frac{\partial SE}{\partial b_1} = 0 ; \quad \frac{\partial SE}{\partial b_2} = 0 \qquad (4.11)$$

This can be done by Newton's method.[25] More specifically if

$$x_1 = a_1 \; ; \qquad x_2 = b_1 \; ; \qquad x_3 = a_2 \; ; \qquad x_4 = b_2$$

then the four equations are

$$0 = f_j = \frac{\partial(SE)}{\partial x_j} = \sum_n 2(I_n^* - I_n) \frac{\partial I_n^*}{\partial x_j} \tag{4.12}$$

where $1 \leq j \leq 4$. The derivatives needed for Newton's method are

$$\frac{\partial f_j}{\partial x_k} = 2\left[(I_n^* - I_n) \frac{\partial I_n^*}{\partial x_k \partial x_j} + \frac{\partial I_n^*}{\partial x_k} \frac{\partial I_n^*}{\partial x_j} \right] \tag{4.13}$$

The first derivatives are

$$\frac{\partial I_n^*}{\partial a_j} = b_j^{-1/2} e^{-n^2/b_j} \tag{4.14}$$

$$\frac{\partial I_n^*}{\partial b_j} = a_j b_j^{-3/2} e^{-n^2/b_j} \left[\frac{n^2}{b_m} - \frac{1}{2}\right] \tag{4.15}$$

The second derivatives are, for $j \neq k$,

$$\frac{\partial I_n^*}{\partial a_j \partial a_j} = 0 \; ; \quad \frac{\partial I_n^*}{\partial a_j \partial a_k} = 0 \; ; \quad \frac{\partial I_n^*}{\partial a_j \partial b_k} \; ; \quad \frac{\partial I_n^*}{\partial b_k \partial b_j} = 0$$

$$\frac{\partial I_n^*}{\partial a_j \partial b_j} = b_j^{-3/2} e^{-n^2/b_j} \left[\frac{n^2}{b_j} - \frac{1}{2}\right] \tag{4.16}$$

$$\frac{\partial I_n^*}{\partial b_j \partial b_j} = a_j b_j^{-5/2} e^{-n^2/b_j} \left[\frac{n^4}{b_j^2} - \frac{3n^2}{b_j} + \frac{3}{4}\right]$$

The program (written by Karen Gleason) operates as follows:

a) Make a first guess for m_c, N_c, m_2, N_2 and choose NMAX- the maximum number of allowed changes in the four variables before the program ends- and R^2. The first guess is calculated by fitting the integrated intensities of orders n=2 and 4 to a Gaussian of variance N_c with magnitude m_c, and also by independently fitting the intensities of the two highest orders to a Gaussian of variance N_2 with magnitude m_2.

b) Compute the square error (SE).

c) Compare (SE/VAR) < $(1-R^2)$

or NLOOP > NMAX

d) If the compare statement is yes, then the program is done. If not, then m_c, N_c, m_2 and N_2 are changed by Newton's method the loop counter NLOOP is incremented by 1 and the new SE is calculated.

It is interesting to comment on the fit of the data to both the single Gaussian, to obtain N, and to the two-Gaussian model to obtain N_c. For uniform distributions (adamantane, squaric acid) the fit to a single Gaussian was generally quite good - R^2 was usually 0.99. For

totally isolated clusters (liquid crystal) the value of R^2 was excellent, usually 0.999. When concentrations of clusters existed as in 1,8-dimethylnaphtalene-d_6, hexamethylbenzene, or amorphous silicon hydride then the fit to a single Gaussian was worse, sometimes as low as 0.92. Here, the two-Gaussian model was used and R^2 was generally 0.98-0.99.

What these numbers seem to indicate is that when the size of the cluster is well-defined at any particular preparation time, then the data can be fit to a single Gaussian. This appears to be the case for uniform distributions, where the size increases monotonically with time, and for truly isolated clusters. For concentrations of clusters the idea was the following: when clusters interact with other clusters, then the intensities are approximated by two independent events. The first is the correlation between spins within a cluster. For the second event the idea is to "redefine" the system by saying that the spins within the cluster are defined as a single spin and that different clusters or "spins" now interact with one another. This second set of interacting "spins" will have a size N_2. Now two sizes can be stipulated: one is the actual size of the cluster and the other is the size of the interacting "spins", N_2, which can perhaps be thought of as a fudge factor. If clusters were not interacting with one another, then the sum of two Gaussians could be used to determine the distribution of clusters present in the system. In this case though, the dynamics are more complicated as clusters are interacting. But assuming that $m_c > m_2$ and that the fit to the two Gaussian model is good, then although cluster size distributions may exist, they occur in low concentrations.

G. References

1. Semiconductors and Semimetals, Hydrogenated Amorphous Silicon, Volume 21, edited by J.I. Pancove (Academic Press, Orlando, 1984).

2. J. Baum, M. Munowitz, A.N. Garroway, and A. Pines, J. Chem. Phys. **83**, 2015-2025 (1985).

3. J. Baum, K.K. Gleason, A. Pines, A.N. Garroway, and J.A. Reimer, submitted to Phys. Rev. Lett.

4. J. Baum and A. Pines, J. Am. Chem. Soc. submitted.

5. P.K. Wang, C.P. Slichter, and J.H. Sinfelt Phys. Rev. Lett. **53**, 82 (1984).

6. a) G. Bodenhausen, Prog. NMR Spectrosc. **14**, 137 (1981).
   b) D.P. Weitekamp, Adv. Magn. Reson. **11**, 111 (1983).
   c) M. Munowitz and A. Pines, Adv. Chem. Phys., in press.

7. W.S. Warren, D.P. Weitekamp, and A. Pines, J. Chem. Phys. **73**, 2084 (1980).

8. a) G. Drobny, A. Pines, S. Sinton, D.P. Weitekamp, and D. Wemmer, Faraday Symp. Chem. Soc. **13**, 49 (1979).
   b) G. Bodenhausen, R.L. Vold, and R.R. Vold, J. Magn. Reson. **37** 93 (1980).

9. a) R.H. Schneider and H. Schmiedel, Phys. Lett. **A 30**, 298 (1969).
   b) W.K. Rhim, A. Pines, and J.S. Waugh, Phys. Rev. Lett. **25**, 218 (1970).
   c) W.K. Rhim, A. Pines, and J.S. Waugh, Phys. Rev. B. **3**, 684 (1971).
   d) A. Pines, W.K. Rhim, and J.S. Waugh, J. Magn. Reson. **6**, 457 (1972).

10. J.B. Murdoch, W.S. Warren, D.P. Weitekamp, and A. Pines, J. Magn. Reson. **60**, 205 (1984).

11. a) A. Wokaun and R.R. Ernst, Mol. Phys. **36**, 317 (1978)
    b) R.A. Hoffman, Adv. Magn. Reson. **4**, 87 (1970).

12. W. Nowacki, Helv. Chim. Acta **28**, 1233 (1945).

13. a) D. Semmingsen and J. Feder, Solid State Commun. **15**, 1369 (1974).
    b) E.J. Samuelson and D. Semmingsen, ibid. **17**, 217 (1975).

14. P.G. De Gennes, The Physics of Liquid Crystals (Clarendon Press, Oxford, 1974).

15. D. Bright, I.E. Maxwell, and J. de Boer, J. Chem. Soc. Perkin Trans. II, 2101 (1973).

16. R.W.C. Wyckoff, Crystal Structures (Interscience New York, 1966), Vol. 6, Part 1, p. 386.

17. a) E.R. Andrew, J. Chem. Phys. **18**, 607 (1950).
b) D.E. Wemmer, Ph.D. thesis, University of California, Berkeley, 1978, pp. 38-43 (published as Lawrence Berkeley Laboratory Report LBL-16119).

18. D.B. Zax, A. Bielecki, K.W. Zilm, A. Pines, and D.P. Weitekamp, J. Chem. Phys. **83**, 4877 (1985).

19. a) P.C. Taylor, Semiconductors and Semimetals, Hydrogenated Amorphous Silicon, Volume 21, Part C., pg. 99.

20. J.A. Reimer, R.W. Vaughan, and J.C. Knights, Phys. Rev. Lett. **44**, 193 (1980).

21. G.D. Cody, T. Tiedje, B. Adeles, B. Brooks, and Y. Goldstein, Phys. Rev. Lett. **47**, 1480 (1981).

22. M.H. Brodsky, Solid State Commun. **36**, 55 (1980).

23. a) S. Emid, Physica. **128B**, 79 (1985).
b) A.N. Garroway, private communication.

24. D.P. Weitekamp, J.R. Garbow, and A. Pines, J. Magn. Reson. **46**, 529 (1982).

25. a) L.W. Johnson and R.D. Riess, Numerical Analysis, Addison-Wesley Publishing Company, 1977.
b) C.J. King, Separation Processes, Chemical Engineering Series, McGraw Hill Book Company, 1980.

V. APPLICATIONS OF COMPOSITE PULSES AND MULTIPLE-QUANTUM METHODS TO SPATIAL LOCALIZATION AND IMAGING

A. Spatially Selective NMR with Broadband Radiofrequency Pulses

1. Introduction

It is often useful in many areas of chemistry to be able to obtain spectroscopic information from a localized region of a sample noninvasively. Spatial localization is desirable in a number of systems, ranging from heterogeneous solids such as coals, catalysts and semiconductors to living tissues and organisms. For example, the elucidation of the action of a catalyst may be aided considerably by restricting observed signals to those originating from the surface layer alone, eliminating the otherwise overwhelming contribution from the bulk. The need for spatial localization is also felt keenly in *in vivo* NMR and magnetic resonance imaging, where signal frequently must be obtained from a selected organ without interference from surrounding tissues. Thus spatially selective excitation, which can be directed at specific sites in a heterogeneous system and which can yield accurate chemical information from these sites, is a highly desirable goal for spectroscopy in general and NMR in particular.

In a recent Communication[1], Tycko and Pines introduced a technique designed to localize NMR signals in space by combining the radio-frequency (rf) gradient of a surface coil[2] with an excitation sequence narrowband in rf field strength.[3-6] The excitation sequence is a variant of a composite π pulse[7] that inverts spin populations

only within a small range of rf field amplitudes. This chapter enlarges upon the earlier work in three important areas.[8] First, a pulse sequence is suggested that has the required narrowband properties with respect to the rf amplitude but at the same time uniformly excites over a substantial range of resonant frequencies. This allows the technique to be used in situations where the observed signals span a large chemical shift range, without requiring unreasonably high rf power. Second, experimental results on a phantom sample and using a surface coil are given to demonstrate both the degree of spatial localization that may be achieved and the chemical shift range that may be covered. Third, we present a brief discussion of the relationship of our method to spatial localization methods proposed by other authors, with the intent of pointing out the experimental conditions under which different techniques may be preferred.

2. Development of Pulse Sequences

a. Narrowband Localized Excitation (NOBLE).

A NOBLE pulse sequence is comprised of two parts.[1] The first is a narrowband inversion sequence P, which inverts spin populations in a narrow range of rf amplitudes centered about a nominal value ω_1^0(rad/sec). The second is a read sequence R, which in the simplest case may be single pulse. The free induction decay (FID) after applying P and R in succession is subtracted from the FID after R alone. The remaining signal arises only from those regions in space where P inverts spins and R excites signal. Signal contributions due to residual transverse magnetization created by P are eliminated either by

dephasing in a delay between P and R or by phase cycling of P. Dephasing may result from an applied pulsed static field gradient, or from transverse relaxation if $T_2 < T_1$.

This method leads to very simple expressions for the signal amplitude and phase. Suppose that P produces an inversion $W(\omega_1,\Delta\omega)$ at an rf amplitude ω_1 and a resonance offset $\Delta\omega$, where W is defined as usual [1,3-7] to run between -1 and 1, with -1 indicating equilibrium spin populations and 1 indicating complete population inversion. In addition, suppose that R excites transverse magnetization with an amplitude $A(\omega_1,\Delta\omega)$ and a phase $\phi(\omega_1,\Delta\omega)$. Then the signal amplitude is proportional to $S(\omega_1,\Delta\omega)$, given by

$$S(\omega_1,\Delta\omega) = [1 + W(\omega_1,\Delta\omega)]\ A(\omega_1,\Delta\omega) \tag{5.1}$$

and the signal phase is $\phi(\omega_1,\Delta\omega)$. An additional factor of ω_1 would be present in Equation (5.1), arising from the detection efficiency, if the same surface coil were used for both excitation and detection.[9] The fact that the signal phase depends only on R is significant. In general, the direction of the net rotation axis of P, loosely speaking the "phase" of P, changes considerably with ω_1. If the signal phase were to depend on the phase of P, contributions to the total acquired signal with different values of ω_1 and the same value of $\Delta\omega$ could interfere destructively.[10] Thus, a loss of sensitivity would result. NOBLE avoids this problem, since only the inversion produced by P and not the phase plays a role.

b. Selective Inversion Sequences

There remains considerable flexibility in the choice of specific sequences for P and R, subject to the constraint that the duration of the sequences must be short compared to T_1 and T_2. Narrowband sequences have been derived using iterative schemes by our laboratory[3,4] and by Shaka and Freeman.[5] The iterative schemes can generate pulse sequences with arbitrarily small bandwidths in ω_1. Typically, however, the bandwidths in $\Delta\omega$ are also small, i.e. $W(\omega_1,\Delta\omega)$ is a strong function of $\Delta\omega$ as well as ω_1. Using fixed point methods, some progress has been made towards the development of iterative schemes for generating inversion sequences that are narrowband with respect to ω_1 and broadband with respect to $\Delta\omega$.[4] For the present purpose, however, we programmed a computer to search for sequences that meet given bandwidth criteria. It was found that less than nine pulses do not meet the inversion profile requirements over both ω_1 and $\Delta\omega$. Therefore, in a typical search, the program examines all pulse sequences composed of nine pulses with nominal flip angles of 180° and with the individual phases in multiples of 15°. The desired values of $W(\omega_1,\Delta\omega)$ are specified for 26 combinations of ω_1 and $\Delta\omega$. The actual values of $W(\omega_1,\Delta\omega)$ are calculated for each possible sequence. The sequence with the smallest variance between the actual $W(\omega_1,\Delta\omega)$ values and the desired $W(\omega_1,\Delta\omega)$ values is selected. Only sequences with symmetric phases are considered, reducing the number of sequences that must be tested and eliminating the need to examine both positive and negative values of $\Delta\omega$.[11] Once a sequence is found, it can be refined by changing the pulse phases in 5° increment. Simulations

indicate that phase errors within 5° of the nominal phase do not appreciably alter the inversion profiles, therefore further refinement of the pulse phases is not necessary.

The sequence $180_{30}180_{205}180_{230}180_{85}180_{0}180_{85}180_{230}180_{205}180_{30}$, which we denote P_0, results from such a search procedure. The contour plot in Figure (5.1.) illustrates the inversion performance. According to Equation (5.1), P_0 allows the signal amplitude at $\omega_1 = \omega_1^0$ to be greater than 75% of its maximum for all resonance offsets in the range $-0.3\omega_1^0 < \Delta\omega < 0.3\omega_1^0$. Significant signal at undesired values of ω_1 can only develop when $|\Delta\omega| > 0.3\omega_1^0$.

c. Read Sequences.

Any sequence composed of an odd number of nominal 180° pulses such as P_0, will invert spin populations when ω_1 is any odd multiple of ω_1^0. Thus large signal contributions may arise from regions in space where ω_1 is approximately an odd multiple of ω_1^0 in addition to the desired region where ω_1 is approximately equal to ω_1^0. In reference 1, Tycko and Pines suggested using a single nominal 60° pulse for R. A nominal 60° pulse becomes a 180° pulse at $\omega_1 = 3\omega_1^0$, making $A(3\omega_1^0,0) = 0$. Bendall has demonstrated the same approach for suppressing high flux signals with depth pulses.[12,13] In Figure (5.2a), we show a plot of $S(\omega_1,0)$ for NOBLE using P_0 and a nominal 60° pulse for R. Although $S(3\omega_1^0,0) = 0$, there is substantial signal on either side of $3\omega_1^0$. Signals on opposite sides of $3\omega_1^0$ have opposite phases so that partial cancellation may be expected, but the suppression is not ideal. The signal at ω_1^0 is reduced from its maximum factor of $\sqrt{3}/2$,

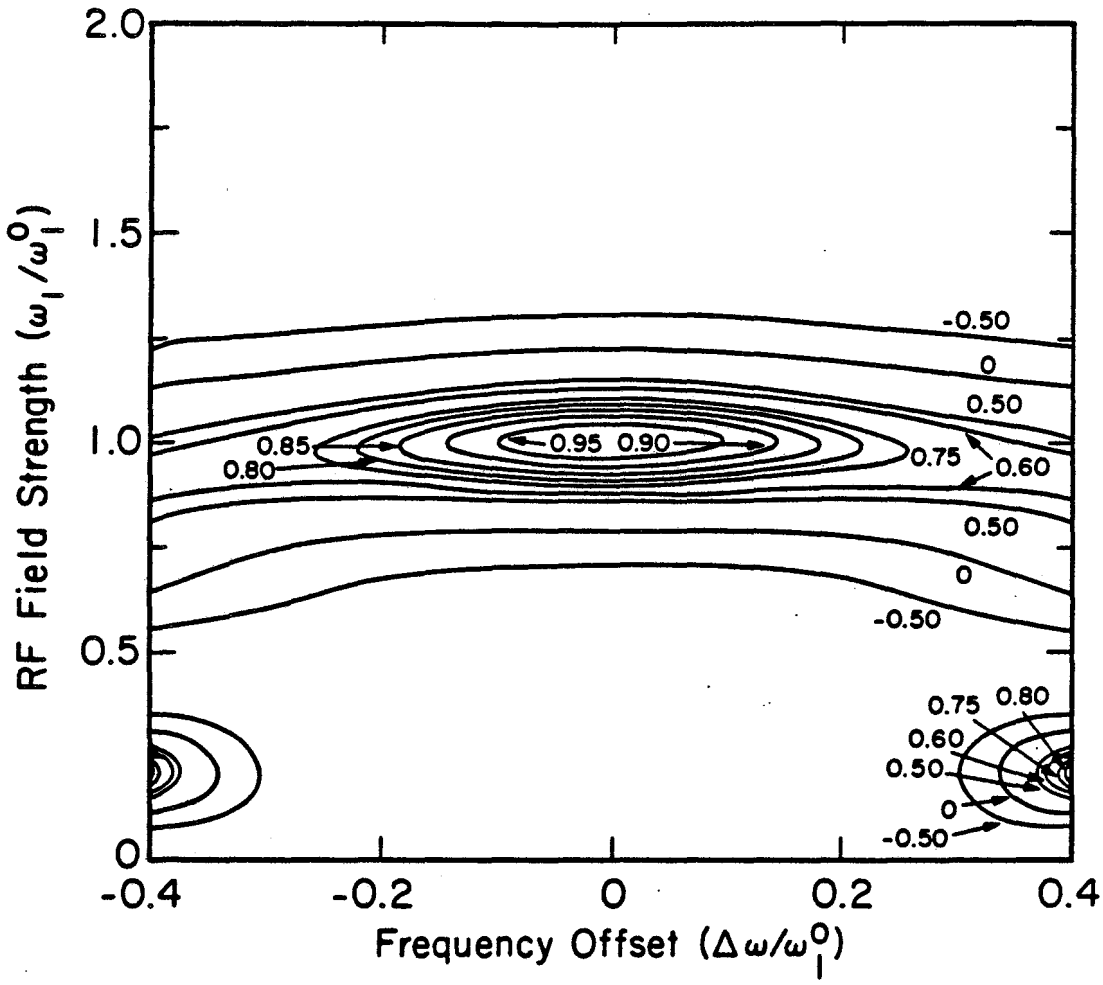

XBL 855-2638

Figure 5.1. Contour plot of inversion performance versus resonance offset ($\Delta\omega/\omega_1^0$) and rf field strength (ω_1/ω_1^0) for the composite pulse sequence P_0: $180_{30}180_{205}180_{230}180_{85}180_{0}180_{85}180_{230}180_{205}180_{30}$. Each pulse is specified by two angles, θ_ϕ, where θ denotes the flip angle and ϕ the phase. P_0 produces narrowband inversion with respect to ω_1 and broadband inversion with respect to $\Delta\omega$.

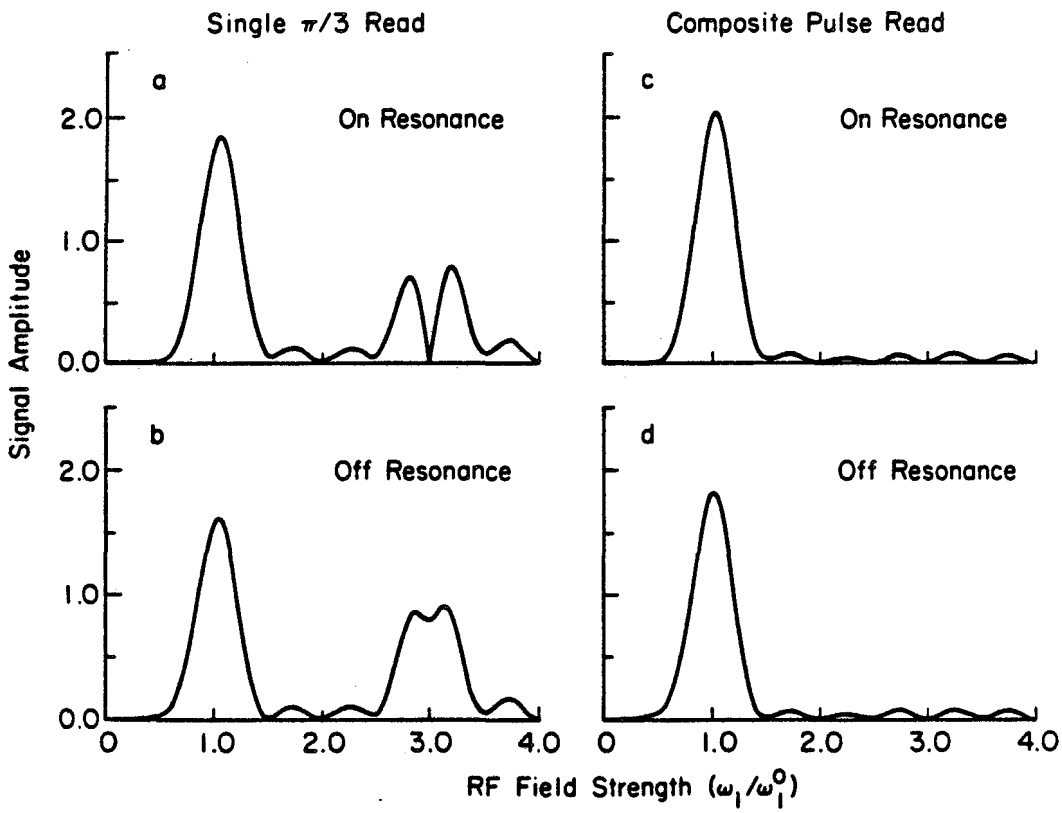

Figure 5.2. Simulations of NOBLE signal amplitude $S(\omega_1, \Delta\omega)$ with the inversion pulse P_0, as specified in Figure (5.1), and various read sequences R:

a) $S(\omega_1, 0)$ for $R = \pi/3$

b) $S(\omega_1, 0.2\omega_1^0)$ for $R = \pi/3$

c) $S(\omega_1, 0)$ for $R_0 = 90_{180}120_{0}30_{90}90_{270}120_{90}30_{0}$

d) $S(\omega_1, 0.2\omega_1^0)$ for $R_0 = 90_{180}120_{0}30_{90}90_{270}120_{90}30_{0}$

An additional factor of ω_1 arising from the detection efficiency with a surface coil is included. The read sequence R_0 of (c) and (d) effectively eliminates the signals from the $3\omega_1^0$ region while maintaining almost maximum intensity in the ω_1^0 region.

since it is excited by a 60° pulse rather than a 90° pulse. In addition, as can be seen in Figure (5.2b), a 60° pulse is not broadband over the desired range of frequency offsets.

A better choice for R would have the following three properties. First, it would be a broadband inversion sequence near $3\omega_1^0$, inverting spins and exciting no signal over large ranges of both ω_1 and $\Delta\omega$. Second, it would excite nearly the maximum signal at $\omega_1 = \omega_1^0$. A sequence that has these properties is $90_{180}120_{0}30_{90}90_{270}120_{90}30_{0}$, which we denote R_0. R_0 is derived from the composite π pulse $270_{180}360_{0}90_{90}270_{270}360_{90}90_{0}$ developed by Shaka and Freeman,[14] simply by dividing all pulse lengths by three. That R_0 has the first property above is a consequence of the work of Shaka and Freeman;[14] that it has the other two properties might be coincidental. Figures (5.2c), and (5.2d) are plots of $S(\omega_1,\Delta\omega)$ for NOBLE using P_0 and R_0. The selectivity with respect to ω_1 and the useful range of $\Delta\omega$ are illustrated; the signal profile is essentially identical between $\Delta\omega = 0$ and $\Delta\omega = 0.2$.

At this point, we stress that other choices for P and R are possible. P_0 and R_0 were selected principally to provide a large bandwidth in $\Delta\omega$ and to eliminate signal contributions from the $3\omega_1^0$ region. Other considerations may require different sequences, for example a P with a narrower bandwidth in ω_1 in order to produce finer spatial resolution.[1,3-5] Read sequences that do not excite signal at higher multiples of ω_1, e.g. both $3\omega_1^0$ and $5\omega_1^0$, can be found.

A potentially important possibility is the use of an adiabatic frequency sweep[15] or an equivalent phase modulated pulse[16-18] as the

read sequence. Adiabatic sweeps discussed in Chapter II can invert spins essentially completely for arbitrarily large values of ω_1 above a threshold ω_1^t that depends on the sweep rate.[17,18] Below ω_1^t, the conditions for adiabaticity[18] are not satisfied and transverse magnetization is created. Thus by placing the threshold between ω_1^0 and $3\omega_1^0$, all contributions to the signal except those near ω_1^0 could be eliminated. In addition, if the fine spatial resolution afforded by P is not required, an adiabatic sweep could be used alone. This would be an entirely new approach to spatial localization.

3. Experimental Demonstration of NOBLE

a. Experimental Design

Experiments were performed at 180 MHz on a phantom sample of $H_2O(\ell)$ using a three turn surface coil. The configuration of the sample and coil is shown in Figure (5.3a). The sample consists of a 10 mm long section of delrin rod with a diameter of 4 mm, into which five holes have been drilled with a spacing of 2.0 mm. The holes are filled with $H_2O(\ell)$ and are labelled as positions 1 through 5 in order of increasing distance from the plane of the coil. The coil diameter is 1.5 cm. To provide a one-dimensional image of the sample, a pulsed field gradient of approximately 1.14 Gcm^{-1} is applied along the long axis of the sample. Figure (5.3b) is a one-dimensional image of the phantom sample obtained by giving a single pulse and Fourier transforming the ensuing FID. Signals from positions 1 through 5 are clearly distinguished. The decrease in signal intensity with increasing number is a consequence of both the smaller pulse flip angle and

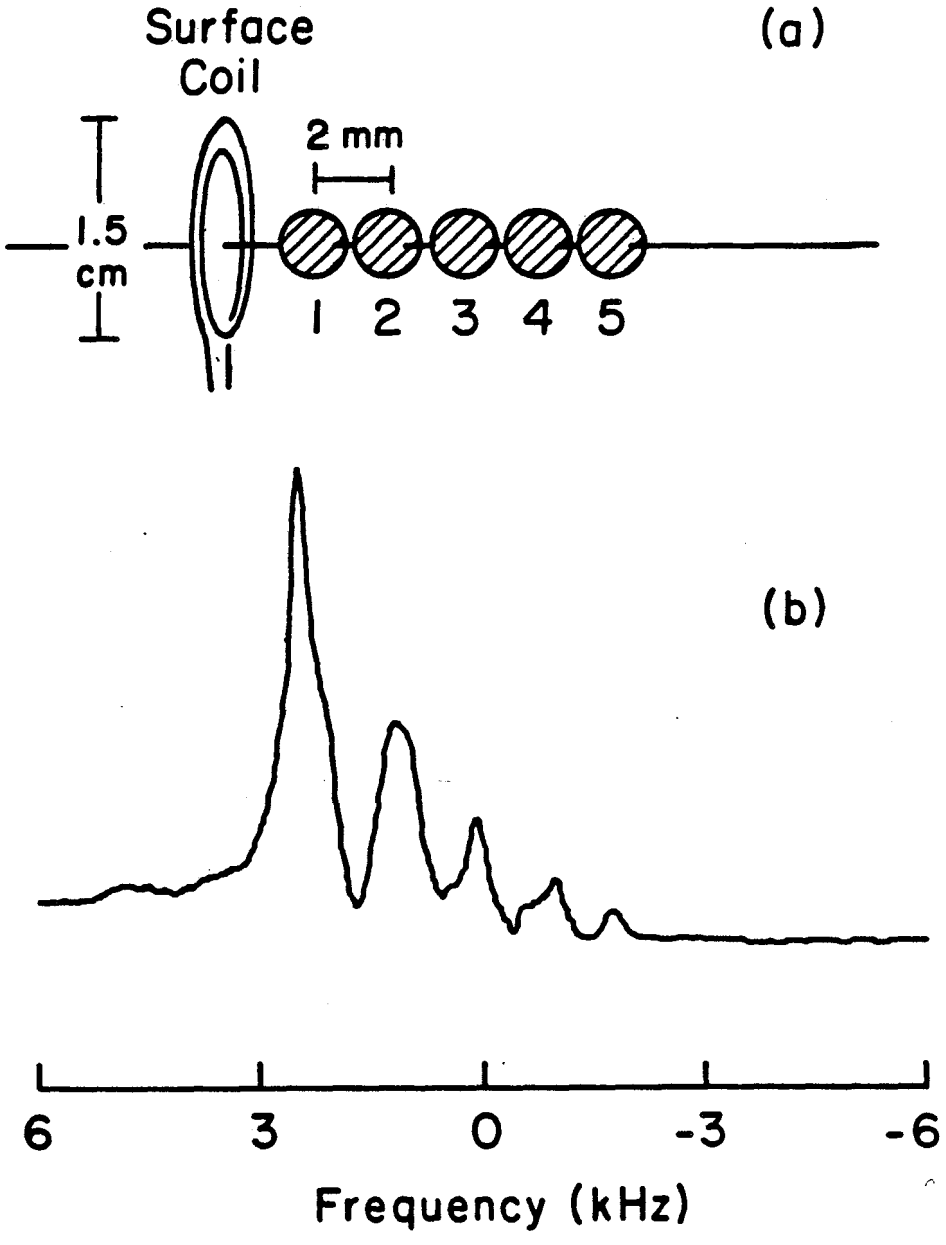

XBL 855-2640

Figure 5.3. Top: Surface coil and sample geometry.
The sample consists of a delrin rod (4mm diameter) containing 5 small holes filled with $H_2O(\ell)$.
Bottom: ^1H spectrum of the phantom sample recorded after a $\pi/2$ pulse at position 1. A static field gradient is used to obtain the one dimensional image.

the reduced detection efficiency with increasing distance from the surface coil. The value of $\omega_1/2\pi$ at each position was determined by adjusting the pulse length so as to produce a null of the signal. In order of increasing position number, the values are 33, 21, 12.5, 7.9 and 4.9 kHz. The experimental timing sequence is shown is Figure (5.4). The static field gradient serves only to allow a direct visualization of the spatial distribution of signal contributions for demonstration purposes and, less importantly, to cause transverse magnetization to dephase during τ in Figure (5.4). The static field gradient is not a relevant component of the spatial selectivity of NOBLE.

b. Experimental Results

Figure (5.5) illustrates the degree of spatial localization resulting from NOBLE. Figure (5.5a) is the image resulting from excitation by R_0; Figure (5.5b) is the image resulting from excitation by R_0 after inversion by P_0. The pulse lengths are adjusted to the rf amplitude at position 3, i.e. ω_1^0 = 12.5 kHz. Figure (5.5c) is the difference of Figures (5.5a) and (5.5b). Appreciable signal remains at position 3 only.

The resonance offset range of the P_0 and R_0 sequences is demonstrated in Figure (5.6). NOBLE is applied with the pulse lengths adjusted to localize the signal to position 3. Without changing the pulse lengths, the rf carrier frequency is changed in increments of 1000 Hz. Good localization is preserved up to resonance offsets of 3000 Hz, or $\omega/\omega^0{}_1$ = 0.24.

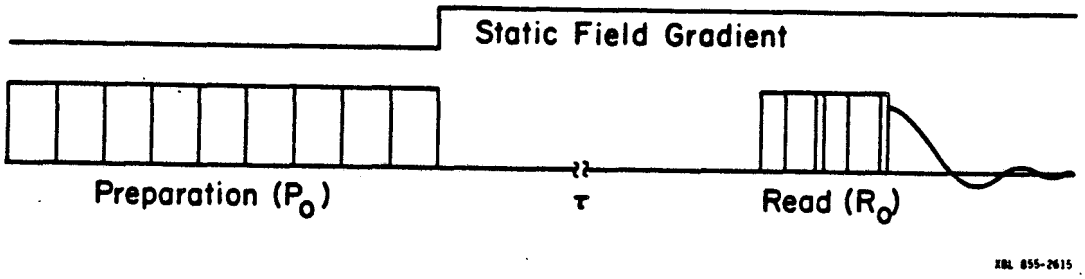

Figure 5.4. Experimental timing diagram. The selective inversion pulse, P_0, shown in Figure (5.1) is followed by a period τ, during which transverse magnetization is allowed to dephase. The free induction decay is recorded following the read pulse, R_0, of Figure (5.2c). A pulsed static field gradient along the long axis is used to provide the one dimensional image of the phantom containing $H_2O(\ell)$. The NOBLE experiment is performed by subtracting the inverted signal from the FID obtained after R_0 alone. The signal that results when the pulses are applied with a surface coil arises only from a localized region in space.

Figure 5.5. ^{1}H spectra obtained according to the NOBLE method for the phantom water sample shown. Pulse lengths were calibrated with reference to the nominal rf amplitude, ω_1^0 = 12.5 kHz, existing at position 3.

a) $R_0 = 90_{180}120_{0}30_{90}90_{270}120_{90}30_{0}$. The spectrum contains signals from all five bulbs.

b) Spectrum read by R_0 following a spatially selective inversion pulse, $P_0 = 180_{30}180_{205}180_{230}180_{85}180_{0}180_{85}180_{230}180_{205}180_{30}$, adjusted for bulb 3.

c) Difference spectrum obtained by subtracting b) from a). Only signal from position 3 is retained in this spatially localized spectrum.

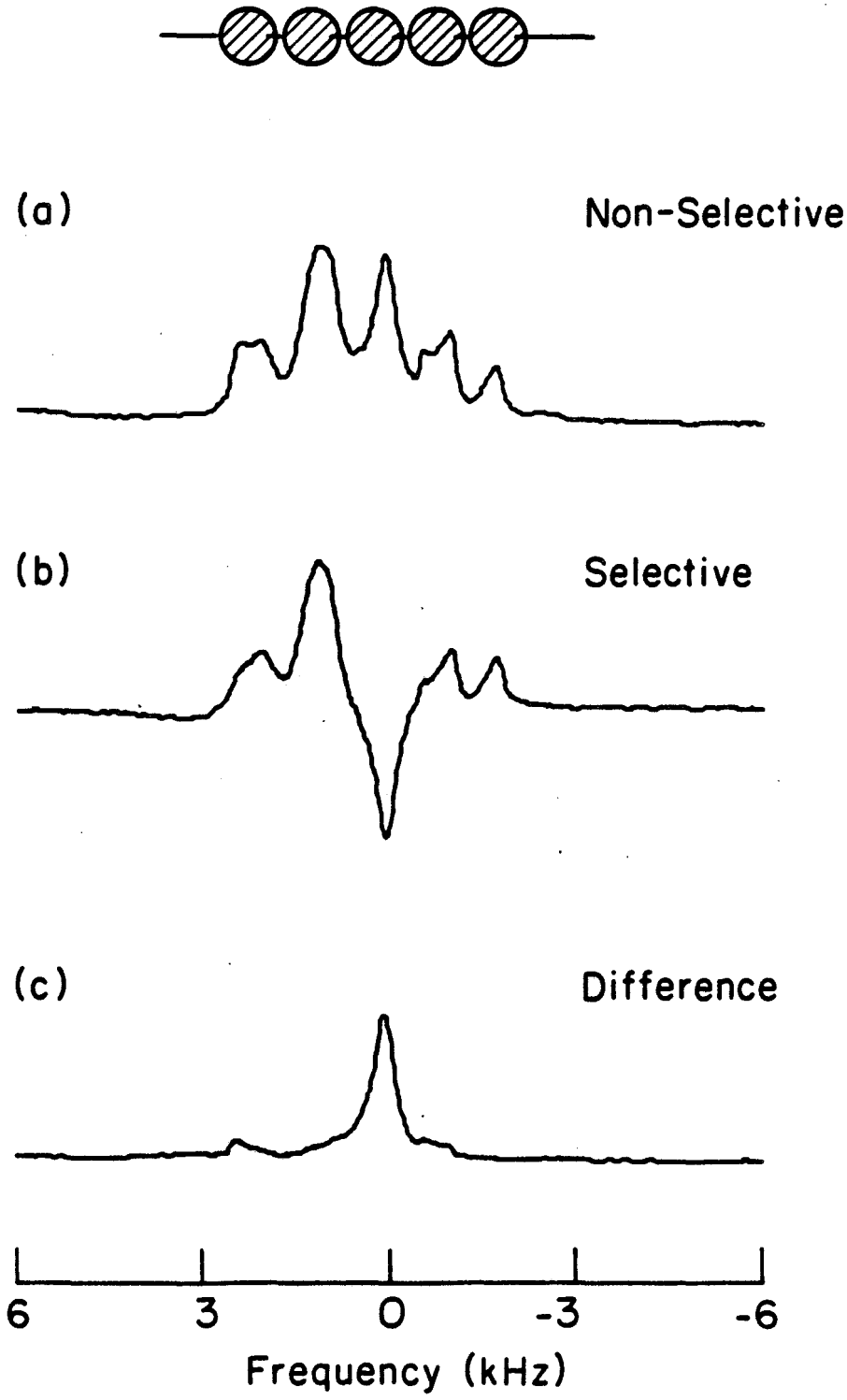
(a)
Non-Selective
(b)
Selective
(c)
Difference
6
3
0
-3
-6
Frequency (kHz)

XBL 855-2641

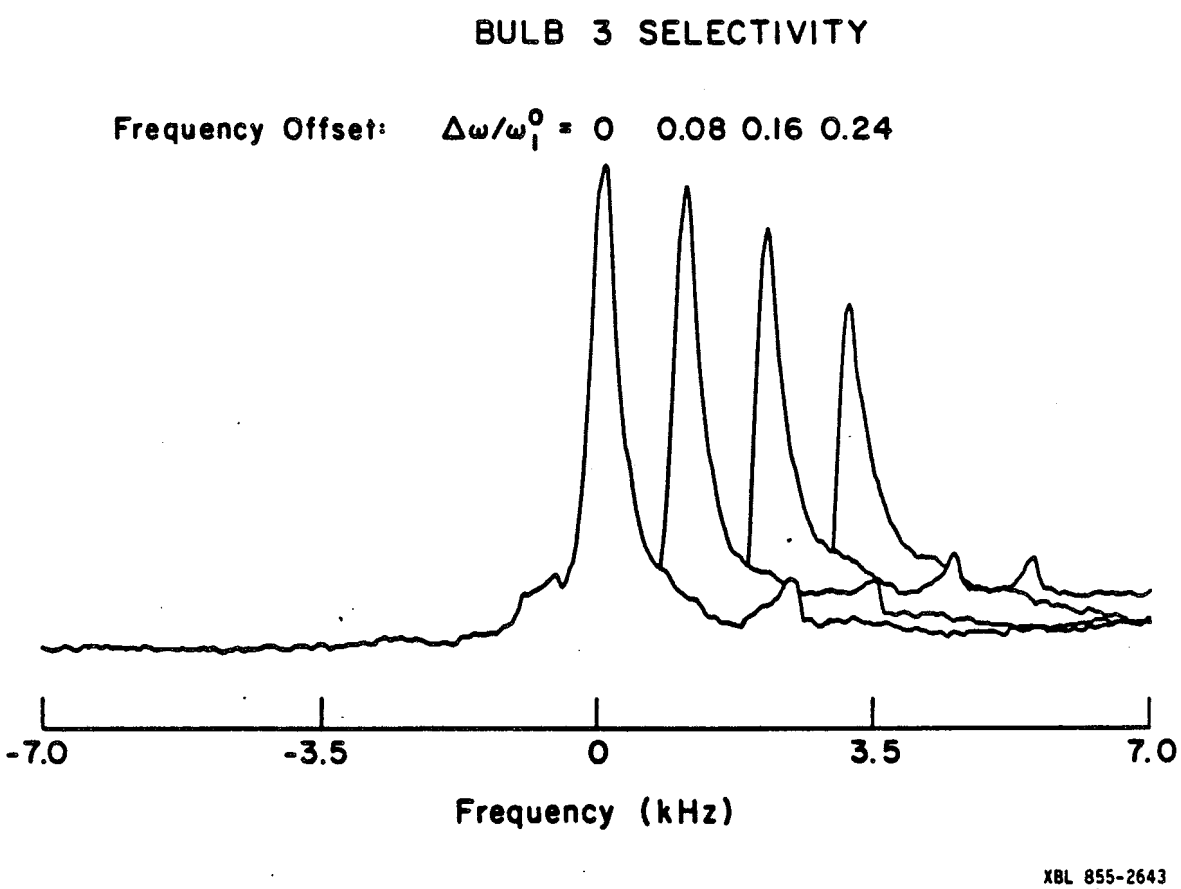

Figure 5.6. Stacked plot illustrating the broadband properties of the composite inversion pulse with respect to resonance offset. Each peak is a spatially localized signal from bulb 3, obtained under NOBLE with frequency offset as marked. Spatial selectivity is achieved successfully up to a frequency offset of approximately 25% of the nominal rf amplitude.

4. Discussion of Spatial Localization Methods

Various methods for spatially localizing NMR signals, with the preservation of spectral information, have been developed. Some of these rely on static field gradients,[19-30] some rely on rf field gradients,[1,5-6,12-13,31-40] and some rely on a combination of the two.[12,41] Methods that rely on static field gradients have the advantage that signals can in principle be localized to a well-restricted sensitive volume, for example a cube. They have the disadvantage that pulsed gradients in three independent directions are required for localization in three dimensions. Methods that rely on rf field gradients have the advantage of comparative simplicity, insofar as probe or magnet design is concerned, and can exploit the sensitivity advantage and partial localization inherent in surface coils.[2,42] The major disadvantage of rf gradient methods, including NOBLE, is the diffuse sensitive volume, as determined by the shapes of surfaces of constant transverse rf fields. Spatial localization achieved by the selection of a particular value of the of the B_1 field is not necessarily restricted to a point on the axis of the surface coil but will also occur along the transverse component of the rf field. This results in a sensitive volume whose shape is defined by the rf field profile of the surface coil. This disadvantage can be overcome to an extent by alternative coil geometries,[43] multiple excitation coils,[37] separate excitation and detection coils,[35] and the combination of rf and static field gradients.[12,41]

For the present discussion, we limit ourselves to rf gradient

methods. In addition to NOBLE, there are two other techniques that have been developed to date to acquire NMR signals only from a limited spatial region in an rf gradient. One of these, that of Shaka et al.,[5,6] also makes use of narrowband inversion sequences. Signals from outside the region of interest are eliminated in a phase cycling scheme involving the coaddition of four[5] or sixteen[6] FID signals. Provided that the same inversion sequence is used, the sensitive volumes of NOBLE and the four step version of Shaka et al. are the same. The latter method is susceptible to destructive interference within the sensitive volume arising from phase variations in the inversion sequence as discussed above. Whether this proves to be a significant distinction in practice is determined by the choice of the inversion sequence and by the signal distribution within the sensitive volume. The sequence $180_0 180_{270} 180_{180}$ demonstrated by Shaka et al.[6] produces no phase variations on resonance, a consequence of the antisymmetric rf phases of such sequences.

Shaka and Freeman have also described another method designed to function over a large range of resonance offsets.[40] Here, composite prepulses, broadband in both $\Delta\omega$ and ω_1, are incorporated into phase cycling schemes in order to achieve the desired localization. As more prepulses are applied, the ω_1 profile becomes progressively narrower. The best signal profile, which covers a large range of resonance offsets and is narrowband in rf field strength, arises from a 24 stage scheme containing three prepulses. The phase of the signal is well behaved with this method.

The second technique is the depth pulse method of Bendall et

al.[12-13,34-39] Depth pulse sequences all consist of strings of pulses combined with specific phase cycling schemes. The pulses themselves do not possess narrowband properties. Rather, the sensitivity to the rf amplitude results from the extensive phase cycling, which cancels signals from undesired spatial regions. Thus, the depth pulse method is conceptually quite different from NOBLE, arising out of the phase cycling tradition in NMR rather than the more recent composite pulse tradition.[7]

Depth pulse sequences that provide localization in the vicinity of $\omega_1 = \omega_1^0$ similar to that in Figure (5.2) require the coaddition of 16 or more FID signals.[13] Procedures for eliminating signal from the $3\omega_1^0$ and $5\omega_1^0$ regions have been suggested, and require 32 and 64 FIDS respectively.[12] The useful resonance offset ranges of the depth pulse sequences are similar to that exhibited using P_0 and R_0.

We expect NOBLE, when combined with a suitable inversion pulse, to be useful under a number of relevant experimental conditions. First consider a situation in which the intrinsic signal to noise ratio is high and in which time is limited. In this case, NOBLE offers the advantage of good time resolution. In addition to the requirement of fewer FID signals, NOBLE can be repeated with an arbitrarily short recycle delay without appreciable degradation of the spatial selectivity. This is because the longitudinal magnetization before each shot in the undesired spatial regions is a constant, independent of the pulse phases in the previous shot, once a steady state is reached. Rapid pulsing can lead to a greater signal to noise ratio in a fixed time.

Another important limit is an experiment with a low intrinsic signal to noise ratio and with no time constraint. In such an experiment, none of the techniques has an overriding, intrinsic advantage. A decision is likely to be made on the basis of experimental convenience. The use of separate excitation and detection coils,[35] and the use of multiple excitation coils to restrict the sensitive volume have been developed for depth pulses by Bendall et al.[37] Ideally, these ingenious multiple coil experiments could be combined with the selectivity of NOBLE.

An alternative for experiments in which considerable signal averaging is permitted or required is to use a rotating frame chemical shift imaging (RFCSI) technique.[31-33] Briefly, a two-dimensional RFCSI experiment consists of collecting a series of FIDS, acquired in the intervals labelled by t_2, following excitation by a pulse of variable length t_1, from a surface coil or other source of an inhomogeneous rf field. A double Fourier transform yields a two-dimensional "spectrum" with spectral information along one axis and rf strength, i.e. distance, information along the other axis. RFCSI clearly differs from NOBLE and depth pulse sequences in that signal from all spatial regions is preserved but is separated by the Fourier transformation with respect to t_1. In order to achieve a spatial resolution and extent comparable to that in Figures (5.2) and (5.5), a minimum of approximately 16 values of t_1 would have to be sampled. Thus the minimum time for an RFCSI experiment is comparable to that of a depth pulse experiment, but is eight times greater than that of a NOBLE experiment. The signal to noise ratio in an RFCSI spectrum is expected

to be less than that in a depth pulse or NOBLE spectrum by a factor on the order of $\sqrt{2}$ for a fixed total number of acquired FIDS.[31] However, spectral information from all spatial regions is acquired at once, making for greater efficiency if such information is desired. In a sense, the relationship of RFCSI to depth pulses and NOBLE is analogous to the relationship of sensitive line methods to sensitive point methods, as explained in discussions of NMR imaging.[44-46]

5. Conclusion

a. Composite $\pi/2$ Pulses

A composite $\pi/2$ pulse sequence narrowband in frequency and broadband in resonance offset would eliminate the need for a difference technique entirely. Progress has been made towards developing $\pi/2$ pulse sequences which are narrowband in ω_1 by using iterative schemes with two fixed points.[47,48] When the initial sequence $(37.5)_{90}$ $(37.5)_0$ $(37.5)_{90}$ is iterated with the scheme [0, 15, 180, 165, 270, 165, 180, 15, 0]$^{(2)}$, where the values in brackets indicate phase shifts, the inversion profile becomes sharper as seen in Figure (5.7). The iteration procedure consists of phase shifting the initial sequence by the phases indicated above and then concatenating the phase shifted parts. A second interation, Figure (5.7c) results in an even sharper profile; now the inversion profile is smoothed out and has also become more narrowband.

When the z-component of the magnetization goes through 0.00, then the transverse magnetization is at a maximum. The slope of the crossing of M_z from -1 to 1 essentially indicates how narrowband in ω_1 the

signal will be. The x-y component of the magnetization is plotted in the bottom of Figure (5.7). After two iterations of the initial sequence with the 9-pulse scheme two important features are observed in the signal profile: the range of rf field strengths over which the signal exists is very narrow and yet the signal is zero out to rf field strengths which are eight times the nominal value. This is a consequence of the properties of the initial sequence as well as the iteration scheme. These sequences can be used as $\pi/2$ pulses from which signal can be obtained from a very localized region in space.

b. Summary

We have presented a composite pulse sequence, narrowband in space and broadband in frequency, which can be used in conjunction with a surface coil to acquire a chemically shifted NMR signal from a localized region of a sample. The 9 pulse population inversion sequence, used in the NOBLE method, spatially localizes signals in an rf field gradient to a region where the rf amplitude ω_1 approximately satisfies $0.75\omega_1^0 < \omega_1 < 1.25\omega_1^0$, and retains a useful resonance offset range of $-0.3\omega_1^0 < \Delta\omega < 0.3\omega_1^0$. Undesired signals arising from spatial regions where ω_1 is approximately $3\omega_1^0$ are suppressed by using a read sequence that is a broadband composite π pulse near $3\omega_1^0$. It is suggested that adiabatic frequency sweeps may be used to suppress signals from regions where ω_1 is a higher multiple of ω_1^0. A combination of these selective techniques with SHARP spectroscopy[49] may allow high resolution surface coil NMR in the presence of inhomogeneous static fields.

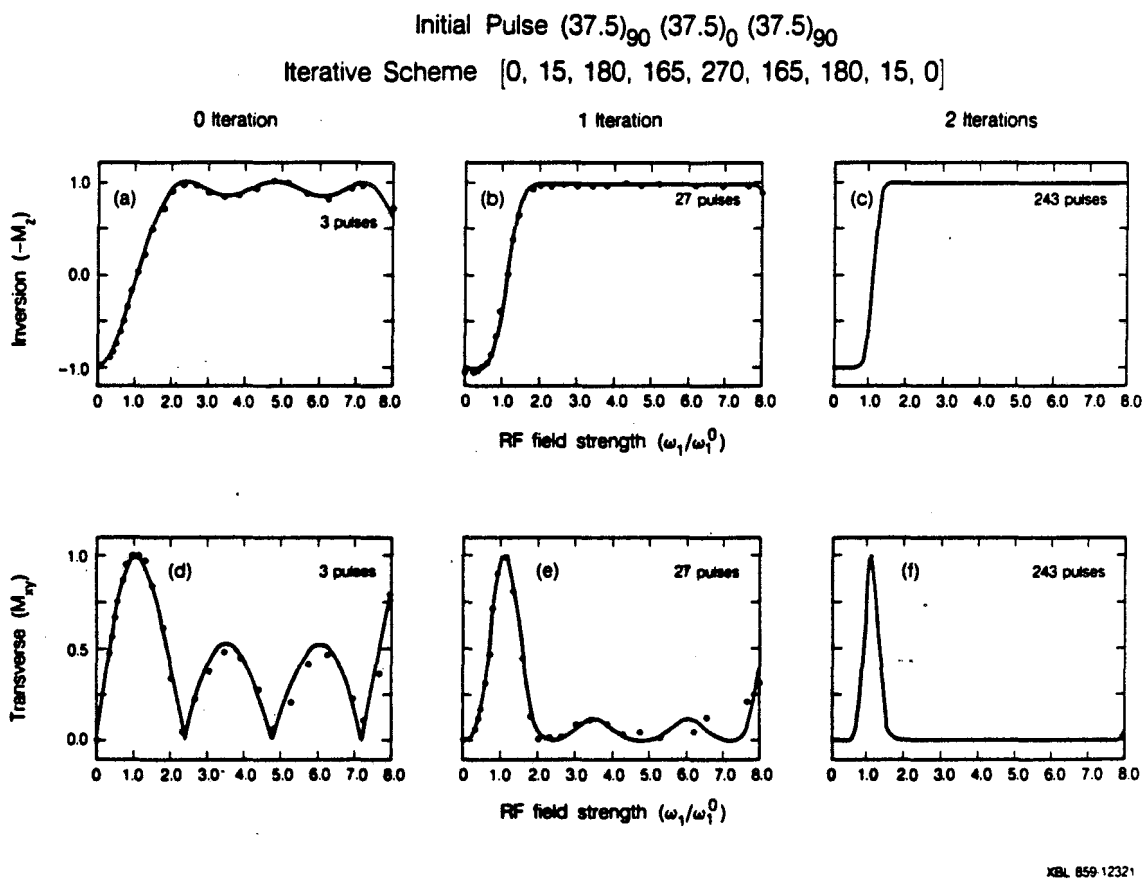

Figure 5.7. Top: Simulations of population inversion as a function of the rf field strength for the sequence $(3.75)_{90}$ $(37.5)_0$ $(37.5)_{90}$(a) and its first two iterates (b) and (c) generated by [0, 15, 180, 165, 270, 165, 180, 15, 0].

Bottom: Simulations of the transverse magnetization M_{xy} as a function of rf field strength for the same pulse sequences as above. In both cases, the features of the inversion (top) and signal (bottom) profile are smoothed out for higher iterations. In addition, the range of rf field strengths over which inversion, or signal, occurs becomes narrower. These sequences can be used as narrowband $\pi/2$ pulses to obtain signal from a very localized region in space.

B. NMR Imaging in Solids by Multiple-Quantum Resonance

1. Introduction

NMR imaging is now a well-established technique for studying biological systems[50]. In its most general form, an imaging method uses a magnetic field gradient to encode the positions of the nuclear spins with a spatially varying Larmor frequency. Once the variations in resonant frequency have been decoded appropriately, an image of the nuclear spin density or, more generally, of any mix of NMR parameters can be created.

In a linear magnetic field gradient, g, the spread of frequencies across a thickness Δz is $g\Delta z$. If features on the order of Δz are to be resolved, then the externally imposed field, $g\Delta z$, must itself be resolved relative to any background or internal field. For solids, the dominant background field is usually the local dipolar field, B_L. In biological systems familiar from ^1H imaging, rapid isotropic molecular motion often averages these internal dipolar fields to zero. However, in a strongly protonated solid, where molecular motion is restricted, a typical value for B_L might be 5G so that a gradient greater than 50 G/cm (0.5T/m) would be needed in order to achieve a resolution of 1 mm. One approach[51-54] to this problem is to reduce the effective local field by a mutliple-pulse line-narrowing sequence.[55-56] The alternative approach is to leave the local field untouched, but to impose a gradient large enough to meet the condition $g \gg B_L/\Delta z$.

2. n-Fold Increase in Gradient Strength

In this section, we demonstrate a prototype imaging experiment for solids based in spirit on this "brute force" method of increasing the gradient, but which relies instead on the properties of multiple-quantum NMR transitions[57] to increase the effective gradient strength by an order of magnitude.[58] Specifically, we intensify the effect of the gradient upon the evolution of the spin system by creating high-order multiple-quantum coherences and following their development in the static field gradient. A multiple-quantum coherence of order $n = M_i - M_j$, where M_i and M_j are the magnetic quantum numbers for high-field states $|M_i\rangle$ and $|M_j\rangle$, evolves n times more rapidly in an inhomogeneous field than the usual single-quantum coherence. That is, if a single-quantum transition in the presence of a field gradient appears with resonance offset $\Delta\omega$, then an n-quantum transition appears at $n\Delta\omega$. This effect was described in Chapter III, Section A.2.b. The linewidths resulting from the effective local dipolar fields do increase with order, as shown in Figure (5.8a); but an n-quantum linewidth does not increase by as much as a factor of n. Therefore, the n-fold increase in gradient strength will still permit rather modest gradients to be used. This feature has been exploited previously in NMR diffusion measurements.[59]

3. Experimental Design

The multiple-quantum pulse sequence, shown in Figure (5.9) is partitioned into preparation, evolution, mixing, and detection

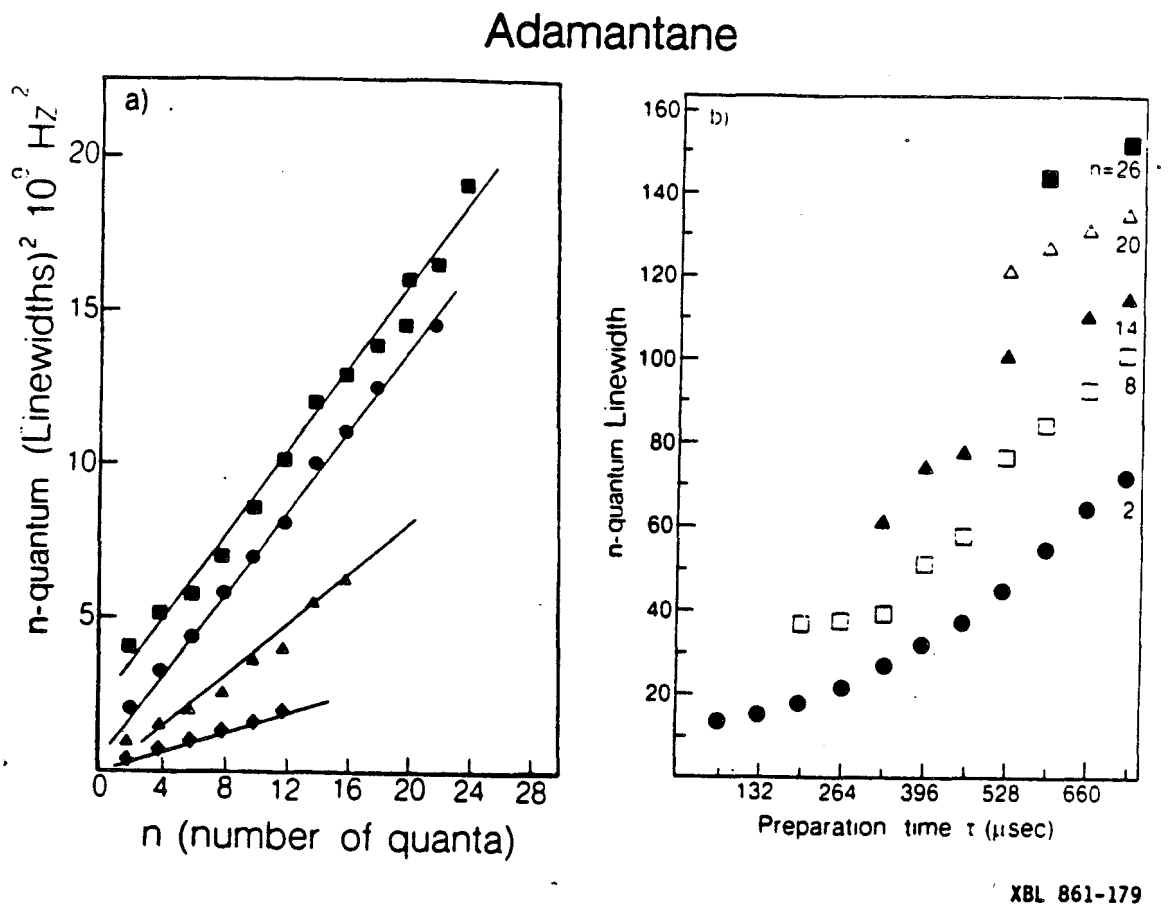

Figure 5.8. a) Square of the linewidth versus n-quantum order in adamantane. The different symbols indicate different preparation times: τ = 660 μsec (squares); τ = 528 μsec (circles); τ = 396 μsec (triangles); τ = 264 μsec (diamonds). The general trend seems to indicate that the linewidth increases with order. b) n-quantum linewidth versus preparation time for dif ferent multiple orders as listed in the figure. The linewidth within an individual order increases for longer preparation times. The multiple-quantum spectra from which these linewidths were calculated were obtained with the pulse sequence shown in Figure (5.9).

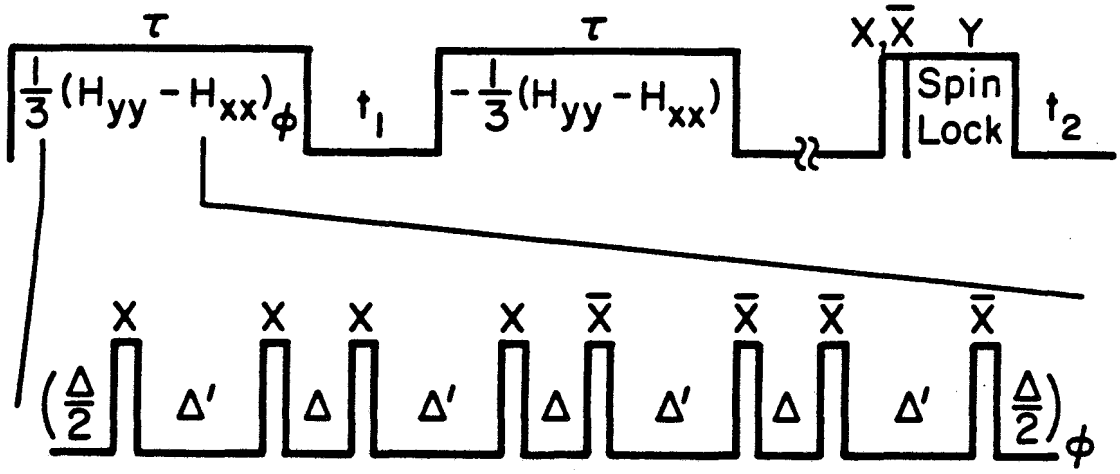

XBL 846-2270

Figure 5.9. The multiple-quantum pulse sequence.
The preparation and mixing periods (τ) comprised of cycles of eight π/2 pulses with duration t_p and rf phases x and x̄, produce average Hamiltonians $\bar{H}^{(o)} = -1/3(H_{yy} - H_{xx})$ for $\Delta' = 2\Delta + t_p$. To separate multiple quantum orders, the relative phase φ between preparation and mixing period is incremented in proportion to the evolution time t_1. About 2 ms after the end of the mixing the z component of magnetization is monitored with an x pulse and a 100μs spinlocking pulse. The time-domain data are Fourier transformed with respect to t_1 to produce the mutliple-quantum spectra of Figure (5.11).

periods. The basic cycle of rf pulses is ($xxxx\bar{x}\bar{x}\bar{x}\bar{x}$), where x and $\bar{x}$ are $\pi/2$ pulses with phases of 0° and 180°, respectively. With the pulse spacing as shown in the figure, the zeroth-order average homonuclear dipolar Hamiltonian is

$$H^{(0)} = \frac{1}{3}(H_{yy} - H_{xx}) = -\sum_{i<j} D_{ij}(I_{yi}I_{yj} - I_{xi}I_{xj}), \tag{5.2}$$

under which coherences of even order can develop in a strongly coupled dipolar system[60]. The coherences then evolve freely for a time t_1 under the influence of the resonance offset and dipolar Hamiltonians,

$$H = \sum_i \Delta\omega_i I_{zi} - \sum_{i<j} D_{ij}(3I_{zi}I_{zj} - \underset{\sim}{I}_i \underset{\sim}{I}_j). \tag{5.3}$$

A phase shift of 90° in the rf pulses creates a time-reversed mixing period[60,61], which is followed by detection of the magnetization using conventional methods. The detection scheme employs spin-temperature inversion[62] to reduce artifacts from reveiver ringing. One point is sampled for each value of evolution time, and the resulting signal is Fourier transformed against t_1. Separation of the multiple-quantum orders according to n is accomplished via the method of time proportional phase incrementation[63] of the pulses in the preparation period. Finally, we alternate the phases of the preparation pulses by 180° to remove any imperfections due to odd-order multiple-quantum contributions.[64]

In imaging experiments the pulse sequence must work properly

under the resonance offsets created by the dc field gradient; in this regard the pulse sequence ($xxxx\bar{x}\bar{x}\bar{x}\bar{x}$) is superior to the ($xx\bar{x}\bar{x}\bar{x}\bar{x}xx$) cycle). The implementation and experimental considerations have been presented in Chapter III, Section E. Though the zeroth order average dipolar and resonance offset Hamiltonians are the same for both cycles, the symmetrization of the first sequence guarantees that the odd-order correction terms to the offset Hamiltonian in the Magnus expansion vanish.[55,56,65] This has been described in more detail in Chapter III, Section D.

4. Experimental Results and Discussion

The phantom used in the multiple-quantum experiment is composed of three parallel glass melting point tubes (1.2 mm i.d., 1.65 mm o.d.), arranged linearly. The center tube is empty, while the outer tubes are loaded with a 4 mm length of compressed adamantane. The sample, consisting of the two cylindrical adamantane plugs (1.3 mm dia. x 4 mm) separated by 2.0 mm, is aligned with its cylindrical axes perpendicular to the z-axis field gradient, as is pictured in the inset of Figure (5.10).

Figure (5.10) shows the 360 MHz ^{1}H single-quantum adamantane spectrum with and without a 48 mT/m field gradient. Although the gradient, which amounts to 20kHz/cm, broadens the line from 12 kHz (full width at half height) to 14.5 kHz, the signals from the two adamantane plugs remain unresolved. The corresponding multiple-quantum spectra of the adamantane phantom are in Figure (5.9). The main peaks represent multiple quantum coherences out to n = 14. Very high-order

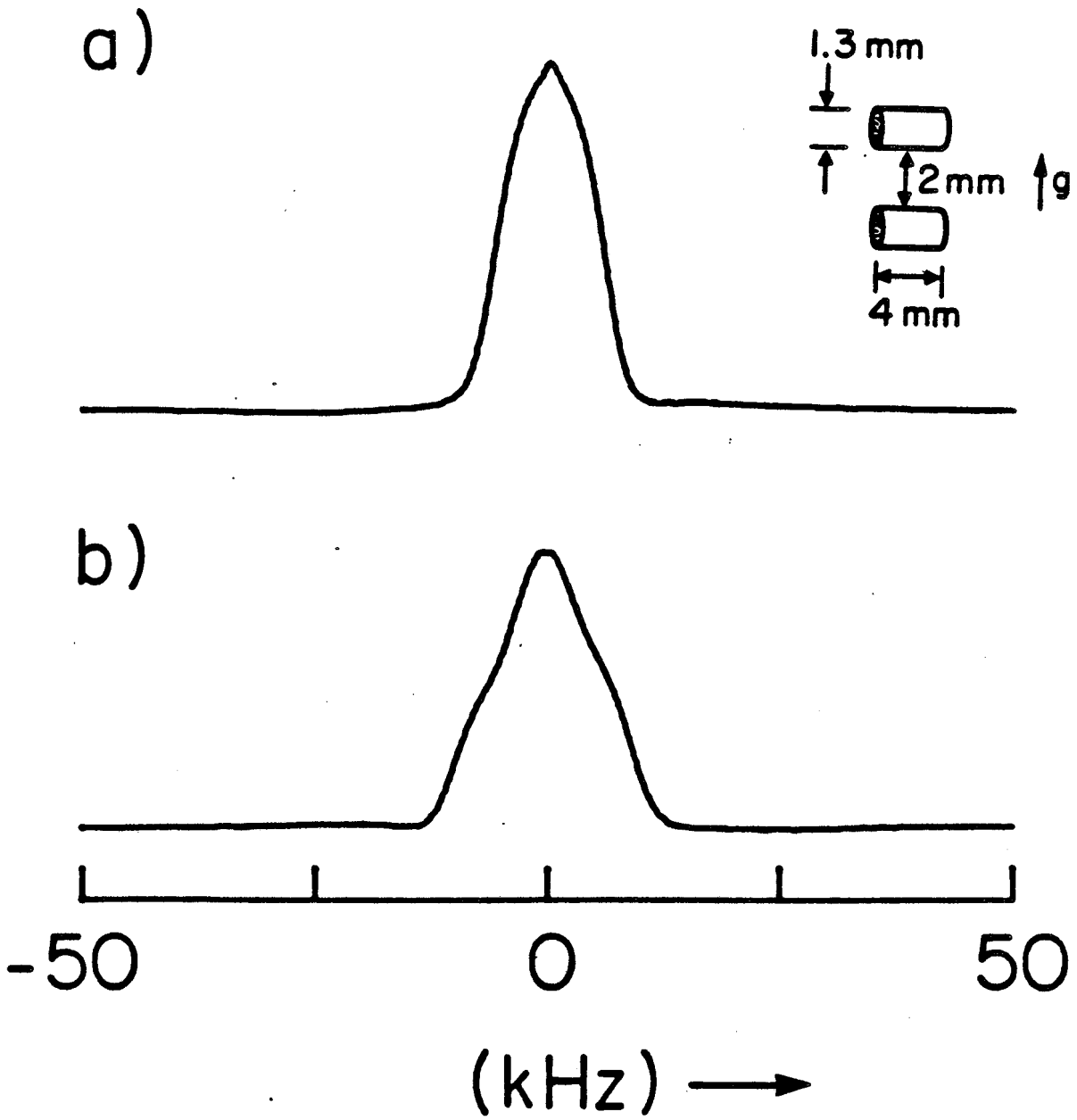

Figure 5.10. Adamantane ^1H (single-quantum) spectra with (b) and without (a) a z gradient of 20kHz/cm. Sample geometry is shown in the inset. The applied gradient is inadequate to resolve the signals from the two adamantane plugs.

coherences ($n > 60$) can be prepared and detected in adamantane[66] but here we have selected, somewhat arbitrarily, a preparation time (τ = 396 μsec) which is sufficient to excite transitions up to $n \approx 20$ with reasonable intensity.

Figure (5.11) clearly demonstrates the attraction of imaging by multiple-quantum resonance. Peaks from the two adamantane plugs just begin to separate at $n = 4$, and are well resolved out at $n = 10$, where the gradient is effectively 10 times larger than for single-quantum coherence.

The multiple-quantum approach also possesses another interesting advantage, which derives from the separation of the evolution and detection periods. The spins are labelled by the static gradient during the evolution period t_1, but are detected later during the t_2 interval. Consequently, while the bandwidth of the evolution frequencies during t_1 might be very great (say 10MHz) in order to facilitate clear separation of the orders, no thermal noise is admitted during this interval. Any thermal noise comes to the receiver during the t_2 interval, but the bandwidth can actually be very narrow here. For imaging, this substantial benefit of the separation of evolution and detection is analagous to the advantage of a pulsed gradient over a steady gradient in diffusion measurements[67]. Realization of this advantage requires that t_1 noise[(57b, p.199)], due to fluctuations in the preparation and mixing periods, be minimized.

We have demonstrated here the essential feature of ^1H imaging by multiple-quantum NMR in strongly coupled solids: spatial resolution is enhanced considerably by the increased effective magnetic gradient

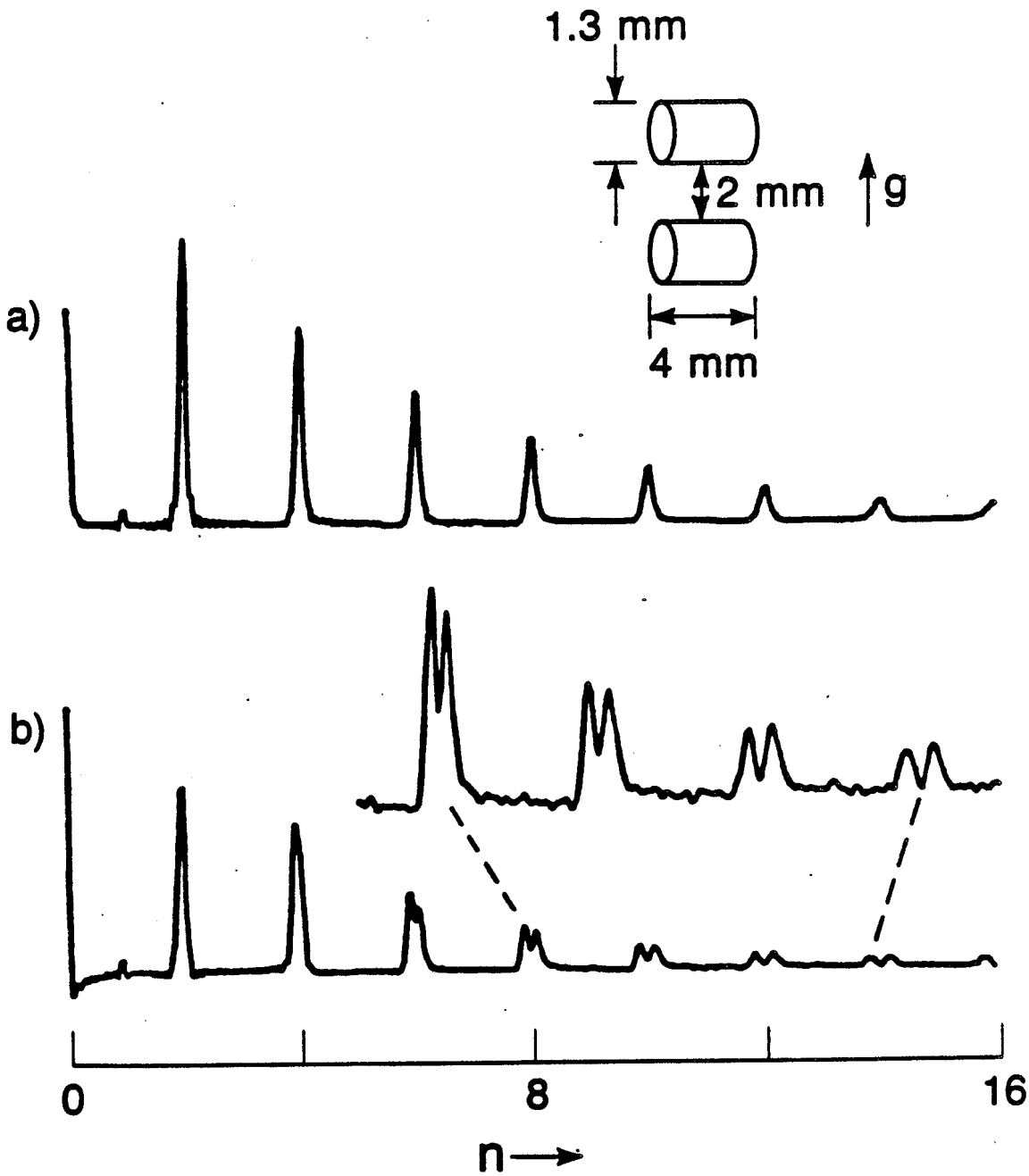

Figure 5.11. Adamantane ^1H (multiple-quantum) spectra with (b) and without (a) a static z gradient. The preparation and mixing times (cf Figure 5.9) are 396μs, corresponding to 6 cycles of the 8 pulse sequence with 3μs π/2 pulses. The t_1 increment is 100 μs and the phase increment is 2π/32; this separates each order by 312.5 kHz. For clarity the vertical scale has been expanded for orders 8-14. Even with a small gradient (20 kHz/cm) the two adamantane plugs can be resolved.

seen by high-order coherences. Although we have displayed transitions of many orders, in an actual imaging scheme it might be advantageous to use only one order. Techniques of mutliple-quantum filtering[68] and of selective preparation[60a] suggest themselves.

C. References

1. R. Tycko and A. Pines, J. Magn. Reson. **60**, 156-160 (1984).

2. J.J.H. Ackerman, T.H. Grove, G.C. Wong, and G.K. Radda, Nature (London) **283**, 167-170 (1980).

3. R. Tycko and A. Pines, Chem. Phys. Lett., **111**, 462-467 (1984).

4. R. Tycko, J. Guckenheimer, and A. Pines, J. Chem, Phys., **83**, 2775-2802 (1985) .

5. A.J. Shaka and R. Freeman, J. Magn. Reson. **59**, 169-176 (1984).

6. A.J. Shaka, J. Keeler, M.B. Smith, and R. Freeman, J. Magn. Reson. **61**, 175-180 (1985).

7. M.H. Levitt and R. Freeman, J. Magn. Reson. **33**, 473-476 (1979).

8. J. Baum, R. Tycko, and A. Pines, Chemical Physics, submitted.

9. D.I. Hoult and R.E. Richards, J. Magn. Reson. **24**, 71 (1976).

10. R. Tycko, H.M. Cho, E. Schneider, and A. Pines, J. Magn. Reson. **61**, 90-101 (1985).

11. M.H. Levitt, J. Magn. Reson. **48**, 234-264 (1982).

12. M.R. Bendall J. Magn. Reson. **59**, 406-429 (1984).

13. M.R. Bendall, in Biomedical Magnetic Resonance. (T.L. James and A.R. Margulis, eds.) p.99, Radiology Research and Education Foundation, San Francisco, 1984.

14. A.J. Shaka and R. Freeman, J. Magn. Reson. **55**, 487-493 (1983).

15. A. Abragam, Principles of Nuclear Magnetism (Oxford University Press, Oxford, 1961), p.44.

16. L. Allen and J.H. Eberley, Optical Resonance and Two Level Atoms (Wiley, New York, 1975), p. 101.

17. J. Baum, R. Tycko, and A. Pines, J. Chem. Phys. **79**, 4643-4644 (1983).

18. J. Baum, R. Tycko, and A. Pines, Phys. Rev. A. **32**, 3435, (1985).

19. P. Bendel, CM. Lai, and P.C. Lauterbur, J. Magn. Reson. **38**,343-356 (1980).

20. P.C. Lauterbur, D.N. Levin, and R.B. Marr, J. Magn. Reson. **59**, 536-541 (1984).

21. M.L. Bernardo, Jr., P.C. Lauterbur, and L.K. Hedges, J. Magn. Reson. **61**, 168 (1985).

22. A. Kumar, D. Welti, and R.R. Ernst, J. Magn. Reson. **18**, 69-83 (1975).

23. T.R. Brown, B.M. Kincaid, and K. Ugurbil, Proc. Nat. Acad. Sci. USA **79**, 3523 (1982).

24. A.A. Maudsley, S.K. Hilal, W.H. Perman, and H.E. Simon, J. Magn. Reson. **51**, 147-152 (1983).

25. J.F. Martin and C.G. Wade, J. Magn. Reson. **61**, 153 (1985).

26. P.C. Lauterbur, D.M. Kramer, W.V. House, Jr., and C.N. Chen, J. Am. Chem. Soc. **97**, 6866 (1975).

27. W.P. Aue, S. Müller, T.A. Cross, and J. Seelig, J. Magn. Reson. **56**, 350-354 (1984).

28. R.E. Gordon, P.E. Hanley, D. Shaw, D.G. Gadian, G.K. Radda, P. Styles, P.J. Bore, and L. Chan, Nature (London) **287**, 736-738 (1980).

29. P.A. Bottomley, J. Magn. Reson. **50**, 335 (1982).

30. K.N. Scott, H.R. Brooker, J.R. Fitzsimmons, H.F. Bennet, and R.C. Mick, J. Magn. Reson. **50**, 339-344 (1982).

31. D.I. Hoult, J. Magn. Reson. **33**, 183-197 (1979).

32. S. Cox and P. Styles, J. Magn. Reson. **40**, 209 (1980).

33. A. Haase, C. Malloy, and G.K. Radda, J. Magn. Reson. **55**, 164-169 (1983).

34. M.R. Bendall and R.E. Gordon, J. Magn. Reson. **53**, 365-385 (1983).

35. M.R. Bendall, Chem. Phys. Lett. **99**, 310-315 (1983).

36. M.R. Bendall and W.P. Aue, J. Magn. Reson. **54**, 149-152 (1983).

37. M.R. Bendall, J.M. McKendry, I.D. Cresshull, and R.J. Ordidge, J. Magn. Reson. **60**, 473-478 (1984).

38. M.R. Bendall, Magn. Reson. in Med. **2**, 91 (1985).

39. M.R. Bendall and D.T. Pegg, J. Magn. Reson. **63**, 494-503 (1985).

40. A.J. Shaka and R. Freeman, J. Magn. Reson. **64**, 145-150 (1985).

41. P.A. Bottomley, T.B. Foster, and R.D. Darrow, J. Magn. Reson.

59, 338-342 (1984).

42. J.L. Evelhoch, M.G. Crowley, and J.J.H. Ackerman, J. Magn. Reson. **56**, 110-124 (1984).

43. M.S. Roos, A. Hasenfeld, M.R. Bendall, R.H. Huesman, and T.F.Budinger, presented at the Third Annual Meeting of the Society of Magnetic Resonance in Medicine, New York, 1984.

44. P. Brunner and R.R. Ernst, J. Magn. Reson. **33**, 83-106 (1979).

45. P.A. Bottomley, Rev. Sci. Instrum. **53**, 1319 (1982).

46. P. Mansfield and P.G. Morris, "NMR Imaging in Biomedicine" (Academic Press, New York, 1982).

47. H. Cho, R. Tycko, A. Pines, and J. Guckenheimer, Phys. Rev. Lett., submitted.

48. H. Cho, R. Tycko, J. Baum, and A. Pines, in preparation.

49. M. Gochin and A. Pines, J. Am. Chem. Soc., in press. M. Gochin, D.P. Weitekamp, and A. Pines, J. Magn. Reson. **63**, 431-437 (1985).

50. (a) P. Mansfield and P.C. Morris, "NMR Imaging in Biomedicine", Adv. Magn. Reson. Suppl. 2, Academic Press, N.Y., 1982, and references therein.
(b) L. Kaufman, L.E. Crooks, and A.R. Margulis ed. "Nuclear Magnetic Resonance in Medicine", Igaku-Shoin, New York, 1981.
(c) P.A. Bottomly, Rev. Sci. Instr. 53, 1319 (1982).
(d) E.R. Andrew, Accts. Chem. Res. 16, 114 (1983).

51. P. Mansfield and P.K. Grannel, A.N. Garroway and D.C. Stalker, Proc. 1st Spec. Colloque Ampere, J.W. Hennel ed., p. 16, Krakow (1973).

52. P. Mansfield and P.K. Grannel, J. Phys. C. **6**, L 442 (1973).

53. R.A. Wind and C.S. Yannoni, J. Magn. Reson. **36**, 269 (1979).

54. H.M. Cho, C.J. Lee, D.N. Shykind, and D.P. Weitekamp, Phys. Rev. Lett. **55**, 1923 (1985).

55. M. Mehring, "Principles of High Resolution NMR in Solids", 2nd ed., Springer-Verlag, New York, 1983.

56. U. Haeberlen, "High Resolution NMR in Solids: Selective Averaging", Adv. Man. Reson. Suppl. 1, Academic Press, N.Y. 1976.

57. (a) G. Bodenhausen, Prog. Nucl. Magn. Reson. Spectrosc. **14**, 137 (1981).
(b) D.P. Weitekamp, Adv. Magn. Reson. **11**, 111 (1983).
(c) M. Munowitz and A. Pines Adv. Chem. Phys., in press.

58. A.N. Garroway, J. Baum, M. Munowitz, and A. Pines, J. Magn. Reson. **60**, 337 (1984).

59. (a) J.F. Martin, L.S. Selwyn, R.R. Vold, and R.L. Vold, J. Chem. Phys. **76**, 2632 (1982).
(b) D. Zax and A. Pines, J. Chem. Phys. **78**, 6333 (1983).

60. (a) W.S. Warren, D.P. Weitekamp and A. Pines, J. Chem. Phys. **73**, 2084 (1980).
(b) Y.-S. Yen and A. Pines, J. Chem. Phys. **78**, 3579 (1983).

61. W. -K. Rhim, A. Pines and J.S. Waugh, Phys. Rev. **B3**, 684 (1971).

62. E.O. Stejskal and J. Schaefer, J. Magn. Reson. **18**, 560 (1975).

63. (a) G. Drobny, A. Pines, S. Sinton, D.P. Weitekamp, D. Wemmer, Faraday Symp. Chem. Soc. **13**, 49 (1979).
(b) G. Bodenhausen, R.L. Vold, J. Magn. Reson. **37**, 93 (1980).

64. A. Pines, D. Wemmer, J. Tang, and S. Sinton, Bull. Am. Phys. Soc. **23**, 21 (1978).

65. U. Haeberlen and J.S. Waugh, Phys. Rev. **175**, 453 (1968).

66. J. Baum, M.G. Munowitz, A.N. Garroway, and A. Pines, J. Chem. Phys. **83**, 2015 (1985).

67. E.O. Stejskal and J.E. Tanner, J. Chem. Phys. **42**, 288 (1965).

68. U. Piantini, O.W. Sorensen, and R.R. Ernst, J. Am. Chem. Soc. **104**, 6800 (1982).

APPENDIX: COMPUTER PROGRAMS

Computer Programs used in Chapter II are versions of CAMPUL, LOPTRAJ and associated subroutines Rabi and RfRabi. The notation in the programs is different from that used in the text. Here

$$\sin \gamma = \frac{1}{\sqrt{1 + (\delta\omega\tau)^2}}$$

or

$$\delta\omega\tau = \frac{1}{\tan \gamma}$$

To simulate the inversion of the MIP over resonance offset, CAMPUL is used. For the linear sweeps and the CAP, the phase function is substituted by

$$\phi(t) = \left(\frac{k}{\omega_1^2}\right) (\omega_1 t)^2$$

and

$$\phi(t) = -\left(q^2 - (\omega_1^0)^2 t^2\right)^{1/2} + q$$

respectively. For all calculations of inversion over resonance offset, subroutine Rabi is used. When the inversion over rf field strengths and/or resonance offset is desired, then rf Rabi must be substituted with appropriate changes in the program.

To calculate the composite pulse sequence from the continuously modulated pulse, a version of Loptraj is used. Again to calculate the best

pulse sequence over offset (as in Loptraj) Rabi is used. Loptraj calculates a pulse sequence with constant phase increments. Minor changes need to be made to calculate a pulse sequence with unrestricted phases; a search over $\delta\omega\tau$ and the cut-off time t_c must be implemented in that case.

For Chapter IV, the program SPLOC5 was designed to find the best pulse sequence for a specified inversion profile over resonance offset and rf field strength.

```
c       Program CAMPUL
c       Calculates inversion over a range of offsets using the MIP phase
c       function.  Flip angles and phases are found directly from MIP by
c       specifying the phase increment.
c
c
        DIMENSION p(3),t(2000),ph2(2000),flip2(2000)
        COMMON theta,ph,flip
c
        pi=4.0*ATAN(1.0)
        radian=180.0/pi
c
        TYPE50
50      FORMAT('$How many resonance offset values?: ')
        ACCEPT*,npt
c
        TYPE60
60      FORMAT('$Enter dw(tau): ')
        ACCEPT*,dwt
c
        TYPE70
70      FORMAT('$Enter the number of pulses: ')
        ACCEPT*,npulse
c
        TYPE65
65      FORMAT('$Enter the increment of the phase in degs: ')
        ACCEPT*,am
c
        TYPE80
80      FORMAT('$What do you want the data file named?: ')
        ACCEPT90,fname
90      FORMAT(A)
        OPEN(UNIT=3,NAME=FNAME,STATUS='NEW')
c
        ione=1
        write(3,39),ione,npt
39      format(i6)
        TYPE95
95      FORMAT('$Enter the offset:')
        ACCEPT*,ext
c
        divs=ext/(npt-1.0)
        voff=0.0
        w1=SQRT(1.0+(dwt*dwt))
        n=(npulse/2.0)+1.0
        amr=am/radian
c
        ph1=amr/2.0
        var=EXP(-ph1/dwt)
        tme=SQRT(1.0-(var*var))
        time=tme/var
        t(1)=ATAN(time)
        ph2(1)=0.0
        flip2(1)=2.0*t(1)
c
        ph1=amr/2.0+amr
c
        DO 200 J=2,n
        var1=EXP(-ph1/dwt)
        tme1=SQRT(1.0-(var1*var1))
        time1=tme1/var1
        t(J)=ATAN(time1)
        ph2(J)=ph1-amr/2.0
```

```
      flip2(J)=(t(J)-t(J-1))
      ph1=ph1+amr
200   CONTINUE
c
      DO 400 I=1,npt
      p(1)=0.0
      p(2)=0.0
      p(3)=1.0
      theta=(pi/2.0)-ATAN(voff)
      freqef=w1/SIN(theta)
c
      DO 500 J=1,n
      K=(n+1)-J
      ph=ph2(K)
      flip=freqef*flip2(K)
      CALL RABI(p)
500   CONTINUE
c
      DO 600 J=2,n
      ph=ph2(J)
      flip=freqef*flip2(J)
      CALL RABI(p)
600   CONTINUE
c
      WRITE(3,40) -p(3)
40    FORMAT(E14.6)
      voff=voff+divs
400   CONTINUE
c
      print540,npulse
540   format(/,15x,i16,1x,'PULSE STEPS')
      print550,dwt,am
550   format(/,5x,'dwtau=',f10.4,5x,'phase increment=',f10.4)
      print560
560   format(//,10x,'PHASE',15x,'FLIP ANGLE',/)
      ph1=0.0
      voff=0.0
      w1=SQRT(1.0+(dwt*dwt))
      theta=(pi/2.0)-ATAN(voff)
      freqef=w1/SIN(theta)
      DO 1000 J=1,n
      K=(n+1)-J
      ph1=ph2(K)*radian
      flip1=freqef*flip2(K)*radian
      PRINT10,ph1,flip1
10    FORMAT(2F18.3)
1000  CONTINUE
c
      DO 1050 J=2,n
      ph1=ph2(J)*radian
      flip1=freqef*flip2(J)*radian
      PRINT20,ph1,flip1
20    FORMAT(2F18.3)
1050  CONTINUE
c
      END
```

```
c       subroutine rabi(p)
c       written by Jim Murdoch.
c       Calculates the evolution of the magnetization vector over a resonance
c       offset resulting from a pulse of specified phase and flip angle.
c
        dimension r(3,3),p(3),pp(3)
        common voff,ph,flip
c
        voff2=voff*voff
        veff2=voff2 + 1.0
        veff=sqrt(veff2)
        vt=veff*flip
        cvt=cos(vt)
        svt=sin(vt)
        cp=cos(ph)
        sp=-sin(ph)
c
        aa=(1.0 + voff2*cvt) / veff2
        cc=voff * (1.0 - cvt) / veff2
        ff=svt / veff
        dd=-voff * ff
c
        cccp=cc * cp
        ccsp=cc * sp
        ffcp=ff * cp
        ffsp=ff * sp
c
        cp2=cp * cp
        sp2=sp * sp
        qq=(cvt - aa) * cp * sp
c
        r(1,1)=aa*cp2 + cvt*sp2
        r(1,2)=qq - dd
        r(1,3)=cccp + ffsp
        r(2,1)=qq + dd
        r(2,2)=cvt*cp2 + aa*sp2
        r(2,3)=-ccsp + ffcp
        r(3,1)=cccp - ffsp
        r(3,2)=-ccsp - ffcp
        r(3,3)=(voff2 + cvt) / veff2
c
        do 20 i=1,3
        sum=0.0
        do 10 j=1,3
10      sum=sum  +  r(i,j) * p(j)
20      pp(i)=sum
c
        do 30 i=1,3
30      p(i)=pp(i)
c
        return
        end
```

```
      subroutine rfrabi(p)
c
c     Adapted from subroutine Rabi to allow for resonance offset
c     effects and different rf field strengths simultaneously.
      dimension r(3,3),p(3),pp(3)
      common voff,ph,flip,rf
c
      rf2=rf*rf
      voff2=voff*voff
      veff2=voff2 + rf2
      veff=sqrt(veff2)
      vt=veff*flip
      cvt=cos(vt)
      svt=sin(vt)
      cp=cos(ph)
      sp=-sin(ph)
c
      aa=(rf2 + voff2*cvt) / veff2
      cc=voff*rf* (1.0 - cvt) / veff2
      ff=svt*rf/veff
      dd=-voff * ff/rf
c
      cccp=cc * cp
      ccsp=cc * sp
      ffcp=ff * cp
      ffsp=ff * sp
c
      cp2=cp * cp
      sp2=sp * sp
      qq=(cvt - aa) * cp * sp
c
      r(1,1)=aa*cp2 + cvt*sp2
      r(1,2)=qq - dd
      r(1,3)=cccp + ffsp
      r(2,1)=qq + dd
      r(2,2)=cvt*cp2 + aa*sp2
      r(2,3)=-ccsp + ffcp
      r(3,1)=cccp - ffsp
      r(3,2)=-ccsp - ffcp
      r(3,3)=(voff2 + cvt*rf2) / veff2
c
      do 20 i=1,3
      sum=0.0
      do 10 j=1,3
10    sum=sum  +  r(i,j) * p(j)
20    pp(i)=sum
c
      do 30 i=1,3
30    p(i)=pp(i)
c
      return
      end
```

```
c       Program LOPTRAJ
c       Calculates a sequence of radiofrequency pulses from the
c       inversion trajectory of the continuously modulated pulse(MIP).
c       This program finds the best composite pulse, broadband over
c       resonance offset, with constant phase increments.
c
        dimension zw(2000),p(3),x(2000),y(2000),z(2000),difx(2000),
     1  dify(2000),th(2000),thp(2000),m1cm2x(2000),m1cm2y(2000),
     1  m1cm2z(2000),w1x(2000),w1y(2000),w1z(2000),dot(2000),
     1  mult(2000),xp(2000),yp(2000),zp(2000),mp(2000),
     1  m12dot(2000),m12nor(2000),coef(2000),m12flp(2000),time(2000),
     1  bth(300),bflip(300),bvoff(300),bcomp(300)
        common voff,ph,flip
        real m1cm2x,m1cm2y,m1cm2z,mult,mp,m12dot,m12nor,m12flp
c
c       Enter initial parameters:
c       npulse: number of pulses in the sequence
c       ndwt: total number of dwt over which to search
c       dwt0: initial value of dwt
c       ddwt: increment in dwt
c       npt: number of points to calculate over a range of offsets
c       vmx: highest value of resonance offset
c       deg: value of the constant phase increment
c
        do 2000 npulse=4,12,4
        ndwt=400
        dwt0=1.0
        ddwt=0.1
        npt=30
        vmx=1.5
        deg=30.0
c
1       bestave=-1.0
        divs=vmx/(npt-1.0)
        dwt=dwt0
        pi=4.0*ATAN(1.0)
        radian=180.0/pi
c
c       Calculate the times which correspond to the chosen phase increment
c
        do 1000 id=1,ndwt
        sum=0.0
        n=npulse/2.0
        q=deg/radian*n
        qn=q/n
        do 5 K=1,n
        var=EXP(-(K*qn)/dwt)
        tme=SQRT(1.0-(var*var))/var
        time(K)=ATAN(tme)
5       continue
c
        ratt0=pi/2.0
        v10=SQRT(1+(dwt*dwt))
        dt=2.0*ratt0/FLOAT(npulse)
c
        x(1)=0.0
        y(1)=0.0
        z(1)=1.0
c
        do 10 I=2,npulse
        K=I-1.0
        J=n-K
```

```
      if(J.eq.0.0) go to 12
      if(J.lt.0.0) go to 13
      tt=-1.0*time(J)
      go to 14
12    tt=0.0
      go to 14
13    J=-1.0*J
      tt=time(J)
c
c     Calculate the on-resonance inversion for a value of dwt
c
14    val=COS(tt)
      pht=-dwt*ALOG(val)
      x(I)=(dwt/v10*val*COS(pht))+(1.0/v10*val*SIN(pht))
      y(I)=(dwt/v10*val*SIN(pht))-(1.0/v10*val*COS(pht))
      z(I)=-SIN(tt)
      tt=tt+dt
10    continue
c
      x(npulse+1)=0.0
      y(npulse+1)=0.0
      z(npulse+1)=-1.0
c
c     Calculation of the constant phase pulse that gives the same
c     evolution of the magnetization between t1 and t2 as the
c     continuously modulated pulse.
c
      do 20 J=2,npulse+1
      difx(J)=x(J)-x(J-1)
      dify(J)=y(J-1)-y(J)
      th(J)=ATAN(difx(J)/dify(J))
      thp(J)=th(J)+pi
20    continue
c
      do 30 I=2,npulse+1
      m1cm2x(I)=(y(I-1)*z(I))-(z(I-1)*y(I))
      m1cm2y(I)=(z(I-1)*x(I))-(x(I-1)*z(I))
      m1cm2z(I)=(x(I-1)*y(I))-(y(I-1)*x(I))
      w1x(I)=v10*COS(th(I))
      w1y(I)=v10*SIN(th(I))
      w1z(I)=v10*0.0
      dot(I)=(m1cm2x(I)*w1x(I))+(m1cm2y(I)*w1y(I))+(m1cm2z(I)*w1z(I))
      IF(dot(I).GE.0.0) go to 30
      th(I)=thp(I)
30    continue
c
      IF(th(2).ge.0.0) go to 21
      th(2)=th(2)+pi*2.0
21    difth=(th(2)-th(3))*radian
      IF(difth.ge.0.0) go to 22
      difth=difth+360.0
22    nth=difth/45.0
      mth=2*(difth/45.0-nth)
      lth=nth+mth
      gth=lth*45.0/radian
      th(2)=th(3)+gth
      th(npulse+1)=th(2)
c
      do 50 J=3,npulse
      do 35 I=J-1,J
      mult(I)=(x(I)*COS(th(J)))+(y(I)*SIN(th(J)))
      xp(I)=x(I)-(mult(I)*COS(th(J)))
      yp(I)=Y(I)-(mult(I)*SIN(th(J)))
```

```
      zp(I)=z(I)
      mp(I)=SQRT((xp(I)**2)+(yp(I)**2)+(zp(I)**2))
35    continue
c
      m12dot(J)=(xp(J-1)*xp(J))+(yp(J-1)*yp(J))+(zp(J-1)*zp(J))
      m12nor(J)=mp(J-1)*mp(J)
      coef(J)=m12dot(J)/m12nor(J)
      IF(coef(J).EQ.0.0) GO TO 49
      IF(coef(J).GT.0.0.AND.coef(J).LE.1.0) GO TO 48
      m12flp(J)=ATAN(SQRT(1.0-coef(J)*coef(J))/coef(J))+pi
      go to 50
48    m12flp(J)=ATAN(SQRT(1.0-coef(J)*coef(J))/coef(J))
      go to 50
49    m12flp(J)=pi/2.0
50    continue
      m12flp(2)=ATAN((x(2)*SIN(th(2))-y(2)*COS(th(2)))/z(2))
      m12flp(npulse+1)=m12flp(2)
c
c     Calculation of the inversion of the magnetization over
c     resonance offsets resulting from the newly found composite
c     pulse.
c
      sum=0.0
      voff=0.0
c
      do 60 J=1,npt
      p(1)=0.0
      p(2)=0.0
      p(3)=1.0
c
      do 70 I=2,npulse+1
      ph=th(I)
      flip=-m12flp(I)
      CALL RABI(p)
70    continue
c
      sum=sum-p(3)
      voff=voff+divs
60    continue
      ave=sum/npt
c
      if(ave.lt.bestave) go to 1000
      bdwt=dwt
      btc=time(n)
      bestave=ave
      do 80 I=2,npulse+1
      bth(I)=th(I)
      bflip(I)=m12flp(I)
80    continue
      voff=0.0
      divs1=0.1
      do 85 j=1,21
      p(1)=0.0
      p(2)=0.0
      p(3)=1.0
      do 87 I=2,npulse+1
      ph=th(I)
      flip=-m12flp(I)
      CALL RABI(p)
87    continue
      bvoff(J)=voff
      bcomp(J)=-p(3)
      voff=voff+divs1
```

```
85      continue
c
c       Search through all values of dwt to find the best inversion
c       performance.
c
1000    dwt=dwt+ddwt
c
        print500,npulse
500     format(///,' BEST AVERAGE CRITERION FOR',i10,1x,'PULSE STEPS')
        print550,npt,vmx
550     format(/,5x,' an average over',i4,1x,'values of woff/w1 from ',
     1  '0 to',f8.4)
        print600,ndwt,dwt0,ddwt
600     format(/,5x,i4,1x,'values of dwt',8x,'initial value:',f8.4,5x,
     1  'increment:',f8.4,/)
        print650,bestave,vmx
650     format(/,5x,'(-W )=',f9.6,' from 0 to',f8.4)
        print700,bdwt,btc
700     format(/,' The best dwt=',f8.4,2x,' The cut off time=',f8.4)
        print701,deg
701     format(/,5x,'The phase incr.in deg=',f5.1)
        print702
702     format(//,5x,'FLIP ANGLE',5x,'PHASE')
        do 90 I=2,npulse+1
        print710,bth(I)*radian,bflip(I)*radian
710     format(5x,f10.5,3x,f10.5)
90      continue
        print705
705     format(//,5x,'OFFSET',12x,'Z-MAG.')
        do 100 J=1,21
        print720,bvoff(J),bcomp(J)
720     format(5x,f10.6,3x,f10.7)
100     continue
        if(deg.eq.90.0) go to 780
        if(deg.eq.45.0)go to 760
        if(deg.eq.30.0) go to 750
750     deg=45.0
        go to 1
760     deg=90.0
        go to 1
c
780     vmx=vmx-0.2
        deg=30.0
        if(vmx.LE.0.4) go to 2000
        go to 1
2000    continue
c
        end
```

```
c       Program SPLOC5
c       Program finds the best pulse sequence for a specified
c       inversion profile over resonance offset and rf field
c       strengths.
c
        Dimension p(3),flipp(100),rf1(100),voff1(100),bflip(10,100),
     1  bphase(10,100),flinc(500),phinc(100),flipmin(100),
     1  phmax(100),phmin(100),phase(100),flipmax(100),av(100),
     1  desinv(100),deswgt(100)
c
        Common voff,ph,flip,rf
c
        type*,'Number of pulses'
        accept*,npulse
        type*,'All initial flip angles'
        accept*,(flipmin(I),I=1,npulse)
        type*,'Incr. of phases 1 to NP'
        accept*,(flinc(I),I=1,npulse)
        type*,'Max.flip angles 1 to NP'
        accept*,(flipmax(I),I=1,npulse)
        type*,'All initial phases'
        accept*,(phmin(I),I=1,npulse)
        type*,'Incr. of phases 1 to NP'
        accept*,(phinc(I),I=1,npulse)
        type*,'Max. phase 1 to NP'
        accept*,(phmax(I),I=1,npulse)
        type*,'Number of offset values'
        accept*,nof
        type*,'Values of offsets from min to max value'
        accept*,(voff1(I),I=1,nof)
        type*,'Number of rf values'
        accept*,nrf
        type*,'Values of rf from min to max'
        accept*,(rf1(I),I=1,nrf)
        type*,'Enter desired inversion at each rf point'
        accept*,(desinv(I),I=1,nrf)
        type*,'Enter weighting at each rf point'
        accept*,(deswgt(I),I=1,nrf)
c
c       set up dummy pulse sequences and variances
c
        ipulse=(npulse/2.0)+1.0
        iv=1
        av(1)=10
30      do 20 K=1,npulse
        bflip(iv,k)=90
        bphase(iv,k)=270
20      continue
        iv=iv+1
        av(iv)=av(iv-1)+10
        if(iv.gt.5)go to 1
        go to 30
c
c       Initialize parameters
c
1       pi=4.0*ATAN(1.)
        radian=180.0/pi
        do 10 I=1,npulse
        flipp(I)=flipmin(I)
        phase(I)=phmin(I)
10      continue
        rf1(nrf+1)=0.0
        voff1(nof+1)=0.0
```

```
      flag=0.0
      npt=nof*nrf
c
2     sum=0.0
      phase(ipulse)=0.0
      phase(1)=phase(npulse)
      I=1
3     phase(I+1)=phase(npulse-I)
      if(I.ge.ipulse) go to 90
      I=I+1
      go to 3
c
90    flipp(1)=flipp(npulse)
      I=1
4     flipp(I+1)=flipp(npulse-I)
      if(I.ge.ipulse) go to 150
      I=I+1
      go to 4
c
c     Calculate inversion over specified offsets and rf values
c     for an N pulse sequence
c
150   voff=voff1(1)
      do 100 Kf=1,nof
      rf=rf1(1)
      do 200 kr=1,nrf
      p(1)=0.0
      p(2)=0.0
      p(3)=1.0
c
      do 300 I=1,npulse
      flip=flipp(I)/radian
      ph=phase(I)/radian
      call rfrabi(p)
300   continue
      var=desinv(Kr)+p(3)
      var=var*var*deswgt(Kr)
160   sum=sum+var
c
200   rf=rf1(kr+1)
100   voff=voff1(kf+1)
c
      avar=sum/npt
      if(avar.ge.av(5)) go to 2000
      av(5)=avar
      if(av(5).ge.av(4).and.av(5).ge.av(3).and.av(5).ge.av(2).and.
     1 av(5).ge.av(1)) then
      iv=5
      go to 1600
      end if
      if(av(4).ge.av(5).and.av(4).ge.av(3).and.av(4).ge.av(2).and.
     1 av(4).ge.av(1)) then
      iv=4
      go to 1500
      end if
      if(av(3).ge.av(5).and.av(3).ge.av(4).and.av(3).ge.av(2).and.
     1 av(3).ge.av(1)) then
      iv=3
      go to 1500
      end if
      if(av(2).ge.av(5).and.av(2).ge.av(4).and.av(2).ge.av(3).and.
     1 av(2).ge.av(1)) then
      iv=2
```

```
      go to 1500
      end if
      iv=1
1500  aver=av(5)
      av(5)=av(iv)
      av(iv)=aver
      do 1200 k=1,npulse
      bflip(5,k)=bflip(iv,k)
      bphase(5,k)=bphase(iv,k)
1200  continue
1600  do 1000 k=1,npulse
      bflip(iv,k)=flipp(k)
      bphase(iv,k)=phase(k)
1000  continue
c
c     Increment values of phases
c
2000  if=ipulse
2500  flipp(if)=flipp(if)+flinc(if)
      if(flipp(if).le.flipmax(if)) go to 2
      flipp(if)=flipmin(if)
      if=if+1
      if(if.le.npulse) go to 2500
c
      ip=ipulse+1
3000  phase(ip)=phase(ip)+phinc(ip)
      if(phase(ip).le.phmax(ip)) go to 2
      phase(ip)=phmin(ip)
      ip=ip+1.0
      if(ip.le.npulse) go to 3000
c
      print*,'flag=',flag
      print*,'Five best flip angles and phases'
      do 4000 iv=1,5
      print*,(bflip(iv,I),I=1,npulse)
      print*,(bphase(iv,I),I=1,npulse)
      print*,'variance=',av(iv)
      print*,'     '
      print*,'     '
4000  continue
      end
```